**School of Science and Engineering**
**Department of Petroleum Engineering**

# Experimental and PFC2D numerical study of progressive shear behaviour of single rough rock fractures

**Mohammad Sadegh Asadi**

**This thesis is presented for the Degree of**
**Doctor of Philosophy of**
**Curtin University of Technology**

**April 2011**

## *Declaration*

*To the best of my knowledge and belief this thesis contains no material previously published by any other person except where due acknowledgment has been made. This thesis contains no material which has been accepted for the award of any other degree or diploma in any university.*

*Name:*

*Signature:* *Date:*

# Abstract

This thesis investigates the progressive shear behaviour and asperity degradation of single rough rock fractures using 2D numerical simulations and laboratory experiments.

The particle flow code (PFC) was chosen for simulation purposes in this work. The fracture and intact sample are modelled as an assembly of circular disks in PFC2D. By performing biaxial test simulations in PFC2D, correlations were obtained between micro and macro properties of the intact sample. These results were used later for guidance to establish the micro properties of models corresponding to mortar samples, based on the macro response obtained from the lab experiments. To define a set of micro properties corresponding to fracture particles and investigate their effects on shear behaviour of both planar and rough fractures, a sensitivity analysis of fracture model micro properties including particle size, particle friction coefficient, and contact bond strength were carried out.

Several synthetic profiles with triangular and sinusoidal geometries were simulated to study their shear behaviour. A prior knowledge of the shearing response of such simple geometries allowed calibration of the model to be made. The results confirmed the observation of different failure modes, i.e. sliding, asperity cut-off, and degradation, as a result of increasing the normal stress. The simulation results were compared with lab experiments that were carried out on synthetic samples with constant height elevations along their thickness. This was the closest geometry that could be used to calibrate 2D models, and a good agreement was found between the results of the two approaches.

The lab shear tests were conducted using a fracture shear cell (FSC). This was a special set up made from modifications on an existing triaxial stress cell. The FSC was capable of applying large shear and normal loads to the sample where the normal load was applied in a constant rate using a pressure cylinder.

Both lab experiments and simulations were performed on pseudo-real as well as rock-like fracture specimens. The directionality in shear strength when the sample was sheared in opposite directions along a horizontal plane was also studied. The 1D Riemannian dispersion parameter ($D_{R1}$) was determined for different profiles' geometries as a measure of roughness. This parameter showed a good correlation with the profile's shear strength. The spline fits to the peak shear strength data for triangular profile geometry as well as the number of rock fracture profiles obtained from literature were developed and presented. A detailed discussion on the simulations and lab experiments will be given and the results presented and interpreted.

# Acknowledgements

Foremost, I want to convey my sincere gratitude to my supervisor, Dr. Vamegh Rasouli for his generous help, support, constant encouragement, and motivation through the hard times I had during my PhD candidacy.

I wish to thank Professor Brian Evans, head of the Department of Petroleum Engineering, Curtin University and chairperson of the thesis committee, for the support and advice offered during my candidacy.

I would like to thank Dr. Yanhua Zhang, associate supervisor of this thesis committee, for the useful technical advice provided to improve the quality of my numerical works.

I also want to express my gratitude to people at the Department of Petroleum Engineering, Curtin University with whom I have had useful discussions and who have provided both friendship and inspiration for my work. Specifically, I would like to thank Mr. Mohammad Sarmadivaleh and Ali Saeedi, PhD students of the department, for their help during my lab experiments.

This work was funded by the Curtin International Research Postgraduate Scholarship (CIRPS). Its support is greatly acknowledged.

I acknowledge Dr. John Harrison for his valuable technical comments, especially at the beginning of this work, and Dr. Peter Cundall for his comments and for providing a code.

Lastly, special thanks go to my beloved parents who never stop giving me their immense support, encouragement and love. I'm proud to be your son! I also express thanks to my brother and sister for their support and kindness.

***To***

***my father and mother***

***for their love and support.***

# Contents

*Page*

## Chapter 4 Laboratorial fracture shear tests



## Chapter 5 Summary, conclusions and recommendations



## Appendixes

# List of figures

*Page*

# List of tables

*Page*

# Nomenclature

| | |
|---|---|
| $\alpha$ | Cut-off angle |
| $\alpha_s$ | Proportion of fracture surface which is sheared |
| $A$ | Amplitude parameter |
| $A_s$ | Contact area over which asperities are being sheared |
| ASTM | American Society for Testing of Material |
| $\beta$ | Shear failure angle |
| BPM | Bonded Particle Model |
| $c$ ($c_r$) | Intact rock cohesion |
| $c_1$ and $c_2$ | Asperity chords |
| $C_f$ | Fracture cohesion |
| CBS | Contact Bond Strength |
| CNL | Constant Normal Load |
| CNS | Constant Normal Stiffness |
| CYM | Continuously Yielding Model |
| $D$ | Fractal dimension |
| $D_{R1}$ | 1D Riemannian Dispersion parameter |
| $D_{R2}$ | 2D Riemannian Dispersion parameter |
| $d_n$ | Dilation angle |
| DEM | Discrete Element Method |
| DHPC | Duplex High Pressure Cylinder |
| $\Delta U_i^s$ | Increment of shear displacement |
| $\Delta F_i^s$ | Increment of shear force |
| $E$ | Young's modulus |
| $E_c$ | Contact elastic modulus |
| $\eta$ | Initial degree of interlocking of the asperities |
| $F_i^n$ | Total normal force |
| FEM | Finite Element Method |
| FSC | Fracture Shear Cell |
| $\phi$ | Friction angle |
| $\phi_B$ | Basic friction angle |
| $\phi_f$ | Fracture friction angle |
| $\phi_r$ | Residual friction angle |

| | |
|---|---|
| $h$ | Asperity height |
| $i$ | Average asperity angle |
| ISRM | International Society of Rock Mechanics |
| JCS | Joint Compressive Strength |
| JRC | Joint Roughness Coefficient |
| $k_n$ | Normal stiffness |
| $k_s$ | Shear stiffness |
| LR | Left to Right |
| $\mu$ | Particle friction coefficient |
| $\nu$ | Poisson's ratio |
| PFC | Particle Flow Code |
| $R_{ave}$ | Average Particle radius |
| REV | Representative Elementary Volume |
| RL | Right to Left |
| $S_i$ | Sampling interval |
| $\sigma_1$ | Maximum principal stress |
| $\sigma_3$ | Minimum principal stress |
| $\sigma_c$ | Confining stress |
| $\sigma_{ci}$ | Intact rock compressive strength |
| $\sigma_n$ | Normal stress |
| $\sigma_n\big\vert_{\alpha=0}$ or $\sigma_n^T$ | Critical normal stress |
| $\sigma_r$ | Transition normal stress |
| $\tau$ | Shear stress |
| $\tau_p$ | Peak shear strength |
| $\tau_r$ | Residual shear strength |
| TTSC | True Triaxial Stress Cell |
| $\theta$ | Asperity angle |
| UDEC | Universal Distinct Element Code |
| UCS | Uniaxial Compressive Strength |
| $U$ | Shear displacement |
| $U_n$ | Total normal displacement |
| $V$ | Normal displacement |
| $V$ | Dilation rate |

## Publications of this thesis

Asadi, M.S., and Rasouli, V., 2011, A DEM simulation proposed to estimate shear strength of rough rock fractures. Submitted to Rock Mechanics and Rock Engineering Jouranl.

Asadi, M.S., and Rasouli, V., 2011, A laboratory fracture shear cell used for simulation of fracture reactivation. Published in Australian Petroleum Production Exploration Association Journal (APPEA).

Asadi, M.S., and Rasouli, V., 2011, PFC2D simulation of directionality in rough fractures shear strength, *in* Itasca Consulting Group, I., ed., 2nd International FLAC/DEM Symposium: Melbourne, Australia.

Asadi, M.S., and Rasouli, V., 2010, Direct shear test simulation of real rough rock fractures. Published in the proceedings of Eurock2010 Symposium: Luasanne, Zwitzerland.

Asadi, M.S., Rasouli, V., and Zhnag, Y., 2010, Coupled Hydro Geomechanical Simulation and Analysis of Fault Reactivation: Influence of Fault Geometry. SPE paper 133070. APOGCE Symposium: Brisbane, Australia.

Asadi, M.S., Rasouli, V., and Tokhmechi, B., 2009, Wavelet analysis of JRC exemplar profiles. Published in the proceedings of Eurock2009 Symposium: Dubrovnik, Croatia, p. 215-220.

# 1 Shear behaviour of rough fractures

A good understanding of the parameters affecting the mechanical response of natural fractures is essential in any rock engineering project for design purposes. Shearing deformation of rock fractures is one of the incidents that affect the stability of rock masses. It is well understood that the morphology of the fracture surfaces (referred to as roughness) plays a major role on hydromechanical behaviour of the fractures. In this thesis, the effect of fracture morphological parameters on shear strength will be studied.

In this Chapter after a brief review of the shear behaviour of rock fractures, the importance of fracture surface morphology on deformation mechanism of shearing fractures will be discussed and the need for further studying this concept will be highlighted. This will be followed by the outline, objectives and significance of this research work and the thesis structure.

## 1.1 Introduction to rock fractures

### 1.1.1 Geometrical properties

In general the rock mass is the total in situ medium containing structural features such as fractures or faults, and rock material refers to the intact rock between discontinuities. In rock mechanics, the term discontinuity refers to any fractures or features of negligible tensile strength within the rock mass (Brady and Brown, 1993). The most common discontinuities are fractures and bedding planes, although faults are an example of large size discontinuities. Discontinuities can have a dominant effect on the response of a rock mass to rock engineering operations. For example, blocks adjacent to a rock face subject to low normal stress may fail because of the existence of an unfavourably oriented discontinuity (Jaeger et al., 2007). As another example, in high stress zones adjacent to an underground excavation (e.g. wellbores), discontinuities can provide planes for shear failure (FJÆR et al., 2008). Moreover, large scale discontinuities (i.e. faults) are prone to slide under critical static and dynamic loads; once the ratio of shear to normal stress acting on fault plane exceeds the frictional strength of the fault surface (Jafari et al., 2003; Sagy et al., 2007).

The word „discontinuity" denotes any separation in the rock continuum having substantially zero tensile strength and is used without any genetic connotation. The word „joint" or „fracture" or „fault" describe discontinuities formed in different geological conditions (Hudson and Harrison, 1997). The term „rock fracture" is used to describe the mechanical discontinuities of geological origin that intersect almost all rock masses. In current study, as we are studying the mechanical discontinuities, the term rock fracture is used throughout the thesis.

The International Society for Rock Mechanics (ISRM) in 1978 has suggested methodologies for determining ten fundamental properties of discontinuities: orientation, spacing, extent, roughness, aperture, filling, wall strength, seepage, number of sets and block size. Figure 1.1 shows these parameters schematically and definitions of these parameters can be found in many rock mechanics textbooks; for example, Hudson and Harrison (1997). In this research work the effect of surface roughness on shear behaviour and asperity degradation of rock fractures will be studied in particular.

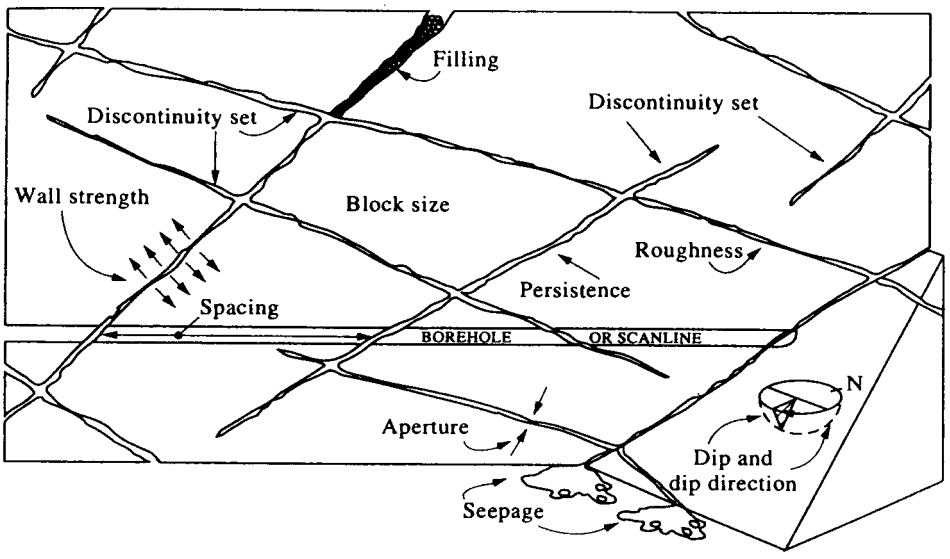


Figure 1.1 Ten discontinuity parameters (from Hudson and Harrison, 1997).

The presence of discontinuities in the form of fractures and other planes of weakness decreases the ultimate strength and stiffness of a rock mass (Brady and Brown, 1993; 2004). Therefore, it is important to quantify the mechanical response of rock fractures in the design, construction, and operation of surface and underground rock structures. One of the most important mechanical characteristic of a rock fracture is its shear strength which will be discussed in Section 1.2.

The topographical features of rock surfaces (i.e. roughness) can affect the mechanical properties of rock masses. For example, as will be discussed later in this

Chapter, the behaviour of two adjacent blocks with a rough interface shearing along the interface is usually affected by the topographical nature of each shearing block. It can be imagined how variation of surface roughness can facilitate or impede the process of shearing.

### 1.1.2 Surface morphology characterisation

In order to describe the complex topography of discontinuities, a large number of parameters may be required. Therefore, characterising or measuring roughness especially as a quantitative parameter is very difficult. Although some parameters have been proposed based on different approaches, few of them are able to represent the effect of roughness and its intrinsic properties on the behaviour of discontinuous rock masses. This is due to the high complexity of rock fracture surface topography.

Patton, in 1966 introduced first and second order asperities reffered to also as waviness and roughness, respectively (see Figure 1.2). Brady and Brown (1993) defined roughness as „a measure of the inherent surface unevenness and waviness of the discontinuity relative to its mean plane" (Figure 1.2.a). Surface irregularities with shorter wavelengths are known as unevenness or particularly roughness (Figure 1.2.b), but larger scale undulation with longer wavelengths is known as waviness. Traditionally, asperity angle, $i$, refers to surface roughness which accounts for all the small and large undulations and wavelengths, as shown in Figure 1.2.

Effects of roughness and waviness are completely different on mechanical response of rock fractures. In small scale fractures, roughness has significant influences on fracture shear behaviour, whereas in large scale fractures such as faults, waviness is the dominant affecting morphological parameter (Barton and Choubey, 1977; Jafari et al., 2003; Patton, 1966). The effect of roughness on shear strength is more pronounced at low levels of normal stress, while at high levels of normal stress, asperity degradation is the dominant failure mode. This is discussed in the next Chapter.

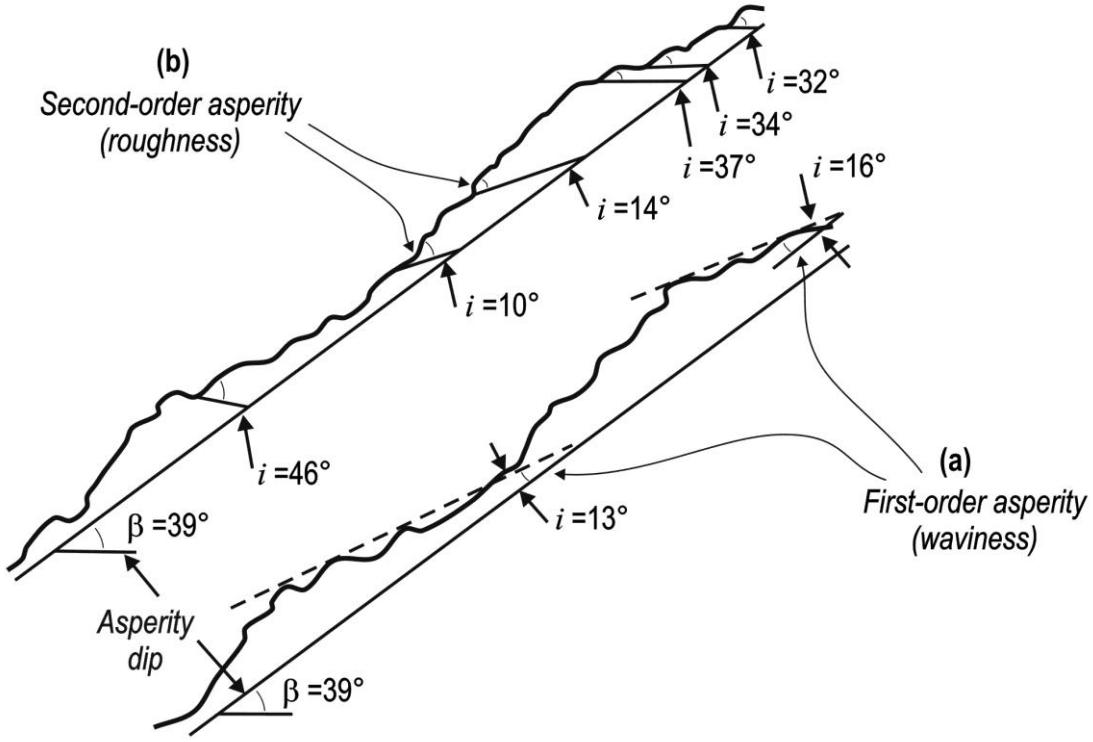


Figure 1.2 Rock fracture surface first and second order asperities (after Patton, 1966).

Assuming a ripple marked surface, it is not trivial to appreciate that roughness is directional dependent when it is considered at different directions. This will result in shear strength to be also anisotropic when it is measured along different directions. This concept was perhaps firstly introduced through some shear tests performed on laboratory samples by Huang and Doong (1990), as shown schematically in Figure 1.3. From this figure, it is seen that by changing the shearing direction values measured for shear strength significantly changes (consider the circle corresponding to 0.1 MPa normal stress).

From practical point of view, sliding along the surfaces of rock fractures may occur in a particular direction, for example fracture sliding intersecting a wellbore. This depends on the kinematic constraints and the external forces (including water pressures, and forces induced by earthquakes) acting on the structure. Therefore, it is imperative to understand the variation of shear strength of rock fractures in all directions. It is also important to note that even for a specified orientation; the shear strength of a natural fracture can be substantially different at a given applied load in different directions. As shown in Figure 1.3, dependency of shear strength to direction reduces as the normal stress increases.

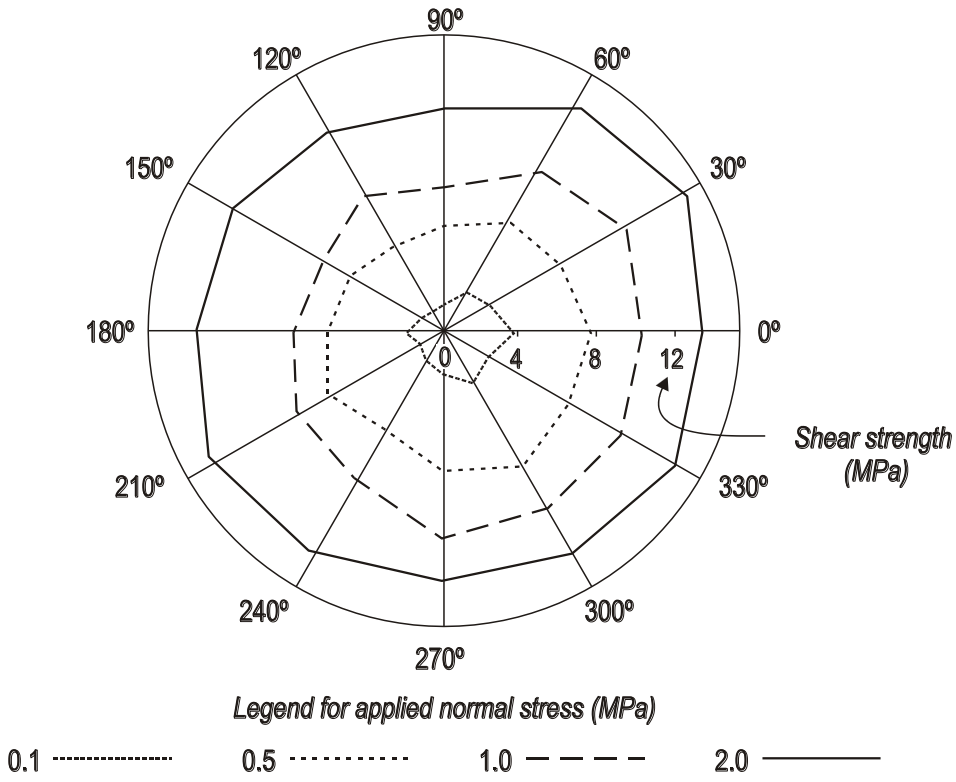


Figure 1.3 Anisotropy of shear strength of a rock fracture (from Rasouli, 2002).

The above discussion shows that fracture surface roughness is anisotropic and hence this property should be taken into account in fracture shear strength and asperity degradation analyses. However, in the next Chapter, it is discussed that few people have integrated this concept in their studies.

It is widely accepted that the mechanical behaviour of rock fractures is scale dependent. The term scale dependency of roughness means that if we determine the roughness of a rock fracture profile or surface as a quantitative parameter (such as the angle of inclination) at different scales, we will obtain different results, as shown in Figure 1.4. Thus the method proposed for roughness determination should allow us to take the effect of this parameter into account.

In practical point of view, the idea of scale in terms of fracture studies can be defined at three levels, as suggested by Vallier et al. (2010). First, the "micro scale" which is the scale of the asperities (less than one centimetre in length); second the "meso scale" which is the scale of the specimens tested in laboratory (about 10 cm in length); and third, the "macro scale" which is the scale of the rock mass (more than one meter in length). Average asperity angle, $i$, varies from one scale to another. these are schematically shown in Figure 1.4

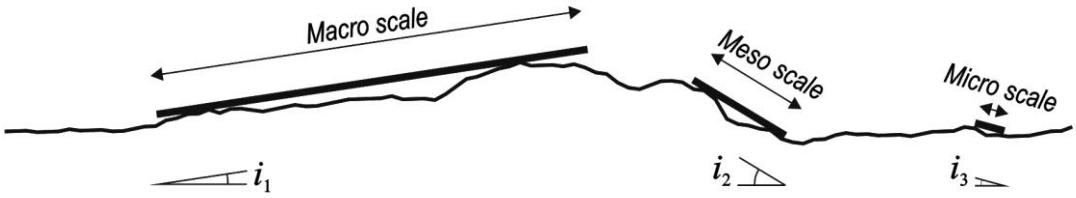


Figure 1.4 Three different levels of scale applied to non-planar fracture studies.

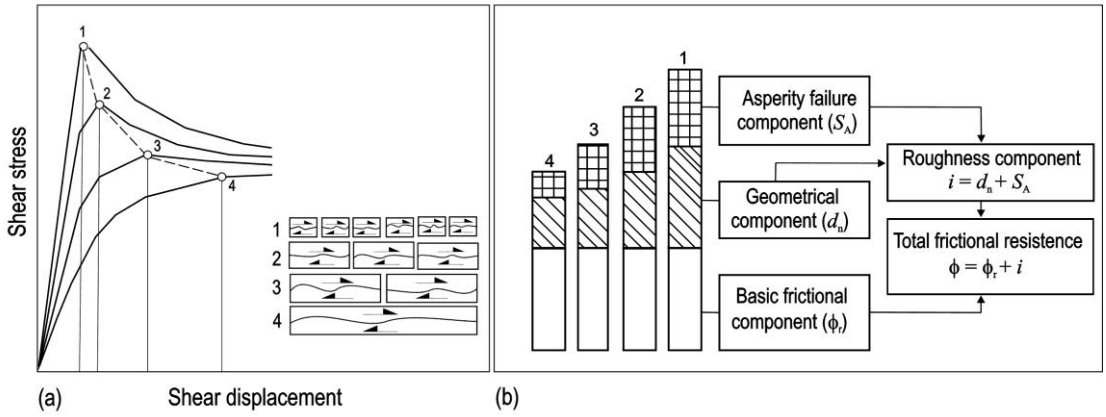


Figure 1.5 Scale dependency of shear strength of non-planar discontinuities (from Rasouli, 2002).

As stated by different researchers the mechanical properties of rock fracture differ when it is considered at different scales (Bandis et al., 1983; Fardin, 2003; Fardin et al., 2001; Rasouli, 2002; Rasouli and Harrison, 2010). This effect is schematically shown in Figure 1.5. It is seen that by increasing the scale, peak shear stress reduces in non-planar rock fractures (Figure 1.5.a). Scale in which fracture studies are carried out can also affect the failure modes within rock fractures shearing: this concept is depicted in Figure 1.5.b.

In this research, according to the above definition, the studies of rock fracture shear behaviour are conducted at meso scale and all numerical and experimental simulations are performed at this scale.

In addition to scale dependency and anisotropy properties when studying the shear strength of rock fractures, it is important to distinguish between filled and unfilled fractures. Filled fractures, ranging from those that contain soft plastic materials such as clay at a microscopic scale, to faults that contain gouge at a macroscopic scale, form particular issues and their shear strength depends on the physical and mineralogical properties of the material lie upon opposite sides of fracture walls (Grasselli, 2001). In contrast, the shear behaviour of unfilled fractures depends on, apart from the level of normal stress acting on the plane of shearing, the properties of the rock fracture walls including rock type, roughness, size of the fracture (scale effect), degree of weathering,

presence of moisture, and fluid pressure. It is important to note that this is the shear strength of unfilled types of fractures which will be studied in particular in this research work.

Having explained the importance of roughness on shear strength of fractures, in the following subsection, most commonly used roughness parameters in rock engineering field applications are briefly reviewed.

### 1.1.3 Roughness quantification methods

The ISRM (1978) classified rock profiles in the three groups of stepped, undulating and planar, and suggested a set of descriptive terms as rough, smooth and slickenside to identify the profile roughness for each group. Patton in 1966 demonstrated the significant effect of joint surface geometry on the shear behaviour of rough fractures by conducting several direct shear tests on the small saw-tooth replicas with different asperity inclinations, $i$, at varying normal stresses.

Later in 1977, Based on experimental works and observations, Barton and Choubey proposed 10 standard profiles (10 cm length) of increasing roughness with assigned roughness coefficients ranging from 0 to 20, so called joint roughness coefficient (JRC). This method involves comparing a profile of a discontinuity surface with JRC standard roughness profiles (Appendix 1) and hence assigning a numerical value to the roughness. However, JRC assessment is subjective and its nature is empirical, the JRC profiles have proved to be of significant value in rock engineering. Hudson and Harrison (1997) stated that "from the practical point of view, only one technique has any degree of universality and that is the JRC". Many researchers have attempted to correct the JRC to build an objective parameter for roughness characterisation (Kulatilake et al., 2006; Tse and Cruden, 1979; Wakabayashi and Fukushige, 1992). However, JRC is still the most commonly used parameter for roughness determination in the field of rock mechanics.

Grasselli (2002), based on a triangulation algorithm which results in a discretisation of the fracture surface into a finite number of triangles characterized roughness in terms of standard deviation of the angles of these triangles. His approach takes into consideration the fracture shear strength directionality.

Statistical parameters in Riemannian geometry developed by Rasouli (2002) and Rasouli and Harrison (2010) based on the distribution of unit normal vectors to the surface, as shown in Figure 1.6, is perhaps the latest development in roughness

determination. Rasouli (2002) presented two parameters $D_{R1}$ and $D_{R2}$ in order to estimate roughness of linear profiles (2D) and rock surfaces (3D), respectively. Their approach accounts for scale effect and anisotropy in roughness determination. $D_{R1}$ concept will be reviewed briefly in the next Chapter.

In current study, the objective is to integrate $D_{R1}$ into fracture shear strength analysis using numerical and experimental analysis of rock fracture profiles and surfaces. This will be presented in Chapters 3 and 4.

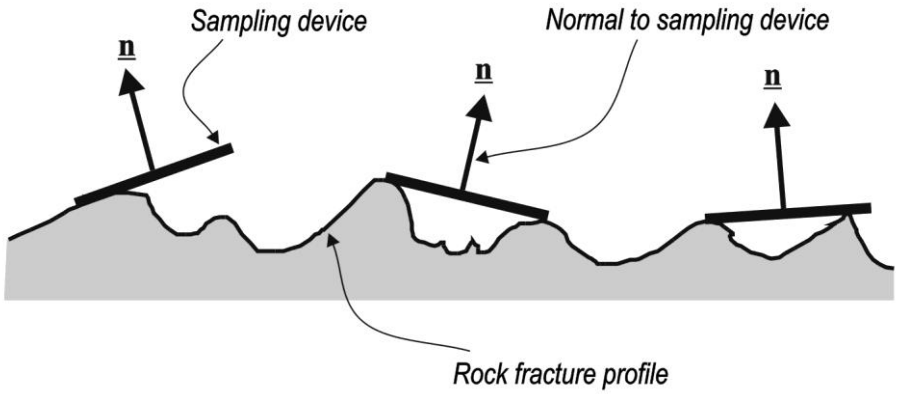


Figure 1.6 Distribution of unit normal vectors to the rock fracture profile, from Rasouli (2002).

## 1.2 Shear behaviour of rock fractures

In Figure 1.7, a fracture plane subjected to the external normal ($\sigma_n$) and shear ($\tau$) stresses is shown. The traction acting along the fracture plane can be resolved into normal and shear components. The normal traction results in normal closure of fractures whereas shear component is responsible for shear deformation of the fracture. Dilation arises because the asperities of one fracture surface must ride up in order to move past those of the other surface, as shown in Figure 1.7.

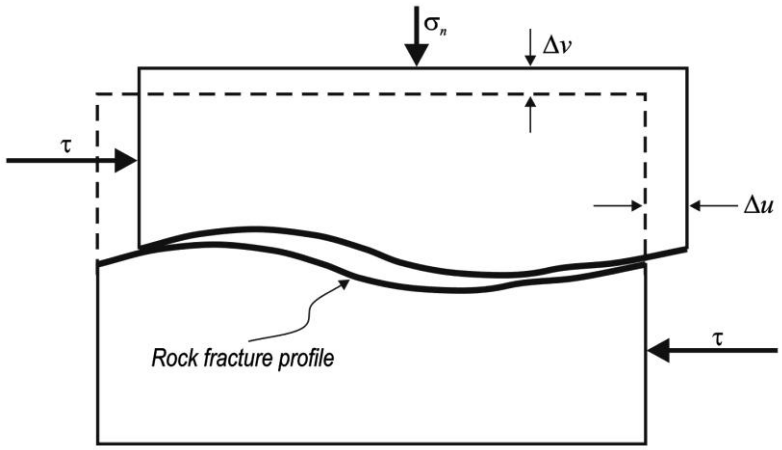


Figure 1.7 Schematic of a fracture sheared under constant normal stress, after Goodman, 1976.

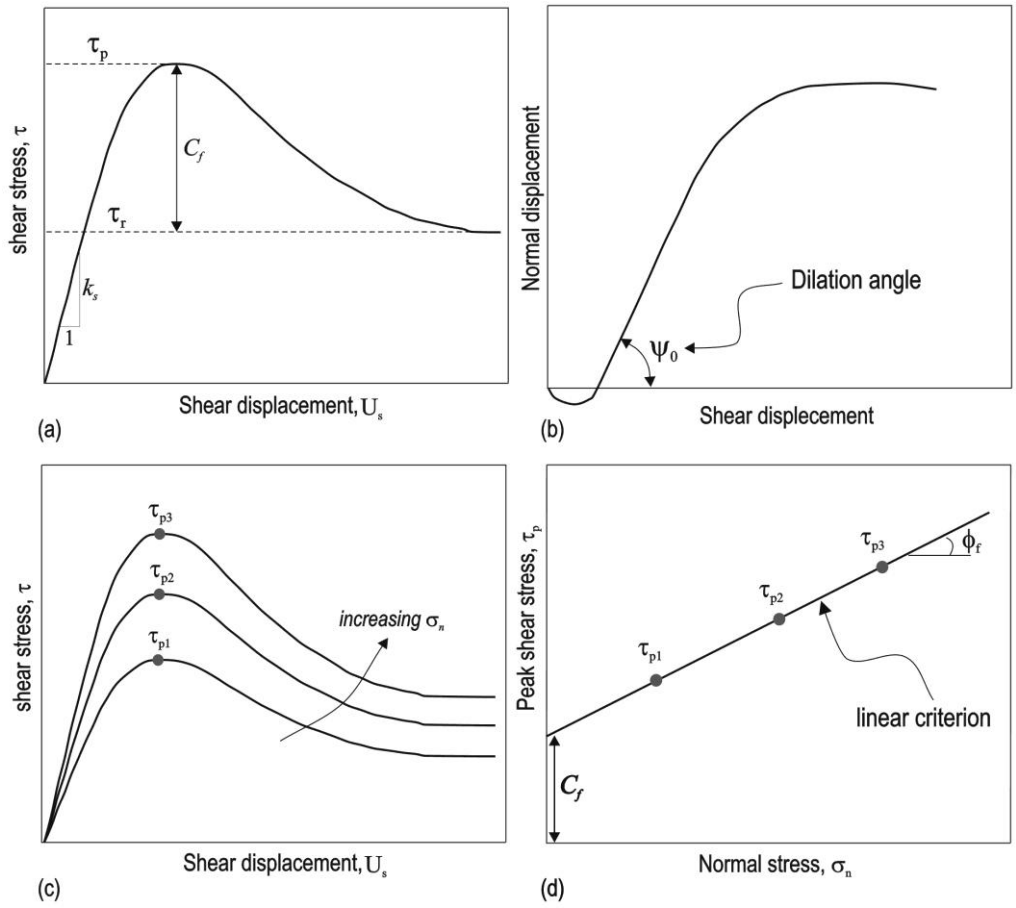


Figure 1.8 Typical curves for fracture under shear conducted under constant normal stress.

Displacement parallel to the fracture plane is called shear displacement and that of perpendicular to the fracture plane is called normal displacement (or dilation) which are denoted by $\Delta u$ and $\Delta v$, respectively. A general plot of the shear stress versus shear displacement, at a constant normal stress, is shown in Figure 1.8.a.

In this figure, the shear stress first increases in a manner that is nearly proportional to the shear displacement. The slope of this line is called shear stiffness, $k_s$, (see Figure 1.8.a). During this stage of deformation, the two fracture surfaces slide over each other"s asperities, causing dilation of the fracture. The yield point marks the initiation of local micro cracks growth until failure. Peak shear stress shown as $\tau_p$ in Figure 1.8.a also known as "shear strength" corresponds to the point at which the asperities begin to shear-off, causing irreversible degradations of the surface asperities (Jaeger et al., 2007). If shear deformation of fracture continues, the peak shear stress will be followed by strain softening regime, during which the reduction in shear stress tends toward a value that corresponds to what is termed the residual shear strength of the fracture ($\tau_r$ in Figure 1.8.a). Residual displacement corresponds to the distance the fracture displaces after peak shear stress before reaching its residual shear strength.

If the fracture is rough, it will tend to "dilate" during shearing as shown in Figure 1.7 (Goodman, 1976). Dilatancy is defined as the normal displacement of the upper block with respect to the lower block measured during shearing, i.e. the slope of normal displacement versus shear displacement curve shown in Figure 1.8.b.

During shearing, as the shear stress accommodates, a rapid increase in the rate of dilatancy is expected, which approaches its maximum at its peak shear stress. Thereafter, the shear stress falls continuously and the fracture also dilates slightly until the residual displacement is reached (See Figure 1.8.b). Initial dilation angle of fracture is measured at the beginning of shearing as

$$\mathrm{d_n} = A \tan \frac{\Delta v}{\Delta u}, \tag{1.1}$$

where $\Delta v$ and $\Delta u$ are the increments of normal and shear displacements, respectively. Fracture dilation angle, $\mathrm{d_n}$, is also shown as $\psi$ in some texts (Figure 1.8.b). More importantly, fracture dilation rate is proportional to fracture surface roughness and its evolution in time. This shows the importance of accurate roughness characterisation to estimate the fracture average dilation.

The behaviour of a fracture under shearing depends very strongly on the normal stress acting perpendicular to the fracture plane. Figure 1.8.c indicates that as normal stress applied to the fracture plane increases, the shear strength increases accordingly (Goodman, 1976; Jaeger et al., 2007). A series of fracture shear tests at different normal stresses generates a series of peak shear stress points through which a fracture shear strength curve can be drawn (see Figure 1.8.d). The most commonly used fracture shear strength criterion is the Coulomb linear friction law as shown in Figure 1.8.d and is expressed for planar fractures as

$$\tau = \sigma_{\mathrm{n}} \tan \phi_{\mathrm{f}} + C_j . \tag{1.2}$$

In this equation $\tau$ is the fracture shear strength at corresponding normal stress ($\sigma_{\mathrm{n}}$), $\phi_{\mathrm{f}}$ is the fracture friction angle, and $C_j$ is the fracture cohesion (Jaeger et al., 2007).

Equation 1.2 does not include the effect of surface roughness. In Figure 1.9, it is seen that for a rough fracture (ideally with an asperity angle *i*), the slope of shear stress versus normal stress is larger than that of a smooth fracture surface. This is applied by adding the asperity angle to the friction angle $\phi_{\mathrm{f}}$. However, as the normal stress increases, due to the degradation of the asperity contacts, above a certain normal stress known as transition normal stress ($\sigma_{\mathrm{T}}$ in Figure 1.9) the rough fracture behaves similar

to a smooth fracture and the slope of the curve as shown in this figure returns to the residual friction angle $\phi_r$. Patton (1966) found the following bilinear functions for peak shear strength, $\tau_P$ as a function of $\sigma_n$:

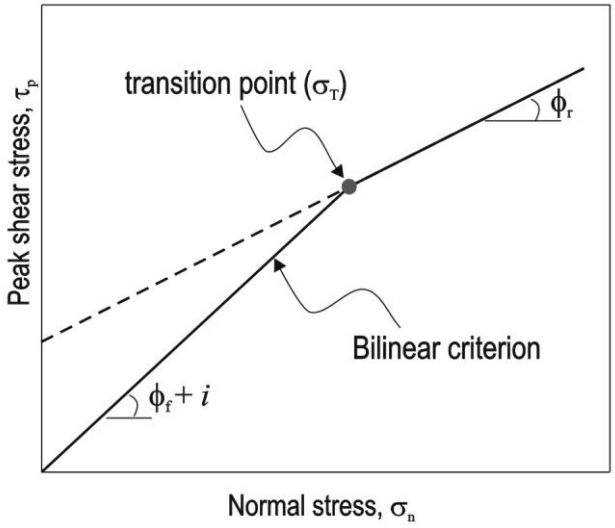


Figure 1.9 Bilinear model for the peak shear strength of rock fractures.

$$\text{for } \sigma_n < \sigma_T: \quad \tau_p = \sigma_n \tan(\phi_f + i), \tag{1.3}$$

and

$$\text{for } \sigma_n > \sigma_T: \quad \tau_p = C_f + \sigma_n \tan\phi_r. \tag{1.4}$$

Equations 1.3 and 1.4 demonstrate the fact that at low normal stresses, shearing mechanism is dominated by fracture profile asperities‟ sliding. However, at high normal stresses fracture possesses a apparent cohesion that is due to the inherent shear strength of asperities and has an effective friction angle of $\phi_r < \phi_f + i$ (Jaeger et al., 2007). Many researchers correlated idealised roughness angle $i$ to different statistical parameters representing morphology of the surface, some of these correlations will be given in Chapter 2.

Significant attempts to the development of fracture shear strength criteria for unfilled rock fractures under low normal stresses have been made by Ladanyi and Archambault (1970), Jaeger (1971), and Barton and Choubey (1977): these will be discussed in Chapter 2. However, few of the strength criteria proposed to date take into account the fact that fracture peak shear strength is anisotropic

At high normal stresses, fracture surface roughness is destroyed and amount of surface degradations significantly affect the peak and ultimate shear strength of fracture. This is perhaps due to the complexities encountered in determination of roughness

evolution. This fundamental concept has not been fully formulated and modelled and there is a need for further research in this area. As stated by Jing and Stephenson (2007), "the strong correlation between roughness and other aspects of fracture behaviour (e.g. scale effects, anisotropy, stress-dependency and conductivity) demonstrate the strong requirement to represent, quantitatively, the roughness of rock fractures in both two and three dimensions, and its evolution with time and deformation paths to develop more reliable constitutive models".

Some of these concepts are looked at in current study through both numerical and experimental shear test simulations of rock fractures.

This research aim at linking roughness parameter $D_{R1}$ with shear strength of fracture profiles and develop correlations based on numerical and experimental simulations of synthetic, pseudo-real, and rock fracture profiles.

## 1.3 Shear strength estimation: analytical, numerical and experimental methods

The past research works have indicated that three principal mechanisms can be distinguished when a rock fracture is sheared at different level of normal stresses.
Asperity sliding (i.e. dilation) is the dominant fracture shear response at low normal stresses. Asperity contact shearing (i.e. asperity cut-off) is the most likely mechanism to occur at medium values of normal stresses. At large normal stresses, asperity contacts degradation (i.e. damage) is expected to be observed during fracture shearing.

Most analytical shear strength criteria can provide a good estimation of sliding but they cannot fully model the asperity cut-off and damage as these mechanisms are highly dependent on evolution of surface roughness. Few attempts have been made to develop analytical and constitutive relations in order to include these mechanisms in the analytical formulae (see for example Huang et al., 2002, and Belem et al., 2007). However these models are expected to give unrealistic solutions as there are different assumptions being made to simplify derivation of the formulae (detailed discussions will be given in Chapter 2).

To overcome the above issue many numerical models have been developed. Recent advances in numerical modelling enable us to simulate fracture shear test in direct manner of force-displacement relations where fracture surface roughness evolves with time and state of stresses. Numerical works carried out by Cundall (2000), Karmai and

Stead (2008), Park and Song, (2009) are the most significant researches in this area. However, in-depth simulations of fracture shearing are still in demand and thus further research in this field is certainly needed. Most of the available simulators use numerical codes which are based on the theory of continuum medium, in particular finite element method (FEM). However, fewer applications of numerical codes which are developed based on distinct element method (DEM) have been reported. This is while it appears that the use of DEM based simulators could be advantageous for fracture shear modelling in the sense that it can model a fractured medium more efficiently and realistically. Therefore, in this study the particle flow code (PFC), which is a DEM based simulator will be used for 2D fracture shear test simulations. The results of such modelling will be presented in Chapters 3 and 4.

Bonded Particle Model (BPM) implemented in PFC has been proven to be a good representative of rock material environment (Potyondy and Cundall, 2004). Asperity sliding, development of micro-cracks, asperity damage, and intact rock failure under high normal stresses are the deformation mechanisms which can be explicitly modelled using BPM during fracture shearing (Asadi and Rasouli, 2010). In PFC, force-displacement curve progresses in time that enables real-time tracing of the fracture shearing behaviour.

Several laboratorial shear tests have been conducted on rough fractures to understand their shear strength (Cho et al., 2008; Grasselli, 2001; Huang et al., 2002; Jafari et al., 2003; Jiang et al., 2004; Lee et al., 2001; Yang and Chiang, 2000). Most of these experiments have been performed under constant normal load (CNL) condition, with fewer being performed under constant normal stiffness (CNS) (Indraratna and Haque, 2000; Li et al., 2008; Olsson and Barton, 2001). This research is not intended to compare the results of these two approaches but is focused on understanding the effect of surface roughness on shear strength. Therefore, the experimental works conducted as part of this research are all under CNL conditions. Recently developed direct shear apparatuses for rock fractures (Barla et al., 2009; Hans and Boulon, 2003; Jiang et al., 2004; Kim et al., 2006) are quite different in terms of normal and shear loading capabilities as well as maximum allowable shear displacement, sample size, and fluid pressure. These differences can limit the applicability of each in determination of strong rock fractures shear strength and asperity degradation during shear test.

For the purpose of laboratory shear tests in current study, an existing true triaxial stress cell (TTSC), which has been originally designed for applying three independent

stresses on a cube sample, was modified. These modifications will be discussed in detail in Chapter 4 and it will be shown that the current set up is able of applying large normal and shear loads to a sample. The experiments have been mainly performed on synthetic samples with different asperity shapes and then on pseudo real fractures whose geometry are identical along the sample thickness. This will allow us to compare the results of experimental tests with numerical simulations using PFC2D. However, the results of experiments on rock-like fracture are also given but 3D numerical simulations are recommended to be developed to compare the results.

The subsequent Sections will describe the objectives and significance of this research, and the way this thesis has been structured.

## 1.4 Objectives of this study

According to the statement of the problem briefly introduced in the above Sections, the objectives of this PhD thesis can be summarised as below:

1) Review the strengths and shortcomings of the commonly used techniques and methods for shear strength analysis of rock fractures.
2) Simulate number of synthetic profiles numerically to obtain a correlation for peak shear strength estimation as a function of profile roughness, material properties and applied normal stress. The PFC2D will be used for the numerical simulations in this study as it was found suitable for modelling a discontinuous medium.
3) Performing shear tests in the lab on different synthetic surfaces with different asperity geometries to understand the effect of roughness and normal stress on the fracture shear behaviour and asperity degradation. For this purpose, a new configuration of fracture shearing device will be applied.
4) Comparison of the PFC2D simulation and experimental results to calibrate the numerical models and establish suitable set of model parameters which lead to a more realistic shear strength test results.
5) Correlate roughness parameter $D_{R1}$ with shear strength of profiles. Correlations will be developed for synthetic profiles and the results for some rock fracture profiles presented will demonstrate potential for such correlation.

## 1.5 Significance of this research

Fracture asperities failure (degradation) and evolution of fracture surface roughness during shearing are problems which have been the subject of many analytical, numerical, and experimental studies. However, the complexity associated with various aspects of these processes requires further research to be conducted in this area.

This research studies aim at investigating the progressive shear behaviour (i.e. contact sliding and asperity failure) of single rough rock fractures. This study is significant in several aspects which are briefly highlighted below:

1) Numerical simulations: in this study a DEM based numerical simulator, PFC2D, has been used to model shear strength and asperity failure of rough fractures with different synthetic and real surface geometries. Several advantages and limitations of PFC2D in modelling realistic behaviour of rock structures and fractured medium will be explained and discussed in Chapter 3 when several synthetic and real rock profiles are modelled. It is to be noted that this study is among a very few studies which has used PFC2D for simulation of rough fractures shear strength and associated failure around the fracture. Perhaps the first and the main work belongs to Cundall (2000) who simulated the shear behaviour of a simple sinusoidal profile and compared to Barton‟s JRC empirical model, but in this work the simulations have been extended to any rock profile geometry and under various loading conditions. The results of simulations presented in Chapters 3 and 4 will show the capabilities and limitations of PFC2D in modelling fracture shear strength and asperity failure during shearing.
2) Lab experiments: In order to calibrate the numerical models performing shear experiments in the lab was essential. The experiments were performed with a fracture shear cell (FSC) which was configured by special set up in the true triaxial stress cell. The modifications made to triaxial cell to allow it for fracture shear experiments are unique practices. Large amount of shear and normal loads that can be applied to the shearing sample is one of the advantages of the FSC. To be consistent with simulations which are in 2D, synthetic fracture surfaces with identical geometry along their third dimension (i.e. thickness) were built in the lab, and mortar with relatively similar micro properties as the PFC2D model was used for sample preparation. All of these concepts and practices are new capabilities generated during this research work which will help to better understand the dilation and failure behaviours of rock fractures under shear.

3) Correlations developed in this thesis between newly developed roughness parameter $D_{R1}$ (Rasouli and Harrison, 2010) and shear strength of synthetic and rock fracture profiles are another novelty in this work. The results of this study show that $D_{R1}$ can be a good quantitative parameter for roughness characterisation of rough fractures. This gives a good reason for a continued study to correlate the 3D version of this parameter, i.e. $D_{R2}$ (Rasouli, 2002) with shear strength of rough rock surfaces whose simulations are performed in 3D.

The above are all innovative concepts which are going to be practiced in this research work and the results are expected to advance the fundamental and applied rock engineering science in this subject.

## 1.6 Structure of the thesis

Based on the objectives of this work the report is structured in different Chapters which are explained briefly below. The thesis comprises five Chapters and two Appendices. These are illustrated in Figure 1.10.

In Chapter 2 different approaches and models proposed for the fracture shear strength analysis in rock fractures will be reviewed. The use of Joint Roughness Coefficient (JRC) and fractal dimension ($D$) in shear strength analysis of real fractures will be discussed in this Chapter. Also, here a brief review of new roughness parameter ($D_{R1}$) is given. In particular, shortcomings of currently used analytical and numerical methods for fracture shear behaviour will be addressed.

An introduction to the bonded particle model (BPM) which is implemented in PFC will be covered at the beginning of Chapter 3. The results of sensitivity analysis of model micro-properties through numbers of biaxial test simulations will be given which is followed by the analysis of model macro mechanical response. Fracture shear test simulation scheme in PFC2D will be introduced and different failure mechanisms will be analysed in this Chapter. The output results of simulation of synthetic profiles using PFC2D will be presented in this Chapter. The results will be compared with data taken from the available literature. Correlations developed to estimate the shear strength of symmetric triangular fracture and number of rock fracture profiles based on PFC2D simulations and profiles‟ $D_{R1}$ which are presented in this Chapter. The extension of these analyses to real rock profiles are presented next in Chapter 3.

The digital elevation data of some rock fractures were extracted using photogrammetry techniques for the simulation purposes. Also the existence of

correlation between $D_{R1}$ and shear strength of some rock profiles will be shown at the end of this Chapter.

In the first part of Chapter 4, the procedure of modifying the existing true triaxial stress cell (TTSC) to perform fracture direct shear tests on small sample blocks of 15cm is explained. Steps of sample preparation will be thoroughly explained. The results of direct shear tests on samples will be given in this Chapter in which different failure mechanisms of fracture and intact rock during fracture shearing are plotted. The fracture shear strength directionality will also be investigated by performing shear tests at different directions. Experimental outputs will be compared against the corresponding PFC2D simulations and applicability of this code to represent rock-like material space will be discussed. Finally at the end of Chapter 4, a real fracture surface will be tested in two opposite directions in the laboratory to demonstrate the application range of the fracture shear cell (FSC).

Chapter 5 draws together the summary, conclusions and recommendations of this work. Finally, substantial reference list and two Appendices of supporting material will be given. These Appendices contain the JRC exemplar profiles and analytical calculations of synthetic profile cut-off strength criterion.

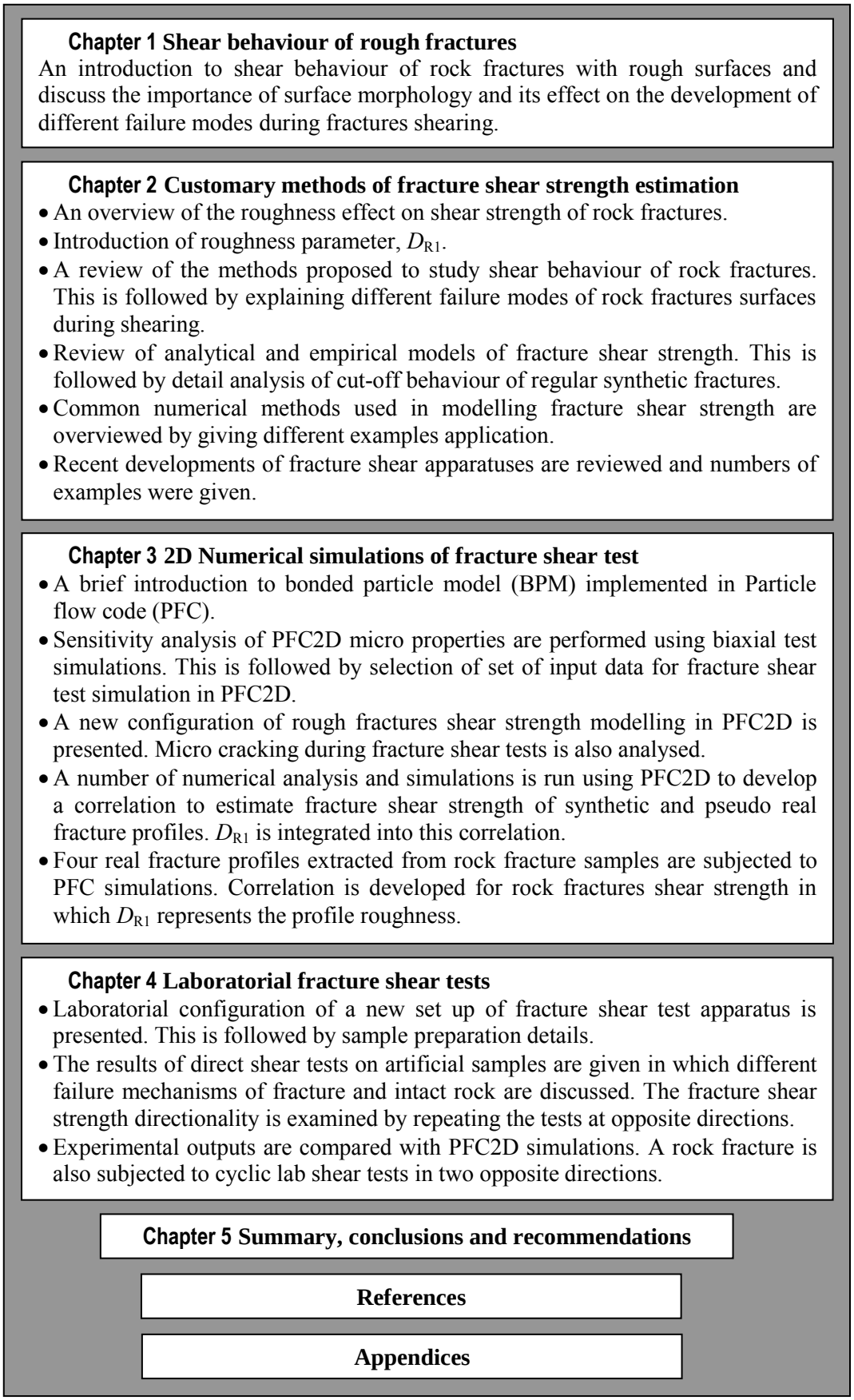


Figure 1.10 Structure of the thesis.

## 1.7 Summary

The first part of this Chapter presented the importance of fracture surface roughness on mechanical behaviour of rock fractures. Scale effect and anisotropy of surface roughness was described as two important properties of fracture surface.

Principles of fracture direct shear test including loading conditions and roughness characterisation were presented according. Evolution of roughness over time particularly under high levels of normal stress was highlighted.

Recent developments in surface roughness characterisation were reviewed and $D_{R1''}$ a newly developed 2D parameter of roughness, was introduced and will be used in the analyses of this work.

In the last part of this Chapter, a brief introduction to current status of numerical simulation of rock fracture shear behaviour was presented. Also, it was mentioned that PFC2D is going to be used in this study for this purpose. Objectives and research significance of this research were highlighted, and the structure of the thesis was outlined in Figure 1.10. Based on this Figure, in the next Chapter, we will continue by presenting the customary and recent advances in fracture shear strength estimation and roughness characterisation.

# 2 Customary methods of fracture shear strength estimation

In most rock engineering problems, the shear strength of rock fractures varies widely under low normal stress levels. This variation is influenced mostly by surface roughness and the strength of the fracture wall. Roughness of fracture surfaces changes depending on the rock type and the manner in which the fractures are formed. Conversely, under high normal stress levels, the shear strength spectrum of fractures and faults is narrow and less dependent on surface roughness (Barton and Choubey, 1977; Priest, 1993). The current rock joint models are capable of predicting the shear behaviour of fracture surfaces to some extent but most of them are unable to include the complex fracture surface characteristics, the effects of infill properties, and the degradation behaviour of asperities (Indraratna and Haque, 2000).

Identification of failure modes along a fracture shearing plane is generally related to the surface roughness and material strength. Fracture sliding, shearing (or cut-off), and asperity contact damage (i.e. degradation) are three common modes of failure which may occur during fracture displacement (Huang et al., 2002). The latter two failure modes, however, found to be more cumbersome to model due to their dependency with surface roughness effect during shearing (Belem et al., 2009). These failure modes may also extend from the fracture planes into the rock matrix which could result in a reduction in rock mass strength. This indicates the importance of appropriate modelling of roughness when shear strength of a fracture surface is studied.

In this Chapter, detail review of most commonly used models of fracture surface roughness is presented. Then different analytical, numerical and experimental approaches for fracture shear strength estimation will be discussed with a special focus on how surface roughness is incorporated in these models.

It is well known that conventional direct shear tests have been carried out to investigate fracture shear behaviour, where the normal stress acting on the fracture interface is considered to be constant namely Constant Normal Load (CNL). Therefore, this particular mode of shearing is suitable for planar fractures where the fracture does not dilate during the test. For rough fractures however, there is an inevitable increase in normal stress due to inhibited dilation by the surrounding rock mass, where the stiffness

exerted on the fractures controls the shear behaviour. This is an idealised mode of shearing under variable or Constant Normal Stiffness (CNS) conditions which are commonly observed in underground excavations (Indraratna and Haque, 2000).

Numbers of analytical and empirical criteria have been developed to estimate the contacts shear strength under CNL and CNS conditions but in majority of them, quantification of fracture surface roughness is the most challenging task. In addition, numbers of numerical simulations and laboratorial experiments have attempted to estimate pre and post peak shear strength of fractures in different loading and boundary conditions. The difficulty encountered to the majority of such models is that they generally characterise the fracture surface roughness using only one unique value which is not adequate. Moreover in many cases, model does not account for the evolution of surface roughness and contact asperity damage, specially after the peak shear strength is reached.

## 2.1 Rock fracture roughness characterization

The shear behaviour of non-planar fractures is significantly influenced by surface properties of the fractures, or in other words, by the surface geometry or roughness. In general, the rougher the fracture surface, the greater the shear strength. Several methods have been proposed for estimation of fracture surface roughness. Indraratna and Haque (2000) categorized these methods in four different groups of joint roughness coefficient (JRC), self-similar and self-affine fractal dimensions, spectral and line scaling method, and continuous mathematical functions such as Fourier transform. Grasselli (2002) based on a triangulation algorithm which results in a discretisation of the joint surface into a finite number of triangles characterized roughness in terms of standard deviation of the angles of these triangles. A statistical parameters developed based on the distribution of unit normal vectors to the surface, is perhaps the latest development on roughness determination. Rasouli (2002) argued that these vectors are circular data and therefore their statistical analysis should be carried out using Riemannian geometry. Accordingly, he presented two roughness parameters $D_{R1}$ and $D_{R2}$ in order to characterise roughness of linear profiles and rock surfaces in 2D and 3D, respectively. In current thesis, $D_{R1}$ will be integrated into fracture shear strength correlations using numerical simulations of synthetic and rock fracture profiles.

The merits of this method against customary methods are presented in Section 2.1.3 within this Chapter. In the following Sections, the most commonly used and recently developed methods of roughness determination are presented.

### 2.1.1 Joint Roughness Coefficient (JRC)

Based on experimental works and observations, Barton and Choubey (1977) proposed 10 standard profiles (10 cm length) of increasing roughness with assigned roughness coefficients ranging from 0 to 20 (see Appendix 1). To estimate JRC for a real fracture, one needs to compare its geometry with these standard profiles and choose the closest one to the fracture. The immediate difficulty in use of this observational method is that the morphology of 3D fracture surfaces is very complicated and the choice of direction at which the surface is looked at (surface roughness anisotropy) can influence the results significantly. JRC is the most widely used parameter for roughness assessment in rock engineering applications, perhaps because of its simplicity. Many works have been carried out to relate JRC to different properties of fractures, for example the shear strength (see Equation 2.16) and the roughness influence on fluid flow response of natural fractures. Despite all these attempts, it should be noted that JRC provides a subjective assessment of profile roughness, and hence it is not appropriate for objective roughness characterisation.

Many researchers have encountered difficulties in using JRC as a parameter for fracture surface roughness determination and proposed alternative objective methods, e.g. artificial neural networks (Lessard and Hadjigeorgiou, 1996), Riemannian multivariate statistics (Rasouli, 2002), Fractal and statistical techniques (Kulatilake et al., 1995), and combined Fourier/Wavelet transforms (Asadi et al., 2009; Indraratna and Haque, 2000). However, most of these approaches are finally correlated to JRC for assessing hydromechanical behaviour of fractured rock masses.

### 2.1.2 Fractal dimension, $D$

A number of researchers have investigated the applicability of various geostatistical and fractal based approaches in quantifying roughness (Dight and Chiu, 1981; Kulatilake et al., 2006; Maerz et al., 1990; Tse and Cruden, 1979; Wu and Ali, 1978). Kulatilake et al. (1995) have pointed out that the values obtained for conventional statistical parameters vary with the measurement scale. Therefore, the surface roughness of rock joints needs to be characterised using scale invariant parameters such as fractal parameters. Several researchers have suggested using the fractal dimension to quantify

rock joint roughness (Fardin et al., 2001; Huang et al., 1992; Kulatilake et al., 1995; Odling, 1994; Power and Tullis, 1991).

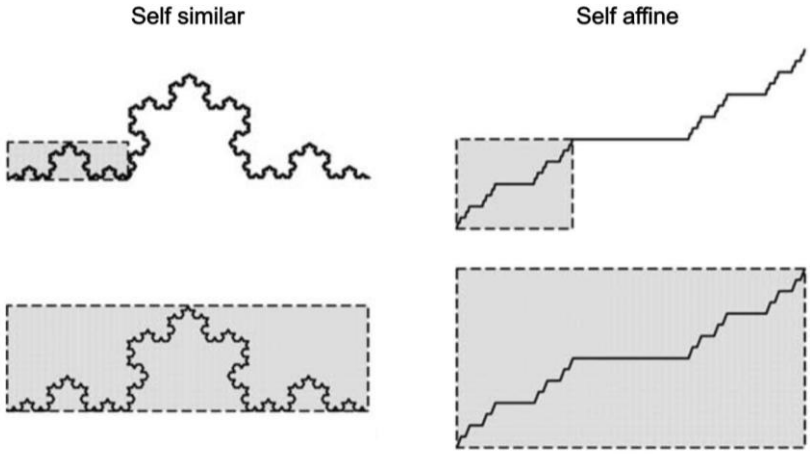


Figure 2.1 Self-similar and self-affine properties surface roughness (Kulatilake et al., 2006).

Fractal geometry introduced by Mandelbrot in 1982 allowed description of irregular shapes which cannot be explained using Euclidean geometry. Fractal surfaces are divided into two groups: A self similar surface is a statistically scale invariant surface, and a self affine surface which is scale dependent, as shown in Figure 2.1. Fracture surface roughness has self-affine properties, as it is scale dependent (Kulatilake et al., 2006). Most methods of calculating the fractal dimension were developed for self-similar fractals, which are scale independent, and do not work for self affine surfaces. Rasouli (2002) argued that on the basis that roughness is a scale dependent phenomenon, the use of this approach seems to be of limited use for roughness analysis.

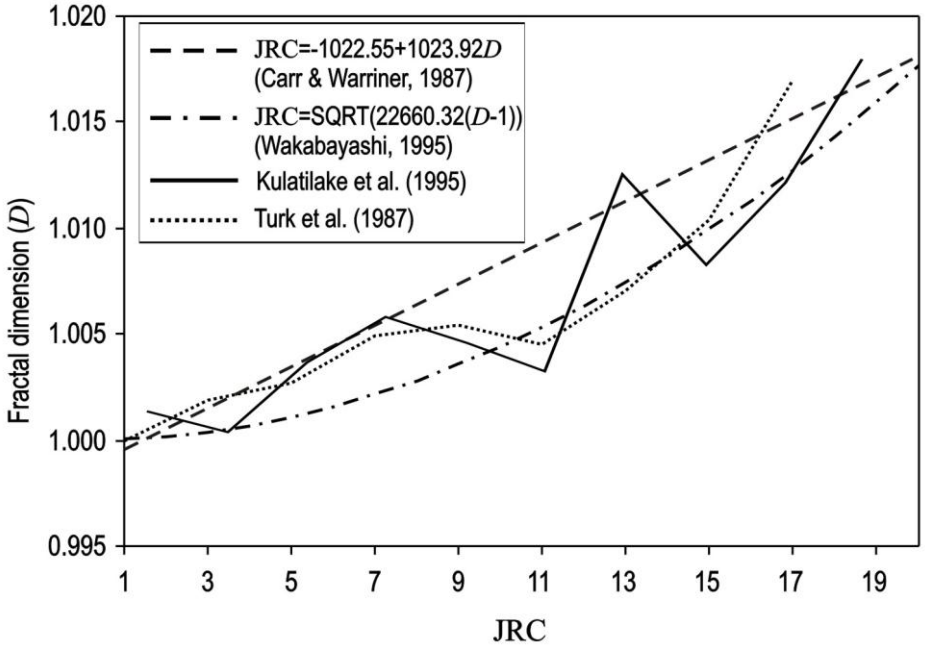


Figure 2.2 Correlations between fractal dimension ($D$) and JRC (Rasouli, 2002).

Kulatilake et al. (2006) also pointed out that the fractal dimension itself is not sufficient and at least two fractal parameters are required to quantify rock joint roughness. They stated that based on the assumption that the profile of rock fractures has self-similar properties, fractal dimension can be used to characterise profile roughness. Many works have attempted based on this assumption to relate profile roughness to fractal dimension, $D$.

Having the ($x$,$y$) coordinates of a profile from roughness measurement, the fractal dimension of the ten JRC profiles can be calculated. The results of these calculations by different researchers are shown in Figure 2.2. It is seen that the values of $D$ vary in a very small range as the JRC changes between 1 and 20. Looking at this figure, it appears that the results of different correlations are quite different. For example, the values obtained by Carr and Warriner (1987) are larger than those obtained by Wakabayashi and Fukushige (1992).

More importantly, the fractal dimension does not monastically increase as we move from JRC=1 to JRC=20. However, on the basis of the stated intent of the JRC system, we should expect that profile's roughness to increase as JRC becomes larger. For example, the plot obtained by Kulatilake et al. (1995) has larger fluctuations than the other curves which shows that the JRC profiles do not follow a similar roughness as originally proposed by Barton and Choubey (1977), as shown in Figure 2.2. Similar issue was reported when JRCs were attempted to be ordered based on their corresponding profile signal energy, using a wavelet approach (Asadi et al., 2009).

Rasouli (2002) also argued that using $D$ for roughness estimation does not provide a unique value as an indication of profile roughness if different methods of calculation are used. This issue has been studied in detail by Tate (1998).

Fardin et al. (2001) used the self affine fractals theorem, and based on that proposed the two parameters, $D$ (fractal dimension) and $A$ (amplitude parameter), to determine roughness of a rock fracture surface as

$$D = 2.29287 + 0.21727e^{\left(-S_i/146.0670\right)} \tag{2.2}$$

and

$$A = 0.01529 + 0.00595e^{\left(-S_i/1684815\right)}. \tag{2.3}$$

In these two equations, $S_i$ is the sampling interval. The important point in the above equations is the limit of these parameters as a result of changing $S_i$. Equation 2.2 shows that theoretically, when sampling size changes from zero to infinity, the maximum

range will be much smaller, and this recalls the earlier noted problem of discrimination between roughness of different rock surfaces.

In consequence, although this approach has improved within the last decade, applicability of that needs to be considered as even when applying the self affine fractal theorem, it may not be possible to compare roughness of different rock surfaces appropriately.

### 2.1.3 Riemannian roughness parameter, $D_{R1}$

The idea of characterizing roughness of a rough fracture based on the distribution of deviation angles from a smooth plate firstly introduced by Barton (1971). Also, Fecker and Rengers (1971) through their practical measurements using a compass mounted on a smooth plate found that as the base plate (sampling scale) increases, the scatter of the measurements decreases. Therefore, statistical analysis of deviation angle is in fact an approach to quantify surface roughness. For example, the standard deviation of angles of the plate measured at different scales and at different orientations could lead to a parameter for characterizing roughness at different scales and orientations. This brief explanation indicates two important properties in roughness measurement: scale dependency and anisotropy.

Extracting unit normal vectors from a surface, Rasouli (2002) analysed these vectors statistically to characterize surface roughness. In a simple case of a linear profile, introducing a hypothetical connected pin sampling device, the unit normal vectors to the profile can be extracted at different scales and on a random sampling basis. This is shown in Figure 2.3.

Rasouli (2002) argued that these normal vectors are all located on a periphery of a unit circle, i.e. these vectors are circular data and therefore statistical analysis of such data is to be carried out in Riemannian space, rather than in Euclidean space, as is a common approach.

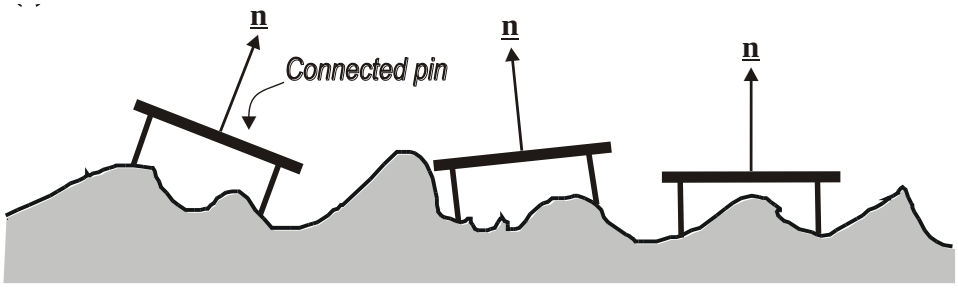


Figure 2.3 Profile sampling techniques (Rasouli, 2002).

A simple difficulty with Euclidean geometry is that, for example, the mean of two unit vectors (0.0, 1.0) and (1.0, 0.0) is (0.50, 0.50), which corresponds to a point located inside the circle, while the original data are points located on the circle. This means that Euclidean geometry does not consider the shape of the data distribution into account.

As shown in Figure 2.4, the transfer of 2D Euclidean data in Riemannian space is obtained by un-wrapping the circle. In this 1D space the data are points located on a line called principal chart, with their coordinates being defined by the distance from a point defined in this line. For the two vectors mentioned above the corresponding coordinates in Riemannian space are points with length of 0 and $\pi/2$, i.e. the curved length on the circle. The simplest 2D geometry in Euclidean space is a unit circle and its correspondence in Riemannian space is a 1D line. All statistical analysis of vectors (including data mean and variance) can now be performed in 1D Riemannian space. For the two example vectors the mean value is $\pi/4$. Once the calculations completed the data can be transferred back to the Euclidean space, i.e. corresponding to the unit circle.

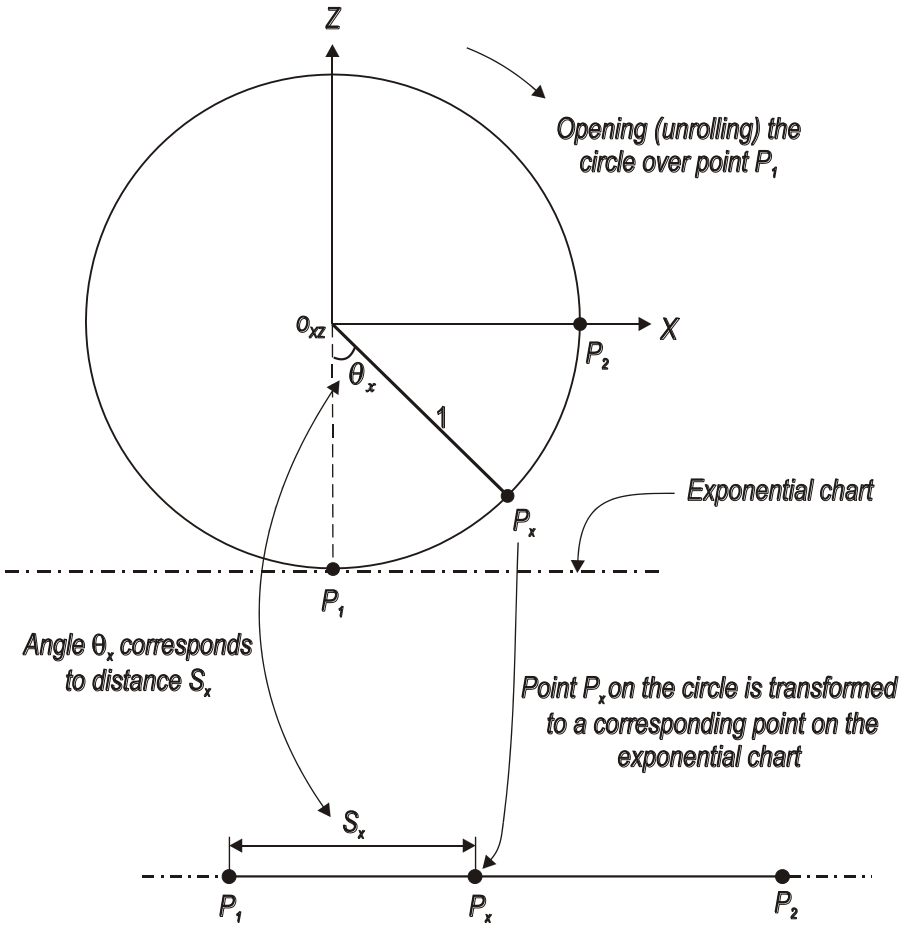


Figure 2.4 Riemannian representation of a 2D unit vector in Euclidean space (Rasouli, 2002).

In this case, one can imagine that, for example, the mean of the data will be located on the unit circle. In the above simple example, the mean vector as is transferred back to the circle shows point (0.50, 0.50) but this time it is located on the circle. In another word, for the case of linear profiles, the data can be considered as their angles with respect to a datum axis. In our example here, the representations of the two vectors in Riemannian space are 0 and $\pi/2$, corresponding to the angle identifying vectors (0.0, 1.0) and (1.0, 0.0).Similar to what explained for a 2D linear profile above, the unit vectors extracted from a rock surface using a hypothetical sampling device will be located on the surface of a unit sphere. The Riemannian representation of a unit sphere is a 2D plane.

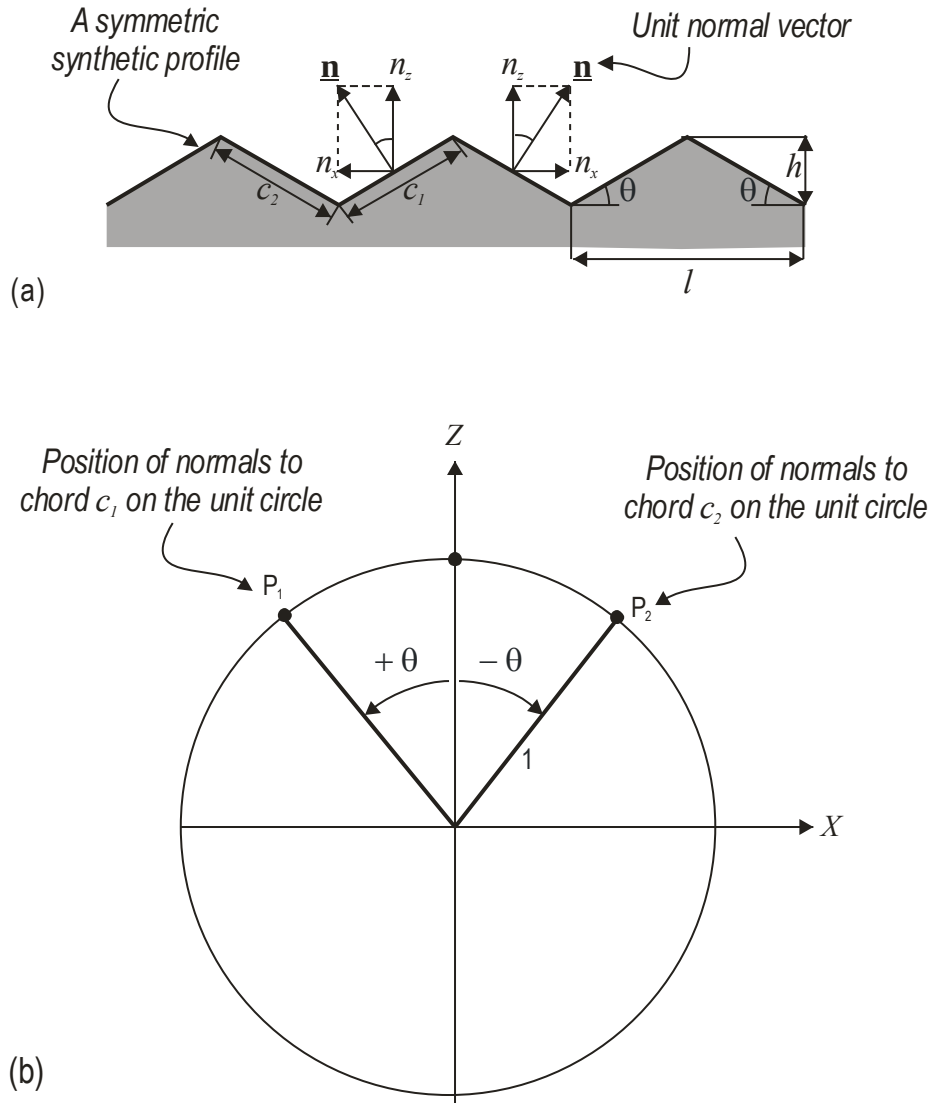


Figure 2.5 Unit normal vectors to a symmetric synthetic profile (Rasouli, 2002).

Transformation of data from a unit sphere to its corresponding Riemannian space is not straightforward and requires complicated mathematical computations. The reader is referred to Rasouli (2002) for detailed discussion on this.

For linear profiles, Rasouli (2002) proposed the 1D Riemannian dispersion parameter ($D_{R1}$) corresponding to the standard deviation of unit normal vectors calculated on the principal chart as a measure of profile roughness. The larger the $D_{R1}$, the rougher the profile.

For a synthetic symmetric triangular profile shown in Figure 2.5

$$D_{R1} = \theta = \tan^{-1}(2h/l). \tag{2.4}$$

which shows that for such a profile the base angle (represented in radians) of the profile is the measure of roughness in Riemannian space.

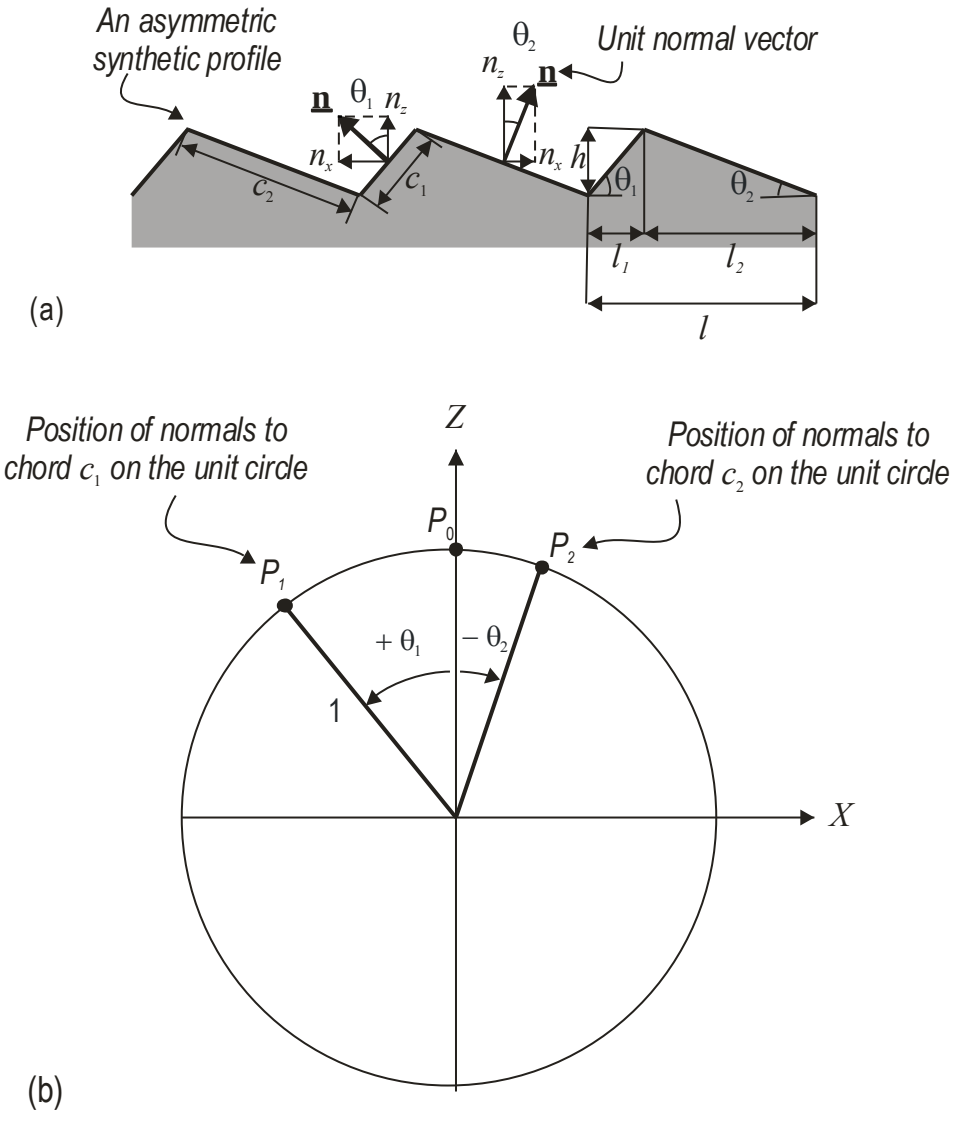


Figure 2.6 Unit normal vectors to an asymmetric synthetic profile (Rasouli, 2002).

$D_{R1}$ changes between 0 and $\pi/2$ but in real rock profiles the base angle is unlikely to be greater than about 10 degrees (i.e. 0.175).

In Figure 2.6 an asymmetric synthetic triangular profile is shown. The geometry of this profile is identified using two angles $\theta_1$ and $\theta_2$ corresponding to chords $c_1$ and $c_2$, respectively. For such a profile $D_{R1}$ is obtained as

$$D_{R1} = \left[ K\left(\theta_1 - \bar{\theta}\right)^2 + \frac{c_2}{c_1} K\left(\theta_2 - \bar{\theta}\right)^2 \right]^{1/2} + \left( K\left(\theta_1\right) + \frac{c_2}{c_1} K\left(\theta_2\right) \right) \tag{2.5}$$

where

$$c_1 = \left(l_1^2 + h^2\right)^{1/2}, \quad c_2 = \left(l_2^2 + h^2\right)^{1/2}, \quad K = c_1/\left(c_1 + c_2\right). \tag{2.6}$$

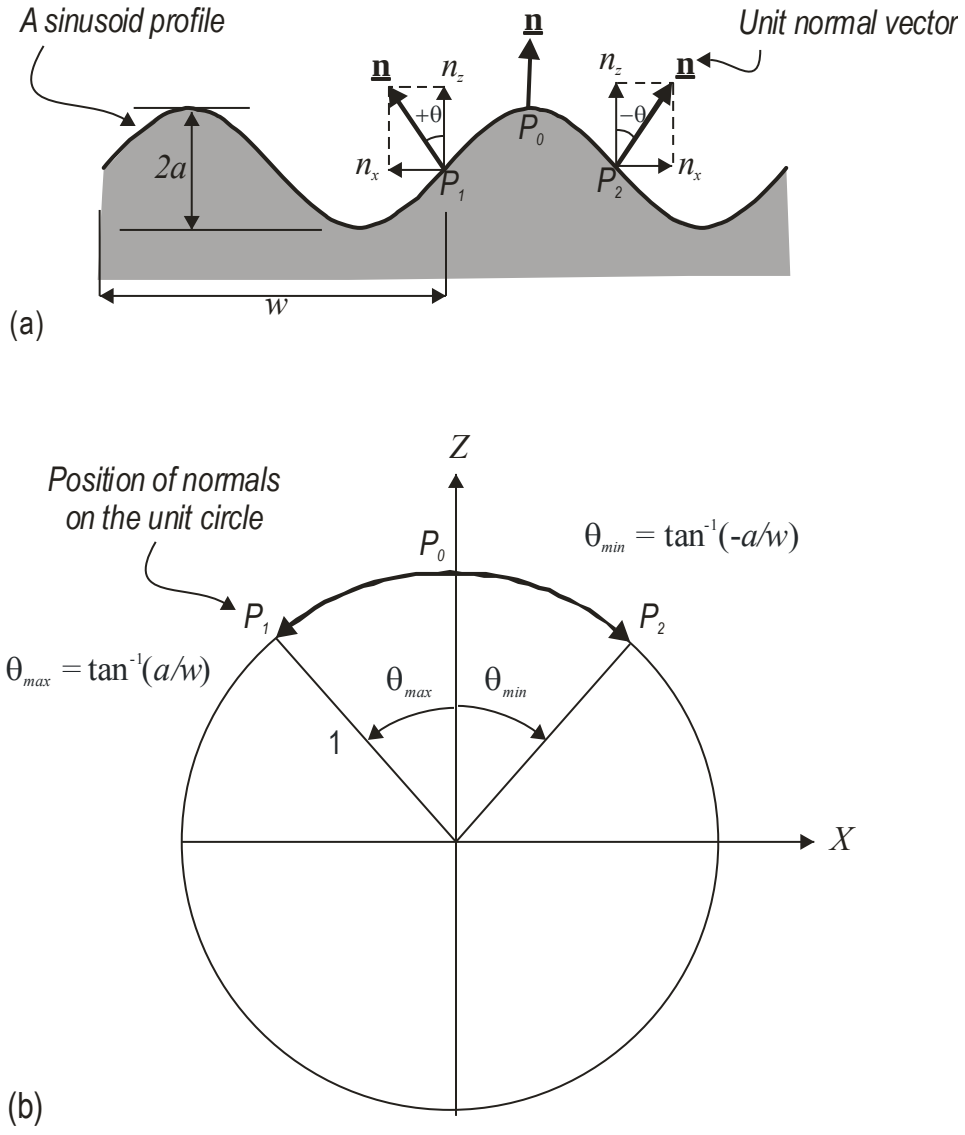


Figure 2.7 Unit normal vectors to a sinusoidal profile (Rasouli, 2002).

As the symmetry ratio ($l_1/l_2$) increases towards unity ($l_1 \rightarrow l_2=l$), it can be seen that Equation 2.5 approaches Equation 2.4, i.e. roughness of a symmetric triangular profile. For a sinusoidal profile in a general form of $z = a\sin bx$, with amplitude $2a$ and wavelength $w = 2\pi/b$ (or aspect ratio $a/w$ where $b = 2\pi/w$ ), as shown in Figure 2.7, calculations of $D_{\mathrm{R1}}$ results in

$$D_{R1} = \left(S_{R1}^2\right)^{1/2} = \left[\frac{2}{3}\left(\tan^{-1}\left(2\pi a/w\right)\right)^3\right]^{1/2} = \left(\frac{2}{3}\right)^{1/2}\left[\tan^{-1}\left(2\pi a/w\right)\right]^{3/2}. \qquad (2.7)$$

which indicates that profile roughness increases as the wavelength ($w$) decreases or amplitude ($2a$) increases, but not as a linear proportion. From this equation the maximum value of roughness is 1.6074. Comparing this equation with Equation 2.4 (with maximum value of 1.57), it can be found that geometrically a sinusoidal profile shows a larger range of roughness values than a synthetic symmetric profile. This is because the maximum deviation of normals on a sinusoidal profile is larger than on the corresponding symmetric profile (Rasouli, 2002).

It was extensively shown that the $D_{\mathrm{R1}}$ has large capabilities to be applied as profile roughness descriptor. In Chapter 3, numerical simulations will be performed on synthetic profiles to estimate their peak and residual shear strengths. Then $D_{\mathrm{R1}}$ of each profile will be linked to its peak shear strength to show the applicability of the parameter, which is the objective of this work.

In the following Sections, fracture shear strength models will be reviewed in separate Sections as analytical and empirical, numerical, and experimental approaches. It was attempted to cover the approaches and models which are somehow related to the objectives of this work.

## 2.2 Analytical and empirical models

In this Section, some of the analytical solutions and empirical relationships for fracture shear strength estimation are reviewed.

### 2.2.1 Coulomb sliding criterion

Perhaps one of the oldest shear strength criteria is the linear correlation proposed in 1776 by coulomb with its modified form known as Coulomb's sliding law. This is appropriate for fractures having planar smooth surfaces. The Mohr-Coulomb criteria which presented based on earlier Coulomb law (Figure 2.8) is expressed as:

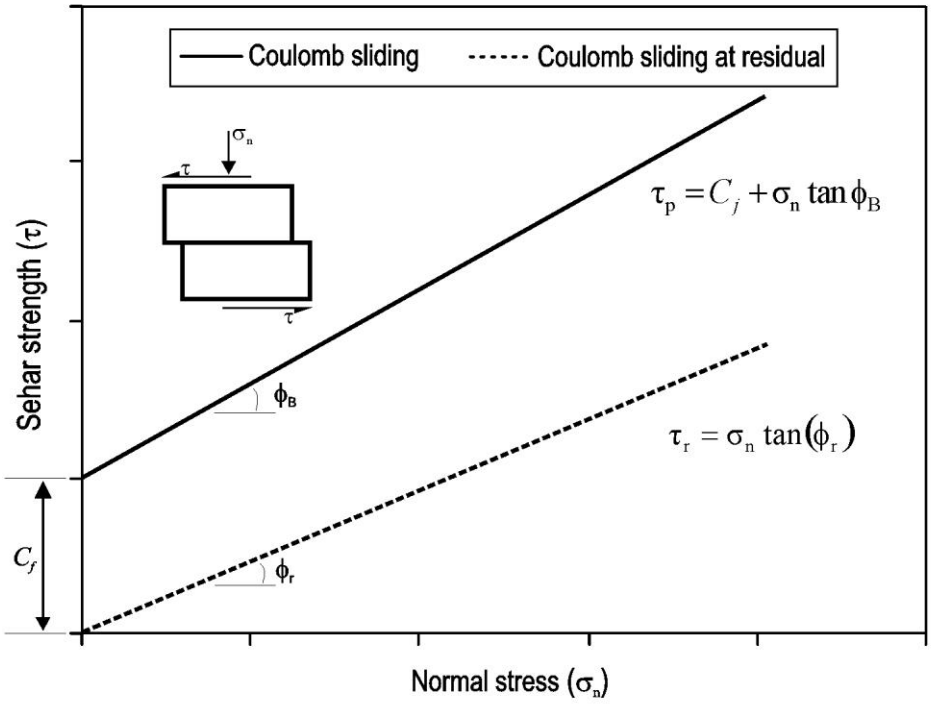


Figure 2.8 Mohr-Coulomb fracture curves at peak and residual shear strengths.

$$\tau_p = C_f + \sigma_n \tan\phi_p . \tag{2.8}$$

where $\tau_p$ is joint shear strength, $\phi_p$ is joint peak friction angle, $\sigma_n$ is normal stress and $C_f$ is the joint cohesion. The criterion can also be used for the residual shear strength by taking $C_f = 0$ and substituting the peak friction angle by residual friction angle, see Figure 2.8.

The Mohr-Coulomb relation is the most widely used criterion for estimating the shear strength of rock fractures. The criterion is suitable for wide range of applications, except at low stresses, where the shear strength of the fractures is being overestimated (Herdocia, 1985). The Mohr-Coulomb criterion has been used to predict shear strength of large scale fractures, i.e. faults which generally considered as smooth fractures. However, this is debatable considering the different effect of roughness and waviness on fractures behaviour as stated by Jafari et al (2003). While it might be acceptable to ignore the effect of roughness (i.e. second order asperities) on fault movements, waviness (or first order asperities) plays a significant role in fault slippage mechanism.

### 2.2.2 Patton's bilinear equation

The undulations and asperities on a natural joint surface have a significant influence on its shear behaviour (Barton, 1973; Patton, 1966). Patton (1966) demonstrated the significant effect of joint surface geometry on the shear behaviour of rough joints by

conducting several direct shear tests on the small saw-tooth replicas with different asperity inclinations, *i*, at varying normal stresses. From these tests he established a bilinear failure envelope shown in Figure 2.9. This figure shows that the failure curve consists of two lines, intersecting at a transition point before which the sliding along the asperities at low normal stresses expected to occur, whereas at higher normal stresses shearing of asperities is the dominant mechanism.

Assuming that the asperities slide along each other at low normal stresses, the peak shear strength was proposed by Patton (1966) as

$$\tau_p = \sigma_n \tan(\phi_B + i), \tag{2.9}$$

where $\tau_p$ is joint shear strength, $\phi_B$ is the basic friction angle (i.e. the angle of frictional sliding resistance along the asperities), $\sigma_n$ is the normal stress and $i$ is the asperity inclination angle (i.e. dilation angle). At high normal stress, where the asperities are assumed to be sheared off and the dilatancy vanishes, the residual shear strength is expressed as (Patton, 1966)

$$\tau_r = \sigma_n \tan(\phi_r). \tag{2.10}$$

where $\phi_r$ is the residual friction angle. Although, such an implication does not account for asperity degradation and evolution of roughness in shearing, it is a good estimate of shear strength of saw-tooth asperities. The geometry of real fractures is too complex and cannot be simply estimated using this simple model.

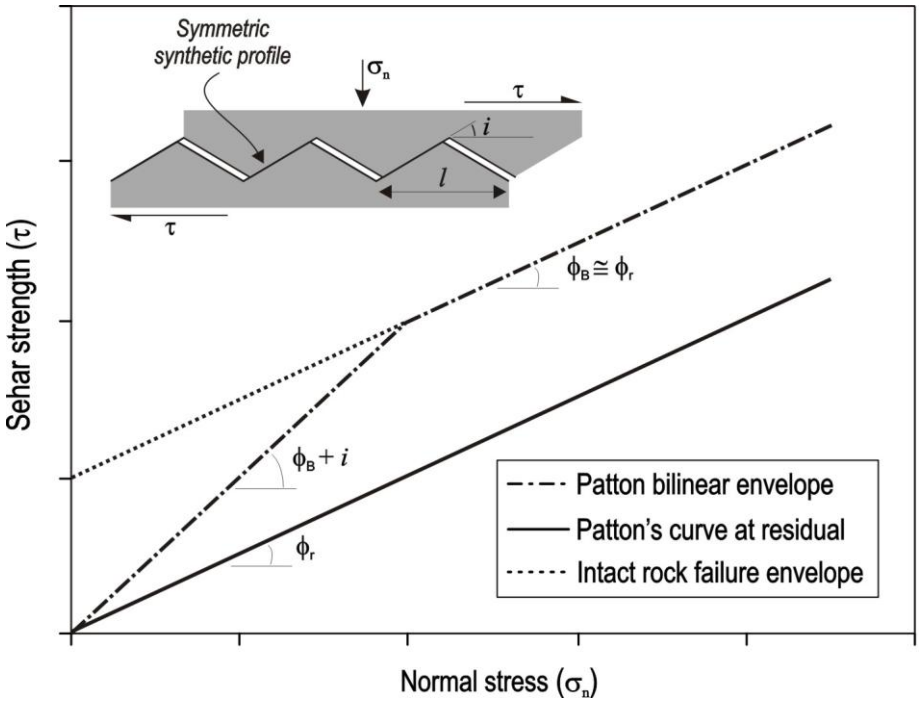


Figure 2.9 Patton bilinear fracture shear strength model proposed for saw-tooth asperities.

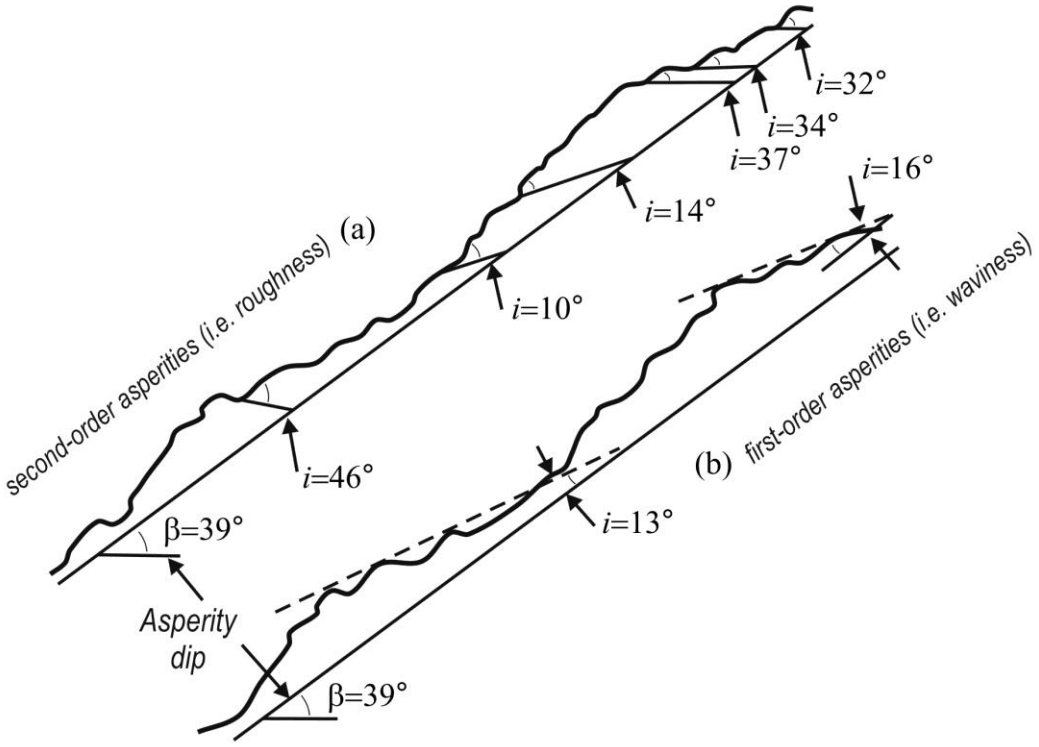


Figure 2.10 First and second order roughness (from Patton, 1966).

In natural fractures, the first-order and second-order asperities introduced by Patton (1966) and shown in Figure 2.10 appear to have different impacts on fracture shear strength. At low normal stresses, second-order asperities influence the shear behaviour of fractures dominantly whereas at high normal stresses this is the first order asperities, referred to as waviness, which plays the major role in shear response of fractures.

Amongst the roughness parameters introduced earlier on, it appears that the $D_{R1}$ concept proposed based on the distribution of unit normal vectors to a profile is capable of capturing both of these roughness components and therefore can be a good representative for roughness characterization. This is further discussed in Chapter 3.

### 2.2.3 Ladanyi and Archambault's criterion

Ladanyi and Archambault (1970) developed a peak shear strength criterion for rock fractures which includes both asperity sliding and shearing-off (i.e. cut-off) behaviours. Their criterion is in the form of

$$\tau = \frac{\sigma_n (1-\alpha_s)(V + \tan\phi_B) + \alpha_s . \tau}{1-(1-\alpha_s)V\tan\phi_B} . \tag{2.11}$$

$\tau$ is the fracture shear strength, $\phi_B$ is basic friction angle of fracture, $\sigma_n$ is the normal stress and $\alpha_s$ is the proportion of fracture surface which is sheared through the intact material ($\alpha_s = A_s / A$ in which $A_s$ is the contact area over which asperities are being

sheared and $A$ is the total projected shear area, see Figure 2.11), $V$ is the dilation rate, $V = dv/du$ at peak shear stress, and $\tau$ is the shear strength of the intact material which is defined as

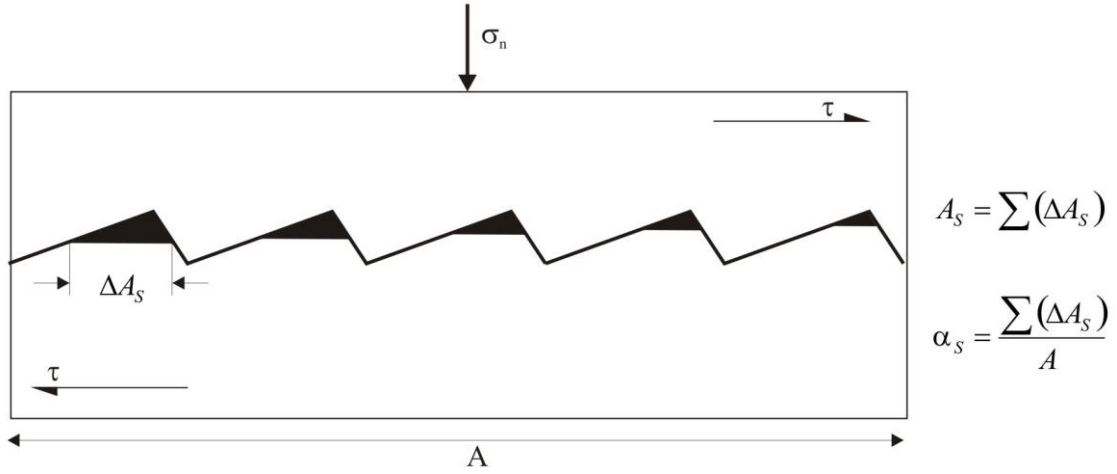


Figure 2.11 Sheared-off asperities and visual demonstration of $\alpha_s$ (after Ladanyi and Archambault, 1970).

$$\tau = c + \sigma_n \tan\phi . \tag{2.12}$$

Equation 2.11 was developed based on dividing the total shear strength into four different components ($S_1$-$S_4$): external work done in dilating against normal force, additional internal work in friction due to dilatancy, friction with no dilation, and shearing of solid asperities. Equation 2.11 is the final form of the criteria where $S_1$ to $S_4$ are replaced with their corresponding functions. A schematic diagram of the sheared-off area is shown in Figure 2.11. One of the difficulties associated with this model is how to determine the $\alpha_s$ and $V$ for rock fractures as they are expected to vary with the normal stress as shown in Figure 2.12.

Substituting Equation 2.12 into Equation 2.11, Ladanyi and Archambault (1970) determined the critical normal stress, $\sigma_r$ as

$$\sigma_r = \frac{c}{\tan(\phi_B + i) - \tan\phi} . \tag{2.13}$$

where $c$ and $\phi$ are the cohesion and friction angle of the intact rock, respectively. This gives an estimate of transition normal stress (see Figure 2.12). Transition normal stress indicates the normal stress above which dilation does not take place along the fracture surfaces as asperities are completely sheared-off.

Taking into account the dependency of the dilation rate and the sheared-off area to the applied normal stress, Ladanyi and Archambault (1980) proposed following correlations

$$\alpha_s = 1 - \left(1 - \frac{\sigma_n}{\eta \sigma_r}\right)^L . \tag{2.14}$$

$$V = \left(1 - \frac{\sigma_n}{\eta \sigma_r}\right)^K \tan(i_0). \tag{2.15}$$

where $\sigma_r$ is the transition normal stress (practically equal to compressive strength of the sample) above which no dilatancy is expected along the asperities. $L$ and $K$ are dimensionless constants with values of 1.5 and 4, respectively. $i_0$ is the geometrical ascending slope of the intact asperities, and $\eta$ is a parameter which takes into account the initial degree of interlocking of the asperities (Ladanyi and Archambault, 1980).

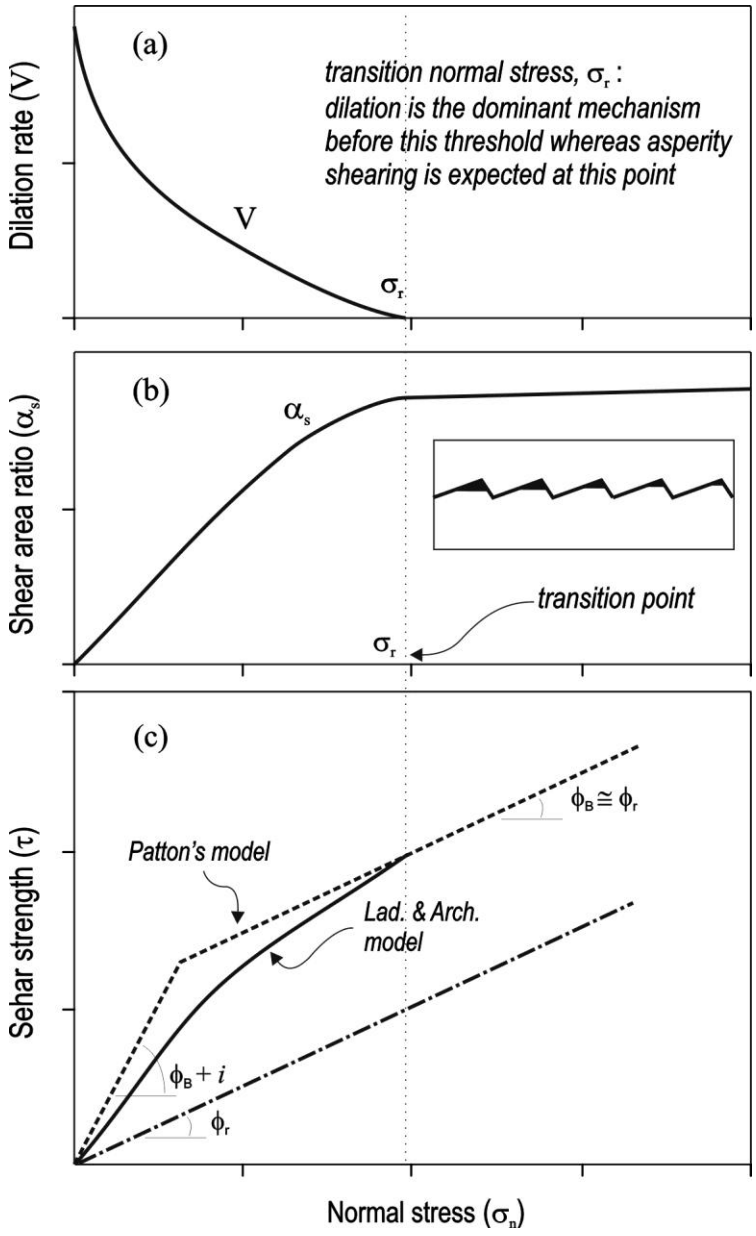


Figure 2.12 Fracture shear strength model for jointed rock (after Ladanyi and Archambault, 1970).

Figure 2.12 shows the Ladanyi and Archumbault's fracture curve, as well as variation of both dilation rate and sheared area ratio with normal stress. Figure 2.12.a shows that approaching the transition point the dilation rate reduces and becomes zero at stresses above this threshold.

However, as depicted in Figure 2.12.b, the ratio sheared-off area increases as a result of applying larger normal stresses but approaches to a constant value at normal stress above the transition point ($\sigma_r$) meaning that failure ultimately occurs within the intact rock. Figure 2.12.c compares the bi-linear failure model proposed by Patton (1966) with curved envelope of Ladanyi and Archambault, 1980.

From the above discussion it may be concluded that although the proposed model appears to be robust in terms of considering various failure modes, its applicability is likely to be limited due to the need for identifying number of constant variables, which practically is not straightforward. Therefore, the need for a simpler model remains on demand. Using a similar concept, Huang et al. (2002) proposed a limit equilibrium approach to determine the shear strength of triangular shaped asperities, which will be discussed later in Section 2.2.7.

### 2.2.4 Barton empirical criterion

Barton (1973) and Barton & Choubey (1977) proposed the most well-known empirical shear strength criterion based on Joint Roughness Coefficient (JRC) and strength parameters of jointed rock mass. The criterion is expressed as

$$\tau = \sigma_n \tan\left( JRC \log_{10}\left( \frac{JCS}{\sigma_n} \right) + \phi_B \right). \tag{2.16}$$

In this equation $\tau$ is fracture shear strength, $\sigma_n$ is the normal stress, $\phi_B$ is the basic friction angle, *JCS* is the joint wall compressive strength and *JRC* is the joint roughness coefficient, introduced in Section 2.1.1. This criterion was developed based on experimental works carried out on more than 100 replicas with different strength properties. The criterion has a similar form as Patton's bilinear law, but here the dilation, *i*, varies as a function of normal stress, in the form of

$$i = JRC \log_{10}\left( \frac{JCS}{\sigma_n} \right). \tag{2.17}$$

Whilst, in contrast to Patton's bilinear shear strength criterion, Barton's criterion has the merit of providing a gradual degradation of friction angle with respect to increasing

normal stress, its application is often limited by the bias in determination of the *JRC* from the standard profiles (Barton, 1973). This issue was discussed in Section 2.1.1.

Since both *JRC* and *JCS* are scale dependent, Barton et al. (1985) developed the following relations, based on their experimental lab works, to estimate the field scale values of these parameters:

$$JRC_n = JRC_0 \left[ \frac{L_n}{L_0} \right]^{-0.02JRC_0} . \tag{2.18}$$

$$JCS_n = JCS_0 \left[ \frac{L_n}{L_0} \right]^{-0.03JRC_0} . \tag{2.19}$$

In the above equations the subscripts 0 and *n* refer to the lab and field scale values, respectively. It is to be noted that the nominal lab scale sample length is $L_0 = 100$ mm.

Although this is the most commonly used criterion for estimation of rough fracture shear strength, its application is limited due to difficulties encountered in *JRC* value estimation. In Chapter 3, it will be shown how, in current work, it is attempted to correlate roughness parameter $D_{R1}$ with shear strength of the profile using numerical simulation of fracture shear strength.

More recently, Asadollahi and Tonon (2010a) and Asadollahi et al. (2010) Revisited Barton's empirical model for fracture shear strength and later modified their model using laboratory experiments. They modified Barton's original model in order to address the following limitations: independency of the peak shear displacement to normal stress; the assumption of zero mobilized *JRC* after 100 times the peak shear displacement for post-peak shear strength; the assumption of zero dilation displacement at up to one-third of peak shear displacement. They collected and analyzed a database of results of direct shear tests available in the literature and introduced an empirical equation to predict the peak shear displacement, which considers the effect of normal stress and works for all types of rock discontinuities, even sawed fractures. This equation is expressed as

$$\delta_{peak} = 0.0077 L^{0.45} \left( \frac{\sigma_n}{JCS} \right)^{0.34} \cos\left( JRC \log\left( \frac{JCS}{\sigma_n} \right) \right). \tag{2.19.a}$$

Using this approach, the post-peak mobilized *JRC* can be obtained using a power-base equation, instead of employing Barton's table. They stated that the new empirical equation for post-peak mobilized *JRC* works for all ranges of displacements. The

modified model can also predict negative compressive dilatancy at small shear displacements.

### 2.2.5 Fracture deformation models

The currently existing fracture deformation models are the Coulomb friction model, the Barton–Bandis joint model (Barton et al., 1985) and the continuously yielding joint model (Cundall and Lemos, 1990). The Coulomb linear deformation model, as explained previously in Section 2.2.1, sufficiently models smooth discontinuities. The Barton–Bandis joint model is more appropriate to explain the non-linear behaviour of rough rock joints (Indraratna and Haque, 2000).

The continuously yielding model (CYM) proposed by Cundall and Lemos (1990) represents plastic deformation during shearing of fracture surfaces. This model can simulate the internal mechanism of progressive damage of the joint under shear. The CYM is more realistic than the standard Mohr-Coulomb joint model in that it could consider the nonlinear behaviour observed in physical tests such as joint shearing damage, normal stiffness changes due to different normal stress levels, and decrease in dilation angle with plastic shear displacement (Cundall, 2008; Indraratna and Haque, 2000).

### 2.2.6 Asperity degradation models

Asperity damage (it is also called asperity degradation) is a potential mechanism which may take place during shearing a fracture plane. This happens in a complicated manner and can influence the ultimate shear strength of the fracture significantly.

During shearing, the joint roughness undergoes continuous changes due to wearing, grinding, breaking and crushing of asperities. The evolution of dilation angle during fracture shearing has been addressed by various laws (Hutson and Dowding, 1990; Ladanyi and Archambault, 1970; Plesha, 1987; Son et al., 2001). Plesha (1987) proposed a plasticity-based model for surface asperity degradation. This concept was studied in further details by Lee et al. (2001). In a recent work by Belem et al. (2007), they proposed explicit joint surface roughness degradation models based on experimental, analytical and previous works to describe the evolution of initial surface roughness under monotonic and cyclic shearing. One of the merits of their work is that shear behaviour of jointed specimens were studied under large cyclic shearing loads (e.g. strong earthquakes), which causes most of the first- and second-order asperities being degraded. Another advantage of the proposed models is that they can predict the

degradation of a fracture surface undergoing shearing as a function of applied initial normal stress, normal stiffness and accumulated shear displacement (Asadollahi and Tonon, 2010b; Belem et al., 2007, 2009).

Characterising roughness in their models using fractal dimension, which is still debatable (see discussion given in Section 2.1.2) is perhaps a weakness of this model. In this work, we partly investigate the degradation mechanism in fracture shearing and show how it is influenced by surface roughness. This is while modelling the continuous change in surface roughness during shearing is very cumbersome: this is one of the elements which add complexity into modelling asperity degradation mechanism.

### 2.2.7 Asperity cut-off mechanism

Huang et al (2002) proposed a simplified analytical model to estimate shear strength of a synthetic crenulated profile with symmetric triangle asperities, as shown in Figure 2.13. This model was developed based on Mohr-Coulomb failure criterion and employing the limit equilibrium analysis of normal and shear forces acting on asperity contacts. They also performed direct shear tests on artificial fractures with symmetric asperities in the lab and validated their developed analytical model.

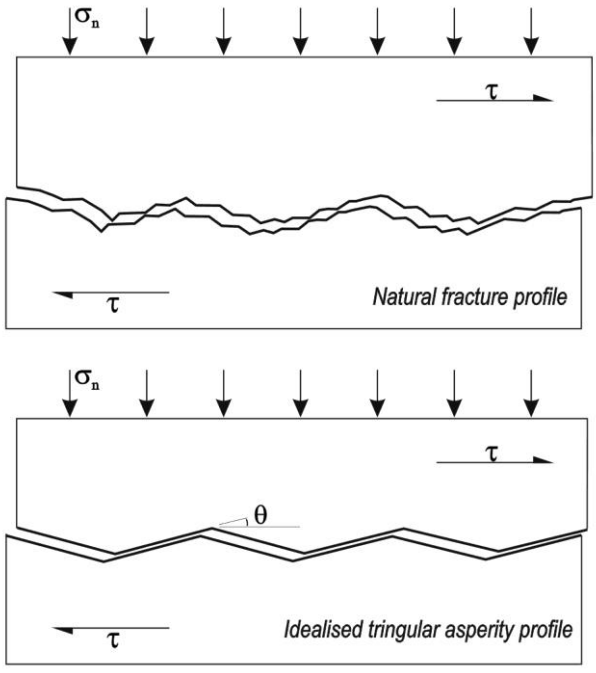


Figure 2.13 Simulation of a rock fracture with an idealised triangular asperity profile (after Huang et al. 2002).

Figure 2.14 shows a shear box containing a symmetric triangular profile with angle θ, chord length *s*, and asperity base length *L* in a material that obeys a linear Coulomb strength criterion. This profile is subjected to both a horizontal shear stress τ acting

from left to the right direction and a normal stress $\sigma_n$ applying vertically. The stiffness of the system is assumed sufficiently high to ensure that failures occur at asperities' upslope (i.e. chord *s*). The limit equilibrium analysis of free body diagram of the broken asperity gives the resultant normal and shear forces on cut-off plane based on normal and shear stresses $(\sigma_n, \tau)$ applied to the shear box. Applying Coulomb's failure criterion the shear strength of the critical plane along which shear failure occurs is defined as

$$\tau = \frac{c \sin\theta / \sin(\theta+\alpha)}{\cos\alpha - \sin\alpha \tan\phi} + \sigma_n \tan(\alpha+\phi), \tag{2.20}$$

where $\alpha$ is the inclination of the critical plane (found by evaluating $d\tau/d\alpha = 0$), $\theta$ is the asperity base angle, and *c* and $\phi$ are the cohesion and friction angle of the intact rock, respectively (details of derivation of the formula is given in Appendix 2).

Equation 2.20 was initially developed based on the assumption that horizontal displacement of the specimen has caused the right chord of the lower block to have previously separated from the upper matched block, and hence forces acting on the right side chord are zero.

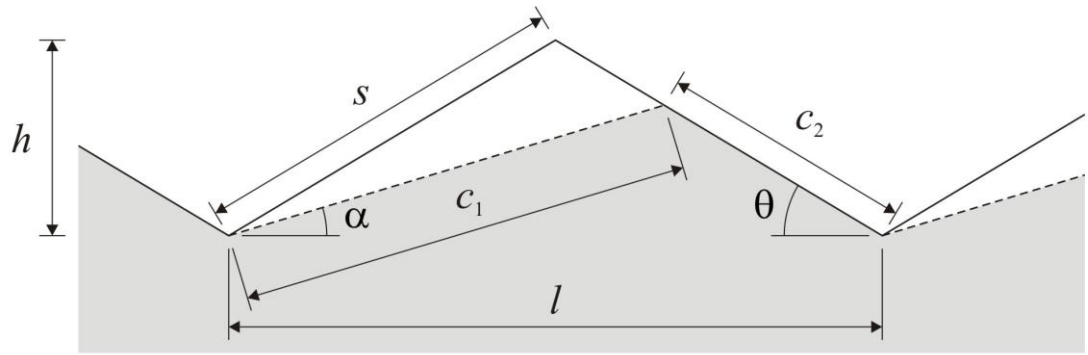


Figure 2.14 Geometrical features of asperity Cut-off in a symmetric triangular profile.

Figure 2.14 shows that after asperity failure is taken place, the profile geometry changes to an asymmetric triangular profile with angles $\alpha$ and $\theta$ corresponding to chords $c_1$ and $c_2$, respectively, where

$$c_1 = l \sin\theta / \sin(\theta+\alpha) \tag{2.21}$$

and

$$c_2 = l \sin\alpha / \sin(\theta+\alpha). \tag{2.22}$$

The normal stress above which the profile roughness will be sheared completely smooth is obtained by evaluating $\left(\mathrm{d}\tau/\mathrm{d}\sigma_{\mathrm{n}}\right)_{\alpha=0}=0$, which leads to

$$\sigma_{\mathrm{n}}\big|_{\alpha=0}=c(\cot\theta-\tan\phi)\cos^{2}\phi. \tag{2.23}$$

This defines the point at which fracture shear strength curve intersects the intact rock material and above which fracture roughness becomes ineffective on peak shear strength behaviour of the fracture. This equation was derived in current study which derivation details are given in Appendix 2.

As discussed in Section 2.2.3, Ladanyi and Archambault (1970) defined this point using their asperity contact model (see Equation 2.13). The comparison between their model and the latter model given by Equation 2.23 is shown in Figure 2.15, where the critical normal stress is plotted versus asperity inclination angle θ or *i*. This figure shows that in both models the asperities sheared off due to increased normal stresses. The difference between the results of the two models comes from the basic friction angle ($\phi_B$) appearing only in Ladanyi and Archambault model. As the asperities are all sheared-off, it is expected that the critical normal stress to be independent of fracture basic friction angle and in this respect the second model is thought to be more appropriate.

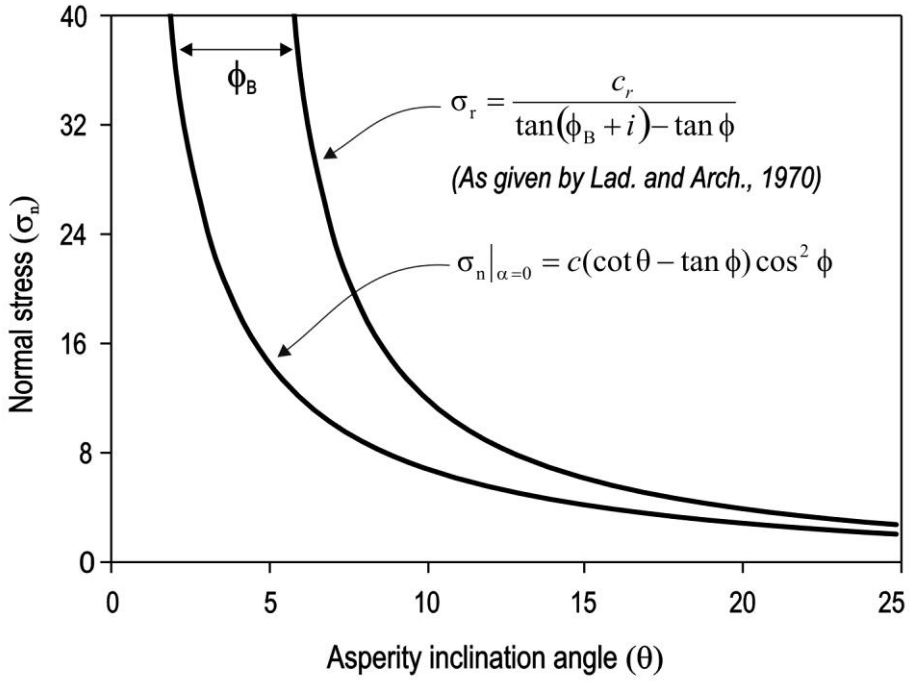


Figure 2.15 Critical normal stress versus asperity inclination angle for a symmetric triangular asperity profile depicted in Figure 2.14.

However, the effect of basic friction angle reduces at higher normal stresses and this is why in Figure 2.15 the two models become less different as normal stress

increases. Equation 2.20 together with the Coulomb sliding model given by Equation 2.8 could be used to represent the shear strength envelope for a synthetic triangular fracture profile. This is shown in Figure 2.16 for different profiles with increased base angles, where the corresponding asperity cut-off angles, $\alpha$, for these profiles are also plotted. As is seen from this figure, the shear strength increases as the normal stress becomes higher and this is larger for rougher profiles (i.e. higher asperity angles).

Also, from Figure 2.16 it can be seen that the cut-off angle decreases as normal stress increases and levels off to zero, which corresponds to a smooth surface where the asperities are sheared off from the base line. In general, the shearing process of fractures is expected to be a combination of contact sliding at low normal stresses, asperity cut-off at relatively high normal stresses, and rock failure at normal stresses larger than the critical normal stress defined using Equation 2.23. These are depicted in Figure 2.17 where the transition point between these three mechanisms may vary as a function of fracture basic friction angle and cohesion properties. It is to be noted that not all of three mechanisms are necessary to occur and depending on the normal stress level the fracture may begin to experience the asperity cut-off or even the failure may start within the intact rock.

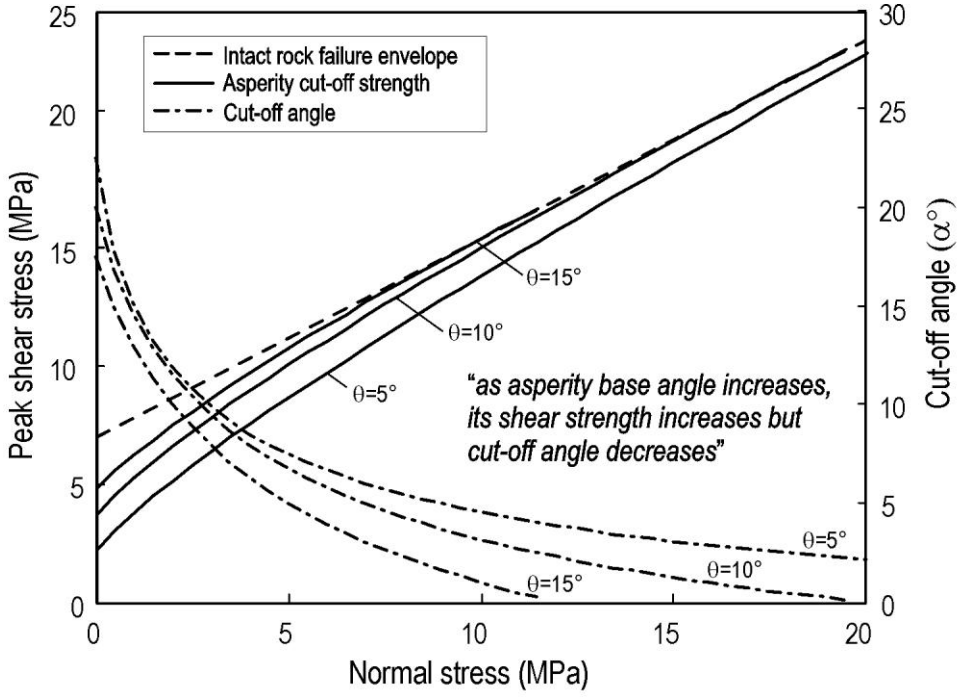


Figure 2.16 Shear strength and asperity cut-off angle of synthetic symmetric triangular profiles as a function of normal stress.

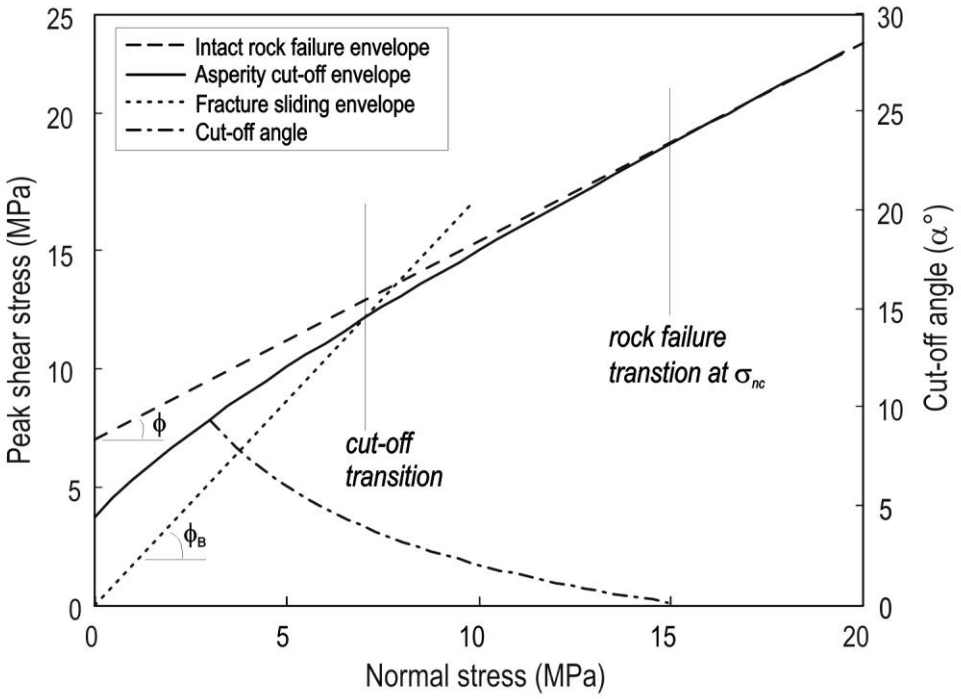


Figure 2.17 Transition between fracture sliding, asperity cut-off, and intact rock failure mechanisms.

Huang et al. (2002) through their lab experiments on two sets of artificial symmetric triangular fractures with base angles of θ = 15° and θ = 30°, reported on four types of failure modes: these are defined as asperity sliding, cut-off, separation, and crushing which occur during fracture shearing. Figure 2.18 schematically shows asperity sliding and cut-off at different normal stresses from their work. It is seen that as normal stress and asperity angle increase, cut-off angle decrease until becomes a smooth surface parallel to fracture plane. For example, with asperity angle of 30 degrees, 1.5 MPa of normal stress gives a horizontal cut-off plane in which asperity is completely sheared-off; it can be identified as critical normal stress at which failures (e.g. large cracks) take place within the intact rock. Further discussion on this will be made in the Chapter 3 together with our simulation outcomes.

Huang et al. (2002), validated the results of their analytical cut-off model by comparing them with experimental results and found a good agreement. Similar behaviour was also observed through the numerical simulation of synthetic profiles, the results of which will be given in Chapter 3.

This phenomenon will be experimentally tested and the results of which will be presented in Chapter 4. The values of critical normal stress obtained analytically using Equation 2.23 in this Section will be used to correlate roughness parameter ($D_{R1}$) with values of peak shear strength obtained from simulations in Chapter 3.

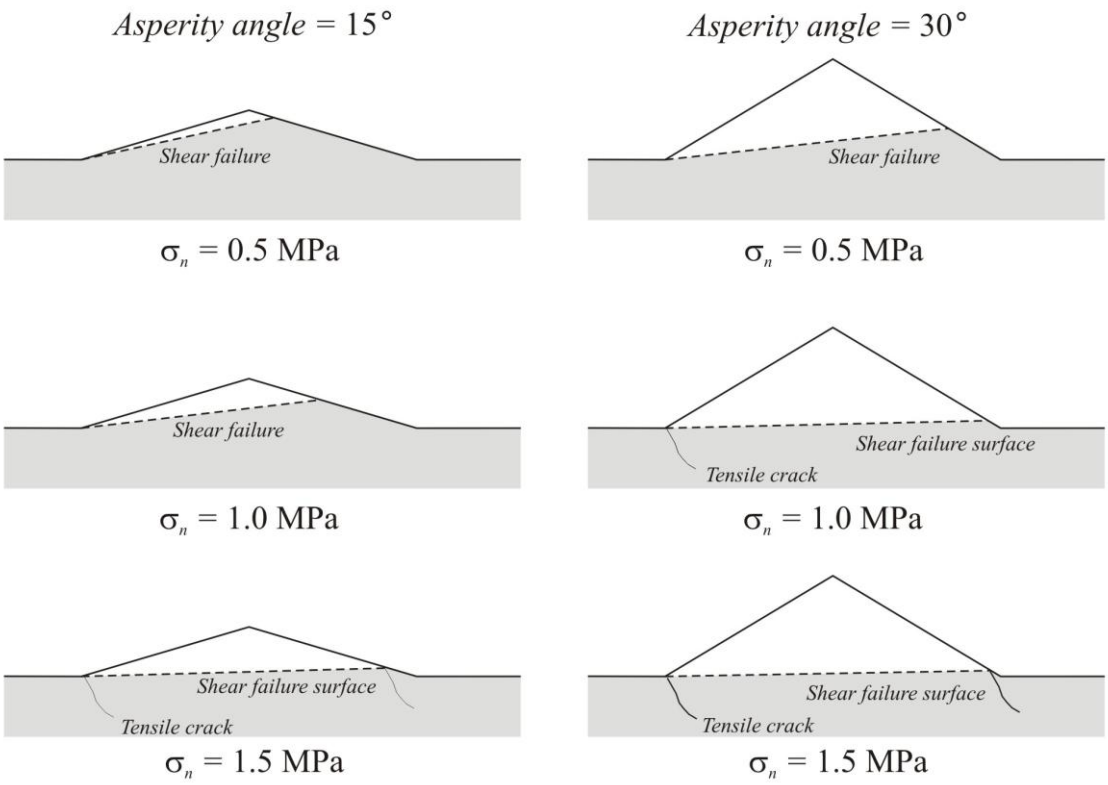


Figure 2.18 Failure modes observed in direct shear experiments (after Huang et al. 2002).

## 2.3 Numerical models

Different numerical models have been used to study the significant influence of discontinuities on the hydro-mechanical and thermal behaviour of fractured rock masses (Cundall and Lemos, 1990; Cundall and Strack, 1979; Ivars et al., 2008; Kulatilake, 1998) . Amongst these, the three most frequently cited constitutive models which have been integrated into the universal distinct element code (UDEC) are Coulomb sliding model, Barton-Bandis joint model and the CYM. The recently developed degradation model by Belem (2007) uses a similar formulation as the CYM and can be implemented in the UDEC. In these models a roughness parameter such as JRC or the average asperity angle, $i$, is used to consider the effects of surface roughness on fracture mechanical behaviour.

Finite difference modelling (FDM) has been widely used in simulation of rock fractures behaviour particularly in large strains conditions. Fast Lagrangian Analysis of Continua (FLAC) in two and three dimensions is commercial code which is based on explicit FDM. Fracture modelling in these codes is done using the interfaces and giving them different fracture geometries and properties. Numbers of joint constitutive models such as Coulomb sliding and Bandis models have been implemented in FLAC, which

can be assigned to the modelled fracture. The difficulty of using FLAC in simulation of rock fractures is due to limited number of grids existing along the fracture profile (especially large scale faults) which influence the modelling of real rock fractures with complex geometries. Moreover, FLAC is used to determine the fracture properties such as normal and shear stiffness by back calculations of Young and shear modulus of intact rock and rock mass from the uniaxial compression test simulations (Rosso, 1976; Swan, 1983).

Many researchers have attempted to model rock fractures behaviour using FDM method implemented in few numerical codes. Majority of the studies are considering the concept of rock slope stability (Verma and Singh, 2010; Yin et al., 2011; Zhu et al., 2009). Wang (2006) studied the shear band, axial, lateral and volumetric strains as well as Poisson's ratio of anisotropic jointed rock specimen using the FLAC. In his analysis, failure criterion of rock was a composited Mohr-Coulomb criterion with tension cut-off. He considered the inclined joint, treated as square elements of ideal plastic material.

The most relevant numerical works to the current study which have been performed within the last decade are taking the advantageous of FEM, DEM, and coupled FEM/DEM approaches to model the rock fracture shear behaviour. The following is the brief review of these attempts by criticising their benefits and merits to the solutions of rock engineering and fracture mechanics problems.

### 2.3.1 FEM based approaches

FEM based approaches are not intended to be used for simulation of fractured media as this is developed initially for modelling continuum bodies. However, researchers have attempted to adopt the FEM based models for simulation of shear strength of fractured rock masses.

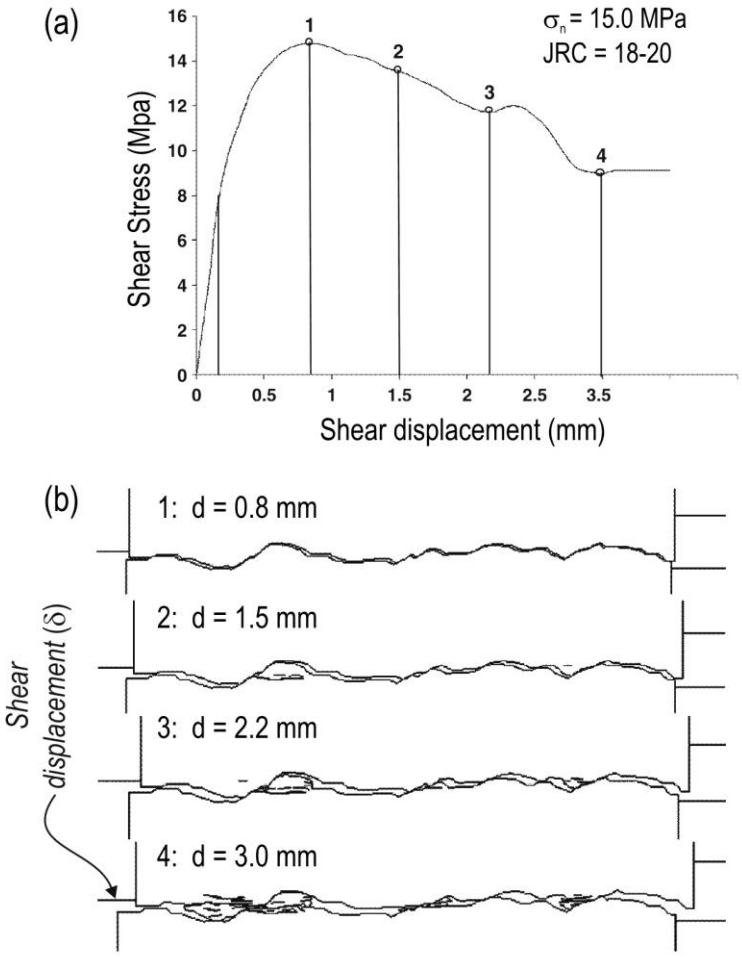


Figure 2.19 (a) Shear stress versus shear displacement curve for profile with JRC=18-20 under 15 MPa normal stress. (b) Displacement of fracture profile upper wall at four stages during the simulation (after Karami and Stead, 2008).

Karami and Stead (2008) performed numerical simulations using Hybrid FEM/DEM code to investigate the process of fracture surface damage and near-surface intact rock tensile failure. They simulated the shear strength of JRC exemplar profiles with JRC values of 5, 10, and 20 in a direct shear tests. They investigated the surface damage mechanisms in terms of joint surface wear or tensile fracturing of the intact rock along the joint plane. Their numerical results agreed closely with published experimental observations. Figure 2.19 gives the results of their studies for profiles with JRC=18-20. Figure 2.19.a shows the shear stress-displacement plot in which four points (1-4) are highlighted starting from peak shear stress and developing to post-peak behaviour showing the residual state of the sheared fracture. Visual comparison between the pre- and post peak behaviours is given in figure 2.19.b.

Karami and Stead (2008) concluded that asperity degradation and propagation of shear-induced micro cracks must be accommodated within the stability analysis particularly for large scale fractures (i.e. faults reactivation analysis). However, this has

not been addressed appropriately within the published studies and needs further research. Although their model seems to be capable of simulating rock fractures deformation under shear loads, it appears to be unable to trace the developments of micro cracks.

Giacomini et al. (2008) performed FEM numerical simulation using a FEM based code called ABACUS to simulate shearing behaviour of synthetic saw-tooth profiles which was previously tested in laboratory experiments by Yang and Chiang (2000). They used the latest version of ABACUS that incorporates an element removal function allowing one to simulate asperity contact damage.

Figure 2.20.a shows the results of their FEM simulations in which degradation of asperity contact is visible while shearing the single asperity fracture from right to left. Degraded material is removed from the model when some degree of damage occurs on asperity contacts and finally shear stress diagram versus shear displacement plotted in Figure 2.20.b. As shown in the figure, there is a good agreement between numerical and experimental results which shows the accuracy of their produced model. These simulations are performed under relatively low normal stresses (here 0.39 and 1.47 MPa), however, it will be useful to perform further simulation under high normal stresses. It must be stated that shear strength of rough fractures are highly affected by the grain size of fracture surface material (which may be referred to as micro-roughness behaviour) and this can affect the initial shear strength of the fractures: this is not taken into account in FEM based simulations since the environment is continuum. We will refer to this concept later in Chapter 3 where it is shown how grain size distribution can significantly affect the micro-roughness (or say first-order asperity) contribution on the ultimate shear behaviour of rough fractures.

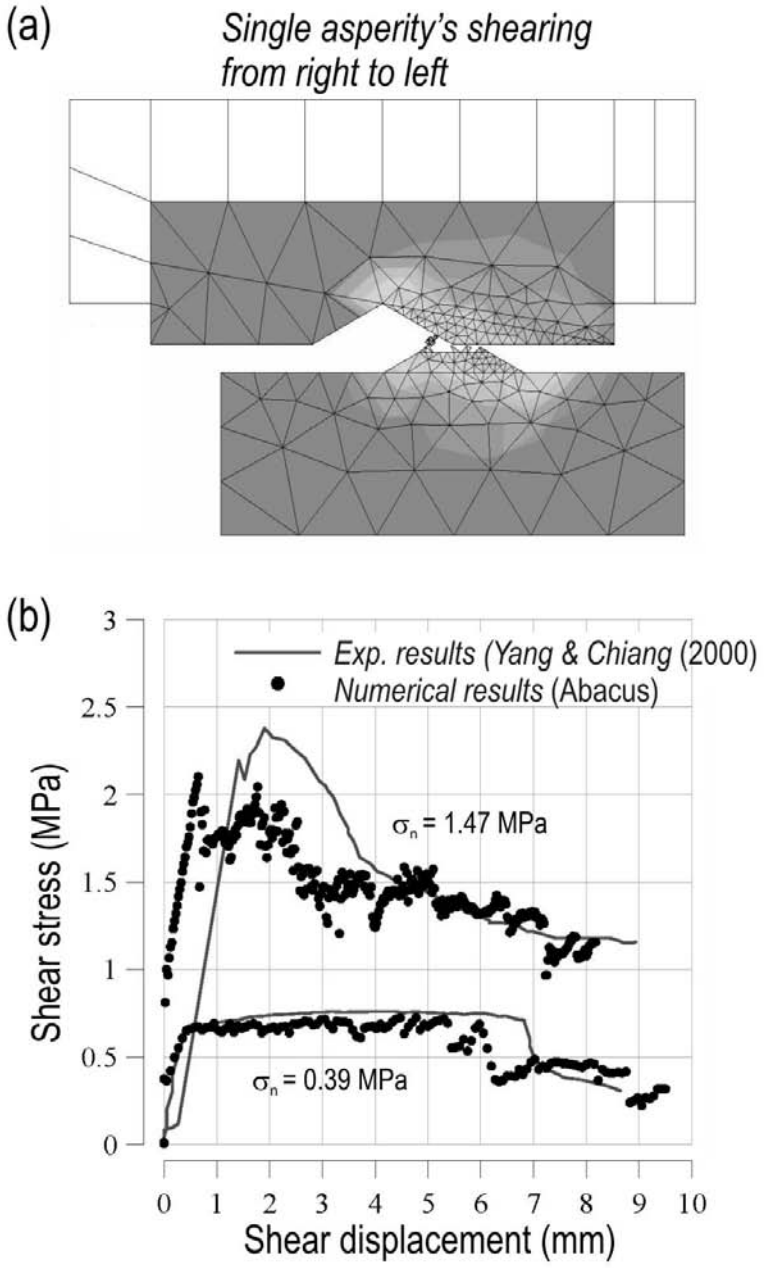


Figure 2.20 (a) Degradation of the contact asperity during shearing, (b) Shear strength versus shear displacement curves, and numerical results versus experimental data at two different normal stresses (Giacomini et al., 2008).

### 2.3.2 DEM based models

Indraratna and Haque (2000) conducted numerical modelling of shear strength of rock fractures using UDEC and studied the effects of infills on fracture shear behaviour. This code has been successfully used to model the shear behaviour of fractured rocks, flow through discontinuities and slope stability problems. The calculations performed in UDEC are based on Newton's second law of motion, mass conservation and momentum of energy principles. These are actually the principals of all DEM based programs. As stated, different joint models are allocated in UDEC program including the linear Mohr-

Coulomb friction model for non-dilatant fractures, the Barton-Bandis model (known as BB model) and continuously yielding model (CYM) for non-linear behaviour of rock fractures.

The continuously yielding model, CYM, (Cundall and Lemos, 1990) can be applied for testing under both constant normal load (CNL) and constant normal stiffness (CNS) conditions. Indraratna and Haque (2000) used this model with preference as they believe it is capable of satisfactorily represent single episodes of shear loading. This model is developed to simulate in a simple manner the internal mechanism of progressive damage of fractures under shearing, the details of its formulation are given by Cundall and Lemos (1990). Some of the shortcomings of this model include the an angular block in UDEC cannot break so it is unable to trace the development of micro cracks and extent of damage zones around the sheared fractures versus time as well as the difficulties in modelling the real fractures geometries. Therefore further improvements are required to enable UDEC simulating the rough fractures shear strength effectively.

Particle flow codes (PFC2D and PFC3D) have been widely used in particle mechanics modelling in a discontinuum media in which the Bonded Particle Model (BPM) is implemented. PFC is a Distinct Element Method (DEM) numerical simulator developed by Cundall and Strack (1979). It has been applied in solving many different rock mechanics problems such as simulating biaxial testing of a rock specimen in laboratory (Potyondy and Cundall, 2004), failure around a circular opening under bi-axial compression (Fakhimi et al., 2002), and also direct shear test of a rock fracture including the effect of fracture surface morphology (Cundall, 2000).

A PFC2D representation of an intact rock sample is an assembly of circular particles with specified statistical size distributions and bounded with four rigid walls. These particles are generated with an automatic particle generator with their radii being distributed either uniformly or according to a Gaussian distribution. Once the bond is installed into the neighbouring particles, the overall mechanical behaviour of the assembly is dominated by the micro-properties for particles and bond. The standard process of generating a PFC assembly to represent a preliminary test model of a rock sample includes particle generation, packing the particles, isotropic stress initialization, floating particle elimination and bond installation (Wang et al., 2003).

Cundall (2000) for the first time used the bonded particle model in particle flow code, PFC, to simulate direct shear tests of rough rock fractures. He used a synthetic

profile which was produced using a sinusoidal wave function. In this approach, fracture track was identified as unbounded path of particles in which contact bond strength of particles contact is zero. The synthetic fracture geometry used in his work is very rough with a *JRC* value of 18-20 (the *JRC* of fracture profile in PFC2D model was roughly estimated by visual comparison with *JRC* standard profiles given in Appendix 1). His model presented with no physical units, therefore the scale (sample size) effect could not be studied through this model. Figures 2.21.a and 2.21.b show the tensile cracks developed along the fracture profile when it is subjected to two normal stresses. As expected, the developed crack zone expands as normal stress increases.

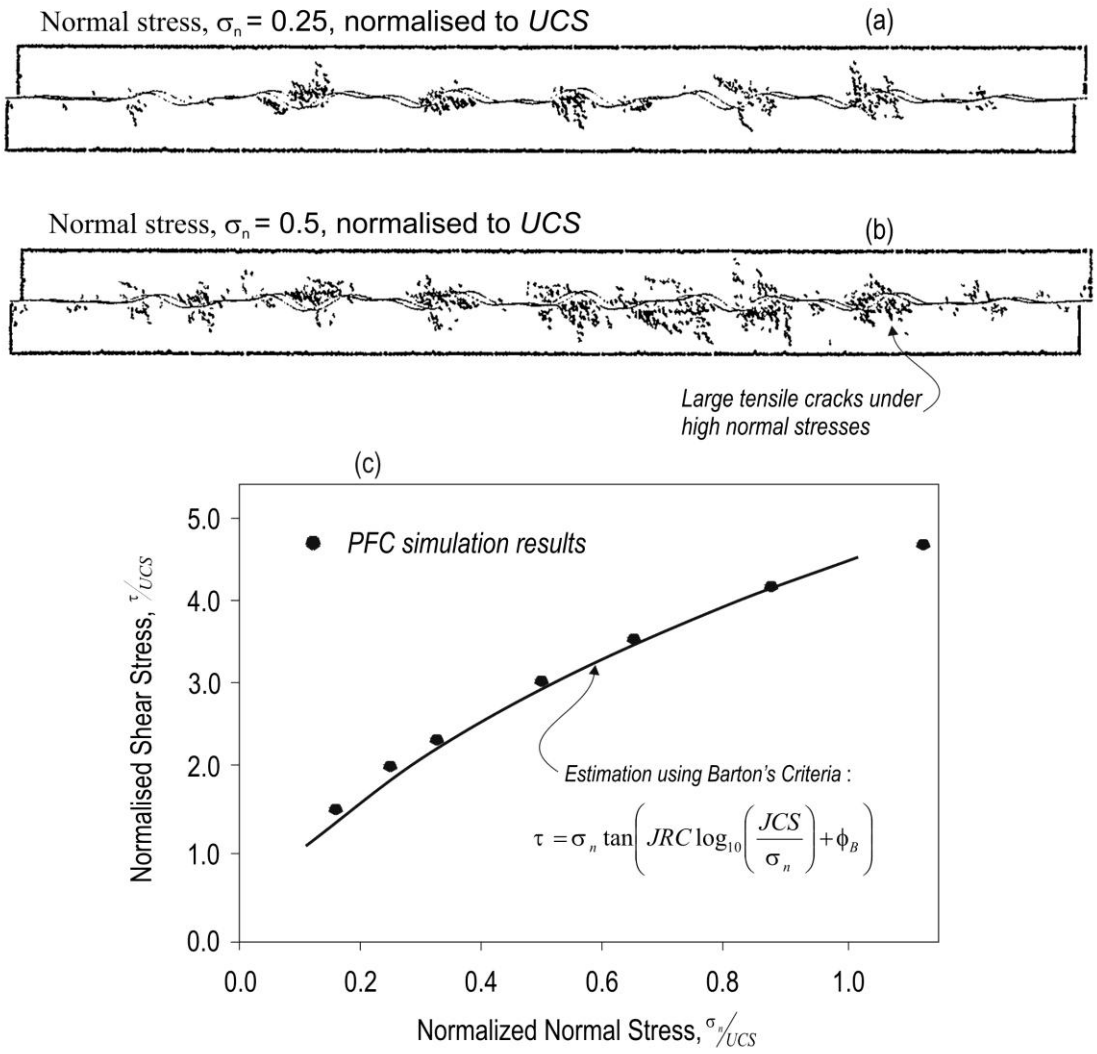


Figure 2.21 A synthetic rough fracture subjected to PFC2D simulation of direct shear test (after Cundall, 2000).

The results of his simulation shown in Figure 2.21.c is comparable with those obtained from Barton shear strength criteria indicating the potential application of PFC2D for fracture shear simulation. It is important to note that the development of tensile cracks can be monitored using such simulations.

Cundall (2000), suggested further investigation on this model in order to study the size effect and the influence of fracture surface roughness on fracture shear behaviour. He also proposed this model to be used for studying the rough faults reactivation mechanism in petroleum field applications. These are some of the motivations of using the PFC2D for the simulation purposes used in current research works.

Similarly, Jing and Stephansson (2007) used PFC2D code to simulate the shear behaviour of rough fractures. They performed primary simulations to show the potential of PFC2D for fracture shear strength estimation. Figure 2.22 shows their PFC2D simulation of direct shear test results for a typical rough rock fracture.

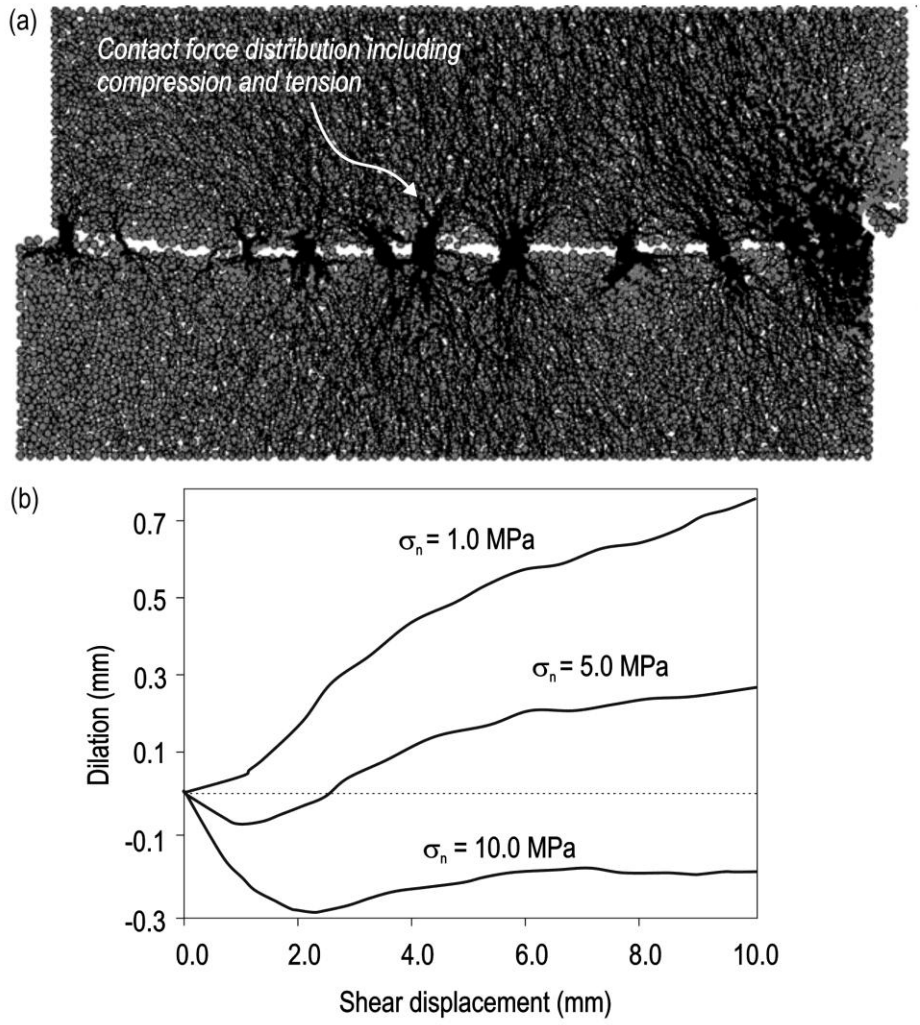


Figure 2.22 PFC2D simulation of direct shear test at different normal stresses for a relatively smooth profile. (a) Distribution of contact forces. (b) Normal dilation versus shear displacement (after Jing and Stephansson, 2007).

Distribution of contact forces through the sheared fracture is shown in Figure 2.22.a. From this figure it is seen that contact forces are developing from the asperity contacts regions, as expected. The plots of normal dilation versus shear displacement curves at different normal stresses shown in Figure 2.22.b indicate larger dilations at

lower normal stresses, which mean lesser effect of roughness at higher normal stress levels. Similar to Cundall (2000), Jing and Stephansson (2007) also recommended further works using PFC2D to better understanding the progressive shearing behaviour of fractures and their contacts degradation.

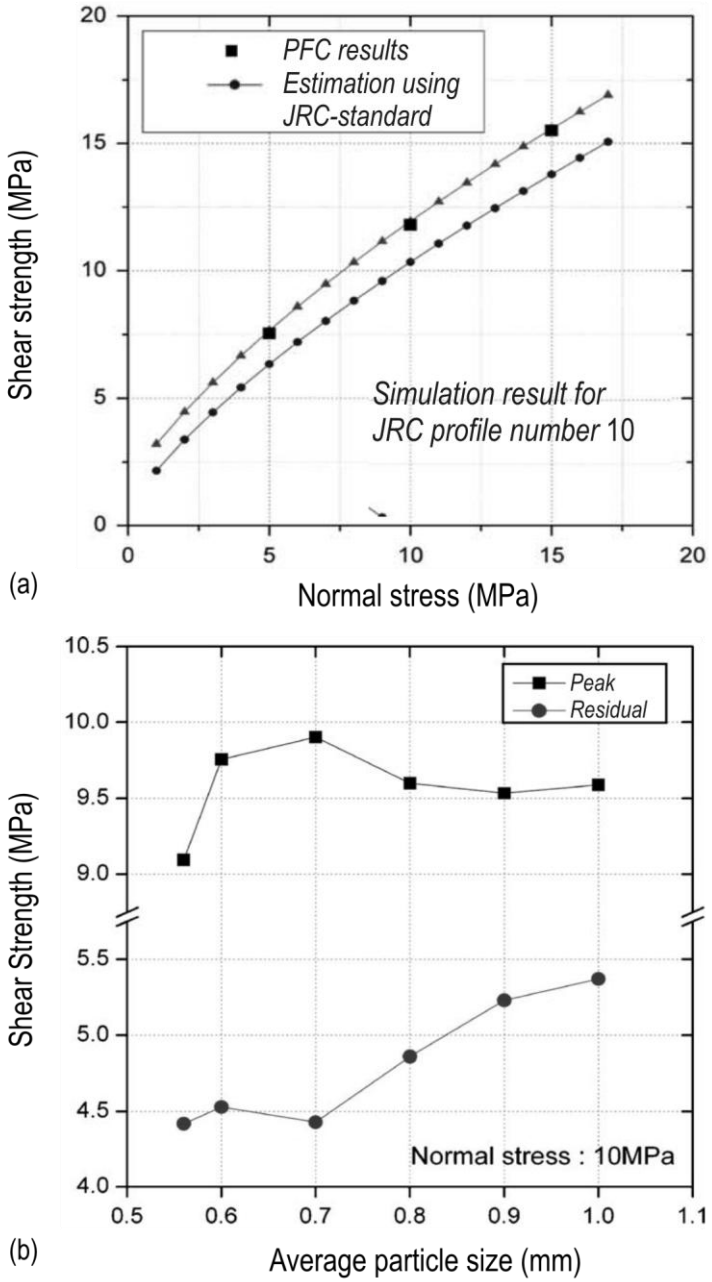


Figure 2.23 (a) Results of direct shear test on JRC profile 18-20, and (b) effects of average particle size on shear behaviour based on PFC3D simulations (Park and Song, 2009).

In a most recent 3D work by Park and Song (2009), PFC3D was used to simulate direct shear tests of rough fractures. They performed number of sensitivity analyses on micro-properties of the model such as particle size, contact bond strength, and friction coefficient. Moreover, they compared their simulation results with Barton's empirical shear strength model by performing simulating shear behaviour of five of JRC profiles.

The results of their work shown in Figure 2.23.a, as an example for profile JRC=18-20 is in close agreement with those obtained from Barton model but the PFC results are more conservative. This is thought to be due to the fact that in PFC simulations, variations of particle size near the asperity contacts, creates a micro roughness (small bumpiness) along the fracture track which may cause an increase in fracture shear strength. This will be discussed in further detail in the next Chapter. Figure 2.23.b shows how the peak and residual shear strength of the fracture changes as the average particle size increases. This is in fact the advantages of using bonded particle model with granular material representing the rock material for fractured rock mass modelling comparing to conventional DEM based simulators with angular contacts such as UDEC. In this research work PFC2D will be used for simulation of fracture shear strength.

## 2.4 Experimental approaches

The shear behaviour of rock joints, which is commonly simulated using numerical methods (e.g. distinct element method), can be experimented in the laboratory using a direct shear apparatus. Different direct shear test equipments have been developed to study the effects of surface roughness on shear strength. These equipments are mainly different in terms of their loading capacity and loading condition, i.e. under constant normal load (CNL) or constant normal stiffness (CNS). In CNL the normal load is maintained constant during the shear process (Barla et al., 2009; Hans and Boulon, 2003; Huang et al., 2002; Indraratna and Haque, 2000; Jafari et al., 2003; Jiang et al., 2004; Yang and Chiang, 2000). Shear testing under CNL boundary condition is beneficial for cases such as non-reinforced rock slopes. In deep formations where the normal stress is extremely high, the shear behaviour of rock fracture is controlled by stiffness (shear and normal). In recent years, direct shear tests under CNS condition has been shown to be more accurate for such cases.

Many researchers have attempted to examine the shear behaviour of rough fractures experimentally (Barla et al., 2009; Barton and Choubey, 1977; Grasselli et al., 2002; Hans and Boulon, 2003; Huang et al., 2002; Indraratna and Haque, 2000; Jafari et al., 2003; Jiang et al., 2004; Yang and Chiang, 2000). These are the recent attempts which have been done to develop direct shear test devices which are aimed at studying the effects of surface roughness and asperity degradation on shear strength of fractures.

Yang and Chiang (2000) studied progressive shear behaviour of composite rock fractures with two different triangle-shaped asperities (15 and 30 degrees) by conducting direct shear tests under CNL condition. They studied the effects of asperity angle and base-length on ultimate behaviour of fracture and stated that the larger the asperity angle and base length, the larger the fracture shear strength. Figure 2.24 shows symmetric triangular fractures with single asperity of 30 degrees after shear tests at two different normal stresses. It is seen that surface degradations increase by increasing the normal stress. They also investigated the effects of asperity angle on shear behaviour of rock fractures. Superimposing the basic shear curves for composite fractures was also carried out in their studies by repeating the tests for artificial composite fractures with two asperities of 15 and 30 degrees asperity angle. Directionality of shear strength was also preliminarily studied in their work by performing two shear tests on fractures having two asperities of 15 and 30 degrees. This was done in their work first by shearing towards smaller asperity and next towards the larger asperity.

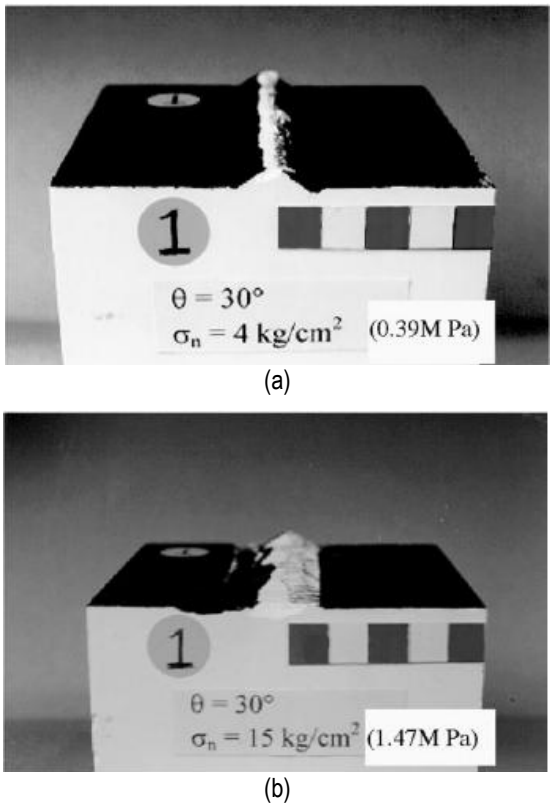


Figure 2.24 Appearance of specimens after shearing at 0.39 and 1.47 MPa normal stresses (Yang and Chiang, 2000).

Similarly, Huang et al. (2002) performed experiments on artificial fractures with regular triangle-shaped asperities with different angles at different normal stresses. They observed asperity sliding and cut-off behaviour in their tests, as discussed in Section 2.2.7. They conducted variety of shear experiments under CNL condition to validate

their theoretical findings in terms of asperity cut-off behaviour at high normal stresses. Asperity cut-off behaviour will be investigated through numerical and experimental analysis in Chapters 3 and 4 of current thesis.

Grasselli (2002) developed expressions for rough fractures shear strength based on experimental results performed at CNL condition. They analysed several rock fracture surfaces based on quantified 3D roughness parameter and investigated the damage and sliding of fracture contact asperities during shearing. They stated that "no damage appears prior to peak stress; damage occurs principally during the softening and residual phases of shearing". In addition, they concluded that it is the asperity degradation at peak-shear stress that initiates sliding.

Jafari et al. (2003) simulated the effects of weak and strong earthquakes (active faults stimulators) and developed mathematical models for evaluating the shear strength of rock joints. They also performed lab shear tests to study asperity degradation under low, intermediate, and high normal stresses. As a result of this work the number of loading cycles, stress amplitude, dilation angle, degradation of asperities and wearing were reported to be the main parameters controlling the shear behaviour of rock joints.

In Chapter 4 of this thesis, modifications will be applied to a true triaxial stress cell (TTSC) in order to perform direct shear tests on fracture planes under CNL. This device was designed in 2009 to simulate the insitu stresses in Geomechanics applications such as hydraulic fracturing and sand production. The TTSC allows vertical and two independent horizontal loads to be applied up to 315 KN in each direction on a 30 cm cube of rock and, at the same time, allows pore pressure to be applied up to 21 MPa (Rasouli and Evans, 2010).

## 2.5 Summary

The main aim of this Chapter was to bring together and review the customary models of surface roughness and fracture shear strength. Fracture shear strength models are categorized as analytical (and empirical) models, numerical simulations, and experimental approaches.

The first part of this Chapter, discussed the importance of surface roughness on mechanical behavior of fractures as well as how complicated is the evolution of surface roughness within fracture shear due to different failure modes, e.g. contact sliding, cut-off, wear, and degradation.

It was highlighted that the idealized models, which ignore the complexity of profile geometry, are not appropriate for roughness determination. Also, as mentioned before, the qualitative parameters and those parameters that are based on visual judgment (for example, JRC as the most commonly used parameter) are not appropriate, as one profile can be interpreted differently by different people.

It was discussed that the $D_{R1}$ is an objective method for roughness characterization. $D_{R1}$ formulas were presented for symmetric and asymmetric triangular asperity and sinusoidal geometries.

The analytical fracture models were presented and it was discussed that the general behaviour of the majority of models are dependent on surface roughness and its degradation as displacements accumulate within the asperity contacts. It was discussed that few of the developed models consider asperity degradation and micro cracking within fractures shearing. This concept will be studied in our numerical simulations.

Number of numerical studies was presented through which FEM and DEM based models were compared. FEM based methods were argued to be used in fracture modeling as they are appropriate for continuum medium and also due to their limitations in simulation of complicated fractures geometries. DEM based models have been thought be useful for fractured rock mass modeling. BPM which is a DEM based model and implemented in PFC, was considered for current numerical simulations as it is capable of modeling different failure modes during fracture shearing including asperity sliding and degradation.

In the last part of this Chapter, a general view of experimental works was presented and fundamental objectives of each method were briefly explained.

In the next Chapter, numerical simulations will be performed on the synthetic profiles shown in Section 2.1.3 to estimate shear behaviour of rough fractures.

# 3 2D Numerical simulations of fracture shear test

The review of literature presented in the previous Chapter indicated that majority of numerical studies to investigate the fracture shear behaviour, are mostly developed based on continuum medium which predict the onset of failure. However, discrete element method (DEM) enables us to investigate the failure progression of a fracture surface during shearing by tracking the extent of the damage zone boundary.

In this Chapter, the mechanical shear behaviour of fractures will be simulated in 2D using particle flow code (PFC2D). Firstly, a brief review of bonded particle model and the process of simulation in PFC2D are given. Accordingly, it will show that PFC2D is able to estimate macro-properties of an intact rock (including UCS and Young's modulus) from its composition micro-properties. Secondly, to demonstrate some fundamental concepts involved in fracture shearing, several synthetic profiles with different geometries will be modelled to study their pre and post-peak shear behaviours. Also, different failure mechanisms observed depending on the loading conditions and fracture geometry will be explained. The simulation results of number of rock fractures will be presented and interpreted.

Ultimately, an attempt is made to correlate the fracture shear strength with the roughness parameter ($D_{R1}$), introduced in Chapter 2.

## 3.1 Bonded particle model

Potyondy and Cundall (2004) stated that "rock behaves like a cemented granular material of complex-shaped grains in which both the grains and the cement are deformable and may break that a conceptual model can explain all aspects of the mechanical behaviour". Various numerical models have been proposed that mimic such a system. They noted that DEM based model for granular materials, so-called bonded particle model (BPM) for rock, directly models this complicated medium and therefore exhibits the evolving behaviours that match well with those of rocks. The mechanical behaviour of rock masses are governed by the development, extent and interaction of micro cracks which can be progressively modelled using BPM.

PFC (Itasca Consulting Group, 2008) is a commercial code based on DEM in which BPM is implemented, and simulates the rock domain using the interaction between an assembly of spheres (in 3D) or circular discs (in 2D). A PFC2D representation of an intact rock-like sample is an assembly of circular particles with specified statistical size distributions and bounded with four rigid walls. These particles are generated with an automatic particle generator with their radii being distributed either uniformly or according to a Gaussian distribution. Once the bond is installed between the particles the overall mechanical behaviour of the assembly is dominated by the micro-properties for particles and bond. The standard process of generating a PFC2D assembly to represent a preliminary test model of a rock-like sample includes particle generation, packing the particles, isotropic stress initialization, floating particle elimination and bond installation (Itasca, 2008; Wang et al., 2003). It is also possible to create particles of arbitrary shape by attaching several particles together that create a cluster of particles acts as independent object called clump logic (Itasca Consulting Group, 2008). As stated in 2004 by Cundall and Potyondy "PFC2D is able to model a brittle solid, by bonding every particle to its neighbour; the resulting assembly can be regarded as a "solid" that has elastic properties and is capable of "fracturing" when bonds break in a progressive manner". Recently, it has been argued by Cho et al. (2007) that bonded clump model can better represent the stress-strain behaviour of intact rocks in which cluster of PFC2D particles are defined as rock grains.

PFC2D simulates the solids as close-packed assemblies of bonded particles: the solid may be homogeneous, or it may contain number of discrete blocks. This system may also be modelled by the distinct element programs such as Universal Distinct Element Code (UDEC), which deal with angular blocks. However, PFC2D is advantageous due to its following abilities as stated by Jing and Stephansson (2007) and Potyondy and Cundall (2004) as:

- It is potentially more efficient, since detection of contacts between circular objects is much simpler than that of angular objects;
- Unlimited displacements can be modelled;
- Blocks can break (since they are composed of bonded particles), unlike blocks modelled with UDEC or 3DEC which cannot break.

As stated by Ivars et al. (2008), "the shortcoming to model a blocky fractured system with PFC2D is that block boundaries are not planar, and the bumpiness affects the fracture response". This can be fixed by assigning smooth-joint contact model

developed by Ivars et al. (2008) to all contacts between particles that lie upon opposite sides of the fracture which can eliminate the bumpiness effects on unrealistic response of the model.

The ultimate mechanical behaviour of BMP is described by the movement of each particle and the force and moment acting at each contact. The fundamental relation between particle motion and the resultant forces and moments causing that motion is provided by Newton's laws of motion (Itasca, 2008).

By modelling a rock-like sample as a collection of separate particles bonded together at their contact points, the simulated material can develop cracks as bonds between the particles break under the normal and shear loads. Particles are assumed to be rigid in PFC models, but deformability of the assembly is derived from normal and shear bonds. Each bond also has a strength that represents intact bonding (cohesive strength). The bond which is broken carries no tension when either a tensile or shear force limit is reached (Itasca, 2008).

As stated at the beginning of the Chapter, this study aims at simulating the shearing behaviour of a fracture in PFC2D assembly, as an interface between two opposite blocks along which the particles are at initially unbounded contacts, as shown schematically in Figure 3.1. The calculation scheme used in PFC requires only simple laws and a few parameters to govern the interactions at the particle and contact level to represent the behaviour of a material including a fracture. On the other hand, other available tools use some constitutive (stress–strain) relations, which involve many parameters and assumptions. Therefore, the PFC can simulate the effect of the fracture roughness and more specifically the asperity degradation in a direct and realistic manner. Moreover, an explicit method allows observations of the loads exerted at the contacts which enable tracking the propagation of bond breakage events at each timestep.

However, the total number of particles required to represent a real situation is limited because of the limited computing capacity, and the model micro-properties are usually not known. These unknown properties require careful calibration process of micro-parameters until the results of laboratory tests verify the macro-scale response of a PFC model (Cundall, 2000; Park and Song, 2009).

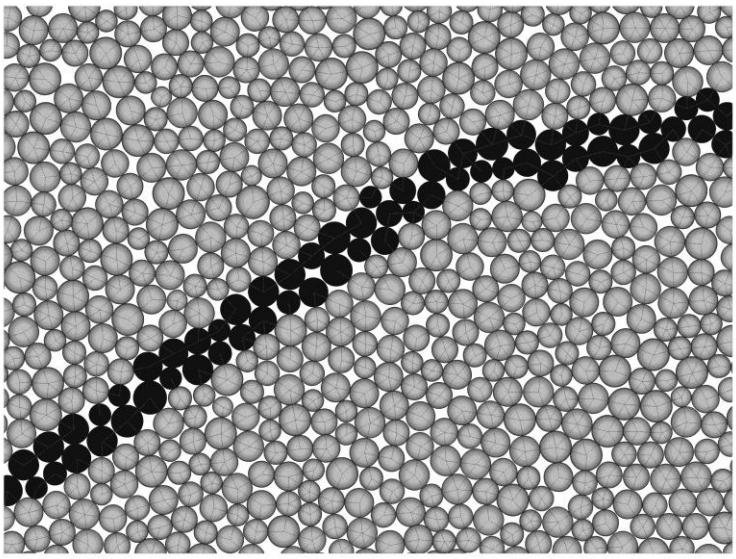

Figure 3.1 PFC2D example model of a rough fracture track (unbonded black balls), bonded particles (gray balls), and contact bonds (dark gray lines) shown in the model.

Many studies have examined the effects of micro-parameters on the macro-scale response for an intact rock and suggested a variety of techniques for reproducing the brittle behaviours of rock-like samples by performing Triaxial and Brazilian tests (Koyama and Jing, 2007; Potyondy and Cundall, 2004).

Mechanical formulations of BPM are available in PFC2D user manual (Itasca Consulting Group, 2008) and can be found in the article presenting the bonded particle model (Potyondy and Cundall, 2004).

### 3.1.1 PFC two dimensional modelling: specifications and limitations

The DEM based numerical simulators, such as the PFC, calculate the basic physical equations of the grain-grain interaction and therefore are more advantageous than commonly used numerical codes. The main advantage PFC is that the rock is modelled in micro scale. As a result of this, investigation of micro fracturing and micro damage of the rock becomes possible. However, similar to other numerical approaches there are some difficulties associated with discrete element modelling. For example, in these models, the rock cement is not appearing physically in the model and its properties are just contributing in solving the force-displacement equations. On the other hand, all the particles are discs with rounded shape whereas in reality rock grains may have any angular shapes which, in turn could cause changes in rock mechanical behaviour of rock mass. Furthermore, particles used in a DEM code are rigid bodies which never fail mechanically during simulations: rock grains however have limited strength and might fail in real life.

DEM based method was chosen for this study since in this method material is modelled in micro scale, so fracturing and failure of the granular material such as rock can be studied in detail. On the other hand, commonly used finite element method (FEM) based software implement failure criteria in order to predict the type and extent of the failure. Well known failure criteria (e.g. Mohr-Coulomb) may not be appropriate for modelling the peak and/or post peak deformation behaviour of some fractured rock structures. In DEM, the rock is modelled using a large number of bonded particles therefore induced micro fractures and the resulting damage can be studied at the micro scale and then explained for upscaling to macro scale. DEM is indeed efficient in modelling granular rock type material.

It is necessary to note that current DEM model is essentially two dimensional and is unable to realistically model the 3D nature of rock behaviour. In FEM modelling there are assumptions based on which 2D models can be used for simulating 3D structures. For instance, plane strain assumption is used when one dimension of the model is much longer than the others. In the DEM code however; the basic difference between the 2D and 3D model is that the round particles in 2D model are disks with unit thickness while in the 3D model particles are perfect spheres. While 3D simulation was a choice, since generating a 3D rock sample with an average particle size of 1.33mm requires a huge computational effort and is a time consuming process, the 2D model was employed for simulation purposes.

Due to the intrinsic nature of 2D particles, the porosity of a 2D model has less flexibility than that of 3D and particles may overlap due to the concept of "soft contacts". In addition, the concept of porosity in 2D and 3D is completely different. The maximum porosity which can be obtained by a sorted 2D model is 21.5% whereas it is 47.64% in 3D. When the particle radii are different, porosity calculation becomes more complicated. It was understood that the range of achievable porosities in a 2D model is between 12% and 18%. In fact it is really difficult to obtain porosities less than 10% in a 2D model. In order to obtain more realistic porosities from such a model, the obtained porosities need to be correlated with the equivalent 3D values. Although a clear relation between 2D and 3D porosity for randomly generated samples does not exist, following general rules should be considered during sample generation procedure (Itasca, 2008).

- There is more void space remaining in a 3D assembly than in a 2D assembly
- In real rocks, the porosities will be higher, because the particles will have "locked-up" before reaching the optimal packing.

- Small particles can easily percolate through a 3D assembly comprised of larger particles, but they can never percolate through a packed model, regardless of relative particle sizes.

For situations in which particle packing has a significant influence upon behaviour, it may be necessary to perform a few simulations using the 3D version of code in order to establish the relevant parameters needed to obtain measured physical responses, and then use these parameters while performing a larger number of parameter studies (Itasca Consulting Group, 1998).

In the following Section, sensitivity analyses of model micro-properties will be presented by performing number of biaxial tests and then a set of calibrated micro-properties are presented which is used for estimation of the intact rock failure envelope and to be used for simulation of fracture shear tests.

## 3.2 Estimation of material properties from BPM

A good knowledge about the mechanical properties of the intact rock is required before simulating a fracture shear test in PFC2D. The macro-properties of the sample are unknown at the beginning of simulation and there is no explicit method to estimate them. However, Yoon (2007) has introduced an analytical-statistical method to define model micro properties which also need to be calibrated with lab experiments. A good approach could be to simulate Biaxial and Brazilian tests in PFC to estimate the sample macro-properties including Elastic modulus, Poisson's ratio, uniaxial compressive strength (UCS), tensile strength, cohesion strength, and internal friction angle (Jing and Stephansson, 2007; Koyama and Jing, 2007; Potyondy and Cundall, 2004). Although very hard, but it is significantly fruitful to correlate the simulation results with laboratorial experiments whether quantitatively or qualitatively.

It is clear that in PFC modelling particle size and distribution differ from one model to another (the process used in this study to choose and calibrate the model micro properties was trial and error). In addition, it is cumbersome to make different models with same macro responses because the computation scheme in PFC is based on time-stepping algorithm and depending on the specifications of the computing tool, the results might be different. However, there are alternatives such as using similar processors and fixing the initial random generator number (for particle assembly initiation) which may assist the users to run the models in the same conditions as another.

In this Section, first, the set up of a biaxial test in the PFC2D is briefly described and the method of determining the macro-properties from the simulations is explained. Then several biaxial tests are carried out by setting certain micro-parameters and analysing the influence of micro-parameter changes on macro-parameters. Linear correlations will be developed between macro and micro-properties which will be used later for generating samples with given properties. Table 3.1 gives four data sets of micro-properties used in the simulations (A, B, C, and D).

The procedure for sample generation and isotropic stress initialisation are similar to that of explained for direct shear test simulation in the preceding Section. Biaxial tests are performed in a 2D box with 5 cm width and 10 cm height in which the upper and lower walls of the sample are given a prescribed constant velocity in vertical direction (here 0.1 m/s) to achieve compression of the sample while the stress on the left and right walls is kept constant at the initial stress value. Figure 3.2 shows the model geometry and boundary conditions. The biaxial test simulations were performed under unconfined ($\sigma_c = 0$) and three different confining stresses ($\sigma_c = 10$, 20, and 30 MPa), and intact rock failure envelope was obtained from corresponding Mohr-Coulomb circles. Estimation of intact rock failure envelope is essentially required to characterise fractured rock mass and determine the type of shearing mechanisms, i.e. sliding, cut-off and asperity degradation.

Table 3.1 shows the range of different micro-properties used for the biaxial test simulations. In each case one property is changed while others are kept constant in order to obtain the macro-property listed in the last column of Table 3.1. In the following subsections the process of estimation of each macro-property from biaxial simulations are explained. Sensitivity analysis of micro-properties in PFC2D biaxial test simulation: the range of values used for each property is marked in bold.

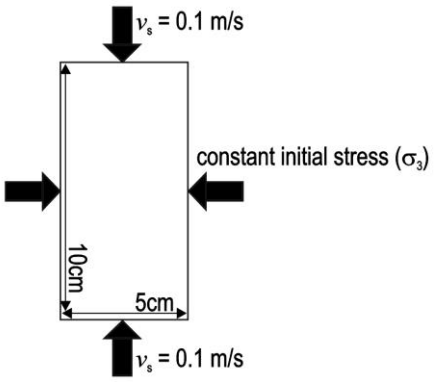


Figure 3.2 Geometry and boundary conditions of Biaxial test simulation in PFC2D.

Table 3.1 Sensitivity analysis of micro-properties in PFC2D biaxial test simulation: the range of values used for each property is marked in bold.

| Data set | Micro-property | Particle average radius (mm) | Number of particles | Contact bond strength (MPa) | Contact elastic modulus (GPa) | Ratio of normal to shear stiffness | Altered macro-parameter |
|---|---|---|---|---|---|---|---|
| A-1 | Particle average radius | **0.993** | **1400** | | 1.25 | 2.5 | |
| A-2 | | **0.745** | **2489** | | | | |
| A-3 | | **0.496** | **5602** | | | | |
| A-4 | | **0.372** | **9959** | | | | |
| A-5 | | **0.257** | **20000** | 60 | 1.25 | 2.5 | UCS = 41.26 |
| B-1 | Contact bond strength | 0.993 | 1400 | **10** | 1.25 | 2.5 | UCS |
| B-2 | | | | **20** | | | |
| B-3 | | | | **30** | | | |
| B-4 | | | | **40** | | | |
| B-5 | | | | **50** | | | |
| C-1 | Contact elastic modulus | 0.993 | 1400 | | **1.25** | 2.5 | Elastic modulus |
| C-2 | | | | | **5** | | |
| C-3 | | | | | **10** | | |
| C-4 | | | | | **15** | | |
| C-5 | | | | | **20** | | |
| D-1 | Ratio of normal to shear stiffness | 0.993 | 1400 | | 1.25 | **0.1** | Poisson's ratio |
| D-2 | | | | | | **1.0** | |
| D-3 | | | | | | **2.0** | |
| D-4 | | | | | | **3.0** | |
| D-5 | | | | | | **4.0** | |

### 3.2.1 Uniaxial Compressive Strength (UCS)

Contact bond strength (CBS) acts as the cement between particles. The contact bond will fail in tensile and/or shear if the applied forces exceed the defined normal and/or shear bond strengths between particles' contacts, respectively. The overall UCS of assembly is sensitive to CBS and this has been studied by few researchers (Potyondy and Cundall, 2004; Yoon, 2007). Since UCS is affected by particles' size and their distribution, defining a unique and applicable correlation between UCS and CBS appears to be cumbersome.

Based on the behaviour of PFC system, one could recognize that UCS is highly dependent on the strength that a bond can endure either in normal and/or shear. The linear regression fit is obtained through a series of biaxial compression simulation by varying the CBS from 10MPa up to about 60MPa. It is assumed that typical laboratory test results of UCS for soft rocks fall within a range between 20 and 80 MPa. Yoon (2007) obtained a linear fit for the hard rocks, which their UCS varies from 70 to 250 MPa. In this study, the obtained regression fit considers the moderate rocks.

Biaxial test simulations are performed to investigate this effect. As shown in Table 3.1, for Set B the CBS is increased from 10 MPa to 50 MPa (that normal and shear bond strengths for this case have similar values and called CBS). Since the bonds in the DEM simulations act as cement between the rock grains, the larger UCS values are expected as the CBS increases. At this stage of simulations, micro-elastic properties of the particles (i.e. contact elastic modulus and particle stiffness) remain constant. Correspondingly, the macro-elastic properties including Elastic modulus and Poisson's ratio are expected to remain constant as the CBS changes. From the stress-strain curves, the UCS corresponding to samples with CBS varying from 10 to 60 MPa are plotted in Figure 3.3. It is seen that a perfect linear trend exists between UCS and CBS. The results show that the larger the CBS, the greater the UCS. This indicates that changing the CBS results in different compression strengths. The CBS is defined with two different values: shear and normal bond strengths (given in Table 3.1).

The particle size can also affect the UCS values, as different particle sizes result indifferent porosity and packing density of the model. To assess this effect, a number of biaxial tests were performed with different particle sizes (corresponding to different total particle numbers in the model) with other parameters being kept unchanged. Data set A in Table 3.2 shows the input values corresponding to this model in which average

particle radius varies from 0.4 to 1.2 mm. Figure 3.4 shows the results of the simulations where a linear correlation with a negative slope fits the data best.

A linear correlation obtained between UCS and CBS as

$$\mathrm{UCS} = 1.3269\mathrm{CBS} + 0.747 . \tag{3.1}$$

which can be used to estimate the assemblies UCS as the variation of CBS.

Figure 3.4 shows how an increase in average particle size results in a small UCS value which is likely to be due to the increase in ultimate porosity and a less denser pack. A linear correlation was obtained between UCS and average particle size, $R_{\mathrm{ave}}$ as

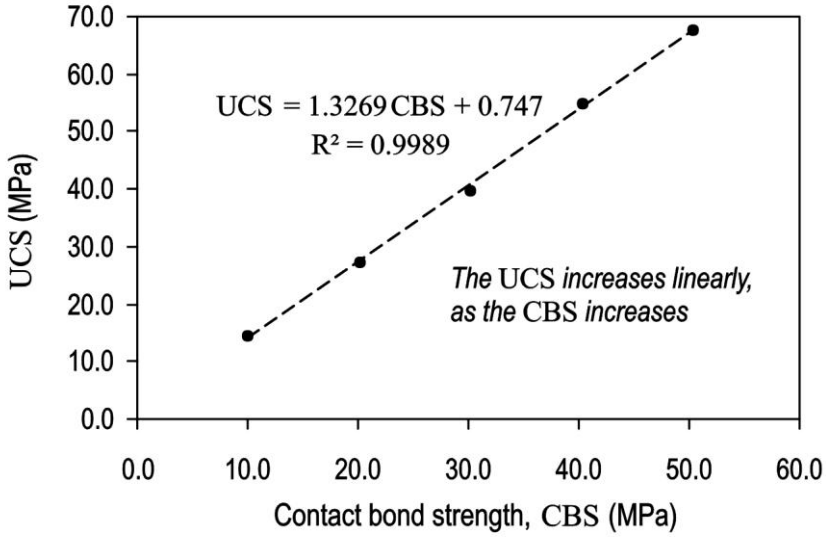


Figure 3.3 Correlation of model CBS and assembly's UCS.

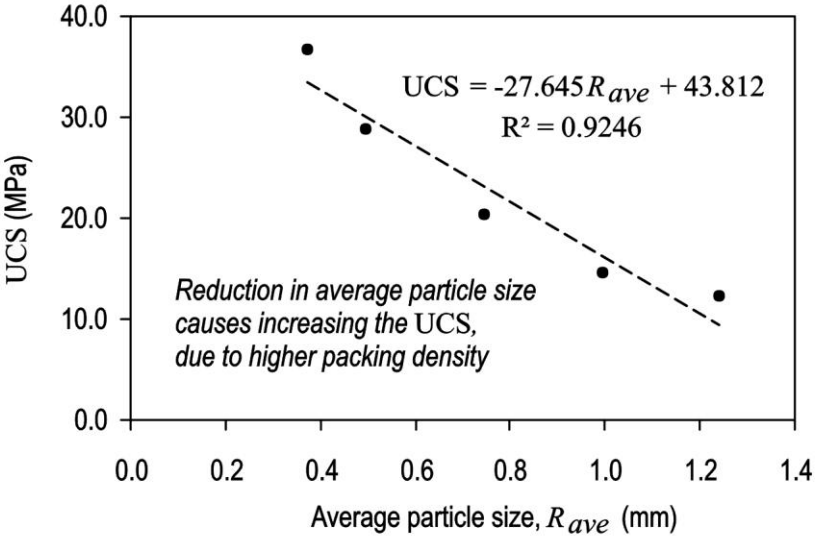


Figure 3.4 Effects of average particle size in assembly's UCS.

$$\mathrm{UCS} = -27.645R_{ave} + 43.812 . \tag{3.2}$$

which can be used to estimate the assemblies UCS as the variation of $R_{\mathrm{ave}}$.

This concludes that for assemblies which use contact bonding, the overall strength of the bonding is inversely proportional to the average particle radius. Thus, to obtain constant sample strength, bond strength must be scaled with the particle radii.

One thing that should be noted here is the ratio of compressive to tensile strength. Generally the tensile strength of the modelled samples is obtained form Brazilian test simulation in PFC. Yoon (2007) obtained the ratios are in between 2.4 and 5.2, which are much smaller than those commonly observed in typical crystalline and sedimentary rocks (5–10 or 20). Bruno and Nelson (1991) stated that modelling grains with simple circular cross sections produces an assembly that distributes compressive loads differently than an assembly composed of more angular grains. The circular grains are more efficient wedges, and the use of exclusively circular sections will therefore tend to underestimate the ratio of the load required to produce compressive failure compared to the load required for tensile failure. He stated that in order to reproduce realistic ratio of compressive to tensile strength, one possible approach might be the use of bonded clump model in which several particles are bound together with specified bond strength to represent angular or blocky grains (Cho et al., 2007). On the other hand, using bonded clump model to simulate fracture shear strength is not straightforward. Potyondy and Cundall (2004) and Yoon (2007) stated that the ratio of UCS to Brazilian tensile strength of bonded particle model should be in the range between 3 and 10. To obtain the reasonable values in the above range, the ratio of shear bond strength to normal bond strength should lie in the range between 1 and 3 which is considered in current study (see Table 3.2).

### 3.2.2 Elastic modulus ($E$) and Poisson's ratio ($\nu$)

Development of DEM mathematic assumes that the contact elastic modulus ($E_c$) is a function of material Elastic (Itasca Consulting Group, 2008). To investigate this, biaxial tests were performed at five different Elastic moduli corresponding to sample Set C in Table 3.1. The Young's modulus is obtained by estimating the slope of the linear portion of stress-strain curve. The results plotted versus corresponding $E_c$ for each sample are shown in Figure 3.5. It is observed that the overall modulus of a two-dimensional assembly is directly proportional to contact stiffness, but is independent of particle radius. A linear correlation was obtained between Young's modulus and contact elastic modulus as

$$E = 0.5564E_c + 0.0742 . \tag{3.3}$$

which can be used to estimate the assemblies $E$ as the variation of $E_c$.

From correlation given in Figure 3.5 it is possible to obtain a good estimate of the sample Young's modulus, however, care must be taken since the micro-parameters used in PFC2D are dependent to each other, and therefore changing one parameter may influence the overall macro-response of the model.

In two dimensional contact models, the relationship between contact elastic modulus ($E_c$) and ball normal stiffness ($k_n$) is defined as:

$$k_n = 2E_c(t). \tag{3.4}$$

$k_n$ is a secant stiffness as it relates the total normal force ($F_i^n$) to the total normal displacement ($U_n$), whereas the shear stiffness ($k_s$) is a tangent stiffness as it relates the increment of shear force ($\Delta F_i^s$) to the increment of shear displacement ($\Delta U_i^s$). These linear relationships can be expressed as:

$$F_i^n = k_n U_n n_i. \tag{3.5}$$

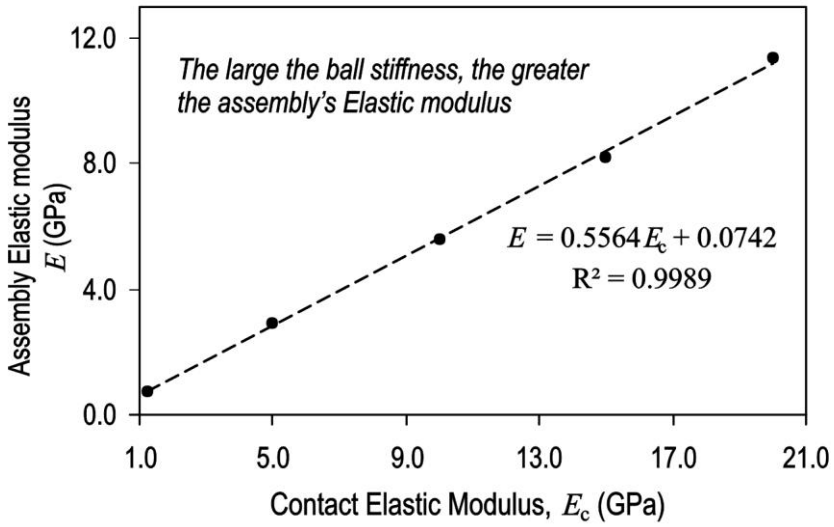


Figure 3.5 Correlation between contact elastic modulus and 2D assembly's elastic modulus.

$$\Delta F_i^s = k_s \Delta U_i^s. \tag{3.6}$$

where $n_i$ is the unit normal vector to the contact plane.

Considering Equations 3.5 and 3.6, the ratio of normal to shear stiffness is expressed as:

$$k_n / k_s = \frac{F_i^n \Delta U_i^s}{\Delta F_i^s U_n n_i}. \tag{3.7}$$

The increment of shear displacement over total normal displacement in micro-scale can significantly change the ratio of radial to axial strain in macro-scale which is the 2D assembly's Poisson's ratio. Therefore, the ratio of particle normal to shear stiffness ($k_n/k_s$) causes significant changes in values of Poisson's ratio which is defined as the ratio of radial strain to axial strain. This is analysed using sensitivity analysis of the given ratio in Equation 3.7. Plot of contact normal to shear stiffness ratio ($k_n/k_s$) versus the overall Poisson's ratio of the assembly is given in Figure 3.6, from which it is seen that the larger the ratio of normal to shear stiffness, the greater the 2D assembly's Poisson's ratio.

The stress conditions in a two dimensional PFC2D test are neither plane strain nor plane stress since there is no "out of plane stress" or "out of plane deformation" (Itasca, 2008). The Poisson's ratio calculated from a biaxial test on a PFC2D material represents the special case of plane stress (with $\sigma_z = 0$) and constant lateral stress. The value of Poisson's ratio so obtained is not strictly comparable to the Poisson's ratio of a real material obtained from a triaxial test; It is calculated as the negative ratio of lateral strain to axial strain as $v' = -\Delta\varepsilon_x / \Delta\varepsilon_y$ . The Poisson's ratio corresponding to a state of plane strain can then be calculated using the general relationship between plane stress and plane strain as $v = v'/1 + v'$ .

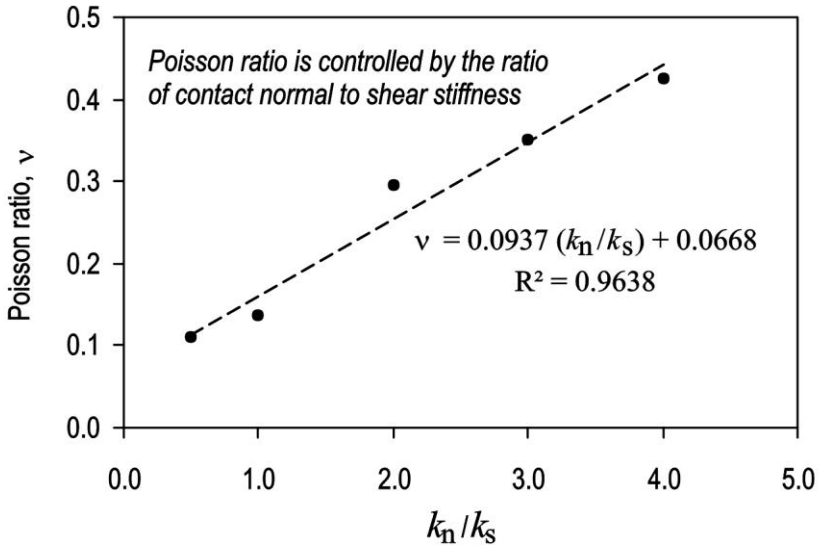


Figure 3.6 Effects of the ratio of contact normal to shear stiffness on 2D assembly's Poisson's ratio.

A linear correlation was obtained between Poisson's ratio and contact normal to shear stiffness ratio as

$$v = 0.0937\left(k_n / k_s\right) + 0.0668 \,. \tag{3.8}$$

which can be used to estimate the assemblies $\nu$ as the variation of $k_n/k_s$.

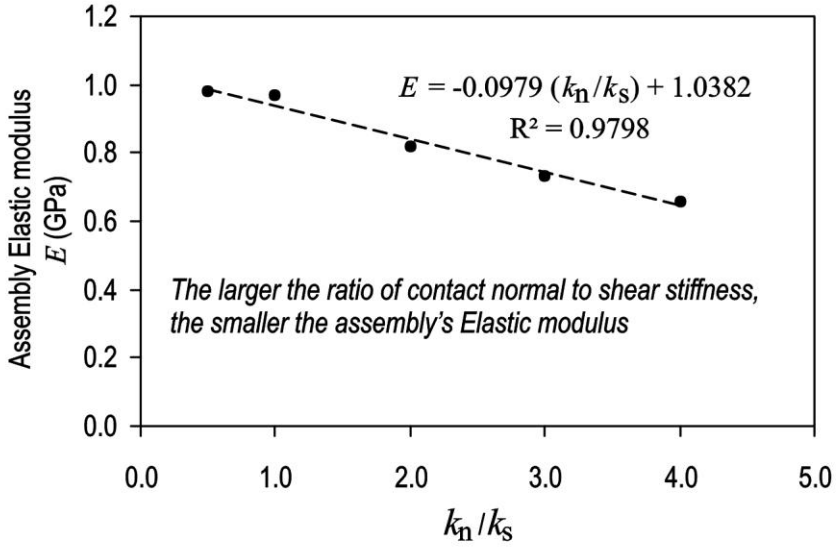


Figure 3.7 Effects of contact normal to shear stiffness on 2D assembly's elastic modulus.

Interestingly, it is observed that as the ratio of normal to shear stiffness increases, the Elastic modulus of assembly decreases (Figure 3.7). This is due to the reduction in shear stiffness as the ratio of $k_n/k_s$ increases.

A linear correlation was obtained between Young's modulus and normal to shear stiffness ratio as

$$E = -0.0979(k_n/k_s) + 1.0382\,. \tag{3.9}$$

which can be used to estimate the assemblies $E$ as the variation of $k_n/k_s$.

It must be stated that the correlations obtained in this Section are case specific which means that they cannot be directly used to determine the macro-properties of any PFC2D model. To repeat these simulations and reach to the same conclusions, the initial condition of the model and composition micro-properties must be same as those used in current models given in Table 3.1. However, the results of this Section can be used as guidance to select a set of micro-properties corresponding to specific type of intact (moderate) rock sample.

## 3.3 Intact rock-like sample failure mechanism

Date set A5 in Table 3.1 represents a fine grain rock-like sample with relatively high compressive strength. The data corresponding to this sample will be used to generate a fracture shear model later in this Chapter.

The Mohr-Coulomb failure criteria is assumed for samples: this is suitable when a contact model is used (Saiang, 2008). Plotting the Mohr circles corresponding to different confining pressures the cohesion strength and internal friction angle of the assembly can be estimated from the intercept and slope of the tangent line to the circles. Here, a number of biaxial tests were simulated under confining stresses of 10, 20 and 30 MPa, respectively.

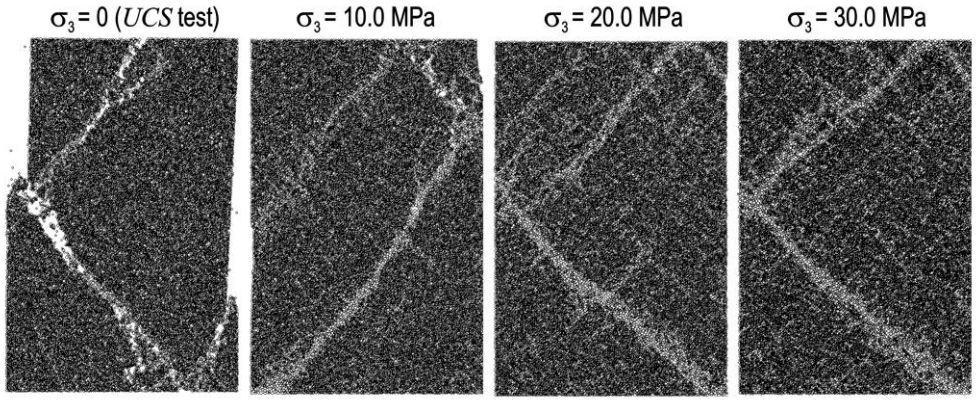


Figure 3.8 Assembly of balls and contact bonds after biaxial tests simulation under unconfined, and confining pressures of 10, 20, and 30 MPa.

Figure 3.8 shows the biaxial samples after the test the lighter gray and white zones show planes of shear failures for each sample. It is seen that the failure pattern is almost similar under different confining pressures. From Figure 3.8 larger lateral displacements are observed for unconfined tests comparing to the cases where confining pressures are applied. As is expected, the number of shear cracks increase as the confining pressure reduces.

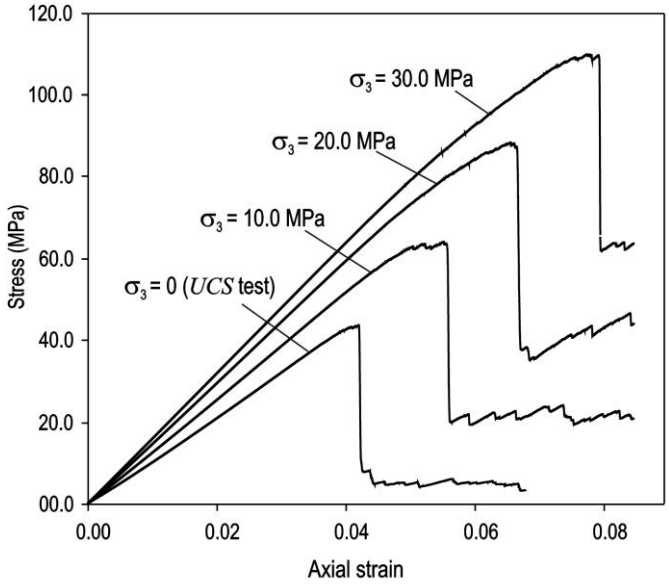


Figure 3.9 Plot of stress versus strain obtained from PFC2D biaxial test simulations at different confining pressures.

Density of the white colours in the samples, which shows the extent of the broken contact bonds, reduces as the confining pressure increases: this corresponds to a more competent behaviour. Figure 3.9 shows the stress-strain curves corresponding to samples shown in Figure 3.8. It is seen that as confining pressure increases, the peak value of compressive strength increases. There is a small difference between $E$ and $\nu$ obtained from these tests which can be due to the large values of confining pressures used in these simulations.

The Mohr circles corresponding to five biaxial tests are plotted in Figure 3.10. The diameter of each circle is equivalent to the difference between the two stress components at the point of failure of samples ($\sigma_1$ and $\sigma_3$). From the tangent line to these circles the friction angle and cohesion of simulated rock-like sample are estimated to be (24±2)° and (14±2) MPa, respectively. Unconfined compressive strength of rock-like sample was obtained from unconfined biaxial simulation to be equal to 41.26 MPa, which represents a relatively strong rock. Equation 3.10 gives a good estimate for compressive strength of rock-like sample based on the Mohr-Coulomb failure criteria:

$$\sigma_{ci} = \frac{2c\cos\phi}{1-\sin\phi}. \tag{3.10}$$

where $\sigma_{ci}$ is the intact rock compressive strength. Using this equation and applying strength parameters ($c$ and $\phi$) obtained from PFC biaxial tests, unconfined compressive strength of the sample material is estimated to be 46.2 MPa which is close enough to the one obtained from UCS test simulation showing the validity of the simulations.

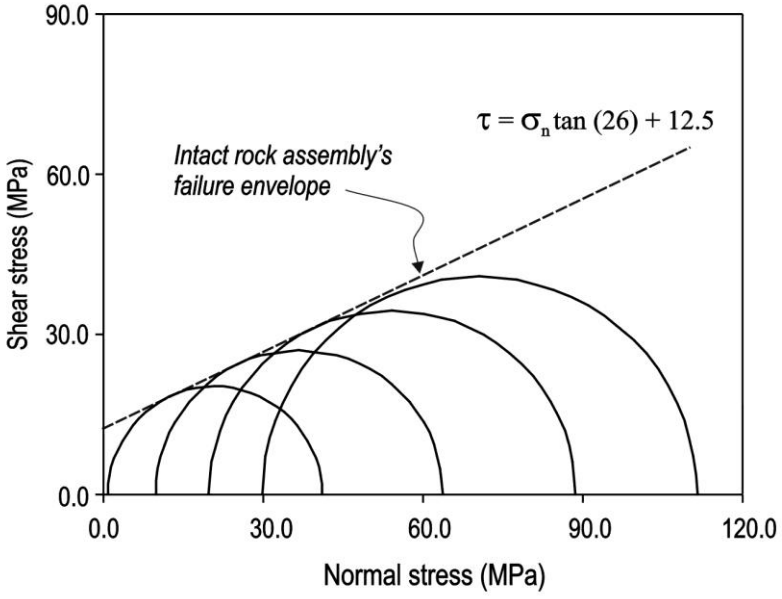


Figure 3.10 Mohr circles corresponding to biaxial test simulations at different confining pressures.

Table 3.2 PFC2D model micro-properties and corresponding macro-parameters used in fracture shear test simulations.

| Property | Value | Assembly's macro-properties |
|---|---|---|
| Sample size, width × height ($cm^2$) | 10×5 | |
| Particle density ($kg/m^3$) | 1000 | $E$ = 1.00 ± 0.25 (GPa) |
| Minimum particle radius, $R_{ave}$ (mm) | 0.257 | $\nu$ = 0.300 ± 0.015 |
| Particle size ratio, $R_{max}/R_{min}$ | 1.5 | |
| Porosity, $n$ | 0.12 | UCS = 40 ± 3 (MPa) |
| Number of particles | 20000 | |
| Contact elastic modulus (GPa) | 1.25 | |
| Contact stiffness ratio, $k_n/k_s$ | 2.5 | $c$ = 14 ± 2 (MPa) |
| Particle friction coefficient, $\mu$ | 0.6 | $\phi$ = 24 ± 2 (º) |
| Normal bonding strength , NBS (MPa) | 60 | |
| Shear bonding strength, SBS (MPa) | 60 | |

Table 3.2 gives the selected micro-properties used in shear test simulations and corresponding macro-properties estimated. This data set was used for modelling mainly because its properties are within the range of relevant models used by other researchers for fracture shearing studies (Asadi and Rasouli, 2010, 2011; Cundall, 2000; Park and Song, 2009; Potyondy and Cundall, 2004; Rasouli and Harrison, 2010). Also, using the available lab facilities it is possible to test samples with these properties in the lab.

The effects of particle friction coefficient will be investigated in Section 3.3.3 when studying the shear behaviour of fractures. This parameter is more pronounced when no contact bond is installed between shearing particles. The particle friction coefficient shown in Table 3.2 corresponds to intact material modelled in PFC2D. However, the value of this parameter must be calibrated to reduce the uncertainty in the results, as those particles lie upon opposite sides of the fracture. The calibration process for this particular parameter is discussed in Section 3.3.3.

The above discussion leads to the conclusion that when studying failure mechanisms of rock fractures using BPM, the four major controlling parameters which significantly change the mechanical behaviours of a sample are grain size, material bond strength, particle friction coefficient and ratio of contact normal to shear stiffness. The general results obtained in this Section will also be employed as guidance in Chapter 4 when modelling a mortar specimen using PFC2D.

Therefore, the micro-properties of the PFC2D assembly should be selected in a way that they represent the macro-properties of the intact rock as closely as possible.

## 3.4 Fracture shearing simulation using PFC2D

The shear behaviour of rock fractures is a function of the effective normal stress acting perpendicular to fracture plane. At low normal stresses, the fracture planes slide along inclined surface with minor damages to the asperity: this corresponds to high values of dilation and friction. At high normal stresses, however, the constraint of normal displacement leads to asperity failures, which corresponds to low friction values. In this study, a number of synthetic and rock fracture profiles will be subjected to shearing simulations in a rock-like sample modelled in PFC2D. The simulations are performed at different normal stress levels to plot the fracture failure envelope. From this plot zones corresponding to different failure mechanisms, including asperity sliding, asperity degradation, and intact rock failure can be distinguished.

A total number of 20000 particles with an average radius of 0.257 mm were generated and packed into a 10×5 $cm^2$ box-shaped region containing 4 walls, as shown in Figure 3.11.a. In order to avoid crystalline packing, particle radii are chosen randomly within a specified size distribution and are uniformly distributed between minimum and maximum particle radius. Once the assembly packing was finished and particle floating eliminated; isotropic stress of 0.1 MPa was applied. Figure 3.11.b shows that the contact normal and shear forces are distributed uniformly in the assembly in an equilibrium state. The contact bond was installed in the sample with uniform distribution and micro-parameters of particles and contacts were adjusted to reproduce a moderately strong intact material (see Table 3.2).

To produce a fracture track in this model, a 2D profile is inserted in the centre of the shear box using a particular function $y = f(x)$ or coordinate points ($x$ and $y$) representing profile geometry. Zero contact bond strength is assigned to all the particles between the upper and lower walls of fracture. A very low particle friction coefficient is assigned to all unbonded particles (known as fracture particles) between fracture walls (see Section 3.3.3). In our model, the friction coefficient shown in the Table 3.2 was assigned to the intact block except those discs located along the fracture particles. Coordinates of desired fracture profile in particular direction must be digitized at sampling intervals smaller than $R_{ave}$ to reproduce a high resolution fracture track in PFC2D model accounting for both roughness and waviness.

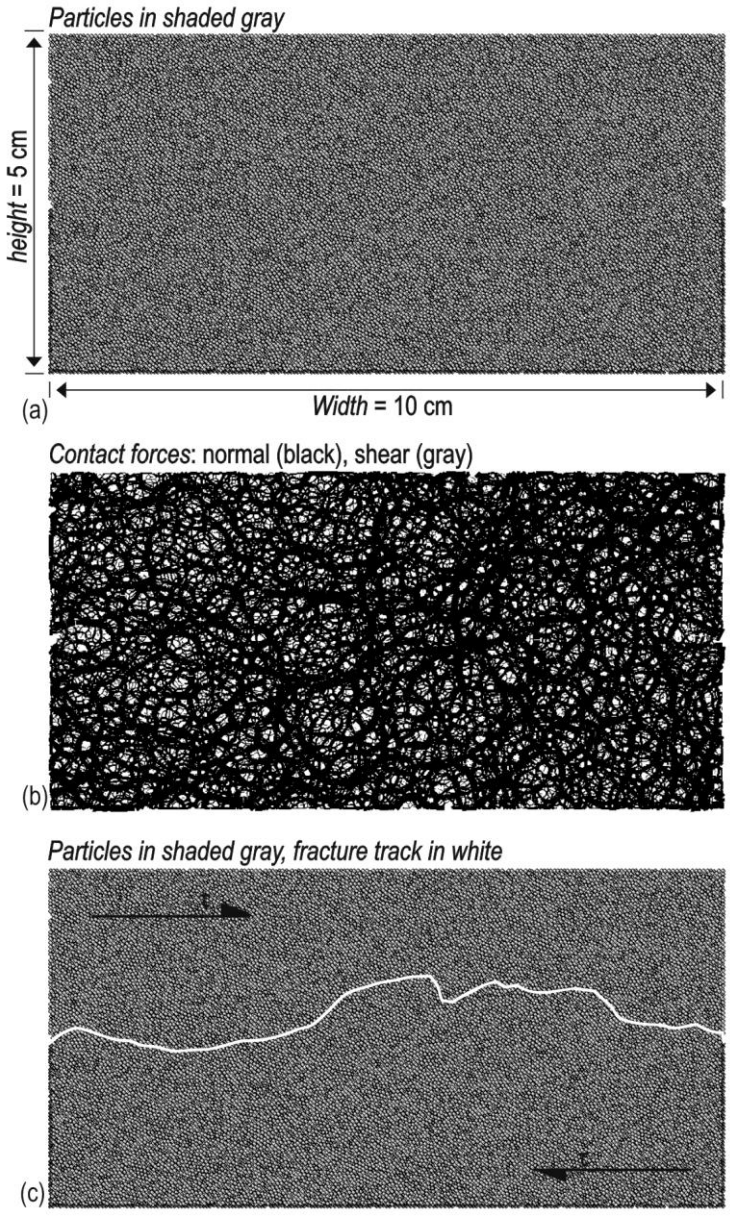


Figure 3.11 (a) PFC2D representation of a rock-like assembly with 20,000 discs of unit thickness, (b) contact force distribution (c) rough fracture profile generated in the centre of the model.

The shear behaviour of fracture is a function of compressive strength of the fracture wall rather than the tensile strength (Barton and Choubey, 1977; Kulatilake et al., 1995; Ladanyi and Archambault, 1970). The tensile strength of the interior of the block can be estimated by performing Brazilian test simulation in PFC2D.

The UCS of this sample was estimated from biaxial test simulation as 41.26 MPa (see Figure 3.10). In Chapter 4, values of UCS and $E$ obtained from corresponding PFC2D biaxial test simulations will be calibrated with corresponding lab results for mortar samples. However, in here, the intact materials are assumed to have macro-mechanical properties of close to moderately strong rocks.

### 3.4.1 Bonding type

As explained earlier, to represent a fracture profile in this study, there is no bond between particles lie upon opposite sides of the fracture. The contact bond was used with minimum effects on the shear strength and asperity degradation of fractures.

As stated by Park and Song (2009), they have studied the effects of bonding type on fracture shear behaviour by performing preliminary shear tests and concluded that there are no major differences between the results obtained from contact and parallel bonded models. As appears from their work, they have calibrated the micro-properties of two models: one with contact bond and the other one with parallel bond to the same UCS and performed direct shear test using these two models. Their observations indicate small differences in the peak shear strength, normal dilation and the shear stiffness obtained from the two models with different bonding types. Moreover, they have mentioned that in the parallel bonded model, more micro cracks develop along the fracture plane and also these models reach their residual state faster than that of contact bonded model.

On the other hand, when studying the asperity degradation during fractures shearing, micro cracks develop through asperity contacts and intact block. This is the situation where the use of parallel bond might be beneficial because contact bonds are unable to avoid the particle rotation which can affect the post-peak behaviour of rock fractures. However, as in current study the failure pattern is taken into around peak shear stress, which is highly influenced by fracture profile roughness, the use of contact bonds found to be sufficiently representative. For these reasons, the contact bonded model which has less micro-parameters was used in this study and applied to all modelling discussed in this Chapter.

For the purpose of this study, normal and shear bond strengths must be distributed uniformly in shear box to ensure consistent response under different loading conditions and fracture geometries. Failure to do so may result in some damage occurring where bond strength is distributed non-uniformly. Also, in order to prevent spurious failure at the boundaries' edges, the strength of those contacts adjacent to the top and bottom edges of the shear box are increased by a factor of ten. Low strength assigned to the contacts at the edge of the box would result in huge amount of shearing energy being dissipated from large tension cracks initiating from doglegs of asperities and propagating to shear box boundaries (i.e. free surfaces), as stated by Cundall (2000).

The effects of contact bond strength on shear behaviour of synthetic fractures are investigated in Section 3.5.1.

Effects of particle size and distribution on shear strength of rough fractures are examined for a shear box composing a single symmetric triangular asperity profile in the following Section.

### 3.4.2 Particle size and distribution

A fracture plane in PFC2D model has an intrinsic roughness even if it is planar. This is because of different size distribution of particles along the fracture plane. The micro-roughness increases along the fracture track with increasing particle size, so by reducing the particle size in the model, this effect becomes less important. However, the fracture compressive strength will decrease with increasing particle size due to the reduction in the number of fracture-contacts bearing the stress, similar to the UCS shown in Figure 3.4. To minimise the effects of intrinsic roughness (or say micro-roughness), as shown in Figure 3.12, a dense pack of particles were used with small size particles' radii ($R_{ave}$ = 0.257 mm). Potyondy and Cundall (2004) stated that "Particle size is not a free parameter that only controls resolution; instead, it affects the fracture toughness and thereby influences damage processes (such as notch formation) in which damage localizes at macro-fracture tips experiencing extensile loading". Koyama and Jing (2007) performed over 200 biaxial simulations to systematically investigate the effects of model scale, particle size, and size distributions of particles on failure process of rocks. Their important findings are summarised as follows:

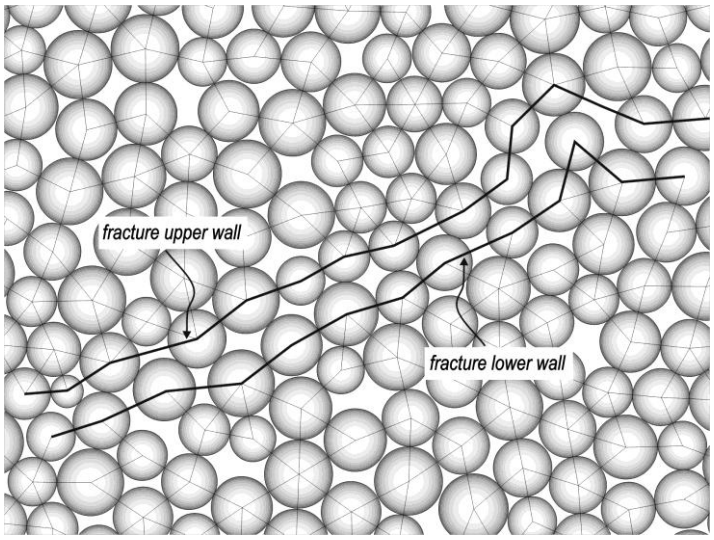


Figure 3.12 Unbounded path of particles represents a rough fracture profile.

- The particle size distribution affects the determination of the representative elementary volume (REV) size. The REV is the sample size above which no significant variation in measured property is expected. The REV size increases as the particle size distribution becomes more heterogeneous.
- The 5 cm minimum diameter of rock specimen for UCS tests of rock as suggested by ISRM is reasonable for rock failure studies in micro-mechanics media.
- For modelling large scale engineering applications using particle mechanics approaches, care should be taken on the effects of model size and particle size distributions on the calibrated BPM model parameters.

Therefore, selection of adequate number of particles is crucial as it affects the behaviour of the entire model. By changing the number of particles in assembly, mean particle radius will change, which in turn affects the ultimate response of the model. Generally, the variation of the results in the models with different mean particle sizes is due to the change in their porosity and therefore the UCS of the pack, as was shown through biaxial test simulations in Section 3.2.1. An increase in particle size results in an increase in the final porosity, which reduces the UCS as stated also by Park and Song (2009) and examined in current study (Figure 3.13).

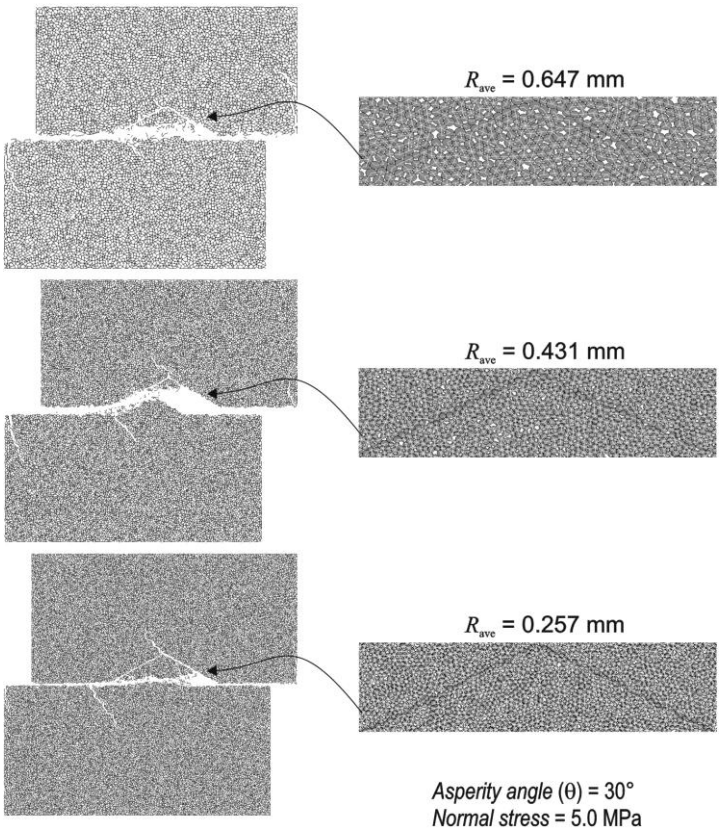


Figure 3.13 Visual demonstration of fracture micro-roughness corresponding to various particle sizes.

To investigate the effects of particle size on rough fracture shear behaviour, five sets of shear test simulations were performed with similar micro-properties for all models summarised in Table 3.2, but each filled with different number of particles resulting different particle radius. The mean particle radius was varied between 0.1 and 1.0 mm which represents the range of small to medium sand grains. Then a symmetric triangular profile (i.e. a crenulated profile) with base angle, θ of 30° was generated in the centre of model to investigate the effects of particle size on shear strength of the profile. Figure 3.13 shows the PFC2D model of the profile being sheared under 5.0 MPa normal stress corresponding to three assemblies with 0.257, 0.431, and 0.647 mm average particle radii, respectively. It is seen, as expected, that by reducing the particle size, since the number of particles increases in the model, a finer failure pattern is observed.

Figure 3.14 shows the peak shear stress versus the mean particle size at normal stress of 5.0 MPa. The peak shear stress reaches a maximum at a mean particle radius of 0.6 mm and then reduces due to a significant reduction in matrix strength. A relatively similar trend was obtained at normal stresses of 1.0 and 10.0 MPa. This variation in shear strength can be due to the superposed effects of the inherent roughness (bumpiness) of fracture surfaces, as discussed. Hence, local particle contact orientations along the fracture surface may cause significant changes in fracture shear strength. It is seen that peak shear stress reduces in fracture models with $R_{ave} \leq 0.4$ mm which is perhaps due to the reduction in strain localisation in particles along the fracture.

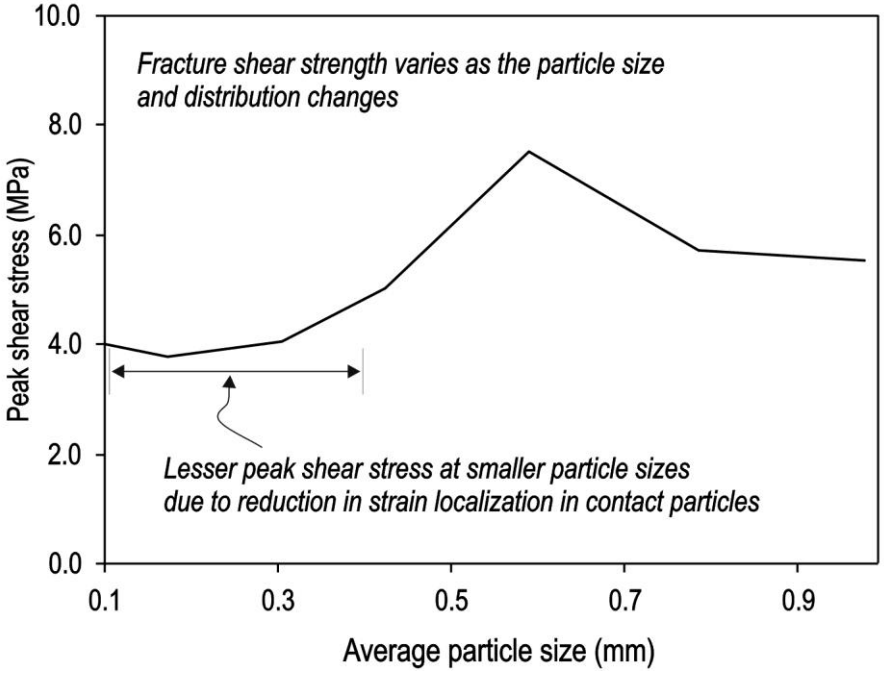


Figure 3.14 Effects of particle size on peak shear stress of a symmetric triangular asperity profile depicted in Figure 3.13.

Therefore, to simulate the shearing of rough fractures, i.e. influence of fracture geometry on shear behaviour which is the purpose of this study; it is advisable to decrease the particle radius to reduce the effects of fracture micro-roughness. In this study, as the major focus is on fracture surface geometry (i.e. both waviness and roughness), the average particle size was set to $R_{ave}$ = 0.257 mm. It is also noticed that when the average particle radius is greater than 0.7 mm ($R_{ave} \geq 0.7$ mm), the peak shear strength would be influenced more by the significant decrease in fracture compressive strength than by an increase in fracture surface roughness. Although, these examples and the obtained results are case specific, a similar concept is applied to fractures with different geometries modelled in this way.

The objective of this study is to investigate the effect of profile geometry (i.e. roughness and waviness) on fracture shear behaviour and therefore the analyses are to be repeated for shear boxes with similar number of particles but different fracture geometries. In this way the effects of generated micro-roughness becomes insignificant in the ultimate model response. However, in all models it was attempted to use the smallest possible particles sizes based on the available computer memory.

### 3.4.3 Fracture particles friction coefficient

The shear strength of fracture modelled in PFC2D is affected by the friction coefficient of unbonded particles along the fracture plane (Cundall, 2000; Lambert et al., 2010; Park and Song, 2009). In contact models such as BPM, if there is no bond between particles (or say after the existing bond is broken), friction coefficient controls the particles sliding. So the value of friction coefficient for particles lie upon opposite sides of fracture is of major importance and must be correlated to the basic friction angle of planar fracture. Here, it is assumed that a typical smooth fracture has the basic friction angle of 30° (Cundall, 2000; Patton, 1966).

In developed models assigning a proper value for fracture particles friction coefficient and estimation of basic friction angle and apparent cohesion of the fracture are important parameters as granular materials create micro roughness along the fracture surface which affects the mobilized peak and residual friction angles of the fracture.

Cundall (2000) and Park & Song (2009) have stated that the friction coefficient of fracture particles must be assigned close to zero to ensure a realistic estimation of shear strength is being made. More recently, Park & Song (2009) simulated the shear strength of fractures in PFC3D and analyzed the effects of particles friction coefficient on shear

strength of smooth surfaces and surfaces with different JRC values. They found that in larger JRCs (JRC > 12), increasing the particle friction coefficient (e.g. from 0.0 to 0.3) affects the fracture cohesion more than its friction angle. They correlated their findings with shear strength obtained from Barton empirical equation.

To understand the effects of fracture particle friction coefficient (i.e. particles located along the fracture profile) on shear behavior of planar and rough fracture profiles, two sets of preliminary PFC2D shear tests were performed under the same conditions but with different particle friction coefficients of 0.05 and 0.6. Shear test simulations were performed for a planar fracture as well as a rough fracture with symmetric triangular profile of 30° asperity angle, as shown in Figure 3.15. This figure shows the fracture envelope (i.e. the curve of peak shear strength versus normal stress) corresponding to two different friction coefficients (i.e. 0.05 and 0.6). It is observed that for rough fractures, a wide increase in particle friction coefficient, i.e. from 0.05 to 0.6, causes only a small increase in fracture macro friction angle property from 47.57° to 51.05°, whereas, fracture apparent cohesion increases from 1.6 to 6.3 MPa which is a significant increase. Asadi & Rasouli (2011) has shown the role of particle friction coefficient on shearing simulation of synthetic fracture profiles using PFC2D modeling.

Effects of fracture profile roughness with particles having very small friction coefficient (here 0.05) on fracture shear behaviour was investigated by simulating a planar and a rough (i.e. 30°symmetric triangular profile) fracture profile.

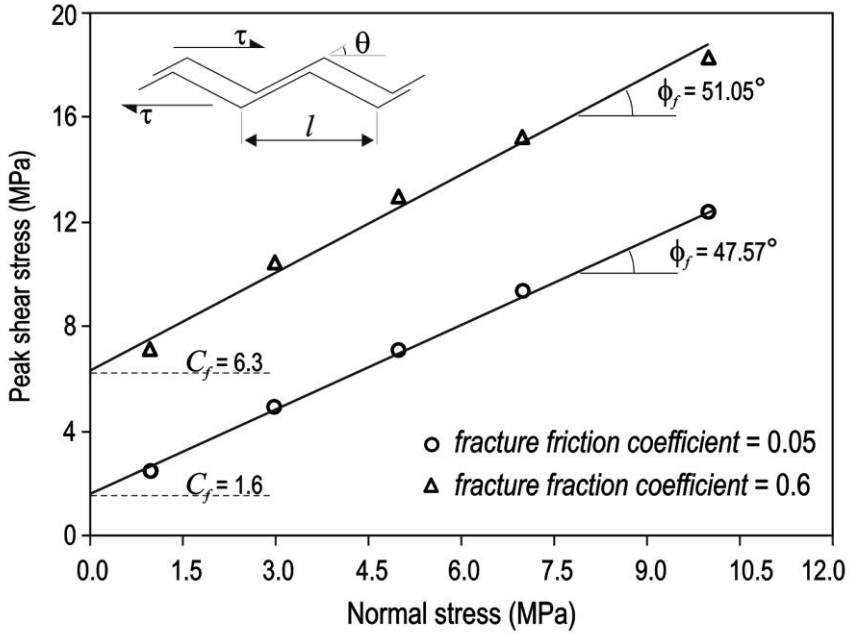


Figure 3.15 Effects of particle friction coefficient on peak shear strength of planar and rough fractures.

The results show that fracture friction angle and cohesion become larger with increasing fracture roughness: friction angle changes from 29.36° to 47.56° whereas cohesion increases from 0.912 to 1.6 MPa (see Figure 3.16). The analysis was repeated for a friction coefficient of 0.6 and results with a similar trend were obtained.

These simulation results together with findings by Park & Song (2009) which showed for JRC > 12 (i.e. rough cases), roughness has larger effects on cohesion than friction angle does. This shows that the value of particle friction coefficient does not significantly change the mechanical shear behaviour of fracture. The large values for fracture friction coefficient will result in overestimation of the apparent cohesion and in turn peak shear strength, as shown in Figure 3.16. This figure indicates that particle friction coefficient of 0.05 for a planar fracture profile results in a basic friction angle of 29.36° for this fracture profile.

Based on the review of literature, data from past work, and preliminary simulation results the following points were considered for modelling rough fractures shear strength in PFC2D in this study:

- In PFC2D simulation of fracture shear strength, roughness has larger effects on cohesion than friction angle. This effect increases as fracture roughness increases.
- Reducing particle friction coefficient close to zero will result in reduction of ultimate shear strength of fracture.

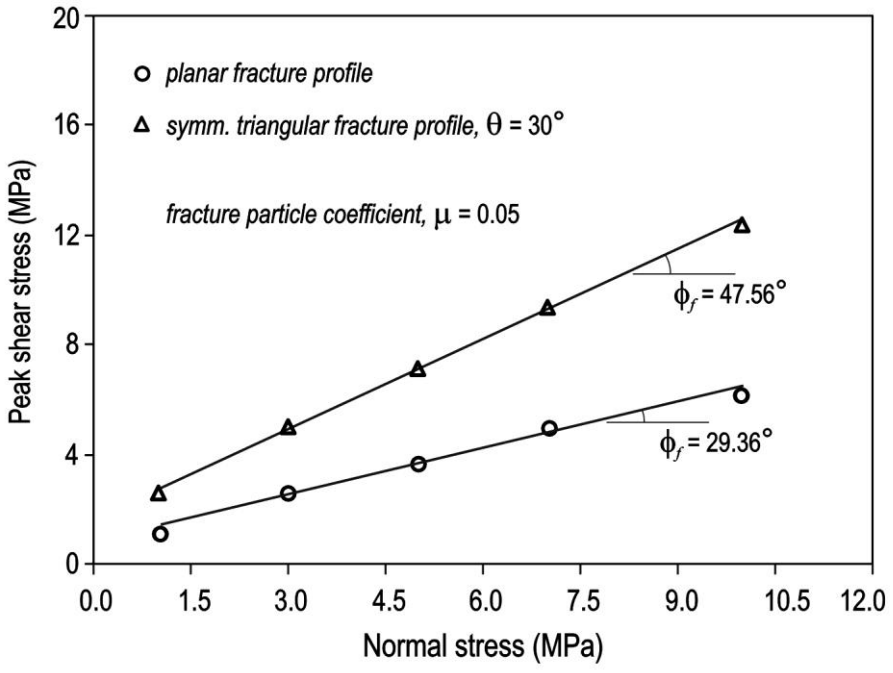


Figure 3.16 Effects of particle friction coefficient on peak shear strength of planar and rough fractures.

### 3.4.4 Boundary conditions and stress calculation

In models presented in this study the normal load is applied vertically to the upper block. To simulate the shear test under Constant Normal Load (CNL) condition, vertical motion of the upper block over the lower block is allowed (i.e. dilatation is permitted). This is controlled by a numerical servomechanism as to keep the vertical reaction force constant at some specified values of normal load. Horizontal shear displacement then applied by giving a velocity to the elements of upper block which displaces against the lower fixed block. The procedure to compute and control the stress state in the sample during the shear test is discussed below.

The boundary particles comprising the upper and lower blocks of the shear box are controlled to perform the shear test. After deleting the walls, all the particles existing in the model are divided into two groups: those located above and below the fracture profile. This allows controlling the velocities of upper and lower blocks independently.

The lower block is kept stationary throughout the test, and the upper block is translated as a rigid unit with constant velocity (i.e. shearing rate) in the horizontal (shearing) direction. Shear and normal loads are applied by giving horizontal and vertical velocities to the upper block. Both normal and shear forces on the upper block are evaluated continuously. The shear stress was calculated by dividing the average shear force of upper and lower blocks by the fracture width. A similar procedure was applied to measure the normal stress using the average normal force applied to the upper and lower blocks which then divided by shear box width to estimate the normal stress. The vertical displacement is controlled by a numerical servo mechanism described in PFC2D user manual (Itasca, 2008).

To control the velocity (displacement) of upper block during shear test, while progressing the program, the numerical servomechanism was applied (Itasca, 2008). The sample is loaded by specifying the velocities of the top and bottom blocks' particles. The state of stress and strain of the sample are computed by taking the average forces of upper and lower blocks divided by shear box width. The strains in both $x$ and $y$ directions are computed as

$$\varepsilon = \frac{L - L_0}{\frac{1}{2}(L_0 - L)}, \tag{3.11}$$

where $L_0$ and $L$ are the original and current sample length in a given direction. As stated, during the loading process, the normal stress is kept constant by adjusting the

velocities using a numerical servomechanism that is implemented by servo mechanism function and a gain parameter. This function determines the stresses and uses a numerical servo-control to adjust the upper block velocities in such a way as to reduce the difference between the measured force and the required force. Based on servomechanism implemented in the model, the following equation gives the velocity of the blocks as

$$u = G\left(f_n^{measured} - f_n^{required}\right). \tag{3.12}$$

where G is the "gain" parameter that needs to be adjusted for different applications based on time steps and contact force area (Itasca, 2008).

In current simulations, shearing velocity was set to 0.3 m/s and gain parameter was adopted in the model for both vertical and horizontal directions to ensure a constant normal stress throughout the shear test with a constant velocity. Displacements are calculated based on the assumption that velocities are constant in each timestep. Having the values for timestep and velocity, displacements can be measured in both vertical and horizontal directions. Histories of shear stress, normal stress, and shear and normal displacements were recorded in each timestep to enable plotting the shear stress-shear displacement and normal displacement-shear displacement curves. It is widely accepted that by increasing the shearing speed (rate), the shear strength of fractures increase. So an appropriate shear loading rate should be considered depending on the applications required.

In this study, a large number of shearing cycles was applied to capture the post-peak behaviour of fracture profiles. A 3.0 mm shear displacement allowed for fractures with 10.0 cm width to undergo a complete failure cycle including the post-peak region.

### 3.4.5 Development of cracks

The advantages of using PFC2D in simulation of fracture shearing is that it can simulate the complex failure process in pre and post-peak stress behaviour of intact rocks with an ability to visualize the entire process of crack initiation, growth, coalescence, localization and complete breakdown process without requiring continuous system re-configuration.

Preliminary simulations were performed on a rock fracture profile shown in Figure 3.17 which aimed at tracing the process of micro cracking (i.e. failure pattern) under different normal stresses. It is expected to observe an increase in the number and magnitude of induced cracks during shearing. Figure 3.17 shows the profile view after

shearing under 3.0 and 7.0 MPa normal stresses, respectively. In this figure, shear failures are shown in gray and tensile cracks in black. It is seen that at low normal stresses (i.e. 3.0 MPa) sliding is the dominant failure mechanism (Figure 3.17.a) as local shear failures are only concentrated around the asperity contacts. Small tensile cracks also develop at profiles doglegs. In comparison, at high normal stresses (i.e. 7.0 MPa), the amount of contact shear failure reduces but large tensile cracks are developing at asperity doglegs which corresponds to either asperity cut-off or intact rock failure (Figure 3.17.b). In this case, dilation decreases significantly which is believed to be due to the concentration of compression forces on shearing chord of fracture profile and the accumulated force tries to open a large tensile crack as shown in this figure.

The above analysis shows the applicability of PFC2D in simulation of rough fractures shear behaviour and asperity degradation.

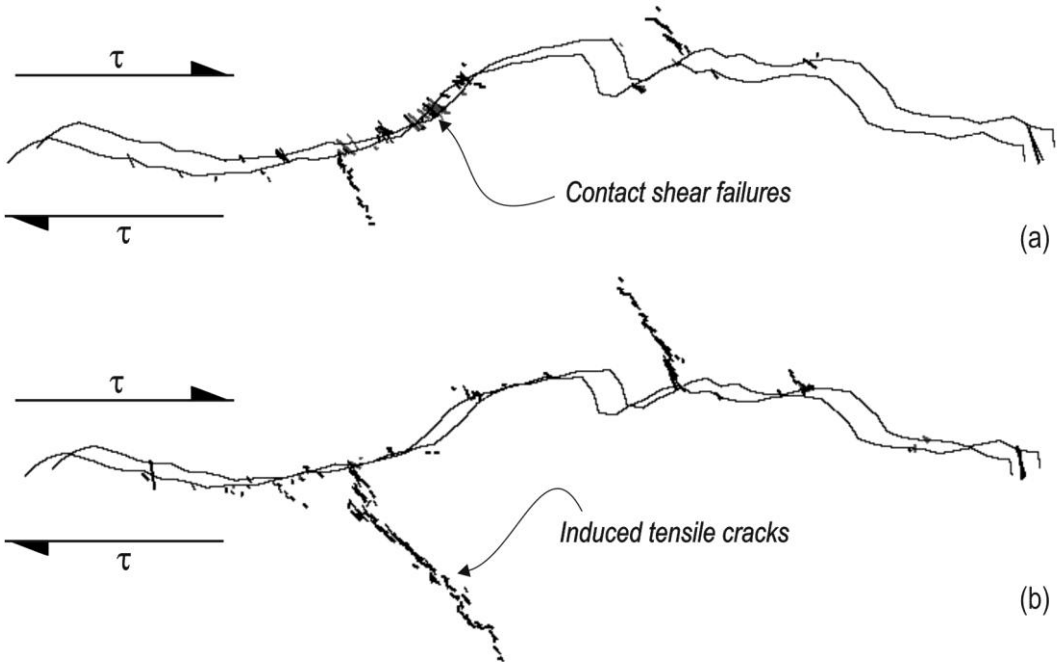


Figure 3.17 Micro cracking pattern after rough fractures shear test in PFC2D at (a) 3.0 MPa and (b) 7.0 MPa normal stress; shear displacement is 3.0 mm.

## 3.5 Shearing simulation of synthetic profiles

As stated in Chapter 2, $D_{R1}$ is 1D Riemannian dispersion parameter developed based on the multivariate analysis of unit normal vectors to a profile to characterise profile roughness. The larger is $D_{R1}$ the rougher will be the profile. It is also well understood that the larger the profile roughness, the greater will be the fracture shear strength. Rasouli and Harrison (2010) have shown the applicability of $D_{R1}$ as fracture roughness

parameter through the analysis of synthetic and rock fracture profiles. They, through analysis of a symmetric synthetic profile, showed the direct correlation between $D_{R1}$ and the fracture shear strength. A part of this research work aims at developing this concept to synthetic profiles with different geometries and also to rock fracture profiles. Therefore, PFC2D was used to simulate fracture shearing behaviour of synthetic profiles with symmetric and asymmetric triangular as well as sinusoidal geometries. This was also extended to the analysis of some randomly generated profiles and later to rock fracture profiles. The results of simulations were compared with profile roughness parameter $D_{R1}$, in order to develop correlations between profile shear strength and its geometry. The results are discussed in the following Section.

### 3.5.1 Symmetric triangular profile

A simple symmetric triangular linear profile with wavelength $l$ and amplitude $h$, as shown in Figure 3.18 can be characterised using either the aspect ratio $h/l$ or the angle θ. For this profile $D_{R1}$ is expressed as (Rasouli, 2002):

$$D_{R1} = \tan^{-1}(2h/l), \tag{3.13}$$

which corresponds to the asperity angle of the profile.

Shearing behaviour of a synthetic profile with symmetric triangular asperity geometry was simulated using PFC2D. In simulations reported here, the asperity wavelength $l$ is assumed to be constant so by increasing the amplitude $h$, the effect of profile roughness in shearing process can be investigated. In this example, profile wavelength is 2 cm, so $D_{R1}$ can be calculated based on the radians of asperity base angle (e.g. $D_{R1}$ for a single asperity with base angle of 30° is 0.577). Consequently, $D_{R1}$ for any symmetric triangular profiles used in this Section can be readily calculated by taking the tangent of asperity base angle, θ.

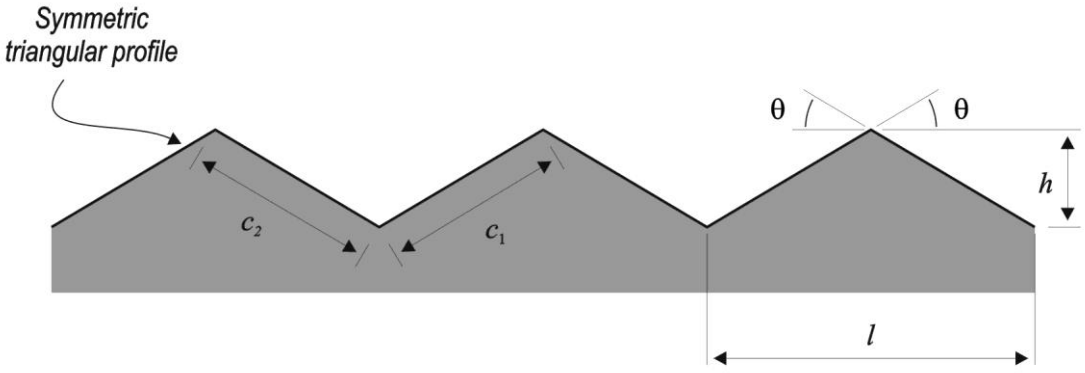


Figure 3.18 Geometrical features of a symmetric triangular profile (Rasouli, 2002).

It is noted that asperity amplitude and wavelength has separate effects on fracture shear strength and care must be taken once different profiles' shear strength are to be compared, in which asperity amplitude *h*, or wavelength *l*, are varied.

The PFC2D fracture shear box used here has the same properties as the one described in detail in Section 3.2 (see Table 3.2). Simulations were performed under variety of normal stresses (from very small, 1.0 MPa to very high, 10.0 MPa). This enables us to plot fractures failure envelopes corresponding to several scenarios.

Figure 3.19 shows the PFC2D model after shearing of a symmetric triangular profile with base angles of 15°, 30° and 45° from left to right direction under normal stress of 5.0 MPa. In this test, horizontal (shear) displacement was allowed up to 3 mm to fully capture the deformation response of the shearing asperity.

The results show that asperity damage increases as the asperity base angle θ increases, but in some cases asperity failure does not occur equally on all the asperities. This is thought to be due to the inherent roughness of the contact asperities which is related to the particle size distribution along asperity contacts as explained earlier.

The cut off plane (discussed in Section 2.2.7 ) along which asperities are sheared off in angles less than asperity base angle θ, are clearly visible at larger asperity base angles (here 30° and 45°), whereas it becomes more difficult to recognise a cut-off plane at smaller asperity angles (i.e. 15° in this example). This denotes the fact that at low asperity angles (e.g. 15°) sliding is the dominant mechanism in fracture shear test (Figure 3.19.a). It is observed that the orientation of cut-off plane is nearly horizontal under a higher vertical stress regardless of the fracture morphology, which is because in this situation, the asperities all fail and the effect of profile roughness becomes insignificant. Separations were observed at down-slope sides of the asperity contacts in both low and high normal stresses. Crushing (i.e. asperity degradation) is occasionally found at the tips of asperities (Figure 3.19.b). Tensile fractures initiate from asperity tips and develop initially at an angle almost perpendicular to shearing direction, followed by wing-crack type fractures propagation at almost 45° to the shearing direction.

Similar failure mechanisms observed in our simulations has been previously reported by Huang et al. (2002) during their direct shear experiments of regular tooth-shaped fractures. In Chapter 4 of this thesis, we will perform several laboratorial shear tests using newly developed fracture shear apparatus to validate the accuracy of the PFC2D simulation results.

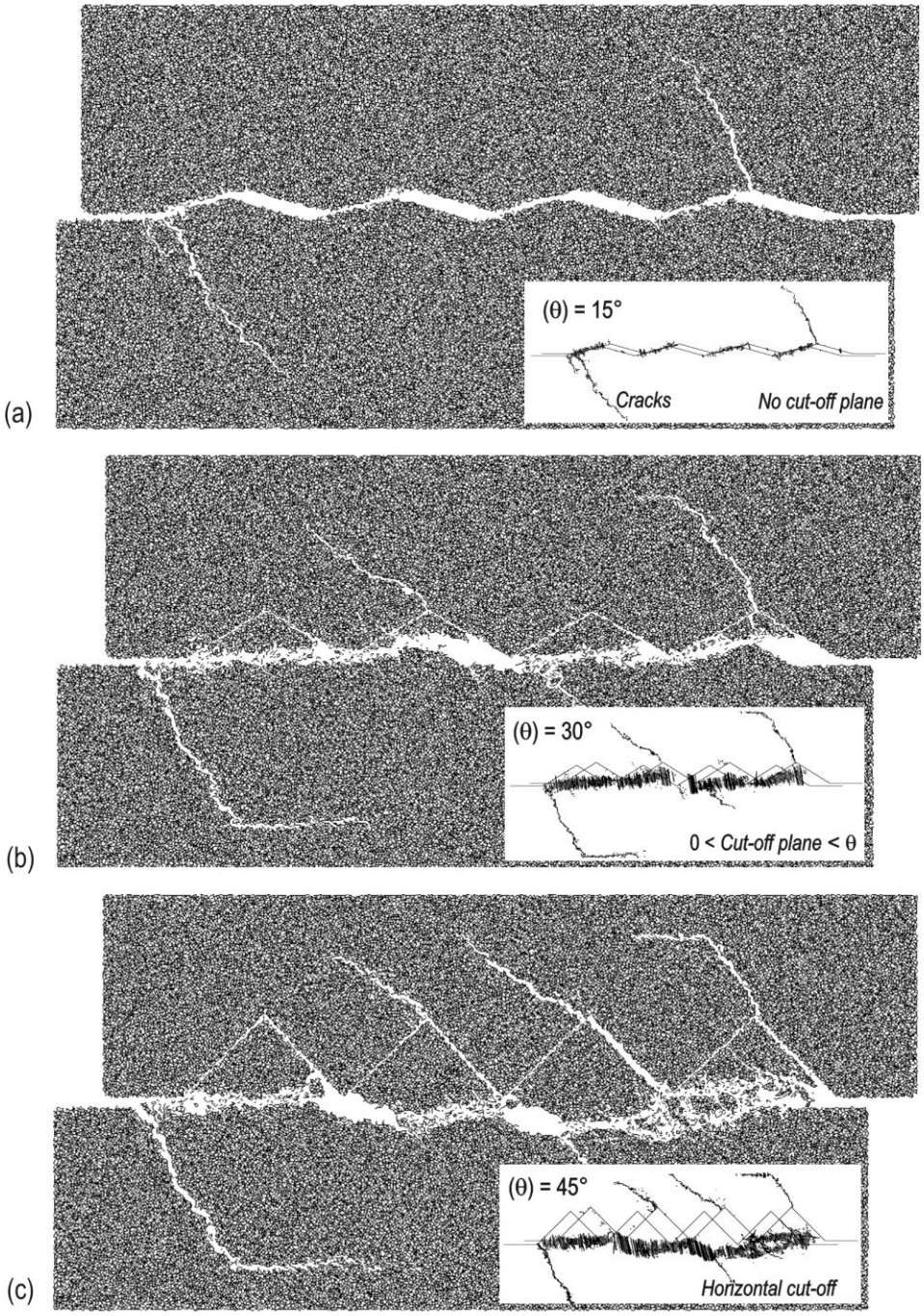


Figure 3.19 PFC2D shearing simulation of symmetric triangular profiles with asperity base angles of (a) 15°, (b) 30°, and (c) 45° under 5.0 MPa normal stress.

As can be seen from Figure 3.19, by increasing the shear displacement, the amount of local degradations increases which affect the residual shear stress and dilation (i.e. post-peak shear behaviour) considerably.

The residual shear stress of fractures in current simulations appears to be significant since in all simulated cases we observe asperity degradation at high normal stresses and after a large displacement of fractures. This predominantly affects the post-peak behaviour of fractures; therefore the difference between residual shear strength of

fractures with different profile's roughness can be identified as the rate of degradation and used for calculation of effective degraded area of asperity contacts.

The advantages of using PFC2D in simulation of fractures shear behaviour is the potential of tracing the development of micro cracks in different timesteps. Once the model is calibrated and the results are in good agreement with physical experiments, simulations can be performed instead of doing costly and time consuming laboratorial tests to capture the post-peak stress-strain curves of fracture shearing. Figure 3.20 shows shear stress versus shear displacement curves corresponding to fractures with asperity angles of 15°, 30° and 45°, respectively. It is seen that as asperity angle increases, peak shear stress of fracture asperity increases, as expected.

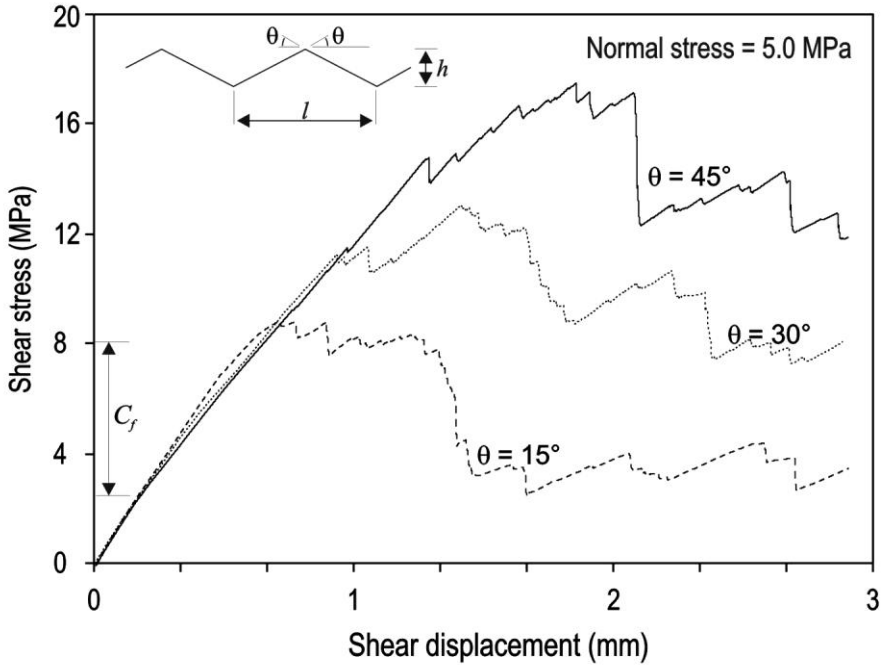


Figure 3.20 Shear stress versus shear displacement curves for asperity angles of 15°, 30°, and 45° under 5.0 MPa normal stress.

From Figure 3.20 it is seen that the difference between profiles with asperity angles of 30° and 45° is significant, which is believed to be due to the fact that as asperity angle becomes larger than a critical value, failures will partially occur through the intact rock, and thereafter the effect of surface roughness reduces.

It is interesting to compare the shear stresses at peak and post-peak states. The difference between peak and residual shear stress ($C_f = \tau_p - \tau_r$) decreases as asperity base angle increases, i.e. profile roughness becomes larger. Comparing the curves for different asperity angles in Figure 3.20 it is seen that the difference between peak and residual shear strength decreases while asperity angle increases: this difference is approximately 5.5, 5.0, and 4.5 MPa for fractures with asperity angles of 15°, 30°, and

45°, respectively (see Figure 3.20). This demonstrates that the chance of local asperity degradations and intact rock failure increases by increasing fracture profile roughness, as shown in Figure 3.19.c. It is also observed that sudden drop of the curve at the peak which occurs when the samples experiences the major tensile cracking, reduces as profile roughness decreases.

Figure 3.21 shows the plot of normal displacement versus shear displacement (i.e. dilation) of symmetric profiles with different asperity angles. A similar dilation is observed for three different asperity angles when the shear displacement is less than about 1 mm. However, for shear displacements larger than 1 mm, dilation increases mainly in larger asperity angles (here 30° and 45°).

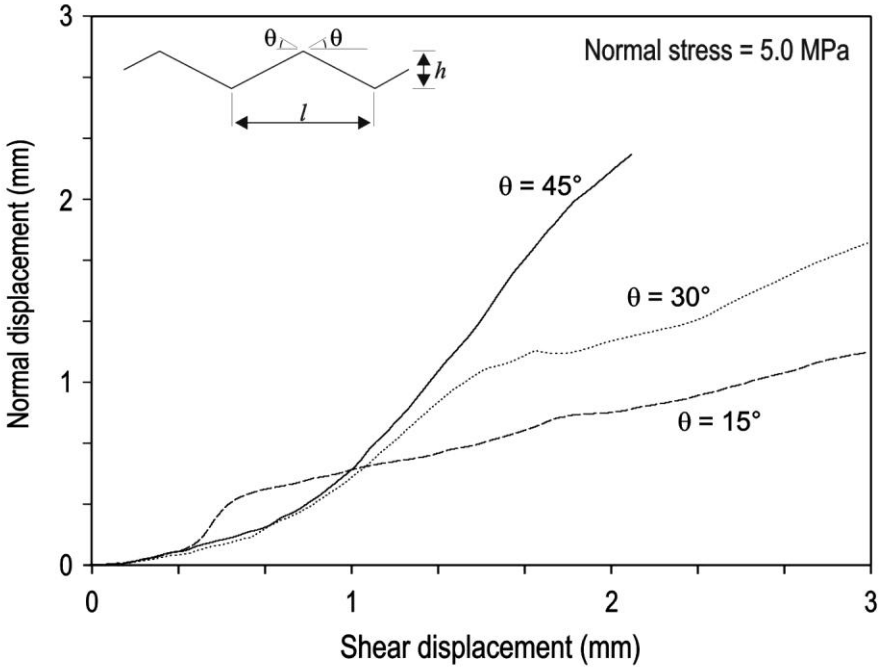


Figure 3.21 Normal displacement versus shear displacement curves (i.e. dilation) for asperity angles of 15°, 30°, and 45° from PFC2D simulations.

This behaviour is included in Barton's dilation equation (Barton and Choubey, 1977) which is expressed as

$$d_{\mathrm{n}} = JRC \log_{10}\left(JCS/\sigma_{\mathrm{n}}\right). \tag{3.14}$$

In this equation dilation, $d_{\mathrm{n}}$, is directly related to the JRC value. As expected and was observed from PFC2D simulation results, by increasing profile roughness, dilation increases.

In Figure 3.22, the effect of normal stress magnitude on shearing process is depicted. This figure shows the results of PFC2D simulation for a symmetric profile subjected to 1.0, 3.0 and 5.0 MPa normal stresses, respectively. The results show that asperity damage increases as the normal stress increases.

It is interesting to note that in Figure 3.22, the cut-off angle decreases as normal stress increases and at normal stresses equal to or more than 5.0 MPa the observed cut-off plane is nearly horizontal. This is in agreement with analytical calculations of cut-off angle which is obtained through the limit equilibrium analysis by Huang et al. (2002) and extended in Section 2.2.7 of current work, as discussed.

Interestingly, from Figure 3.22 it is seen that by increasing the normal stress, more asperities enter into the failure mode. Also, it is observed that at normal stress of 1.0 MPa (Figure 3.22.a), cut-off plane develops in two asperities only but the others are only slide over the lower block. However, by increasing the normal stress to 5.0 MPa (Figure 3.22.c), the asperity cut-off occurs almost uniformly in all four asperities along the fracture profile.

This also shows the significant effect of high normal stresses on post-peak behaviour of fractures where both first and second order asperities are prone to fail. The post-peak behaviour of fractures during shearing is also more influenced by material (here rock-like assembly) strength than that of fracture surface geometry since in post-peak state of stress at high normal stresses, asperities have already been sheared-off or degraded.

Shear stress versus shear displacement is plotted in Figure 3.23 for a symmetric profile with asperity angle of 30°. From this figure it is seen that peak shear stress increases as normal stress increases. Also large differences are observed between profile dilation when it is sheared under different normal stresses. Figure 3.23 also indicates how dilation reduces as a result of increasing the normal stress.

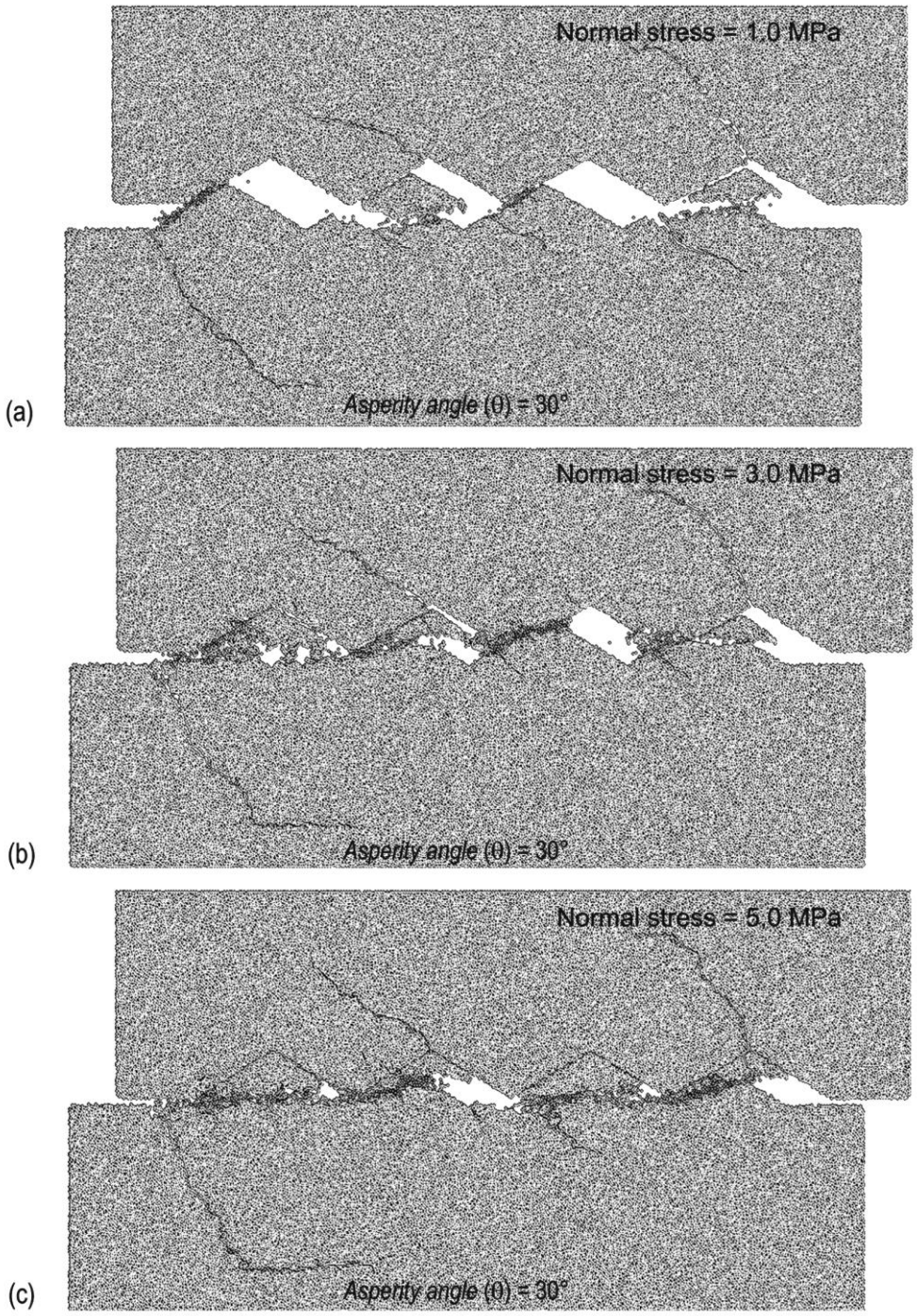


Figure 3.22 Effects of normal stress on asperity shearing: (a) normal stress = 1.0 MPa, (b) normal stress = 3.0 MPa and (c) normal stress = 5.0 MPa.

To estimate the normal stress corresponding to very low dilations (close to zero), simulations performed under very high normal stresses. It was observed that asperities are completely sheared-off under normal stress equal or above 15.0 MPa with no noticeable dilation. Similar results have been reported by Huang et al. (2002) in their experimental works on profiles with base angles of 15° and 30° under different normal stresses. They confirmed that as asperity base angle and normal stress increase, dilation decreases.

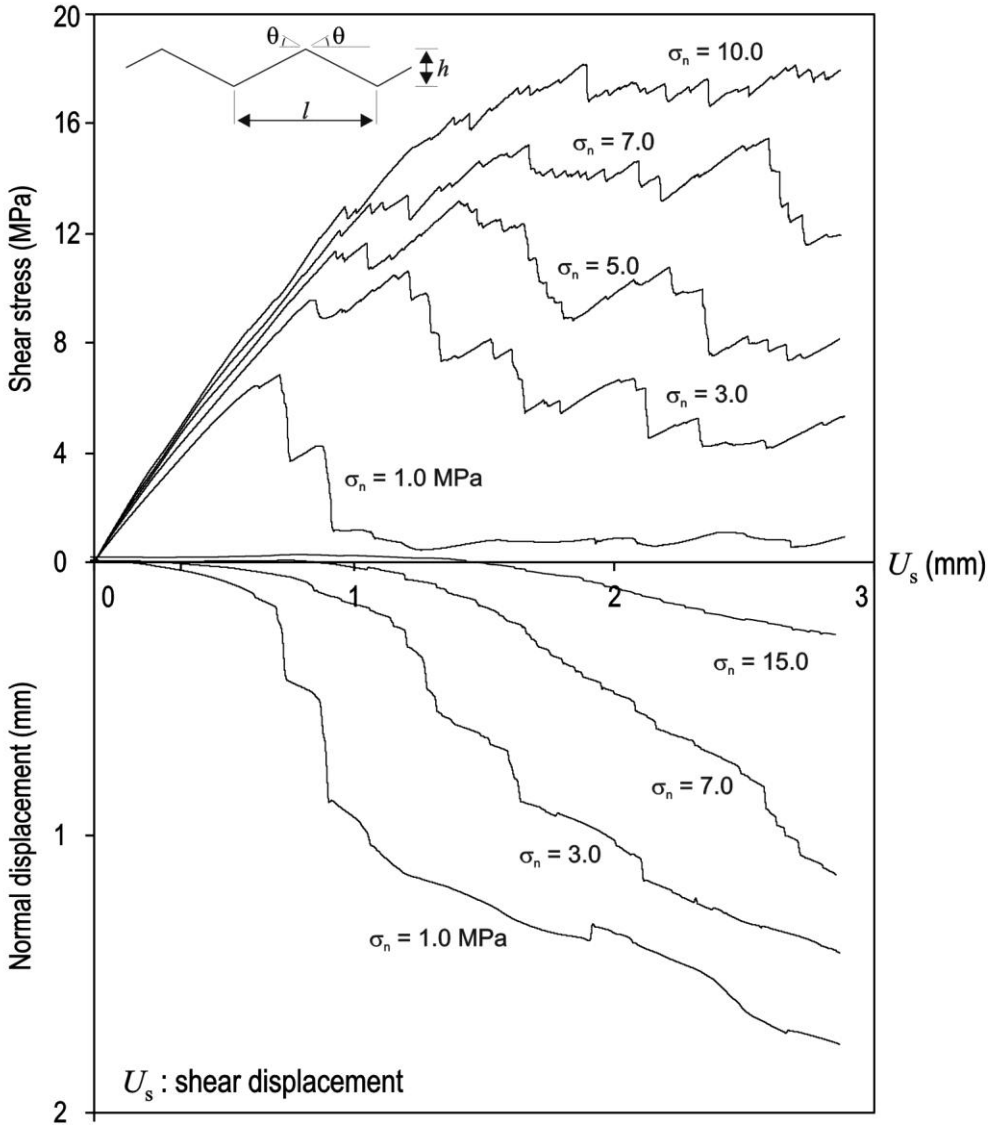


Figure 3.23 Shear stress versus shear displacement and dilation curves for a profile with asperity angle of 30° under different normal stresses after 3.0 mm horizontal shearing.

Effects of shear displacement on evolution of asperity degradation are also seen in Figure 3.23. It is seen that at shear displacement corresponding to peak shear stress, dilation increases significantly, and then gradually decreases.

The shear strength of symmetric triangular profiles with base angles of 15°, 30° and 45°, corresponding to $D_{R1}$ values of 0.262, 0.523 and 0.785, respectively, are shown in Figure 3.24. As expected, the results indicate increasing shear strength with both increasing normal stress and profile roughness. It is seen that almost all profiles intersects intact rock criterion at a particular normal stress value. Interestingly, a correlation is observed between profile base angle and this intersection point: as profile base angle or $D_{R1}$ increases, the point of intersection moves towards left, i.e. failure of intact rock begins sooner or profile roughness becomes less dominant in failure of the rock. This, again, demonstrates the fact that at low normal stresses, sliding is the most

dominant mechanism, whereas at high normal stresses, asperity cut-off and degradation mechanisms are more likely to take place.

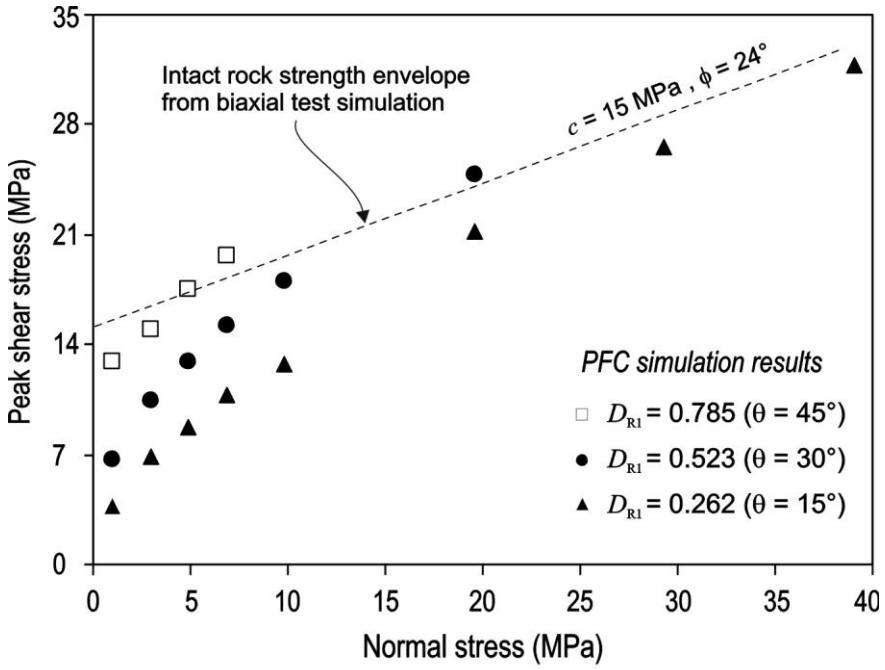


Figure 3.24 Shear strength of symmetric triangular profiles with different asperity angles at different normal stresses obtained from simulation.

The point at which fracture shear strength curve intersects the intact rock material is the point above which fracture roughness becomes ineffective on shear stress of the fracture profile as profile asperities will be sheared off completely smooth. The normal stress corresponding to this point, $\sigma_n|_{\alpha=0}$, can be analytically estimated from Equation 2.23 (in Chapter 2) by substituting the current PFC2D rock-like assembly's strength properties ($c$ and $\phi$) in this equation:

$$\sigma_n|_{\alpha=0}(\text{MPa}) = 15(\cot\theta - \tan 24°)\cos^2 24°. \tag{3.15}$$

In Table 3.3 the results of normal stress corresponding to the cut-off angle zero obtained from analytical solution and simulations for fractures with asperity angles of 15°, 30° and 45° are given. From this Table, a close agreement is observed between the results of the two approaches; however, the simulation results appear to be lower than those of analytical solutions. Interestingly, it is seen that as the asperity angle increases, the difference between the results obtained from the two methods becomes larger. This could be due to a more complicated failure mechanism at high normal stresses, which may be either an asperity cut-off or degradation. This complexity is not adequately captured using a simple analytical formula and therefore the PFC simulation can be fruitful in that regards.

Table 3.3 Normal stress corresponding to complete asperity shearing-off.

| Asperity base angle, θ° | $\sigma_n\|_{\alpha=0}$ from PFC2D simulations (MPa) | $\sigma_n\|_{\alpha=0}$ from Analytical solution (MPa) | $D_{R1}$ |
|---|---|---|---|
| 15 | 40.8 | 41.146 | 0.261 |
| 30 | 14.9 | 16.109 | 0.523 |
| 45 | 5.1 | 6.944 | 0.785 |

Yet, it is to be noted that in real situations it is very unlikely to have rock fractures with asperity angles of as high as 30° (Barton, 1973; Patton, 1966). The importance of this transition point, i.e. $\sigma_n|_{\alpha=0}$, is its potential for developing correlations between $D_{R1}$ and shear strength of the profile from PFC2D simulation results as will be explained in Section 3.5.

#### Effects of contact bond strength

Since the UCS of the material is highly affected by the bond strength between particles' contacts, assigning a proper value to bond strength is important (see the discussion in Section 3.2.1). As was shown before, the CBS and UCS are linearly correlated in a BPM, but the correlation is dependent on average particle size of the rock-like assembly. Therefore, the CBS will be referred to in our analysis here. The effect of CBS on fracture shear strength was examined by simulation of number of shear tests with a wide range assumed for the CBS. Sensitivity analysis was performed for two different symmetric triangular fracture profiles with 15° and 30° asperity base angles under different normal stresses. The aim of this analysis was to investigate the effects of material internal strength on fracture shear strength. In these simulations, the CBS ranges from 30 to 150 MPa as given in Figures 3.25 and 3.26.

From Figure 3.25 it is seen that as normal stress increases, dependency of shear strength to material strength increases (i.e. slope of the linear correlation increases from 0 to 0.0339, corresponding to normal stresses of 1 to 10 MPa). Figure 3.26 shows similar results for an asperity with 30° base angle, where the slope of the linear correlations increases from 0.025 to 0.0676, corresponding to normal stresses of 1 to 10 MPa). Comparing Figures 3.25 and 3.26 brings us to the conclusion that the shear strength shows to be more sensitive to material internal strength (here CBS) at high normal stresses and high asperity angles (i.e. larger profile roughness).

This is believed to be due to the extent of micro-cracking within the process of material bond breakage. As the chance of sliding decreases by increasing the normal

stress, a large number of micro-cracks are developed in the asperity contact area due to the concentration of shearing forces. In this situation the rock material strength (here CBS) plays a more influencing role in bond breakage than fracture surface properties.

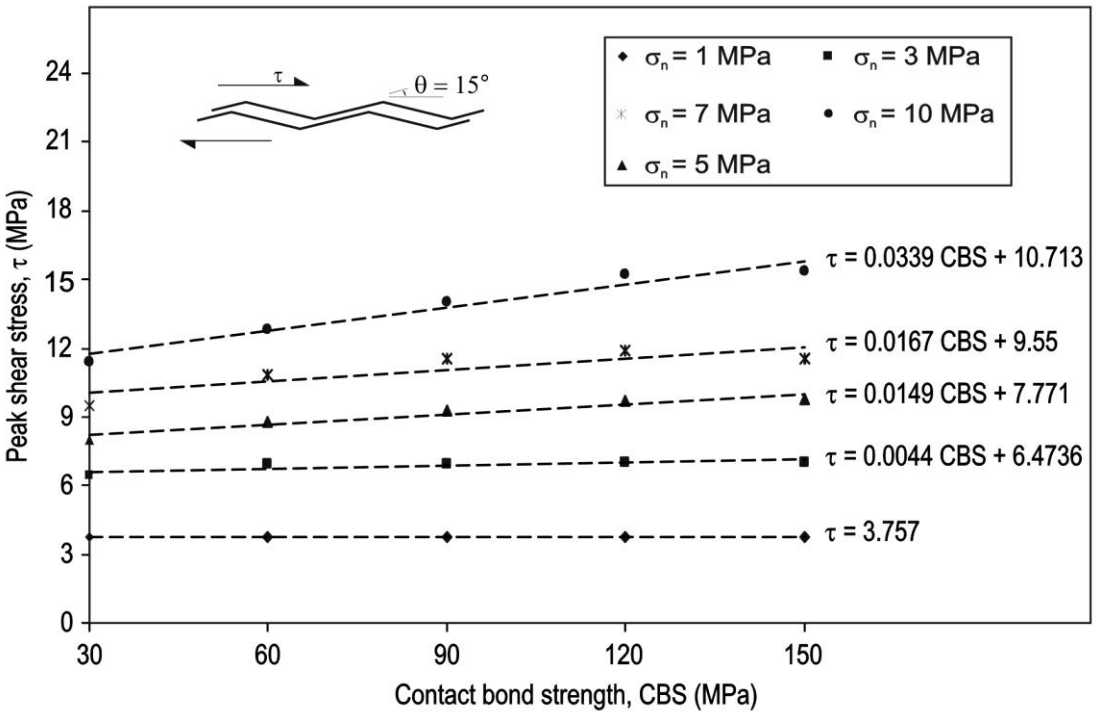


Figure 3.25 Effects of CBS on peak shear stress of symmetric triangular profiles with base angle of 15° at different normal stresses.

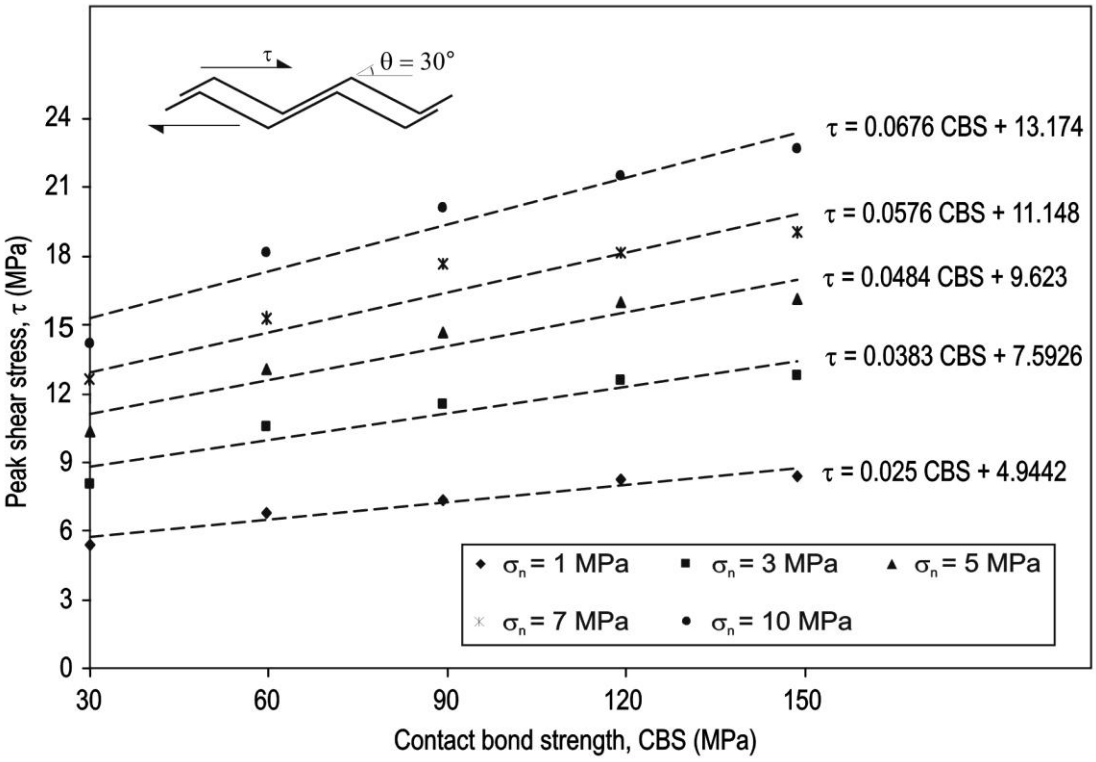


Figure 3.26 Effects of CBS on peak shear stress of a symmetric triangular profile with base angle of 30° at different normal stresses.

### 3.5.2 Asymmetric triangular profile

For an asymmetric synthetic triangular profile with its geometry being characterised using angles $\theta_1$ and $\theta_2$ corresponding to chords $c_1$ and $c_2$ (Figure 3.27), $D_{R1}$ is obtained from Equation 2.5 (Rasouli and Harrison, 2010) as:

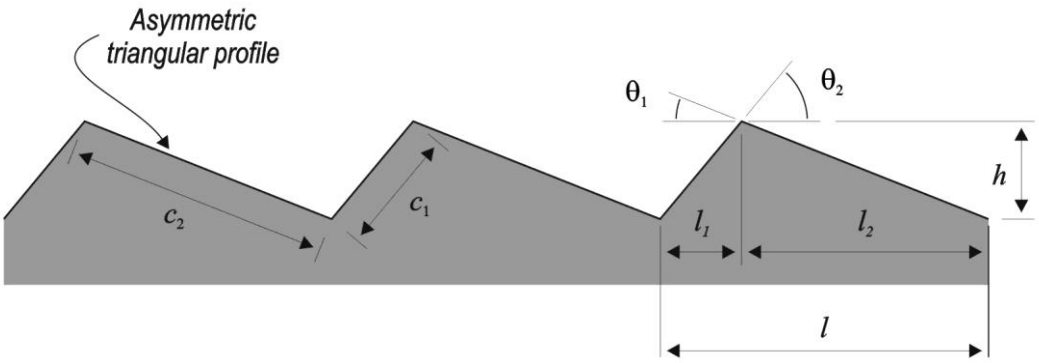


Figure 3.27 Geometrical features of an asymmetric triangular profile (Rasouli, 2002).

Geometry of asymmetric triangular profiles from their (*x,y*) coordinates data was generated in PFC2D shear test model. Several shear test simulations, similar to those of symmetric profiles, were performed considering different symmetry ratios ($l_1/l_2$) for the profile and assuming a wide range of normal stresses.

Figures 3.28.a to Figure 3.28.c show the results of simulations for profile symmetry ratios of 0.25, 1 and 4 under 1.0 MPa normal stress, respectively. As is expected, for such profile geometry the shear strength is directional dependent. The results shown in Figure 3.28 correspond to shear tests from left to the right direction. From this figure it is seen that peak shear stress increases as the symmetry ratio increases. In Figure 3.28.a, asperities are degraded since chord $c_1$ with a higher angle than chord $c_2$ faces against the shearing direction and this resists upward movement of upper block along the lower block.

Figure 3.28.b exhibits a behaviour of symmetric profile which is a special case of asymmetric profile with $l_1/l_2 = 1$, as explained. In Figure 3.28.c symmetry ratio has increased to 4, corresponding to a lower angle for chord $c_2$ than chord $c_1$, in which dominantly sliding of asperities along each other is observed. This indicates the directional dependency in shear strength of an asymmetric profile: shearing the profile with symmetry ratio of 4 from left to right corresponds to shearing the profile with symmetry ratio of 0.25 from right to left.

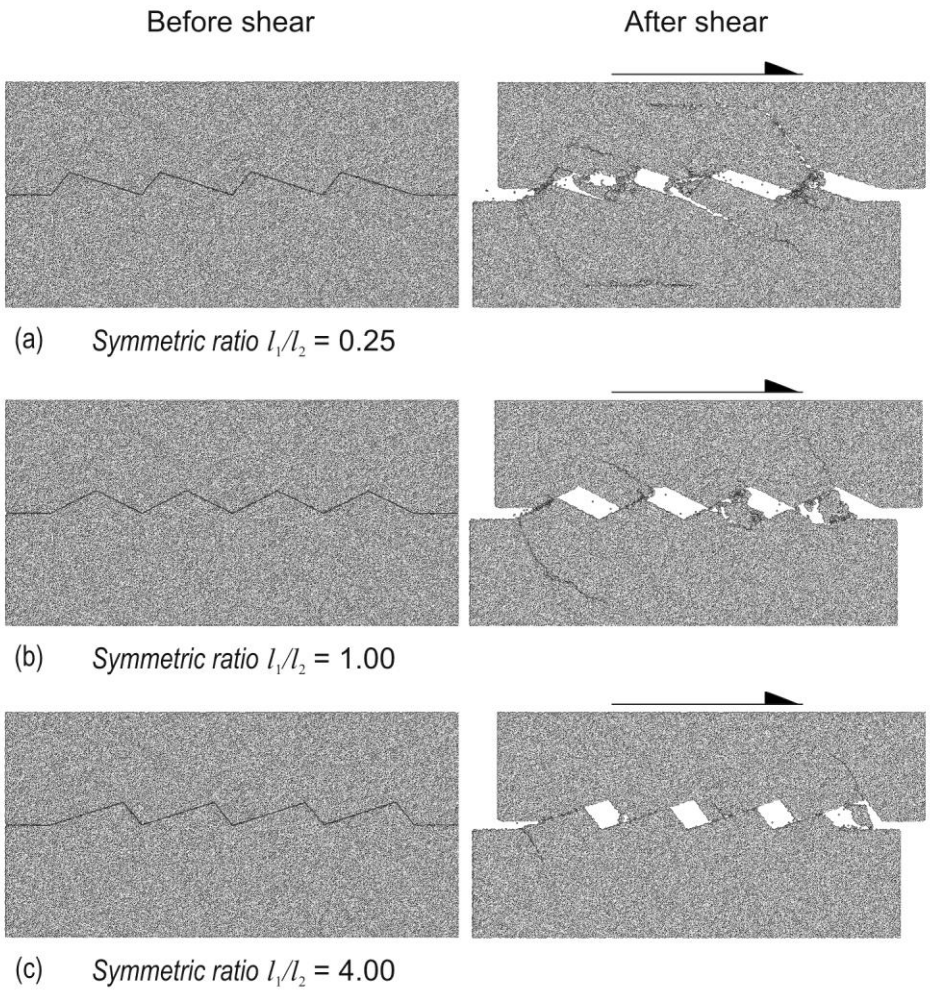


Figure 3.28 Effects of asperity symmetry ratio on profile shear strength: (a) $l_1/l_2$= 0.25, (b) $l_1/l_2$= 1.0 and (c) $l_1/l_2$= 4.0 under 1.0 MPa normal stress.

This suggests that for a fracture profile, using a single roughness parameter to be used for estimation of its shear strength may not be appropriate but different roughness values need to be used depending on the shearing direction. Figure 3.29 gives shear stress versus shear displacement curves for profiles with symmetry ratios of 0.25, 1, and 4 at 1.0 MPa normal stress where shearing taken place from left to right direction. It is seen that as profile symmetry ratio decreases, not only peak shear stress increases but post-peak behaviour exhibits significant changes. This figure also shows the effect of normal stress on fracture shear strength and asperity failure. It is interpreted from the plot that as the normal stress increases (i.e. 5.0 and 10 MPa), the amount of degradation increases and post peak shear strength appears to be larger as well as that fracture reaches its residual state sooner than that of under 1.0 MPa normal stress.

As expected, by reducing the symmetry ratio, asperity degradation takes place which causes an increase in the post-peak shear strength of fracture profile as stated also by Karami and Stead (2008) in their Hybrid FEM/DEM numerical simulations.

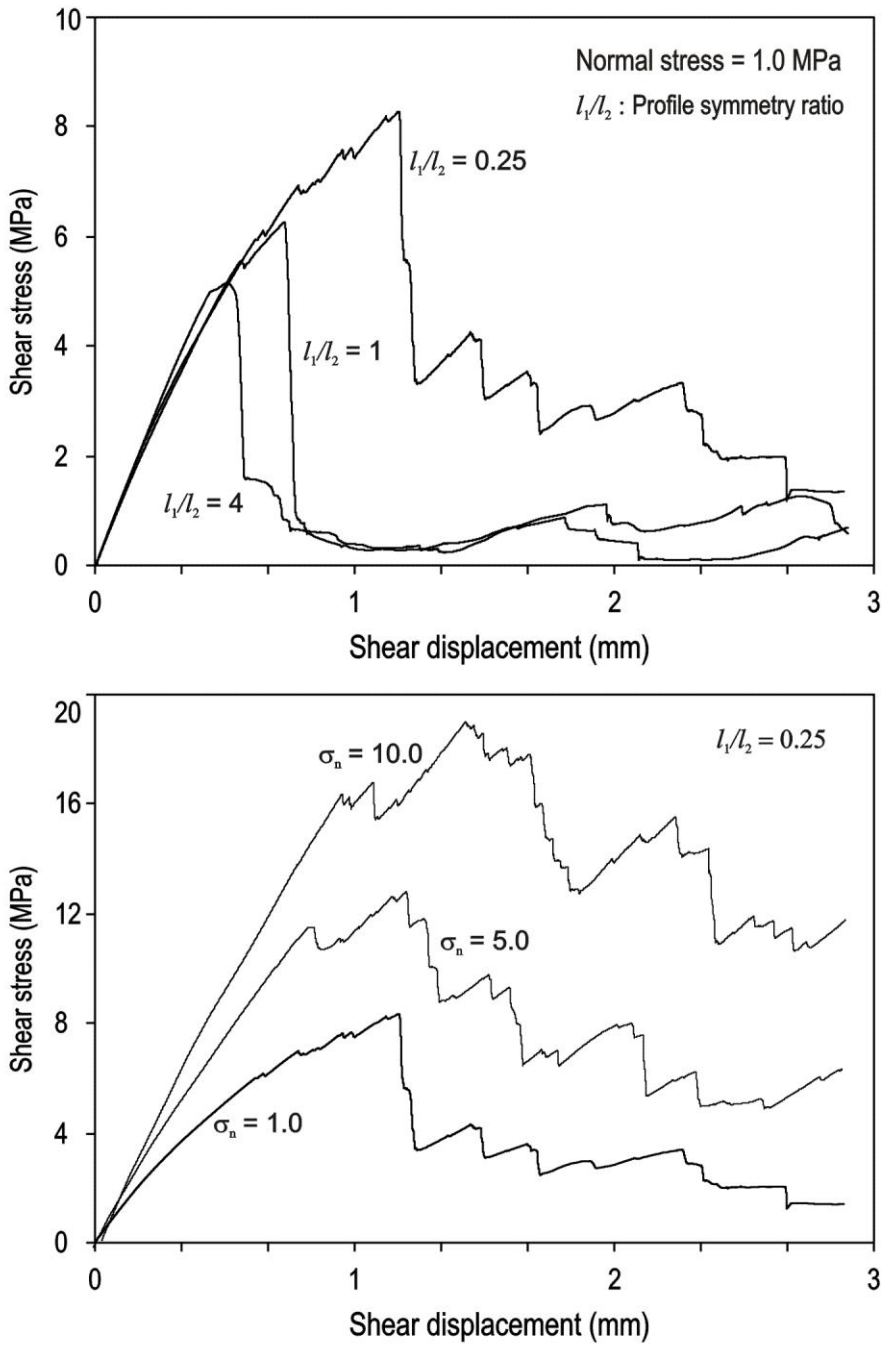


Figure 3.29 Shear stress versus shear displacement curves for an asymmetric profile with different symmetry ratios.

### 3.5.3 Sinusoidal profile

A sinusoidal profile given by $z = a\sin bx$, with amplitude $2a$ and wavelength $w = 2\pi/b$ (or aspect ratio $2a/w$) is shown in Figure 3.30. $D_{R1}$ for this profile is expressed as :

$$D_{R1} = \sqrt{2/3}\left[\tan^{-1}(2\pi a/w)\right]^{3/2}. \tag{3.16}$$

Equation 3.16 shows that profile roughness increases nonlinearly as the wavelength (w) decreases or amplitude (2a) increases. Comparing this to Equation 3.13 shows that, geometrically, a sinusoidal profile has a larger range of roughness values than does a symmetric triangular profile.

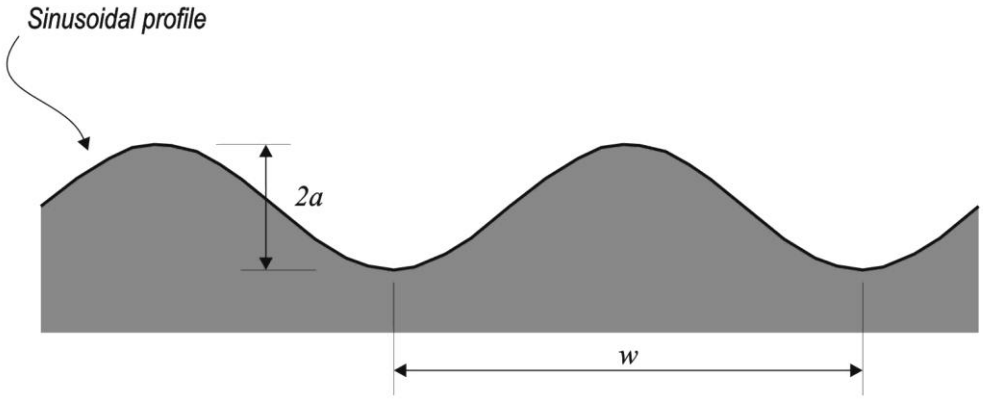


Figure 3.30 Geometrical features of a sinusoidal profile (Rasouli, 2002).

This is because the maximum deviation of unit normal vectors to a sinusoidal profile is larger than that of a symmetric triangular profile of equivalent aspect ratio. A profile with sinusoidal asperities was simulated in PFC2D shear test model. Similar to triangular profiles, here we assume constant asperity wavelength, so by increasing the asperity amplitude, the effect of fracture profile roughness in shearing behaviour to be investigated. Simulation of sinusoidal profiles was carried out for different aspect ratios (i.e. $2a/w$) under normal stresses of 1.0, 3.0, and 5.0 MPa, respectively. Figure 3.31 shows the results corresponding to two different aspect ratios and at 1.0 MPa normal stress. In this figure, the results of a symmetric triangular profile with similar aspect ratios are shown for comparison purposes.

The results given in Figure 3.31 indicate that in general shear strength of profiles increases as profile aspect ratio increases. It is observed that both shear and tensile cracks in both profile geometries develop at almost similar locations, however sinusoidal profiles exhibit larger shear strength as well as more damages comparing to triangular profiles. This, from a mechanical point of view, is perhaps due to the larger surface exposed in shearing a sinusoidal profile than that of a triangular profile. Figure 3.32 shows a comparison between shear strength of synthetic triangular profiles with 30° base angle (dashed line) and the corresponding sinusoidal profile with aspect ratio of 0.288 (solid line).

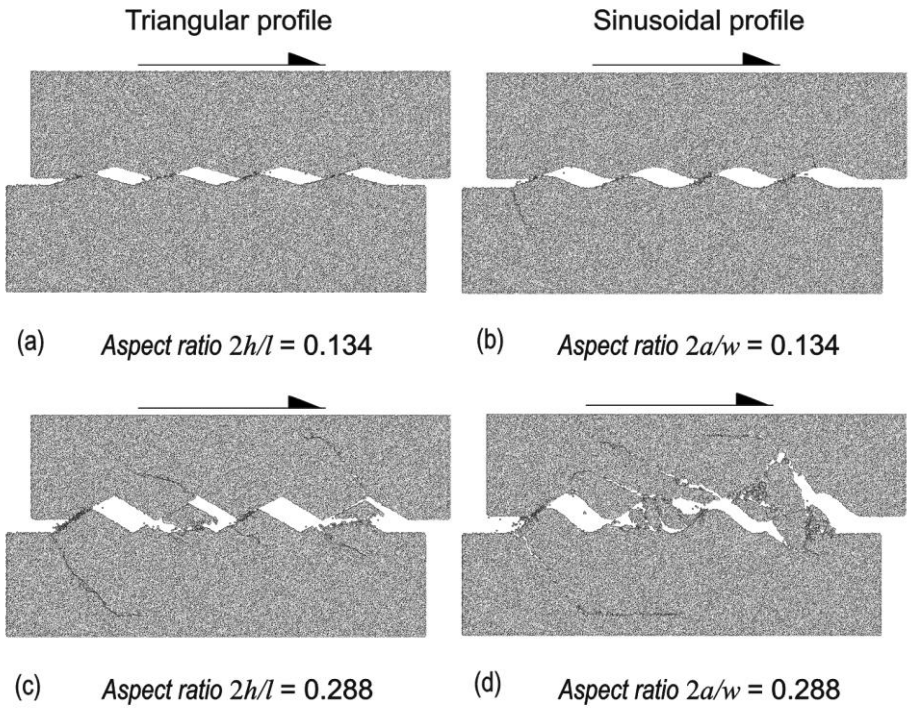


Figure 3.31 Comparison between shearing response of a synthetic triangular (a and c) and a sinusoidal (b and d) profiles under 1.0 MPa normal stress.

A considerable difference between peak shear stress of these profiles is observed which is likely to be due to the effect of the shape of asperities, as explained before. Also, as previously mentioned, by increasing profile roughness, post-peak shear behaviour varies considerably and this is also the case here: in Figure 3.32, the residual shear strength changes from about 0.5 MPa for a triangular profile to approximately 3.0 MPa for a sinusoidal profile. Figure 3.2 also indicates the effect of normal stress on fracture shear strength and asperity failure. It is interpreted from the plot that the shearing behaviour of sinusoidal profiles is fairly similar to the corresponding triangular profiles, with the only difference of that sinusoidal profile fractures exhibit larger peak and perhaps post peak shear strengths than that of triangular profile fractures.

Table 3.4 shows the comparison between $D_{R1}$ values obtained for simulated profiles together with peak and residual shear stresses. It is seen that peak and post-peak shear stresses as well as corresponding $D_{R1}$ are larger for sinusoidal profiles, as explained earlier. It is interesting to note the profiles behave similarly in pre and post-peak state of stress. This shows that the appearance of sharp asperities along the fracture profile will reduce the peak and residual shear strength significantly. This also can be applied in differentiating between shear behaviour of hammered and corrugated surface fractures: a hammered fracture is less prone to have spiky and sharp asperities than a corrugated surface.

Table 3.4 Comparison of roughness and shear strength of a triangular and sinusoidal profile.

| Fracture ID | Property | Peak shear stress (MPa) | Residual shear stress (MPa) | $D_{R1}$ |
|---|---|---|---|---|
| Triangular profile | θ=30° , $2h/l$ = 0.288 | 6.0 | 0.45 | 0.280 |
| Sinusoidal profile | $2a/w$ = 0.288 | 7.3 | 2.10 | 0.515 |

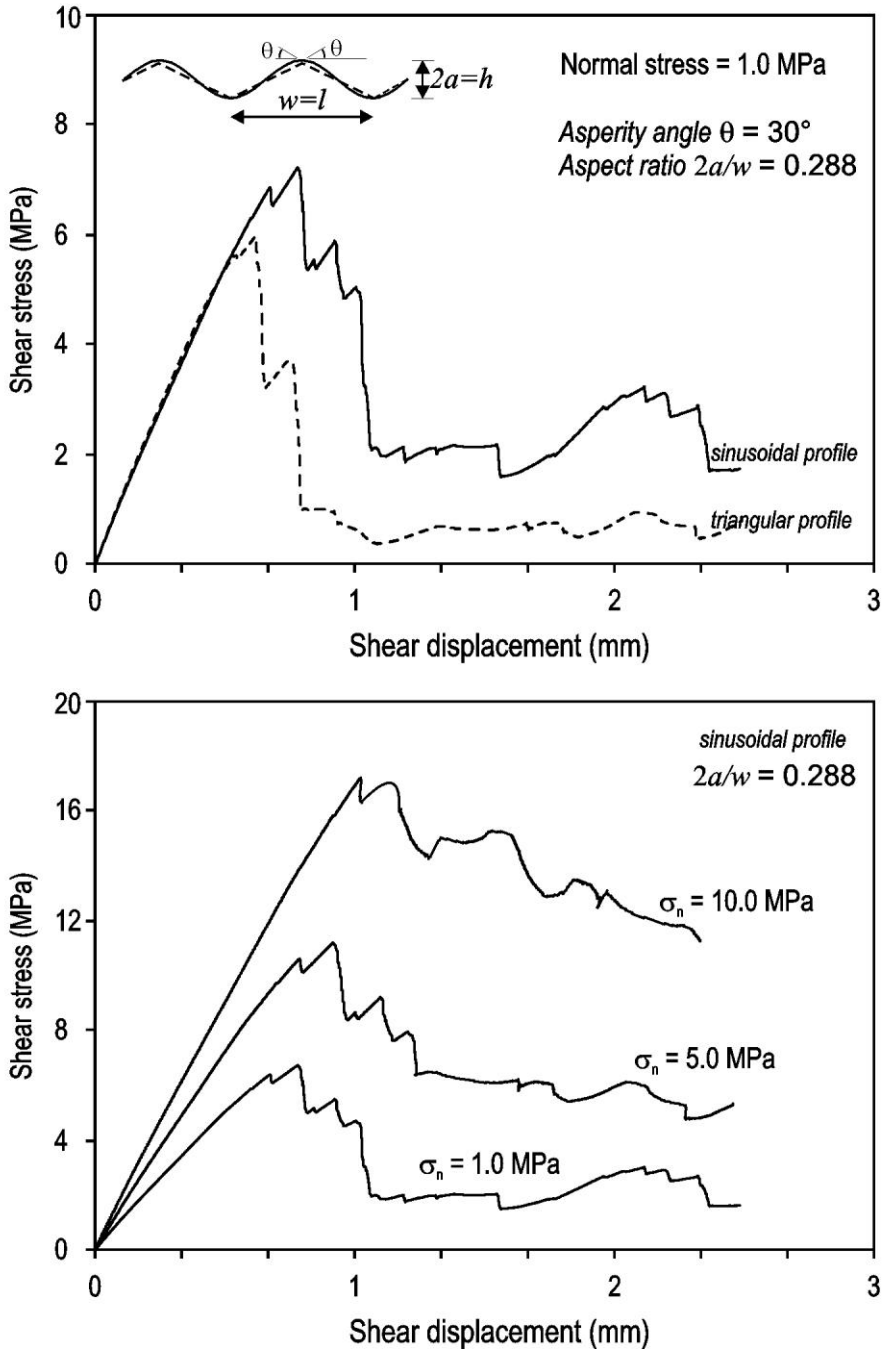


Figure 3.32 Comparison between shear strength of synthetic triangular (a and c) and sinusoidal (b and d) profiles under 1.0 MPa normal stress.

The above results obtained from PFC2D simulation confirm that sinusoidal profiles shows a larger range of roughness values than does a corresponding symmetric triangular profile. This demonstrates why $D_{R1}$ is thought to be a good representative parameter for profile roughness, as $D_{R1}$ is larger for a sinusoidal profile than a symmetric triangular profile with similar symmetry ratio.

### 3.5.4 Randomly generated profiles

To assess the applicability of $D_{R1}$ in estimation of fracture shear strength of more complex geometries, number of profiles was generated using a simple linear random generation algorithm. The width of profiles is 10 cm and asperities' amplitude varies between 0.0 and 0.5 cm. Generated profiles (named A to J) are shown in Figure 3.33 with the corresponding $D_{R1}$ value calculated using ($x$,$y$) coordinate data of profiles.

In general, $D_{R1}$ is estimated from the statistical analysis of normal unit vectors corresponding to a rock fracture profile extracted at a given scale (see Section 2.1.3).

From Figure 3.33 it is seen that profiles A to E consist of ten asperities, where profiles F to J consist of five asperities. The symmetry ratio ($l_1/l_2$) for all 10 profiles was assumed 3, which allows studying the fracture shear strength directionality.

Observationally, $D_{R1}$ of profiles with 10 asperities are expected to be larger than those with 5 asperities (profiles F to J). This is perhaps due to having large asperity wavelength for profiles F to J which results in smaller asperity base angles than that of profiles A to E. Accordingly, assuming that a correlation exists between profile roughness and shear strength, the shear strengths of profiles A to E are expected to be larger than those of profiles F to J.

PFC2D numerical simulations were performed using the fracture shear box explained earlier. All the model micro-properties and corresponding macro-properties are the same as those used for simulations of synthetic profiles (see Table 3.2).

The simulations performed in opposite directions to investigate direction dependency in shear strength estimation. Three different normal stresses of 1, 5, and 10 MPa were used to capture different failure mechanisms. Similar to a symmetric profile, 3 mm shear displacement allowed a complete observation of the shear response throughout to the post-peak region. The results of simulations are discussed below.

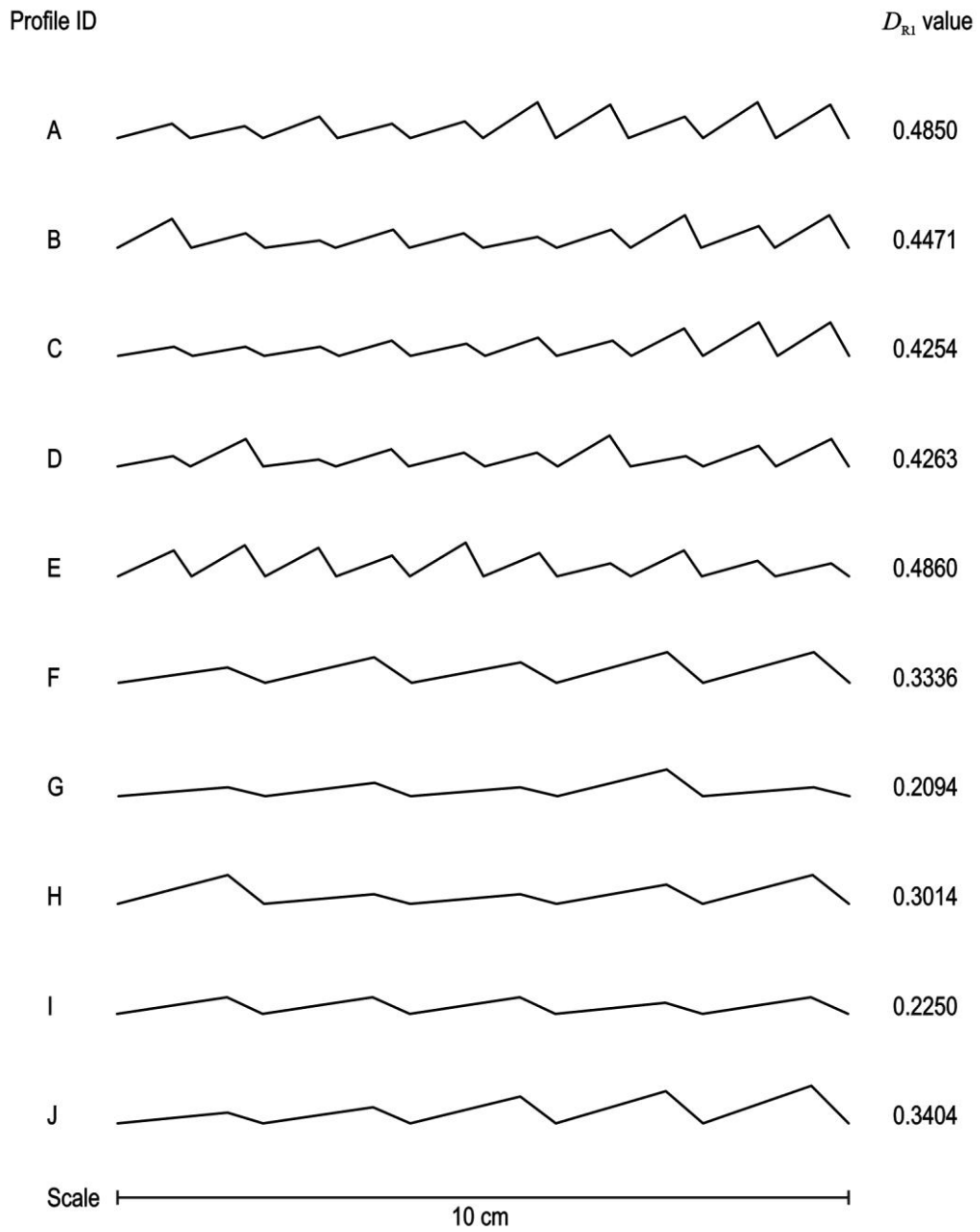


Figure 3.33 Randomly generated profiles with different $D_{R1}$ values. Profile's projected length is 10 cm.

Figure 3.34 shows the view of profiles A to E after being sheared at 1.0 MPa normal stress. Profiles on the left column correspond to left to right shearing (LR direction), whereas on the right column the results of shearing from right to left (RL direction) are shown. In both cases, upper block moves over the lower block with a constant shear rate applied to the model while lower block is fixed.

From Figure 3.34 it can be seen that in shearing profiles A and C form left to right, profile C which have less harsh asperities in the direction of shearing exhibits lesser shear resistance than that of profile A.

It is noted that 1.0 MPa normal stress is not large enough to develop tensile cracks through intact sample as is seen in most cases given in Figure 3.34.

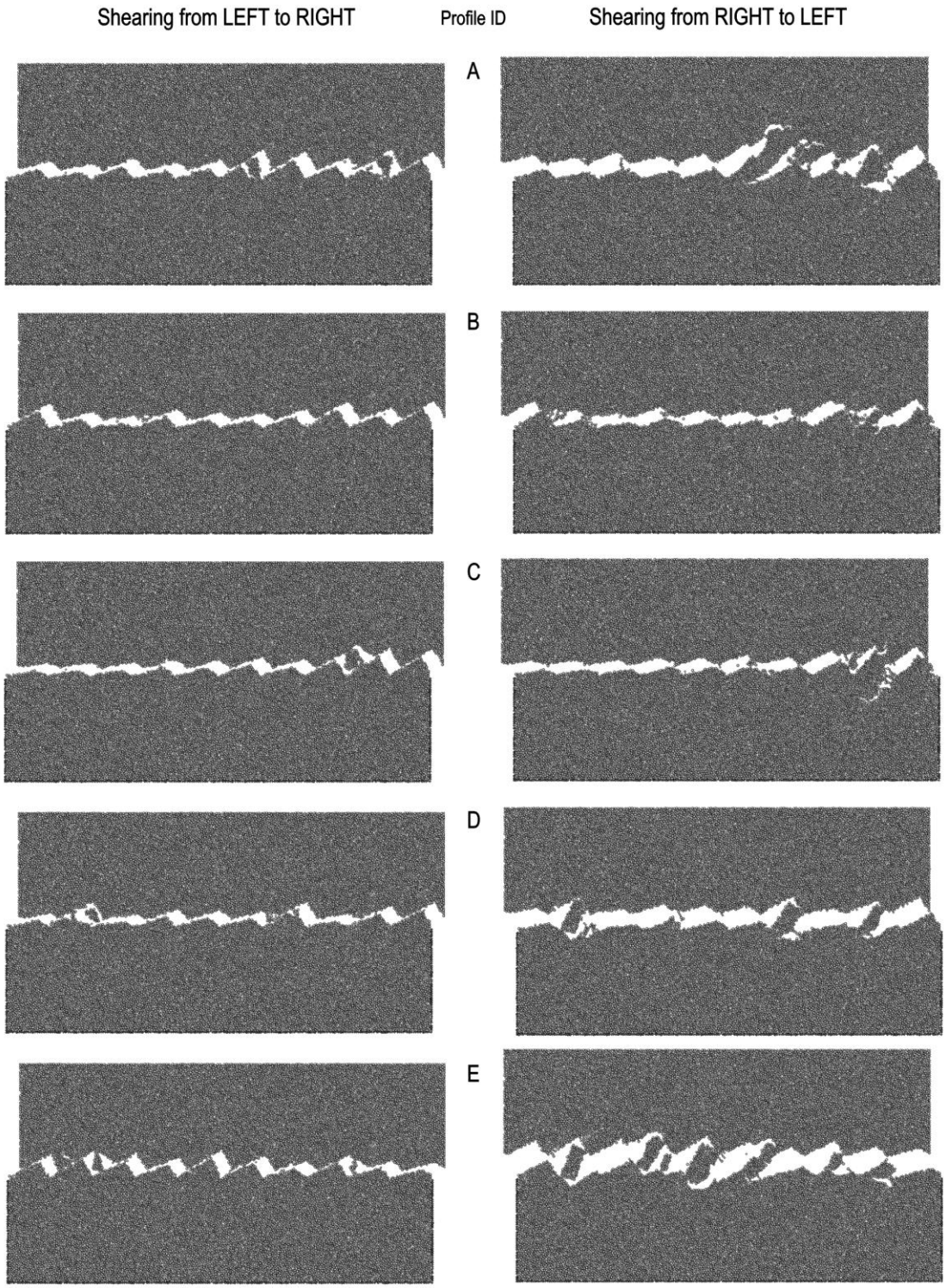


Figure 3.34 View of sheared samples (profiles A to E) in PFC2D fracture shear test box under 1.0 MPa normal stress.

Significant differences are obtained between the results of profiles shearing in two different directions (i.e. LR and RL) illustrating the directional dependency of fracture shear strength. Shear strength of fracture profiles is much higher when they are sheared from right to left, as expected. As stated, every single asperity along the profile has the symmetry ratio ($l_1/l_2$) of 3 which causes severe directionality to profiles' shear

strength. This can be quantified by measuring the average mean angle of asperity's left and right chords ($\theta^+$ and $\theta^-$), respectively. Furthermore, asperity damage is observed in profiles A and C when sheared from right to left and the extent of damage can be traced by recording the data at different shear displacements. Asperity cut-off is also observed in profiles D and E where the high angle asperities are located against the shearing direction.

Figure 3.35 shows the curves of shear stress versus shear displacement for profiles A to E and for shearing from left to right. Similar results for shearing in opposite direction are given in Figure 3.36. From these figures it appears that profiles are sheared more easily in the LR shearing direction than that of RL direction since the values obtained for fracture shear strength is larger in LR direction.

Considering the post-peak behaviour of factures, it is understood that when shearing in RL direction (Figure 3.36), the majority of shearing energy is spent on developing the tensile cracks at asperities doglegs and propagating them through the fracture or even the intact rock. This increases the residual shear strength of these fractures in comparison with those sheared in LR direction (Figure 3.35). Also by comparing the shear stress versus shear displacement curves of profiles A to E in LR direction, it is seen that those with higher asperity amplitudes result in larger residual shear strengths (e.g. profile D): this is important when comparing the peak and post-peak shear behaviour of rough fractures.

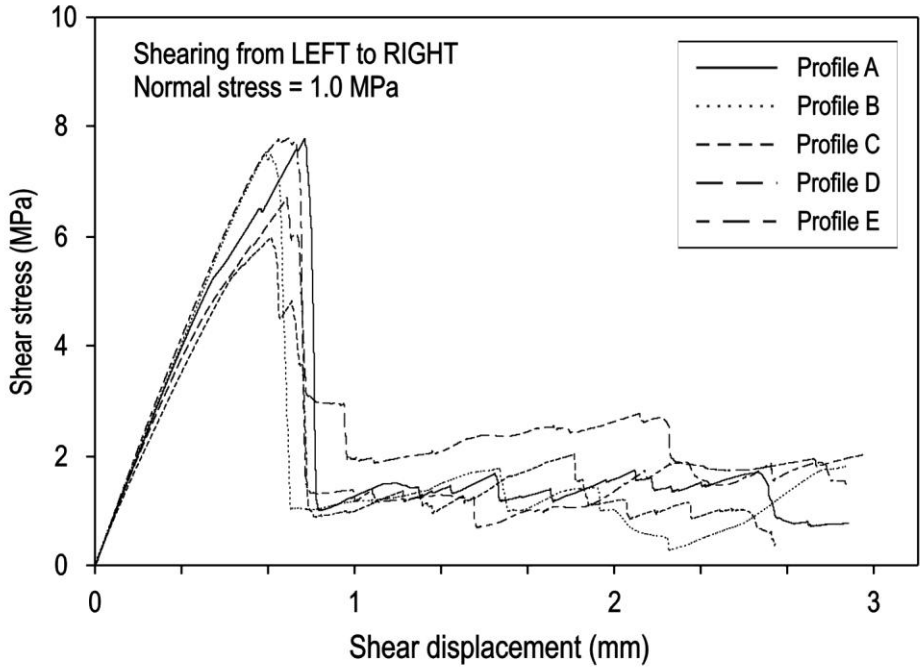


Figure 3.35 Shear stress versus shear displacement curves for profiles A to E simulated at 1.0 MPa normal stress: shearing from left to right.

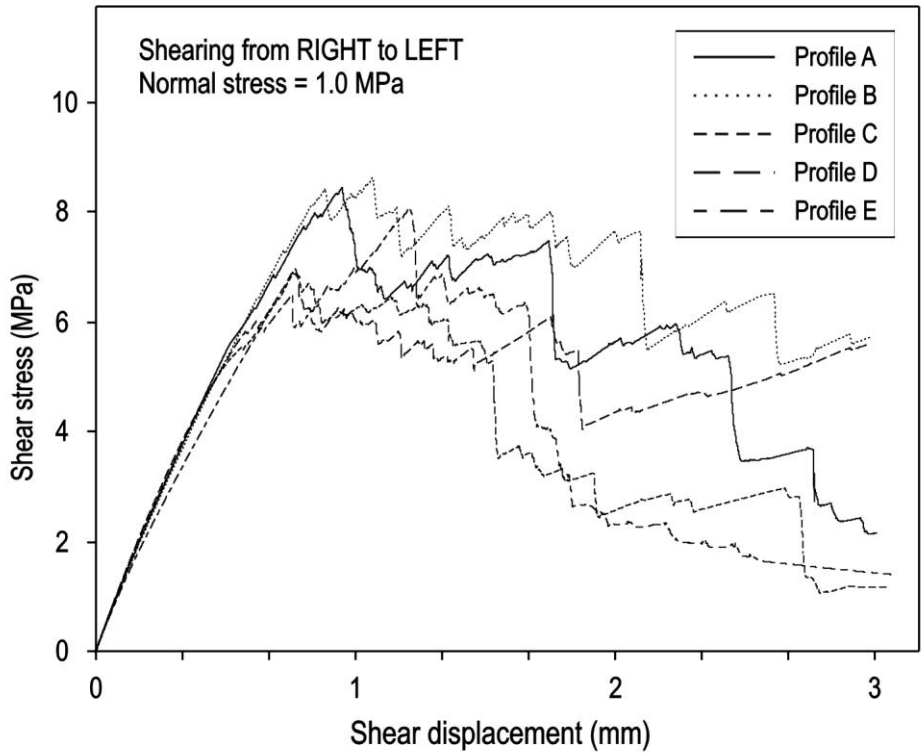


Figure 3.36 Shear stress versus shear displacement curves for profiles A to E simulated at 1.0 MPa normal stress: shearing from right to left.

From Figure 3.36 is seen that when profile E is sheared in RL direction, it has large peak shear stress and small residual shear stress in comparison with other profiles. As stated before, the difference between peak and residual shear stresses is considered as fracture cohesion ($C_f$).

Figure 3.37 shows profiles F to J after being sheared under a normal stress of 1.0 MPa, with samples sheared from left to right direction shown on the right column. Shearing in both directions results in the upper block moving over the lower block with an applied constant shear rate and while the lower block is fixed.

The major difference between the shearing response of profiles A to E and profiles F to J is the effect of number of asperities along each profile (i.e. 10 for profiles A to E and 5 for profiles F to J). Firstly, it is seen that less asperity breakage and cut-off occur in profiles shown in Figure 3.37. This is perhaps due to the decrease in number of asperities which may result in reduction of surface roughness and shear strength.

Generally, magnitude and extent of asperity damage in profiles F to J is much less than that of profiles A to E (compare Figures 3.34 and 3.37). Figure 3.38 shows the curves of shear stress versus shear displacement for profiles F to J when they are sheared in LR (top) and RL (bottom), respectively. From this figure it is seen that the peak shear stresses are smaller comparing to profiles A to E with 10 asperities.

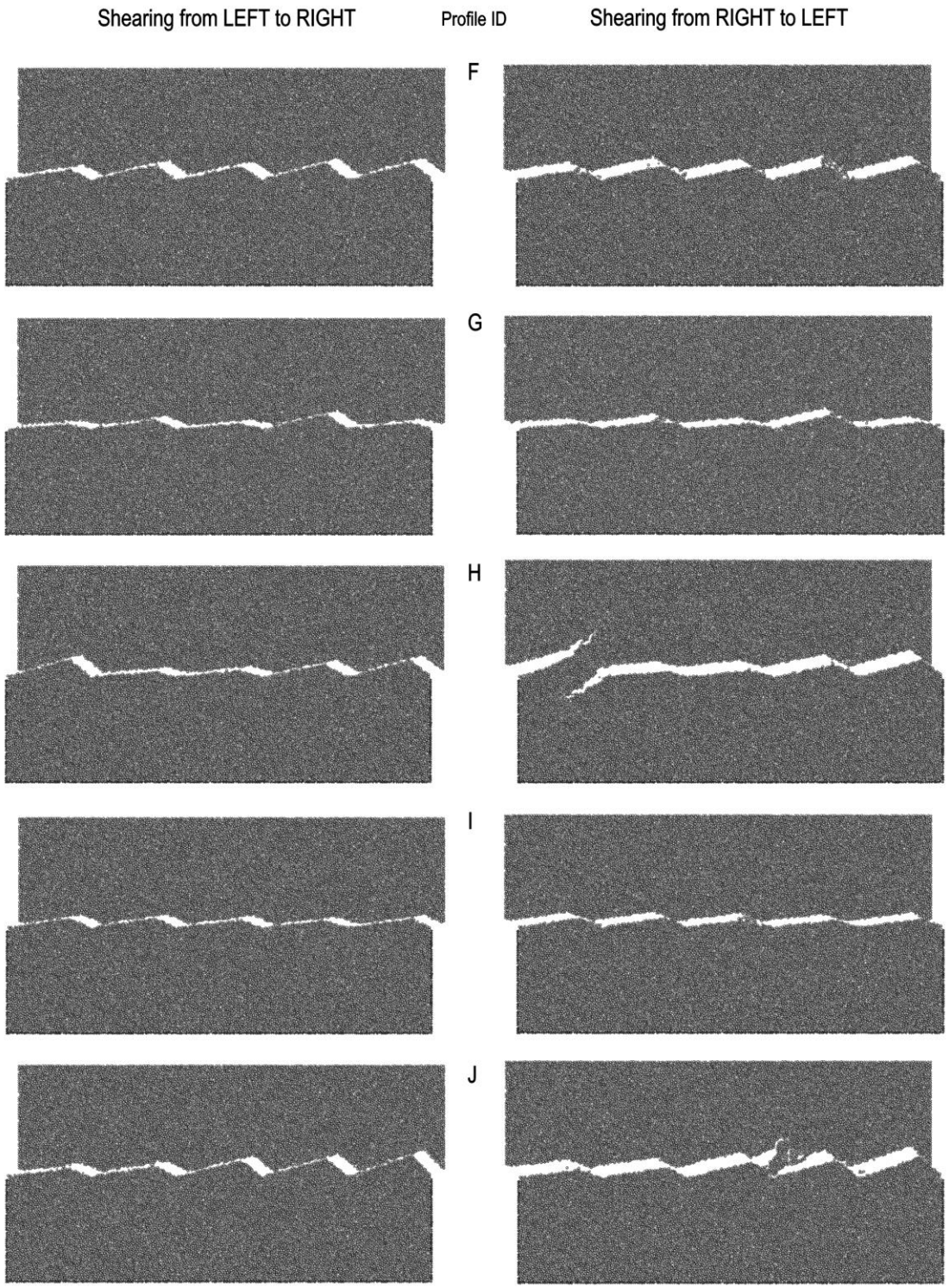


Figure 3.37 View of sheared samples (profiles F to J) in PFC2D fracture shear test box under 1.0 MPa normal stress.

This demonstrates that profile roughness increases as the asperity wavelength decreases (or say asperity amplitude increases). Larger wavelengths results in a more flat and planar profile, which in turn reduces the shear strength (compare Figures 3.35 and 3.38). It is interesting to note that the peak shear stress of profiles A to J follows a similar trend as profiles' $D_{R1}$ values listed in Figure 3.33: this correlation will be discussed in this Section.

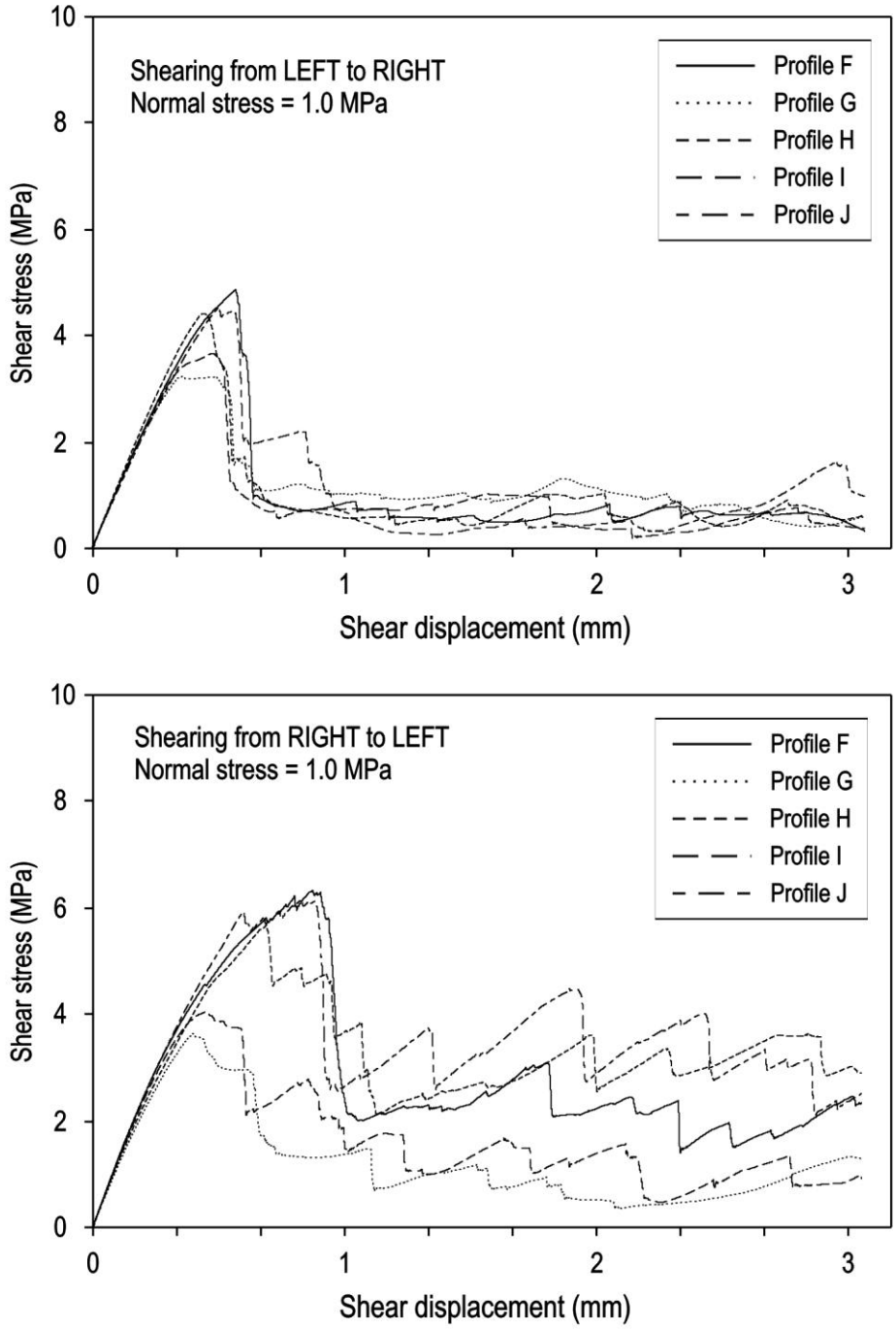


Figure 3.38 Shear stress versus shear displacement curves for profiles F to J simulated at 1.0 MPa normal stress: shearing from left to right.

Comparing the shear stress versus shear displacement curves of all profiles (A to J) when are sheared in RL direction (Figures 3.36 and 3.38, bottom), it is seen that the residual shear strength of profiles with 10 asperities is much higher than those with 5 asperities. Comparing shear stress versus shear displacement curves, profiles A to E do not show a large reduction when they transit from peak to the residual stress level. However, this transition occurs with a noticeable reduction for profiles F to J. This difference is most likely as a result of the first set of profiles having larger number of

asperities. This shows how the existence of large amplitude asperities (corresponding to larger number of asperities) increases the residual shear strength. Similar to profiles A to E, profiles F to J show directional dependency in their shear strengths, however, this appears to be more significant for rougher profiles, i.e. A to E as the difference between their peak shear strength in opposite directions are larger.

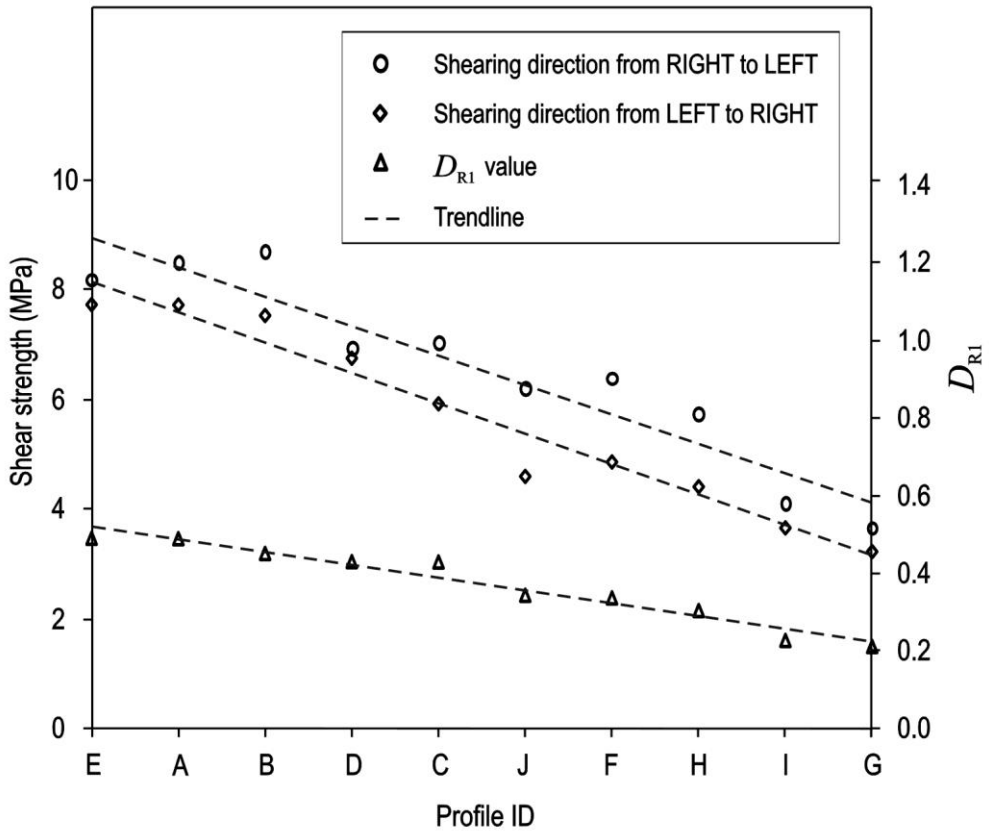


Figure 3.39 Shear strength of profiles A to J in both directions together with profiles' $D_{R1}$values.

In Figure 3.39, the shear strengths of profiles A to J obtained in both directions are shown. The shear strengths are ordered according to their $D_{R1}$ values, which is also plotted in this Figure. The results demonstrate how shear strength is a function of profile geometry or roughness. A linear correlation fits the data, however small fluctuations are observed.

In Figure 3.40, profiles A to J are shown where they are ordered from roughest to the smoothest from top to bottom. As is seen from this figure, $D_{R1}$ decreases from 0.4860 corresponding to profile E (here the roughest profile) to 0.2094 corresponding to profile G (the smoothest profile). Visual comparison of profiles in Figures 3.40 also verifies that the general trend obtained from PFC2D simulations and $D_{R1}$ analyses are in very good agreement. This analysis demonstrates the applicability of $D_{R1}$ in estimation of fracture shear strength. In the next Section correlations are developed between $D_{R1}$and shear strength of a simple symmetric triangular profile.

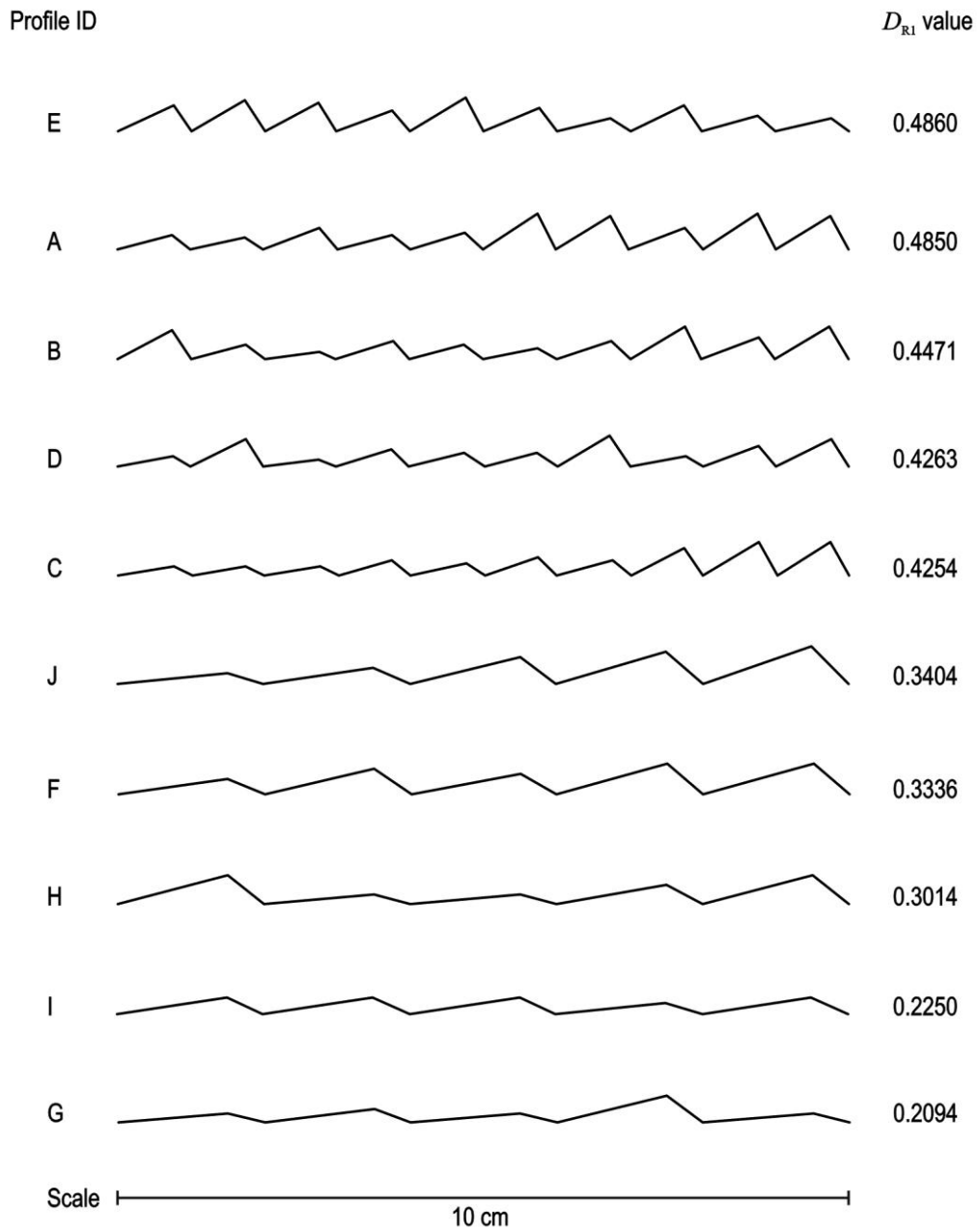


Figure 3.40 Profiles A to J ordered according to their corresponding $D_{R1}$.

## 3.6 Correlating fracture profile $D_{R1}$ and shear strength

As stated before, the objective of this study is to incorporate the effect of profile roughness, which is characterised using $D_{R1}$ parameter, in the calculation of profile shear strength. This is ultimately believed to be an approach to be used in estimating the shear strength of fractures instead of performing costly and time consuming physical tests in the lab. In this Section, correlations between $D_{R1}$ and shear strength of a simple symmetric triangular profile are developed. Similar approach can be used for other profile geometries.

To express the shear strength in terms of profile asperity angle we use a parametric cubic spline curve. In the mathematical field of numerical analysis, cubic spline fitting is a form of interpolation where the interpolant is a special type of piecewise polynomial called a spline.

In parametric from, cubic splines are expressed by start point ($p_1$), end point ($p_2$), and control as many as control points (here two control points ($cp_1$ and $cp_2$) which lie between start point and end point (Figure 3.41). Between the start point $(x_1, y_1)$ and end point $(x_2, y_2)$ spline curves may be expressed as (Piegl and Tiller, 1997):

$$\begin{aligned} X &= Ax_1 + Bx_{p1} + Cx_{p2} + t^3 x_2 \\ Y &= Ay_1 + By_{p1} + Cy_{p2} + t^3 y_2 \end{aligned} \tag{3.17}$$

where $(x_{p1}, y_{p1})$ and $(x_{p2}, y_{p2})$ are two control points that determine the shape of the spline curve. The coefficients $A$, $B$ and $C$ are given by

$$A = -t^3 + 3t^2 - 3t + 1,\ B = 3t^3 - 63t^2 + 3t,\ C = -3t^3 + 3t^2 \tag{3.18}$$

where $0 \le t \le 1$.

In Section 3.4.1, we plotted peak shear stress versus normal stress for symmetric triangular profiles with asperity angles of 15, 30, and 45 degrees, based on the PFC2D simulation results. The normal stresses corresponding to the point at which fracture shear strength curves intersects the intact rock material, $\sigma_n|_{\alpha=0}$, for three mentioned synthetic profiles, were calculated analytically and verified by simulations (see Table 3.3). $\sigma_n|_{\alpha=0}$ is used as the end point of cubic splines. In the following, parametric cubic splines are to be fitted to the data plotted in Figure 3.24. To do that, we use the following assumptions:

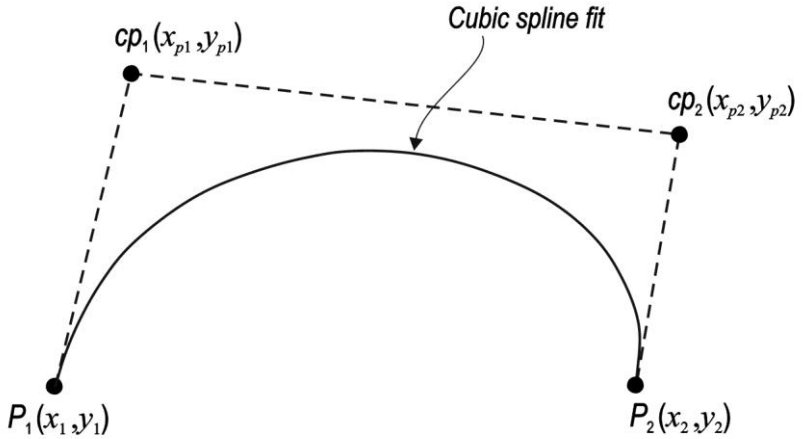


Figure 3.41 Schematic of parametric cubic spline with four points.

- The fracture is assumed to have no cohesion and hence the start point is at the origin, i.e. $(x_1, y_1) = (0,0)$.
- The end point $(x_2, y_2)$ is where the shear strength curve meets the intact rock criterion, and determined using Equation 3.15 and the peak strength criterion of the intact rock (i.e. $\tau = c + \sigma_n \tan\phi$) as

$$(x_2, y_2) = \left( c(\cot D_{R1} - \tan\phi)\cos^2\phi,\, c\left( \cos^2\phi + \frac{\sin 2\phi}{2\tan D_{R1}} \right) \right). \tag{3.19}$$

- The tangent vector at the origin is vertical, so the first control point takes a general form of $(x_{p1}, y_{p1}) = (0, y_{p1})$.
- The second control point is $(x_2, y_2) = (0, y_{p2})$, where the value of $y_{p2}$ is equivalent to the cohesion ($c$) of the intact rock. This ensures that all curves are tangent to the intact rock criterion at their intersection with this curve.

Together, these assumptions show that the only variable controlling the fit of the cubic spline to the results of the numerical analysis is the position of the first control point, i.e. $y_{p1}$.

The mechanical properties of the rock (cohesion and friction angle, $c$ and $\phi$) and the roughness angle ($\theta$, which is $D_{R1}$ for a symmetric triangular profile) are other factors in the calculations.

For any particular value of $D_{R1}$, it is straightforward to identify the value of $y_{p1}$ that gives the best fit spline to the numerical analysis output. The results of this are given in Figure 3.42, and show that cubic splines fit the data well. The values of $y_{p1}$ corresponding to the $D_{R1}$ values of 0.262, 0.523 and 0.785 are -2, 1 and 8, respectively. These results lead to the relation

$$y_{p1} = 29.18 D_{R1}{}^2 - 11.46 D_{R1} - 1, \tag{3.20}$$

which has a coefficient of determination close to unity.

The assumptions listed above, together with Equation 3.20, means that Equations 3.17 can be written as

$$\begin{aligned} \sigma_n &= ct^3(\cot D_{R1} - \tan\phi)\cos^2\phi \\ \tau &= (3t^3 - 6t^2 + 3t)(29.18 D_{R1}{}^2 - 11.46 D_{R1} - 1) + 3ct^2(1-t) + ct^3\left( \cos^2\phi + \frac{\sin 2\phi}{2\tan D_{R1}} \right) \end{aligned} \tag{3.21}$$

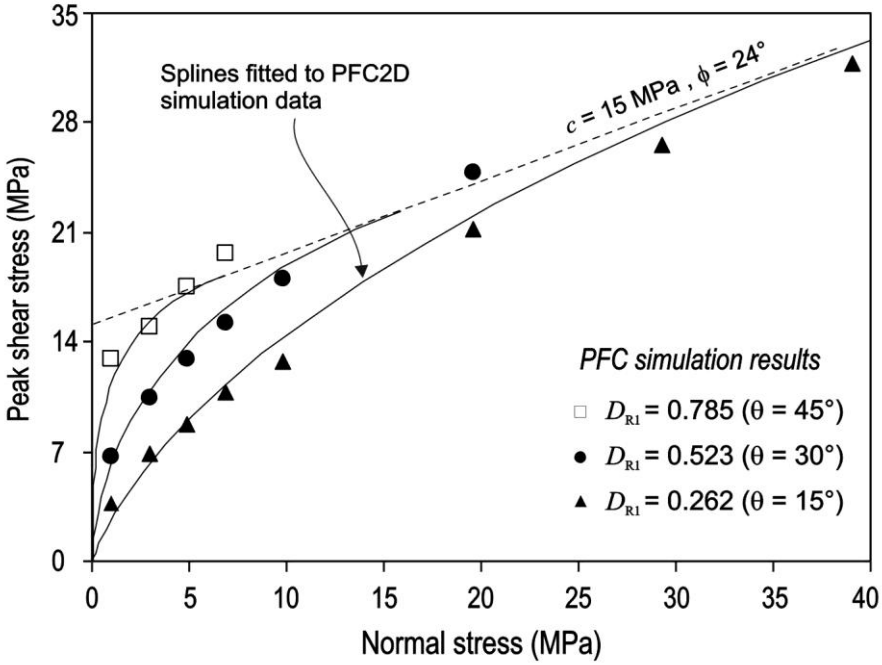


Figure 3.42 Cubic splines fitted to the shear strength data of symmetric triangular profiles obtained from PFC2D simulations.

which allow an estimated shear strength curve to be produced for other profile asperity angles. Similar methodology will be used to estimate the shear strength of rock fracture profiles, as is discussed in the next Section.

## 3.7 Analysis of rock fracture profiles

Several rock fracture profiles were simulated using PFC2D to study their shear behaviour and then investigate the possible correlation between $D_{R1}$ and profile's shear strength.

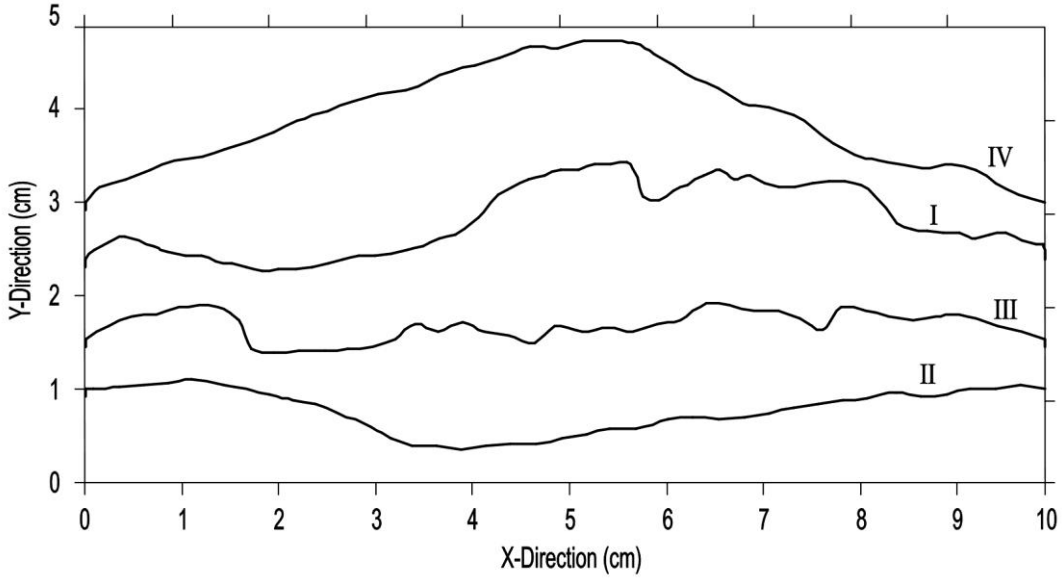


Figure 3.43 Geometry of rock fracture profiles (I to IV) after Rasouli and Harrison, 2010.

Here the results of analysis of four rock fracture profiles (profiles I to IV, after (Rasouli, 2002) whose geometries are shown in Figure 3.43 are reported. $D_{R1}$ for these profiles, which were estimated numerically at a sampling size of close to zero, are 0.3612, 0.1911, 0.3404 and 0.3543 for profiles I to IV, respectively (see Figure 3.43). According to $D_{R1}$ values profile I is expected to be the roughest with highest shear strength and profile II the smoothest with the lowest shear strength amongst these four fracture profiles. Close shear strength is expected for profiles I and IV based on $D_{R1}$ comparison of these profiles.

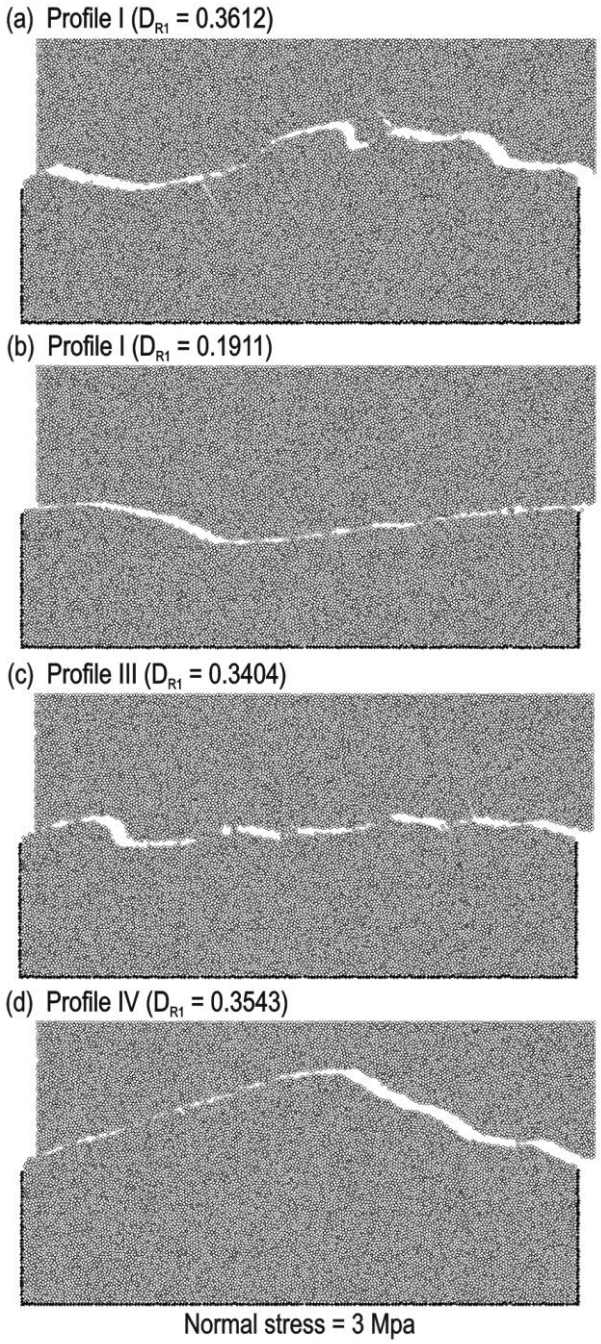


Figure 3.44 Visual comparison of shearing progress of rock fracture profiles (I to IV) with different roughness ($D_{R1}$) at 3.0 MPa normal stress modelled in PFC2D.

PFC2D shear test model was used to simulate shear behaviour of these profiles. Fracture profiles (I to IV) were modelled in a shear box with the same specifications and micro-properties applied to synthetic profiles (see Table 3.2). Simulations were performed at different normal stresses to produce the curve of peak shear stress versus normal stress. Figure 3.44 shows profiles after shearing at a 3.0 MPa normal stress. Similar to the simulation results of synthetic profiles, it was observed that by increasing the normal stress, asperity damage increases and the chance for sliding decreases.

Interestingly it was found that $D_{R1}$ shows an ascending trend with increasing profiles' shear strength: this shows possible correlations between $D_{R1}$ and shear strength for these rock fractures. Figure 3.45 shows peak shear stress versus shear displacement for profiles I to IV. It is seen that as profile roughness ($D_{R1}$) increases, peak shear stress increases. There are fluctuations in residual shear stress of fractures and the trend observed for peak shear stresses of profiles I to IV, is not seen here. This can be due to the major differences between waviness (or say bumpiness) of the fracture profiles which has longer lasting effects (that can be extended to the post-peak region) on shear behaviour of fractures than that of roughness.

The shear strength of profiles was also estimated at different normal stresses. Figure 3.45 shows that shear strength increases as both profile roughness ($D_{R1}$) and normal stress increase. Similar to synthetic profiles, cubic splines were fitted to simulation data as shown to be the best possible fits.

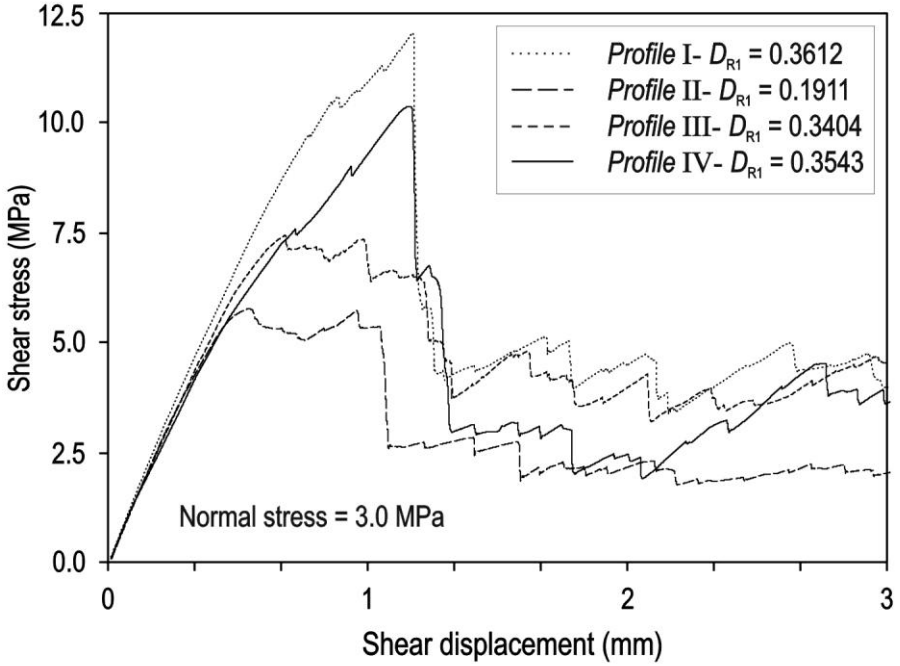


Figure 3.45 PFC2D simulation of rock fracture profiles (I to IV) with different roughness ($D_{R1}$) at a 3 MPa normal stress.

To determine the end points of cubic splines a simplified approach based on analytical solutions developed for symmetric triangular profiles was utilised. Base angle θ of a symmetric triangular profile, corresponding to $D_{R1}$ of each rock profile, was calculated and then Equation 3.15 was used to determine the end point of splines. The values of $y_{p1}$ corresponding to $D_{R1}$ values of 0.1911, 0.3404 and 0.3612 are -3, 0 and 7, respectively. These results lead to

$$y_{p1} = e^{(57.94 D_{R1} - 18.624)} - 3.008, \tag{3.22}$$

Substituting this equation in Equation 3.17, shear strength curve corresponding to rock fracture profiles with different $D_{R1}$ could be produced. Applying the same procedure as used for symmetric profiles and employing Equation 3.17, the shear strength curve corresponding to a fracture with roughness $D_{R1}$ and corresponding intact rock properties of $c$ and ϕ for range of normal stresses can be estimated as:

$$\begin{aligned} \sigma_n &= ct^3\left(\cot D_{R1} - \tan\phi\right)\cos^2\phi \\ \tau &= \left(3t^3 - 6t^2 + 3t\right)\left(e^{(57.94 D_{R1} - 18.624)} - 3.008\right) + 3ct^2(1-t) + ct^3\left(\cos^2\phi + \frac{\sin 2\phi}{2\tan D_{R1}}\right) \end{aligned} \tag{3.23}$$

which is similar to the Equation 3.21 obtained earlier for synthetic profiles; the only difference is in control point 1 in which $y_{p1}$ is related to profile $D_{R1}$ based on Equation 3.22. Figure 3.46 shows the cubic splines obtained from Equation 3.23 fitted to peak shear strength data obtained from PFC2D simulations.

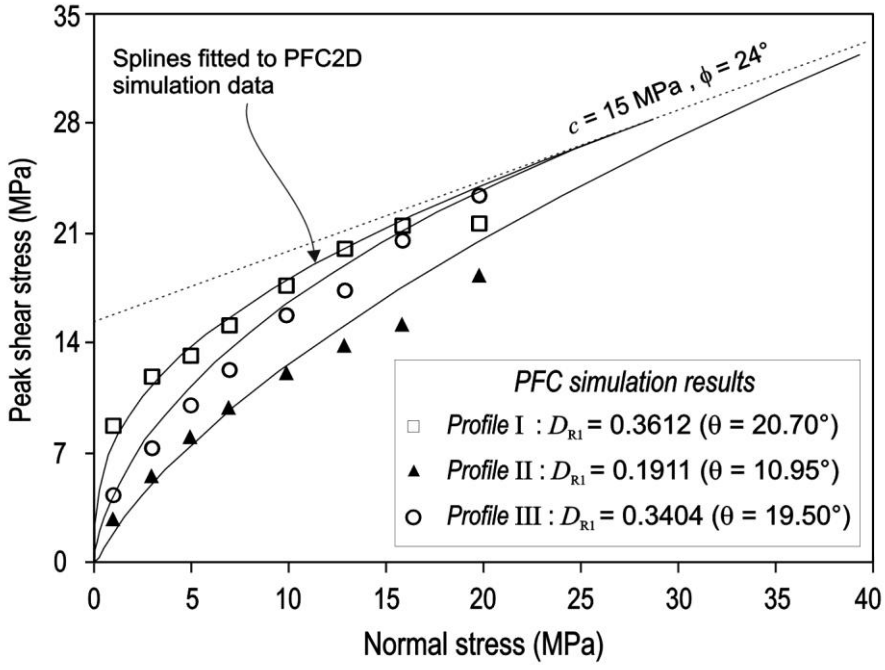


Figure 3.46 Cubic splines fitted to shear strength data of rock fracture profiles.

The analyses here showed that the fracture peak shear strength data are well fitted by cubic splines which in turn can be give good estimates of profile shear strength. Although the applicability of this correlation may be limited at this stage but it clearly indicates that $D_{R1}$ is a representative parameter to characterise profile roughness and could be employed in shear strength estimation of rock fractures.

## 3.8 Summary

The first part of this Chapter presented the theory of BPM which is implemented in PFC as a DEM based code. Then usefulness of using PFC2D in simulation of rock-like material was discussed and its shortcomings were addressed. This was followed by performing sensitivity analyses on PFC2D micro-properties to obtain corresponding macro-response of the model. Most influencing micro-parameters in PFC2D models including particle size, contact elasticity, ratio of contact normal to shear stiffness, and bond strength were analysed by performing several biaxial test simulations. Rock-like assembly's UCS and $E$ were determined based on biaxial test simulations and correlations were developed for different scenarios. Finally, a set of micro-properties corresponding to moderately strong material was selected and applied to fracture shear test simulations in all models used in this study.

Later, the PFC2D simulation scheme for fracture shear test was explained in detail. Effect of micro-roughness on ultimate shear behaviour of fractures was investigated by performing shear test simulations of synthetic fracture profiles. Fracture Particles friction coefficient was calibrated for smooth and rough fracture profiles and sensitivity of shear strength to this micro-parameter was discussed. Effects of intact material bond strength on asperity degradation during fractures shearing was analysed in detail. In addition, it was explicitly shown how PFC2D is capable of tracing the development of micro-cracks during fracture shearing at different normal stresses.

Accordingly, synthetic and rock fracture profiles were numerically simulated and direct shear tests were carried out using PFC2D. Effects of profile roughness, shearing direction, and normal stress on fracture shear strength and asperity degradation were thoroughly investigated. During fracture shearing, evolution of asperity degradation was visually and quantitatively presented and discussed based on the observed failure patterns. Peak and residual shear strength and failure mechanisms of the simulated fractures corresponded well to those reported in previous laboratory tests and analytical models, suggesting the feasibility of reproducing a fracture using BPM.

In the last part of this Chapter, roughness parameter ($D_{R1}$) was calculated for synthetic and four rock fracture profiles. It was found that in most cases, the values of peak shear strength estimated by PFC2D are well correlated with profile $D_{R1}$. Also, $D_{R1}$ was correlated to peak shear strength and parametric cubic splines were fitted to the data obtained from PFC2D simulations. Correlations were developed for both symmetric triangular and four rock fracture profiles.

The next Chapter presents the lab experiments carried out to simulate shear behaviour and asperity degradation of rough fracture surfaces.

# 4 Laboratorial fracture shear tests

Several lab studies have been reported on fracture shear tests. These are performed under constant normal load (CNL) or constant normal stiffness (CNS) loading conditions.

In this Chapter, modifications made on an existing true triaxial stress cell (TTSC) with the purpose of using it for shearing experiments of fracture surfaces under CNL conditions are explained.

The large loading capacity and large size cell of the TTSC together with the use of accurate hydraulic pumps capable of applying constant shear velocity are the main elements in this shearing device which allows experiments to be carried out on a wide range of fractures with different mechanical and geometrical properties. The results of a number of experiments performed on synthetic and rock-like fracture samples will be presented and compared with PFC2D simulation results.

## 4.1 Shear tests in the lab

The shear behaviour of rock fractures, which was simulated using DEM numerical method in this research study, can be experimented in the laboratory using a direct shear apparatus. Different direct shear test devices have been developed to study the effects of surface roughness on shear strength. These devices are mainly different in terms of their loading capacity and loading condition, i.e. under constant normal load (CNL) or constant normal stiffness (CNS). In CNL the normal load is maintained constantly during the shearing process (Barla et al., 2009; Hans and Boulon, 2003; Huang et al., 2002; Indraratna and Haque, 2000; Jafari et al., 2003; Jiang et al., 2004; Yang and Chiang, 2000). Shear testing under CNL boundary conditions is beneficial for cases such as non-reinforced rock slopes. In deep formations where the normal stress is extremely high, the shear behaviour of rock fracture is controlled by stiffness (shear and normal). In recent years, direct shear tests under CNS conditions have been shown to be more realistic for such cases.

Yang and Chiang (2000) studied progressive shear behaviour of composite rock fractures with two different triangle-shaped asperities (15 and 30 degrees) under CNL

condition. They studied the effects of asperity angle and base-length on the shear behaviour of fractures. They confirmed that the larger the asperity angle and base length, the large the fracture shear strength. Similarly, Huang et al. (2002) performed experiments on artificial fractures with regular triangle-shaped asperities with different angles under CNL conditions. They observed asperity sliding and cut-off mechanisms in their tests and developed a mathematical formula to estimate rough asperities shear strength (see Section 2.2.7). Jafari et al. (2003) simulated the effects of weak and strong earthquakes (active faults stimulators) and developed mathematical models for evaluating the shear strength of rock joints. They also performed different lab shear tests under CNL and CNS conditions and studied asperity degradation at low, intermediate, and high normal stresses. As a result of this work the number of loading cycles, stress amplitude, dilation angle, degradation of asperities and wearing were reported to be the main parameters controlling the shear behaviour of rock joints; these failure modes are reported within the shear experiments of the current study discussed in Section 4.4.

The current work introduces the modifications applied to a true triaxial stress cell (TTSC) in order to perform direct shear tests on fracture planes under CNL conditions. The TTSC was designed in 2009 to simulate the in-situ stresses in Geomechanics applications such as hydraulic fracturing and sand production. This cell allows vertical and two independent horizontal loads to be applied up to 315 KN in each direction on a 30 cm cube of rock (Rasouli and Evans, 2010).

The fracture shear cell (FSC) is the shearing device designed based on modifications of TTSC, and allows the fracture shear tests to be conducted under high normal and shear loads (maximum applied load is 315 KN). The normal load is kept constant during the fracture shear test using a duplex cylinder and the shear load is applied on a constant velocity using high pressure pumps when they perform under constant flow rates.

In this Chapter, after a description of the device, the results of the experiments carried out on synthetic and rock-like fractures will be presented. PFC2D numerical simulations are also carried out to compare to the lab results.

## 4.2 Description of the device

A top view of the TTSC is shown in Figure 4.1 where the horizontal stresses are applied independently through two sets of rams. The Linear variable differential transducer (LVDT) shown in this figure record the displacements of the ram. The normal stress is applied using the vertical ram after the top lid of the cell is in place. An

LVDT placed between the vertical ram and the top lid records the normal displacement if it occurs. The horizontal stresses are transferred to the sample, which is a cube of 30cm in size, through the internal plates. In order to ensure that the plates do not experience any bending or torsion forces during loading it is important that the sample is cut accurately in size and its sides are polished to be precisely parallel. This reduces the chance for asymmetric load distribution across the plates and therefore the sample. The maximum displacement of the rams is also limited to 2cm. This is adequate for direct shear experiments performed in the lab scale.

The pressure can be applied using hydraulic pumps with a maximum pressurisation capacity of 15000 Psi (see Figure 4.2.a). However, fluid injection is performed under a constant flow rate with a maximum capacity of 650 cc/hr using high pressure pumps, as shown in Figure 4.2.b. Four pumps are capable of the total constant flow rate of 2600 cc/hr when required. All loads and displacements are constantly monitored during the test. The data acquisition system shown in Figure 4.3.a receives the readings through different channels at the rate of one data per second (it is also adjustable) and transfers them into a monitoring PC, shown in Figure 4.3.b.

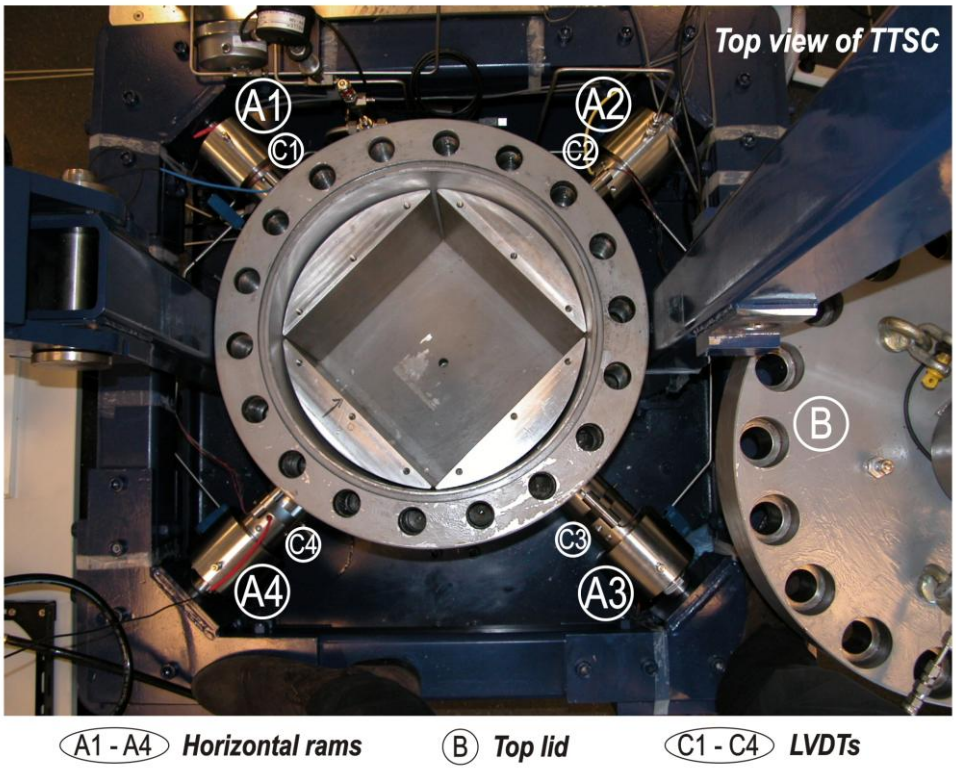


Figure 4.1 A top view of the TTSC where the horizontal stresses applied independently through two sets of rams; LVDTs are shown in each ram.

All the loads including horizontal and vertical are recorded with high accuracy by load cells located in the rams. Displacements are also recorded by five LVDTs

corresponding to the movement of each ram (four horizontal and one vertical); these are the major data recorded during the experiments. Furthermore, the cell can be sealed when the top lid is in place and this shows the unique capability of the cell which can be performed at saturated states (i.e. applying pore pressure).

In order to use the TTSC for fracture shearing experiments some modifications were applied, the details of which are described in this Section.

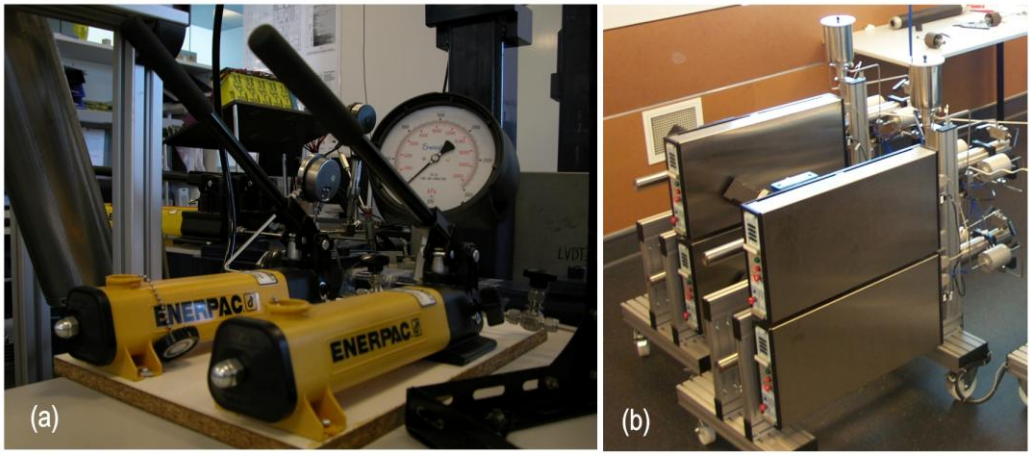


Figure 4.2 (a) Handy pumps for applying normal stress and (b) Automatic high pressure syringe pumps for applying constant shear rate.

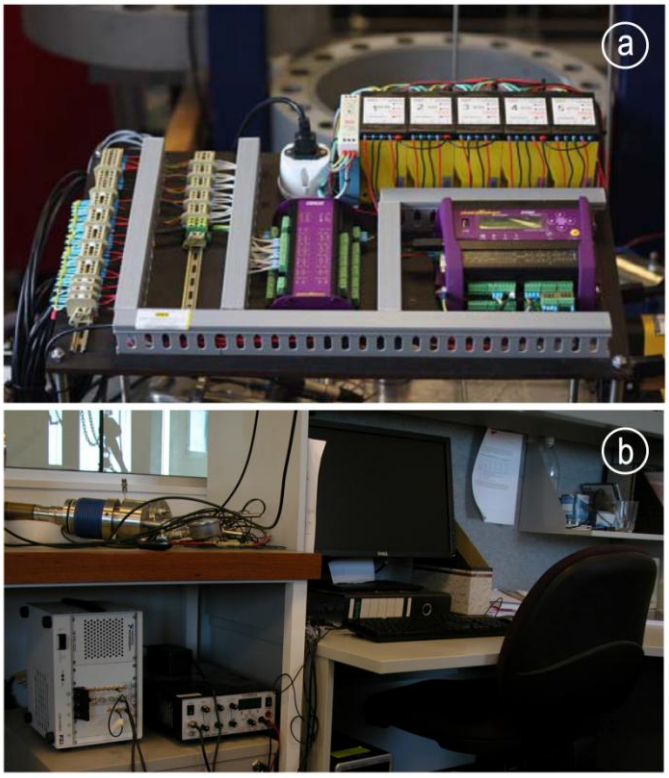


Figure 4.3 (a) Data acquisition system and (b) monitoring PC.

### 4.2.1 Fracture shear test configuration

Performing a fracture shear test using the TTSC requires only one horizontal ram to come into motion in order to shear the upper block of the shearing sample over the lower block, whereas the other three rams are kept stationary during the test. In order to achieve this requirement, based on the current design of the TTSC, a sample size of 20cm×15cm×10cm was adopted with a configuration similar to that shown in Figure 4.4. The shearing area of this sample is 150cm2 which enables the shear stress to be applied up to 21 MPa according to the maximum load capacity of the tool (315 KN).

In this figure, a synthetic sample having symmetric triangular asperities is shown. The specimen size can be adjusted further close to the boundaries of the stress cell to suit, but the chosen size was found to be adequate for the purpose of this study. This figure shows a number of rigid shims being placed around the sample to limit the lower block of shearing samples inside the cell and prevent it from any lateral, axial, and rotational movements.

The "T" shaped shim (labelled I in Figure 4.4) in the left of the sample transfers shear load to the upper block ensuring the load is applied to the centre of the plates. Shim II prevents a forward movement of the lower block during shearing. As seen from this figure the normal stress is applied to the sample through another shims sitting on top of the sample as a cap (shown as III). Also, in order to limit lateral movement of the lower block two shims are set on both sides of the sample with their height being lesser than the height of the lower block. This is depicted in Figure 4.4 where the perspective of the sample configuration is shown.

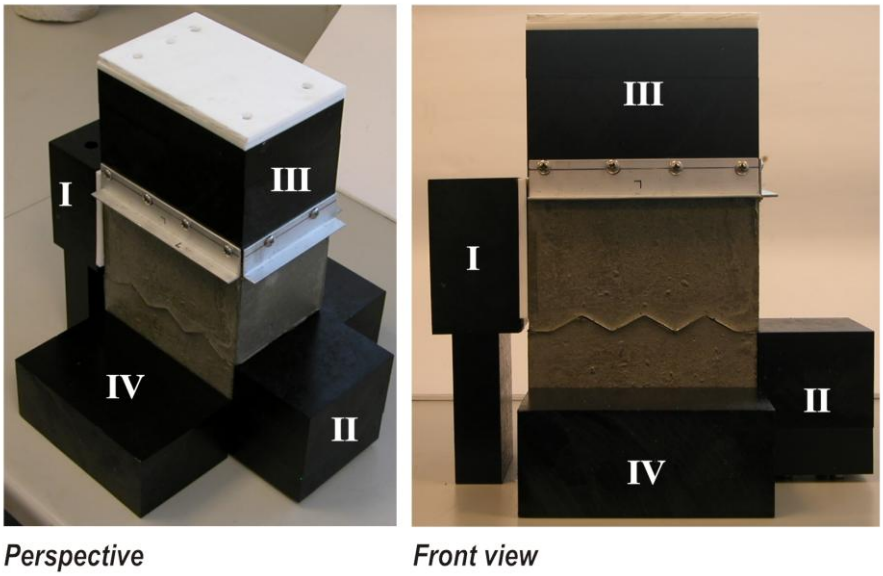


Figure 4.4 Shearing specimen confined by rigid shims, (a) Perspective and (b) Front-view.

Two Teflon sheets are also used: one is placed between the top shim (III) and the vertical ram and the other between the T shaped shim (I) and the shearing side of the specimen. The purpose of using these Teflon sheets is to minimise the friction in the sliding components of the device which may affect the shearing response of the fracture. The one attached to shim I, is used to ensure the dilation of the sample (i.e. vertical movement of the upper block over the lower block) during shearing under CNL.

### 4.2.2 CNL Loading configuration

In the CNL shear experiment, dilation of the upper block over the lower block is expected as a result of the normal load being constant. Therefore, in direct shear tests, the normal load is kept constant during the shear loading using hydraulic pumps.

For this purpose, in the modified system presented here, a duplex high pressure cylinder (DHPC) was designed, a photo of which is shown in Figure 4.5. The cylinder consists of two chambers isolated using a diaphragm, one side is filled with nitrogen gas to a pressure equivalent to the normal stress required for the experiment and the other side is filled with oil. In this figure, the pressure gauge shows 300 Psi pressure on the vertical ram which in turn applies a 3.5 MPa constant normal stress on the shearing sample (see also Figure 4.6 for more clarifications).

Figure 4.5 Duplex high pressure cylinder (DHPC) to apply constant normal load.

In the event of dilation (i.e. normal displacement) of the upper block, the gas is compressed but the pressure is kept constant. This causes an equivalent amount of oil to be returned from the vertical ram to the DHPC which in turn results in an upward movement of the vertical ram. By recording the load cell data placed in the vertical ram, the fluctuations of normal load applying to the specimen can be measured which in turn is related to the amount of oil displaced. This system ensures a constant normal load being applied to the sample during shearing.

This device is capable of applying a constant shear load to the shearing specimen using high pressure pumps which can be performed either in constant pressure or constant flow rate, as explained in Section 4.2. This is believed to be a more appropriate approach in applying the shearing velocity to the sample throughout the experiment compared to the more commonly used methods. Table 4.1 compares the configurations of the apparatus developed in this work (A in the table) against two other direct shear test devices recently developed by Barla et al., 2009 (B in the table) and Jiang et al., 2004 (C in the table). This Table indicates an increased capacity of normal and shear loads with a larger specimen size in the current tool.

The latter improvement reduces the likelihood of sample motion in the form of lateral displacement and in particular twisting around the vertical axis, when the fracture surface is very rough (i.e. high angle asperities).

The experimental results obtained from shearing synthetic fracture blocks presented in Section 4.4 will show that how, for samples with high angle asperities (e.g. 45 degree base angle for a symmetric triangular profile sample) the induced tension cracks developed from asperity contacts propagate through the intact rock to some extent and then stop. The results match well with those observed from 2D numerical simulations. Figure 4.6 gives a schematic front view of the apparatus showing all the components and connections used in the current modification. In this figure, different parts are given a symbol and the legend below the figure shows the corresponding names. The connection of DHPC to and from normal ram is also shown in this figure.

Table 4.1 Comparison between three different shear test apparatus recently developed.

| Feature | A | B | C |
|---|---|---|---|
| Loading system | CNL | CNL & CNS | CNS |
| Maximum normal load (KN) | 315 | 100 | 400 |
| Maximum shear load (KN) | 315 | 100 | 400 |
| Maximum shear displacement (mm) | 20 | 18 | 20 |

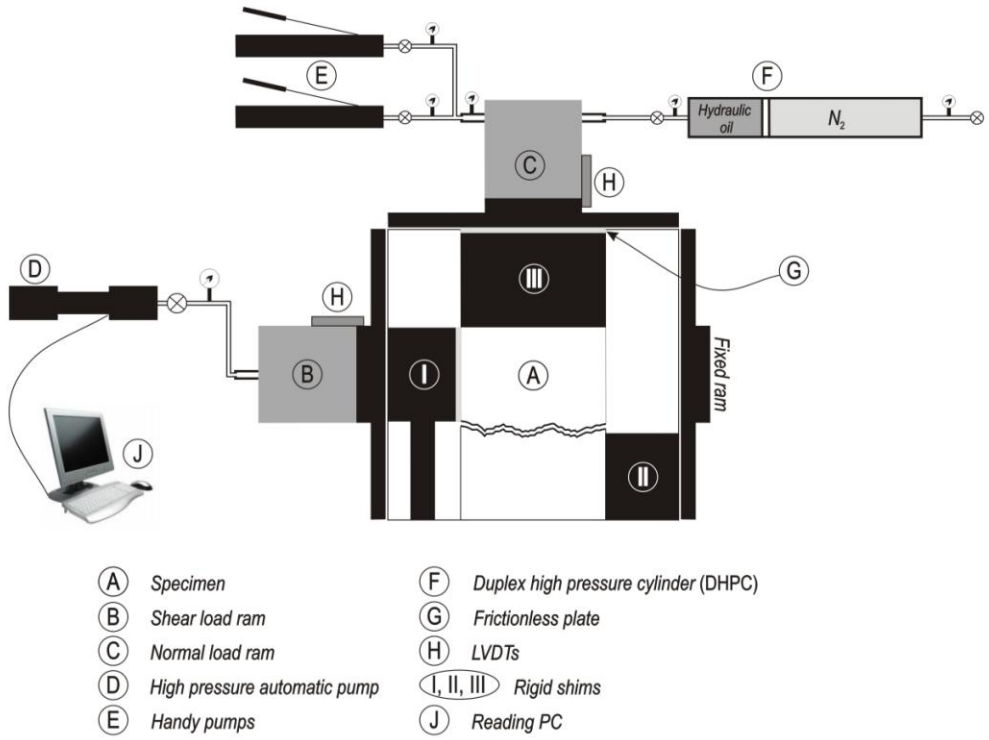


Figure 4.6 Schematic view of the specimen showing the system configuration.

One of the unique configurations of the FSC is that when the top lid is placed onto its position, the inner part of the cell becomes completely isolated from the outside. The sealing is mainly a result of metal to metal contact and is further supported by O-rings placed between the top lid and the upper part of the cell. This means the cell can be pressurised by any fluid or gas to a certain pressure (here 21 MPa). According to this ability, the sample used for the shear test could be saturated in fluid inside the cell.

Although the modification proposed here allows shear testing under CNL conditions, there is no practical reason why the experiment cannot be performed under CNS conditions using the FSC. This condition (CNS) can be adopted for FSC by inserting constant stiffness springs between the vertical ram and the upper block of the shearing sample. The original TTSC is made in such a flexible manner that allows various changes to be adopted in order to perform the experiment under CNS loading conditions.

## 4.3 Sample preparation

To understand the fractures shearing mechanisms in the lab and draw some conclusions, simple synthetic samples were tested first. Mortar synthetic fracture specimens with symmetric triangular shape asperities were made and subjected to direct shear tests using FSC.

To prepare the synthetic samples, a metal mould as shown in Figure 4.7 was built. The artificial plates (galvanized iron of 5 mm thickness) with defined surface geometries, is placed in the middle of the mould. For instance, Figure 4.7 shows a fracture with a 45 degree asperity angle. Filling the mould with desired material, such as mortar, produces the synthetic fracture geometries. The procedure for sample preparation is discussed below and in this study only one set of material composition was used to ensure similar mechanical properties for all tested samples. This allows a consistent comparison between lab and simulation results. The geometry of these synthetic surfaces allows, to a large extent, a reasonable comparison of the lab results with 2D models simulated in PFC.

As seen in Figure 4.7, the shearing block has a width of 15cm, a height of 20cm, and a thickness of 10cm. A shear box with this size is to be created in PFC for 2D simulations to represent lab size tests.

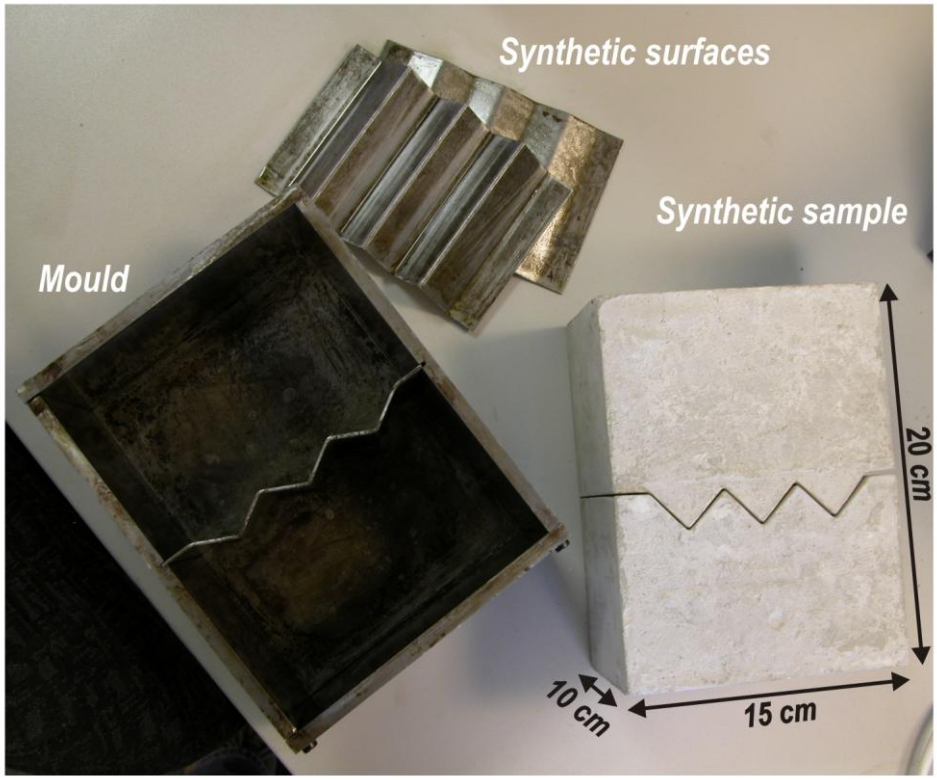


Figure 4.7 A metal mould used to prepare synthetic rough fracture geometries.

A rock fracture surface from a core sample (usually with a diameter of less than 5cm) can also be accommodated in this mould with the remaining space filled with high strength mortar. This allows for the testing of real fracture surface versus synthetic ones. This technique is used to prepare a rock-like fracture block explained in Section 4.4.3. A number of blocks with identical fracture geometry (i.e. symmetric and asymmetric

triangular) was made under the same conditions to perform shear tests under a variety of normal stresses and in opposite directions, along the fracture horizontal plane.

Hard plates were used to shape symmetric triangular asperities as well as pseudo-real fracture geometries, where variation of surface elevation is only in the x-z plane. This was thought to be the closest approach to be able to compare the lab results with 2D simulations run in PFC. A set up for making a synthetic symmetric fracture surface is shown in Figure 4.7.

The properties of the mortar material used for making the synthetic samples in this work are given in Table 4.2. Removing the plate soon after the mortar is cured, a mate fracture geometry is produced. The samples are saturated in water for 28 days, as per ASTM guidelines, to reach their ultimate strength before they are tested in FSC.

Estimation of mechanical properties of the samples used for lab experiments is essential as the results are compared to corresponding PFC2D simulations. For this purpose, we adopted a similar approach in this study to what was proposed by Lambert et al. (2010). They calibrated the results of lab UCS tests with PFC2D biaxial tests. The micro-properties of both mortar material and the generated PFC2D model are given in Table 4.2.

We also used the results of PFC2D micro-properties sensitivity analyses presented in Section 3.2 as guidance to tune the macro-response of this model. For instance, Equation 3.2 was considered which gives a correlation between the assembly's UCS and average particle size. However, this equation could not be directly employed here to estimate the UCS of PFC2D model as the bond strength used in this correlation is 60 MPa, while here it is reduced to 35 MPa to obtain a smaller value of UCS.

To obtain similar UCS values for all blocks tested in this study, the synthetic samples were made up of a volumetric combination of 20% cement, 65% fine grain sand, and 15% fresh water as it gives a moderately high strength mortar.

This combination was found to be suitable for the purpose of the current work, where studying the failure of the asperities is the main focus. This is, however, different than that used by Lambert et al. (i.e. 45% cement and 55% sand) with the samples expecting to have a larger UCS and Young modulus.

The results of UCS tests performed in the lab and corresponding PFC2D biaxial test simulations are presented in the following Section.

### 4.3.1 Unconfined compressive strength (UCS) tests

Figure 4.8 shows a cylindrical sample with a 52mm diameter and 104 mm height (close to ISRM recommendation standards) used for UCS tests. Five samples were made from a similar material (see Table 4.2). UCS tests were performed by applying a relatively low velocity to ensure that the tests are performed in quasi-static loading conditions. Loads and displacements were recorded during the tests.

The average UCS obtained from testing the samples was 29.2 MPa. Figure 4.9 shows one of the sample after the UCS test in which the plane of failure shows an average angle of $\beta = 30\pm2°$ with respect to the loading direction. This angle is related to the intact sample friction angle through the linear Mohr Coulomb criterion as

$$\beta = 45 + \frac{\phi}{2}, \tag{4.1}$$

which results in an average internal friction angle of 30±2° for the tested sample. Having the UCS and friction angle of the sample, an estimation of the sample cohesion can be made using the Mohr Coulomb criterion which is presented in the form of

$$\sigma_{ci} = \frac{2c\cos\phi}{1-\sin\phi}. \tag{4.2}$$

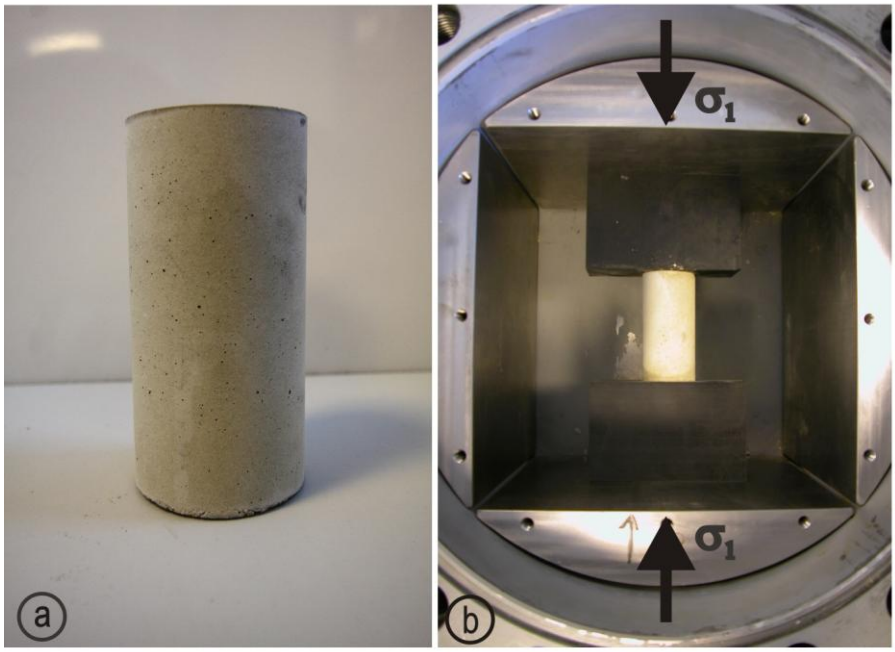


Figure 4.8 UCS test on a cylindrical sample using the TTSC.

Table 4.2 Micro-properties of mortar sample and PFC2D rock-like assembly.

| Property | Mortar | | PFC2D |
|---|---|---|---|
| | Cement | Sand | Assembly |
| Average particle radius (mm) | - | - | 0.3247 |
| Density (kg/m$^3$) | 1380 | 1380 | 1380 |
| Contact elastic modulus (GPa) | 18 | 25 | 20 |
| Ratio of particle normal to shear stiffness ($k_n/k_s$) | 2.5 | 2.5 | 2.5 |
| Particle friction coefficient | 0.35 | 0.35 | 0.40 |
| Contact normal bond strength (MPa) | 65 | 60 | 35 |
| Contact shear bond strength (MPa) | 65 | 60 | 35 |

Figure 4.9 Cylindrical sample before and after the UCS test showing the shear failure plane.

From this equation, an average cohesion and internal friction angle for the sample obtained to be 7.0 MPa and 32 degree, respectively.

PFC2D biaxial test simulations were performed under unconfined and confined compressive stress conditions to determine the UCS and E. The micro properties of the model are given in Table 4.2 and the PFC2D simulation scheme for biaxial tests was explained in Section 3.2.

Here, the same procedure was used for model generation but the average particle radius was set to 0.322mm. Although this is few millimetres larger than that considered for simulations in Chapter 3, it is in the range of fine grain sandstones which was used

Table 4.3 Rock strength properties correlated with lab tests and PFC2D simulations.

| Property | Mortar | |
|---|---|---|
| | Lab experiment | PFC2D |
| UCS (MPa) | 29.2 | 31.5 |
| *E* (GPa) | 8.051 | 9.54 |
| *c* (MPa) | 7.0 | 7.5 |
| $\phi$ (deg) | 32 | 29 |

for mortar preparation in the lab. This allows for a comparison of lab and simulation results. Based on PFC2D biaxial simulations, an average UCS of 31.5 MPa was estimated for a rock-like assembly which is very close to the value obtained from lab tests (i.e. 29.2 MPa). Based on the Mohr-Coulomb analysis, the failure envelope of the sample is plotted in Figure 4.10. PFC2D biaxial test simulations were performed, under confined compressive strength where it was assumed the PFC models were representing this loading condition, after several tests were carried out.

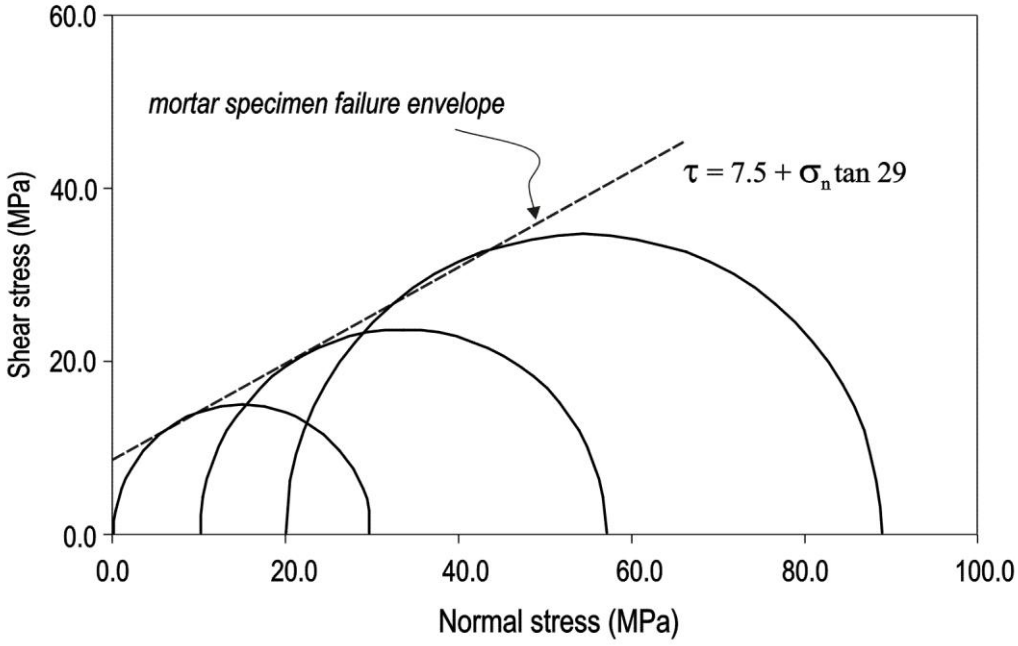


Figure 4.10 Mohr-Coulomb representation and failure envelope of mortar sample modelled in PFC2D.

From this envelope, cohesion and internal friction of the intact sample corresponding to lab samples and the PFC2D models are measured as 7.5 MPa and 29°, respectively. Table 4.3 shows the average UCS and E for mortar correlated with UCS experiments and PFC2D biaxial test simulations where five different randomly packed particles were subjected to biaxial tests and the average values obtained are given here. It can be seen that the values obtained from the lab tests and PFC2D simulations are similar, so the model and sample are expected to behave similarly under compression loading conditions.

In the PFC2D models presented in this Chapter, the results of which will be compared with lab experiments, a particle friction coefficient of 0.05 was applied to the fracture zone particles in all models to produce realistic curves for fracture shear strength (see Section 3.4.3).

Strength parameters of the testing material computed and measured in this Section will be used to plot fracture rock failure envelopes and later to discuss failure mechanisms during fractures shearing.

## 4.4 Fracture shear tests using FSC

In this Section, the results of shear tests conducted using FSC for synthetically made symmetric triangular and pseudo-real fractures as well as a rock-like fracture will be presented. For the synthetic samples, where the third dimension (thickness) of the samples exhibits identical amplitude, the lab results are compared with PFC2D simulations.

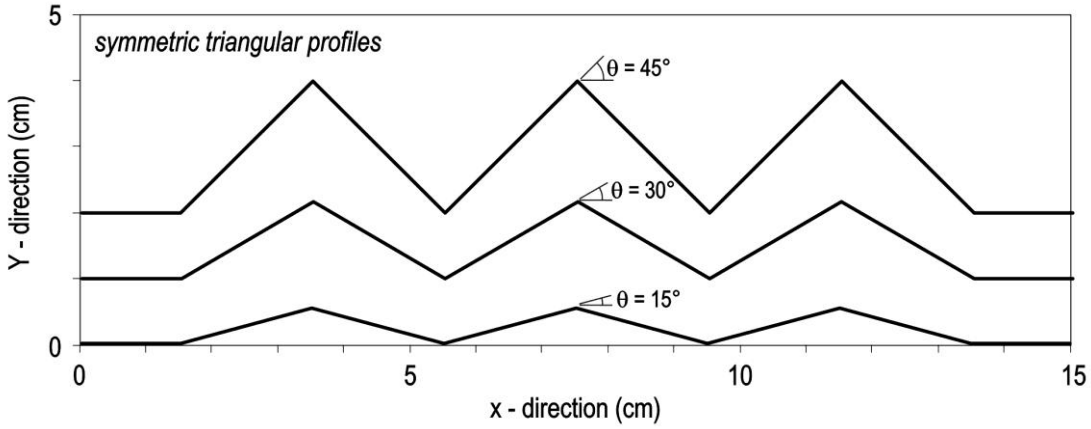


Figure 4.11 Cross-sections of symmetric triangular fractures with 15°, 30°, and 45° asperity angles used for shear tests.

### 4.4.1 Symmetric triangular asperity fractures

Different synthetic fractures with symmetric triangular asperities of 15°, 30°, and 45° base angles, shown in Figure 4.11 are subjected to direct shear tests. Amplitude and wavelength of asperities as well as the profiles' length are shown in this figure.

Shear tests will be performed at two different normal stresses (low and high) and in two opposite horizontal directions (LR: shearing the upper block from left to right and RL: shearing the upper block from right to left) along the fracture horizontal plane. As can be seen from this figure, a constant asperity wavelength of 4 cm was used for all three geometries. In Section 3.4.4 the influence of changing asperity wavelength and height in shearing mechanisms was discussed.

Figure 4.12 shows the view of the samples built in the lab based on the procedure and using material properties given in Section 4.3.

Fracture shear tests were performed using FSC and constant normal stresses of 1.5, 2.0, and 2.5 MPa were applied to the samples during different shear experiments using the DHPC.

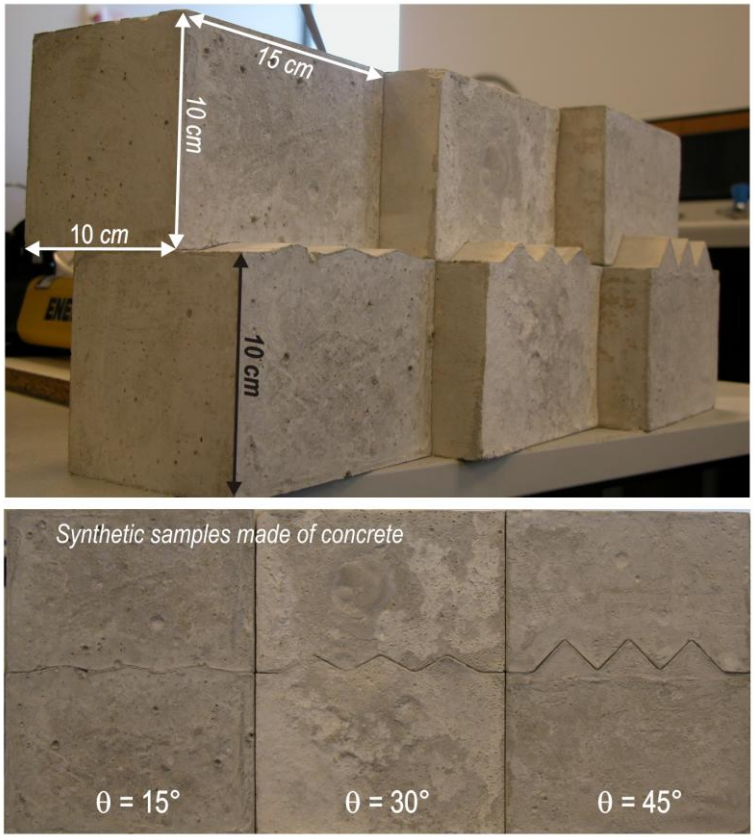


Figure 4.12 Synthetic samples with triangular shape fracture surfaces.

Shear load was applied on a constant velocity of 0.5 KN/min to the samples. Each test took approximately two hours to complete and this period of time was adequate for the sample to reach its residual state. Therefore, the post peak behaviour of sheared fractures was also recorded after the samples' upper block was displaced horizontally up to 1.0cm.

The shear load and displacements were recorded during the experiments using a high precision data recorder and the curve of pressures versus time plotted constantly during the tests on the computer screen for instant observation of a sample shearing response. Figure 4.13 shows the view of samples after the shear test under 2.5 MPa normal stress. This is the largest normal stress applied to the samples and found to be large enough to cut-off the high amplitude asperities (e.g. 45°). The asperities in the rough sample tended to shear-off during the experiment and this resulted in a larger peak shear stress, whereas for the sample with lower asperity angles (e.g. 15°) the dominated shear mechanism was the sliding of the upper block over the lower block.


Figure 4.13 View of samples after shear experiments under 2.5 MPa normal stress.

Curves of shear stress versus shear displacement at a normal stress of 1.5 MPa were produced based on recorded data and plotted for each case which are presented in Figure 4.14. A peak shear stress of 4.3 MPa followed by a sharp reduction to a residual stress of 3.2 MPa is observed for the rougher sample (i.e. 45° asperity angle). However, the results for the sample with the lesser asperity angle showed a gradual increase in

shear stress but a levelling off at approximately 1.39 MPa shear stress and no sudden reduction in stress was observed for this sample.

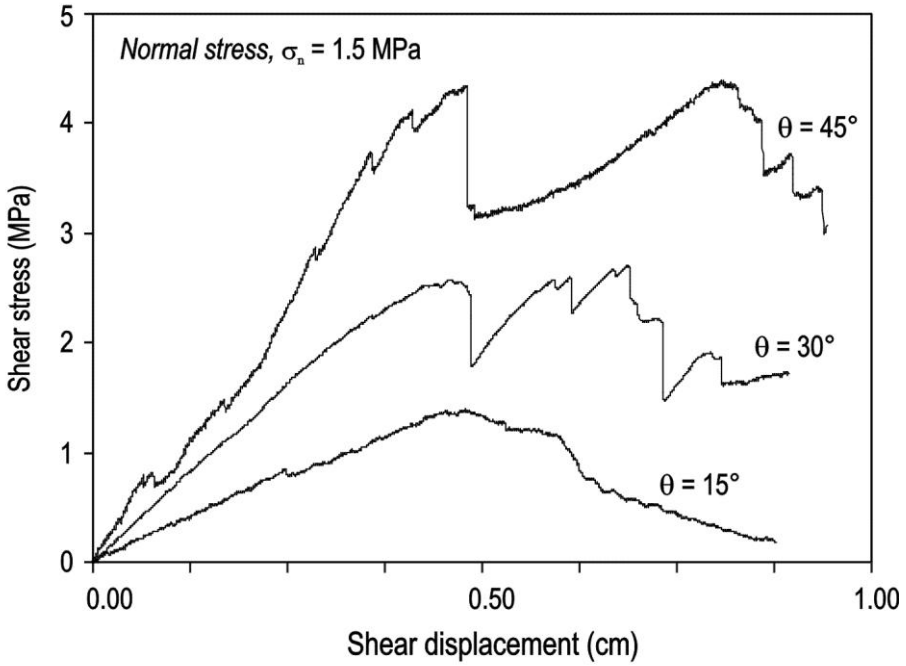


Figure 4.14 Plot of shear stress – shear displacement for symmetric triangular fractures based on lab shear tests conducted at normal stress of 1.5 MPa.

In Figure 4.15, the shear test results for a fracture with an asperity angle of 15° conducted at normal stresses of 1.5, 2.0, and 2.5 MPa are plotted. It is seen, as expected, that as normal stress increases, both peak and residual shear strength of the fracture increases.

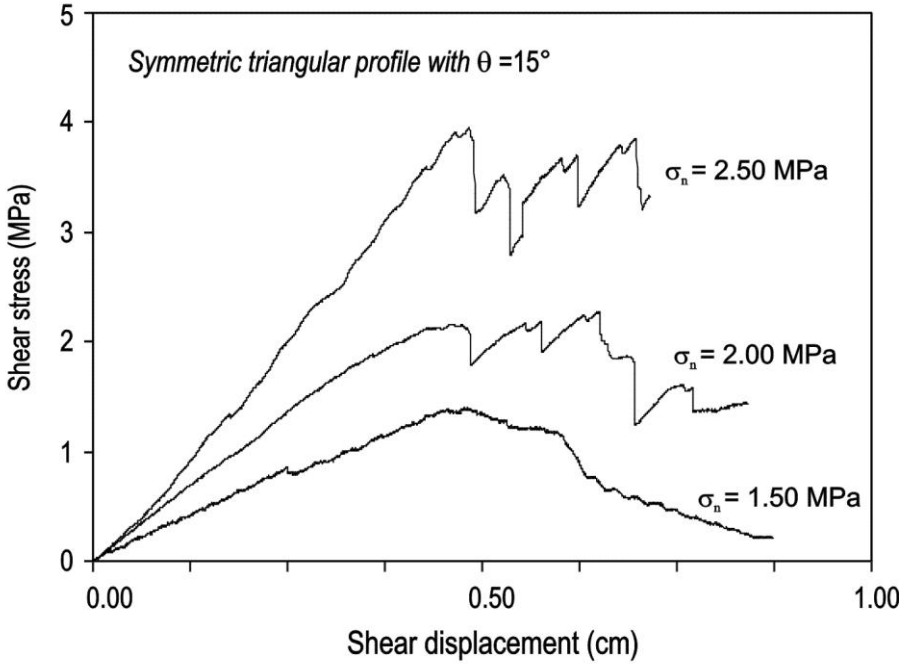


Figure 4.15 Fracture with asperity angle of 15 degree sheared in lab at different normal stresses.

At larger normal stress, shear stress at higher levels fluctuates as the asperities are being degraded, and tensile cracks are developing through the intact sample. Once all the asperities are sheared-off completely, residual shear strength is reached. This is observed at a normal stress of 2.5 MPa as shown in Figure 4.15.

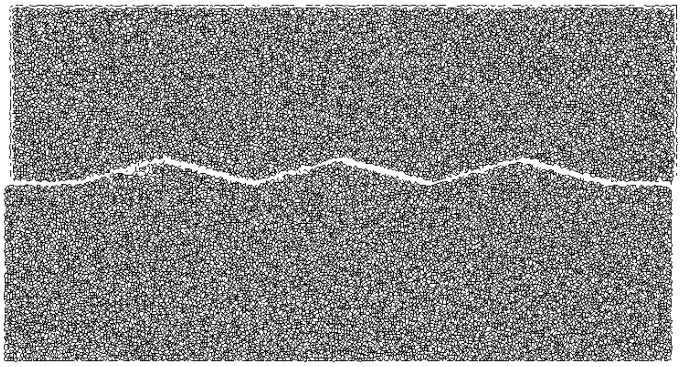

(a) *Asperity angle* = 15º

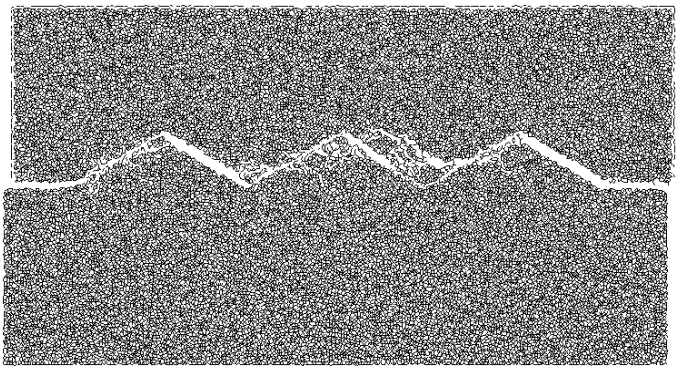

(b) *Asperity angle* = 30º

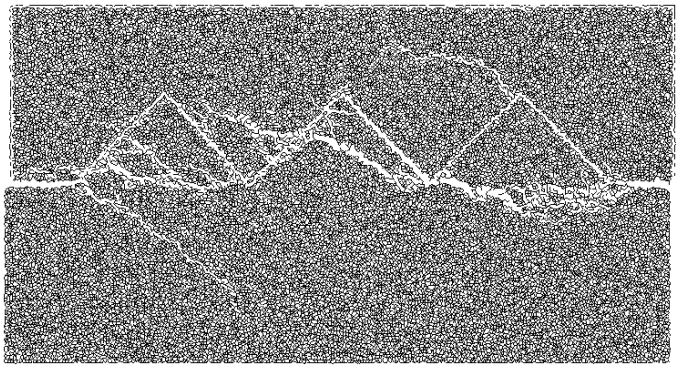

(c) *Asperity angle* = 45º

Figure 4.16 PFC2D simulations of fracture shearing with geometries depicted in Figure 4.11, after 1.0 cm shear displacement at 2.5 MPa normal stress.

The observation of the sample after completion of the test indicated a major tensile crack in the sample which could be linked to the sudden drop of stress in shear stress-shear displacement curves (see Figures 4.14 and 4.15).

PFC2D simulations were conducted to compare the results with lab experiment findings. Figure 4.16 shows the results correspond to a normal stress of 2.5 MPa. In these simulations the sample size, material properties, and fracture geometries were chosen to be identical to lab samples.

A good agreement is observed between lab and PFC2D results. From Figure 4.16 it is seen that by increasing the asperity angle, fracture mode changes from asperity sliding to cut-off and tensile cracking which is consistent with the lab observations of Figure 4.13, to a large extent.

Since the stiffness of this model is sufficiently high, development of micro-cracks is limited and more pronounced at larger asperity angles (e.g. 45° asperity angle), as shown in Figure 4.16.

Plot of $\tau$-$\sigma_n$ for the fracture with an asperity angle of 30° is shown in Figure 4.17 corresponding to both lab experiments and PFC2D simulations. From this Figure, a similar trend is observed from both approaches, but PFC2D appears to overestimate the peak shear strength. This is believed to be due to the cohesive effects of the fracture particles friction coefficient laying on opposite sides of the fracture, as explained in Section 3.4.3. It is seen that the trend of envelopes obtained from both PFC2D and lab results are almost similar.

The plot of Figure 4.17 allows estimation of fracture surface mechanical properties to be made. Considering the cohesion along the fracture surface, $C_f$ being the difference between peak and residual shear stresses (see Figure 4.15), the shear strength of the fracture ($\tau_p$) can be represented as a function of fracture friction angle ($\phi_f$) through Mohr Coulomb failure criterion as

$$\tau_p = \sigma_n \tan(\phi_f + \theta) + C_f . \tag{4.3}$$

where $\theta$ is the asperity angle of the fracture.

From the fracture failure envelopes shown in Figure 4.17, friction angles of 29° and 27.3° were measured from lab tests and PFC2D simulations, respectively. As these are very close together, the overestimation of peak shear strength by PFC2D is thought to be due to the cohesive effects of the fracture particles friction coefficient laying upon opposite sides of the fracture particles, in the PFC2D model

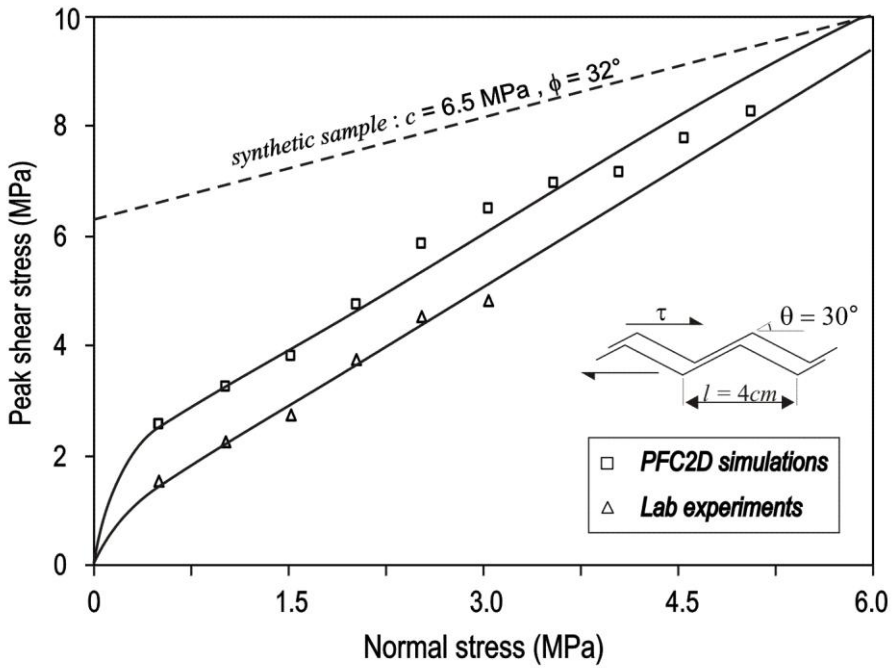


Figure 4.17 $\tau$-$\sigma_n$ curve estimated from lab tests and PFC2D simulations.

Since, fracture shear tests were not performed for normal stresses larger than 3.0 MPa, discussions on fracture shear behaviour at larger normal stresses will be made based on PFC2D results.

In Figure 4.17, the slope of the curve corresponding to the fracture with an asperity angle of 30° is $(\phi_f + \theta)$=59°. However, when the normal stress exceeds a threshold it is expected that the asperities are completely sheared-off and failures develop into the interior of the block. The normal stress corresponding to this critical behaviour could be analytically estimated for a symmetric triangular asperity fracture as

$$\sigma_n^T = c(\cot\theta - \tan\phi)\cos^2\phi, \tag{4.4}$$

where $\sigma_n^T$ is the critical normal stress, $c$ is the rock cohesion, and $\phi$ is the rock internal friction (see Section 3.4.1). If the failure envelope of the intact sample is added onto the fracture failure envelopes, $\sigma_n^T$ can be identified. This is shown in Figure 4.17 for an asperity angle of 30° where it is seen that the fracture intersects the intact sample failure envelope at almost a 5.5 MPa normal stress level. By reducing the fracture surface roughness, the transitional normal stress will be shifted to larger values. This, as explained in Sections 2.2.7 and 3.4.1, is because larger asperities with sharper teeth are more likely to be sheared-off earlier than smaller asperities with small aspect ratios. From Figure 4.17, it appears that the shearing mechanism for a sample with $\theta$=30° is

expected to be mainly sliding along asperities at normal stresses less than 3.0 MPa with asperity shearing more likely to occur at normal stresses beyond this.

Figure 4.17 also shows that by increasing the normal stress, the difference between lab and PFC2D results appears to reduce. This is because at larger normal stresses, both methods are expected to give close results. As stated, the most probable parameter for overestimation of shear strength by PFC2D is friction of particles laying on opposite sides of the fracture which in this case (i.e. large normal stresses) has lower effects on shear strength since the dominant failure mechanism is not asperities' contact sliding but it is asperity cut-off and degradation along the fracture plane.

### 4.4.2 Pseudo-real fractures

Pseudo real fracture blocks were built artificially using mortar and according to the procedure for sample preparation which was explained in Section 4.4.1. The block has an identical geometry along its thickness and this will result in comparable lab results and those obtained from PFC2D simulations. The samples (A and B) are shown in Figure 4.18 with a cross-section shown in Figure 4.19.

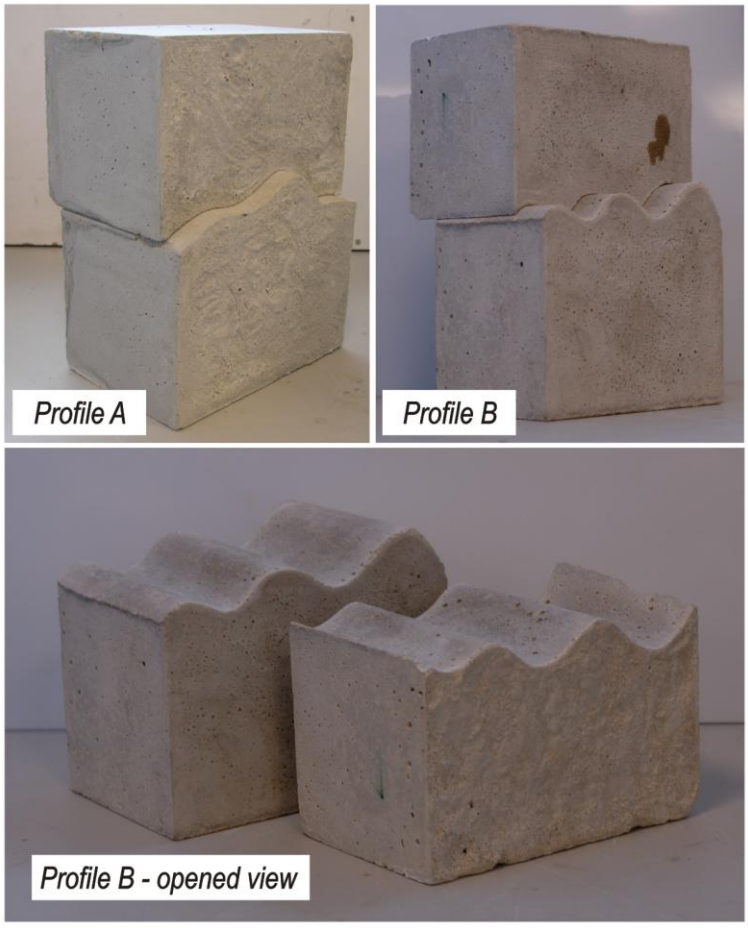


Figure 4.18 Shearing block with A and B fracture geometries prepared for lab shear tests.

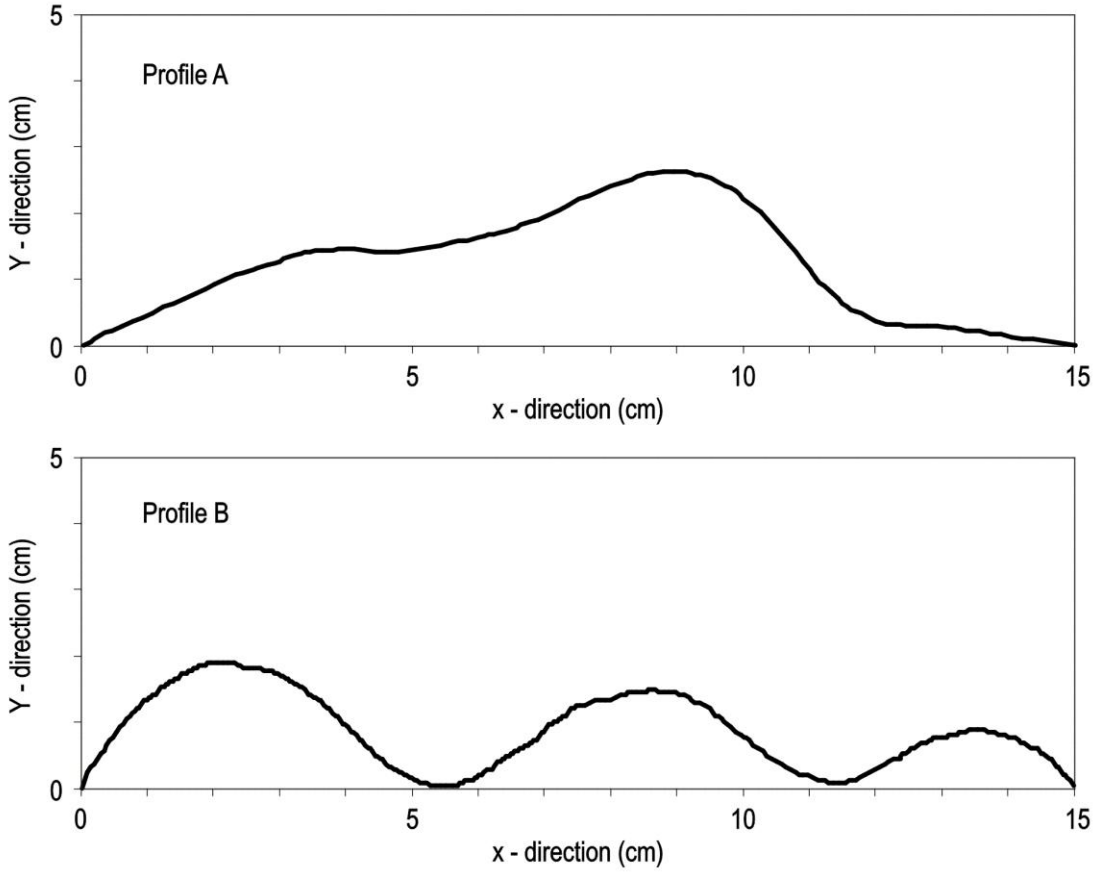


Figure 4.19 Geometry of pseudo-real fracture profiles A and B extracted from prepared testing block.

The micro and macro properties of samples A and B are similar to those given in Tables 4.2 and 4.3, respectively. Both samples were subjected to shear tests in two opposite directions to investigate directional dependency in shear strength estimation. Visual observation of profiles in Figure 4.19 shows that profile A includes one major asperity which appears to be steeper on one side than another, whereas profile B includes three asperities with different heights. These two profiles were chosen amongst several tested geometries to show, as examples, the importance of rough asperities in shear strength estimation.

The results of lab experiments and PFC2D simulations for these two samples are reported below.

#### Profile A shearing analysis

Shearing procedure, testing configurations, and the sample's material micro and macro properties are similar to the symmetric triangular asperity fractures discussed in the previous Section.

In Figure 4.20, the view of the fracture block A after shear tests in opposite directions (i.e. LR and RL) are shown. These tests are performed at normal stresses of

1.5 and 2.5 MPa and a shear displacement of up to 1.0cm was allowed. The results indicate a distinguished shear behaviour depending on the shearing direction. Fracture shearing in RL direction at both normal stresses of 1.5 and 2.5 MPa, causes sliding of the upper block against the lower block and minor asperity contact damage is observed. Looking at Figure 4.18 this is due to the fact that the left chord of the single large scale asperity in this fracture exhibits a smaller angle compared to that of the right side.

The fracture shearing in a RL direction however, as shown in Figure 4.20, shows the development of a large crack through the intact sample for both normal stresses of 1.5 and 2.5 MPa is observed.

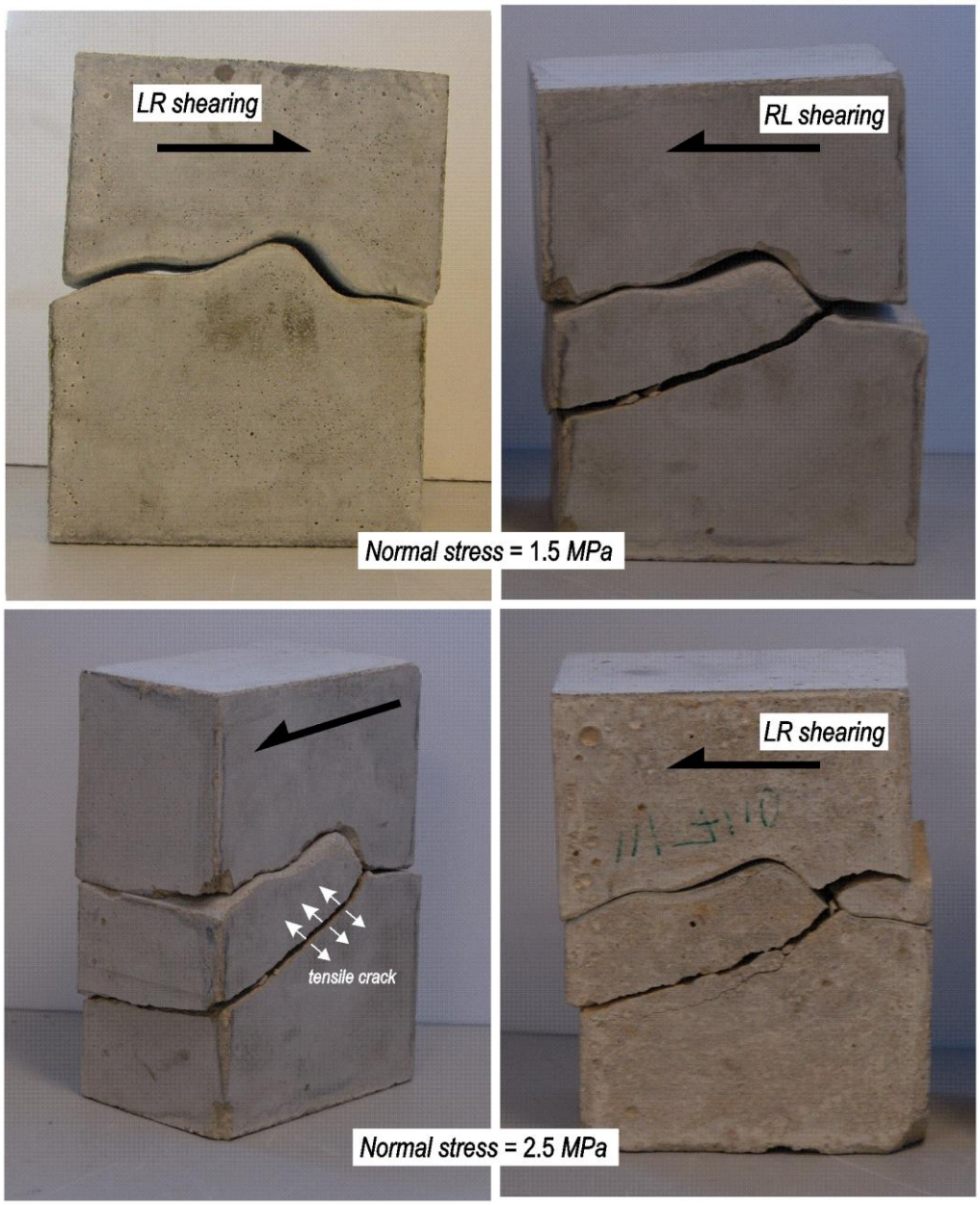


Figure 4.20 Profile A block view after shear tests at 1.5 MPa normal stress in opposite directions (top) and at 2.5 MPa normal stress (bottom).

This means that for these particular geometry and material properties, the failure due to shearing in a RL direction occurs within the intact sample and the post peak behaviour will depend on the material mechanical properties (i.e. tensile strength), instead of fracture surface parameters. The failure pattern for this case when a normal stress of 2.5 MPa was applied indicates the extent of several micro-cracks from the large crack, which is a result of shear stresses concentrated along this surface. These results are in agreement with what is expected from a visual observation of the profile geometry. The fracture experiences a large step when it is sheared from right to left and this causes the failure to develop within the rock texture in a tensile mode.

To investigate directional dependency of shear strength using PFC2D simulations, the profile A sample was subjected to shearing simulation in both directions (i.e. RL and LR). Figure 4.21 shows the profile after simulation at 2.5 MPa normal stress.

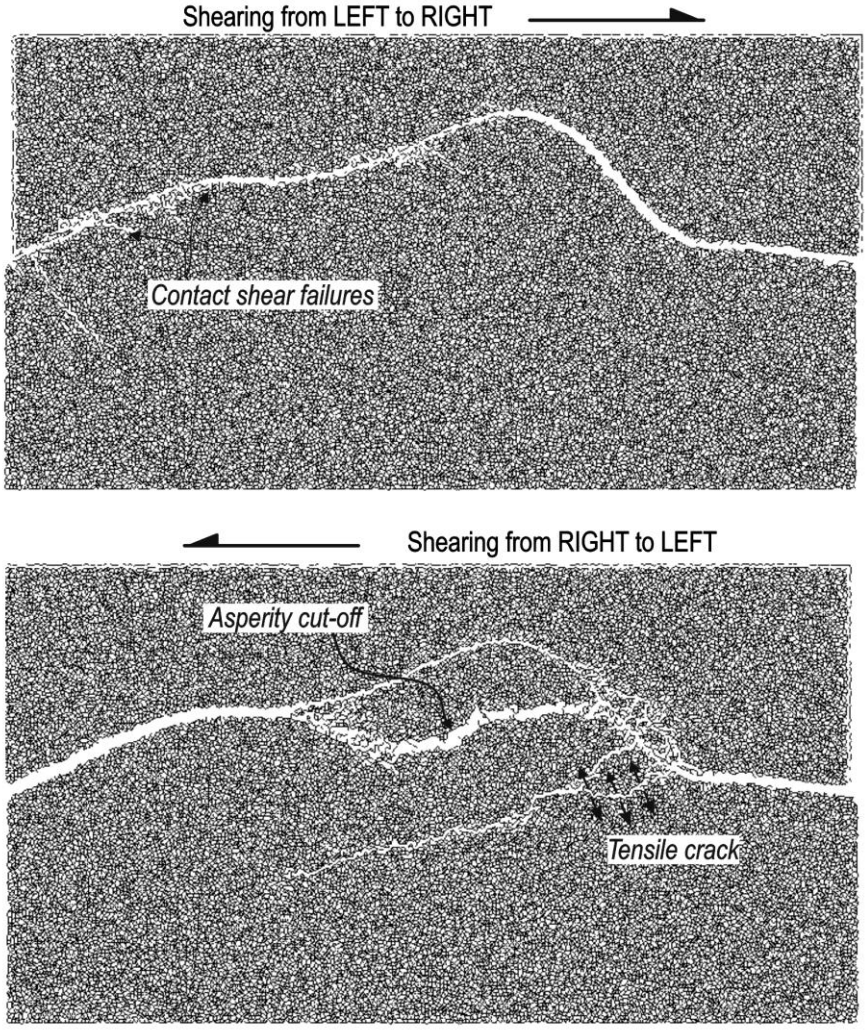


Figure 4.21 PFC2D simulation of profile A shearing in opposite directions, LR (top) and RL (bottom) at 2.5 MPa normal stress.

This figure shows that the dominant mechanism in LR direction is sliding, whereas the tensile and shear failures are expected to develop through the large asperity and intact sample when the fracture is sheared in the opposite direction (i.e. RL). In the latter case, i.e. shearing in RL direction, in addition to the extension of a large crack within the intact sample, a clear asperity cut-off is also observed in which the upper part of the asperity is dislocated and displaced due to shear stresses.

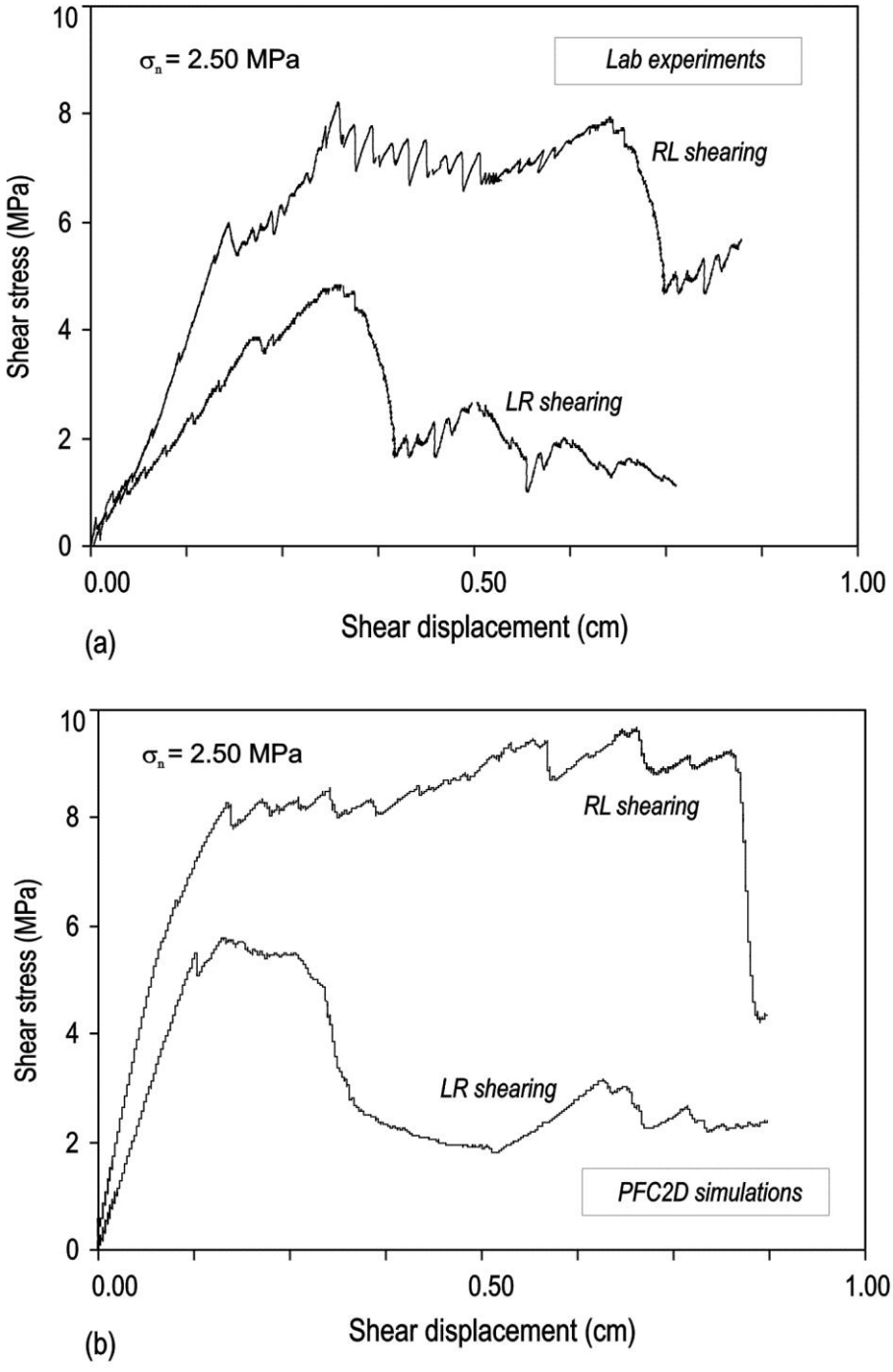


Figure 4.22 Shear stress versus shear displacement curves of Profile A shearing at 2.5 MPa normal stress, (a) results of lab shear tests and (b) results of PFC2D simulations.

Comparing the lab and PFC2D results, a good agreement is observed in terms of location and extent of tensile cracks (see Figures 4.20 and 4.21).

Figure 4.22 shows the plot of shear stress versus shear displacement obtained from lab shear tests and PFC2D simulations. Results are shown for shearing in both directions, i.e. LR and RL.

A large difference is observed in shear behaviour due to a changing of the shear direction. As expected, the pre peak and peak shear stress of the profile is larger when it is sheared from right to left than that of the opposite direction.

The post-peak (or residual) shear stress is also higher when the fracture is sheared in a RL direction. Lesser dilation is observed when shearing has taken place in a RL direction compared to that in an opposite direction, which is due to profile geometry. It is also important to note that the relatively sharp reduction observed in Figure 4.22 at the peak is because of the large asperity height or roughness for the profile we used here for demonstration purposes, which is similar to what was seen for synthetic profiles. However for real fractures, in general, a smooth reduction of stress after peak is expected.

The above analyses show why the shearing direction as well as the state of shear stress, i.e. pre or post peak, must be taken into account when characterising the ultimate shear strength of fractures. This is caused by surface roughness and therefore proposing an appropriate method to quantify roughness and integrate it with shear strength of the surface is important.

#### Profile B shearing analysis

In Figure 4.23, the view of fracture B after a shear test from left to right (at normal stress of 2.5 MPa and maximum shear displacement of 1.0 cm) is shown. However, tests were performed at normal stresses of 1.5 and 2.5 MPa and in both directions on this sample.

This sample includes three sinusoidal asperities with different amplitudes and wavelengths along the horizontal plane and it was therefore interesting to see the percentage of contribution of each asperity in shearing resistance when it was tested in LR or RL directions. In the first test, which was performed under 1.5 MPa normal stress, the sliding of upper block asperities over the lower block was observed with a small dilation taking place. Also, similar to profile A, under this low normal stress, minor asperity contact damage (called asperity contact wear) was also observed.

However, when normal stress increased to 2.5 MPa, the shearing mechanism was completely changed and as can be seen from Figure 4.23, all asperities experienced failure but in different fracturing modes. In LR shearing it was seen that the first two asperities (from the left) of the lower block were sheared off and detached from the rock body. However, the most right asperity with a larger amplitude and wavelength experienced a large crack which extended to the intact sample itself.

These results confirm the theories of failure mechanisms discussed in Sections 2.2 and 3.4 and despite the extensive attempt of the author, very few similar lab works were found available to visually illustrate this.


Figure 4.23 Profile B block view after shear tests under 2.5 MPa normal stress and 1.0 cm shear displacement from left to right.

Figure 4.24 shows a close view of the asperities of fracture B inside the FSC soon after the completion of the experiment. From this figure it can be seen that the first two asperities (a and b) are completely detached from the lower block with no further direct contribution in the shearing process. However, they fill in the fracture aperture space as gouge material and this can, depending on the mechanical properties of the rock material, significantly affect the post peak shear strength of the fracture. The PFC

simulation takes this process into account, while it is ignored when simple analytical calculations are used for shear strength estimations.

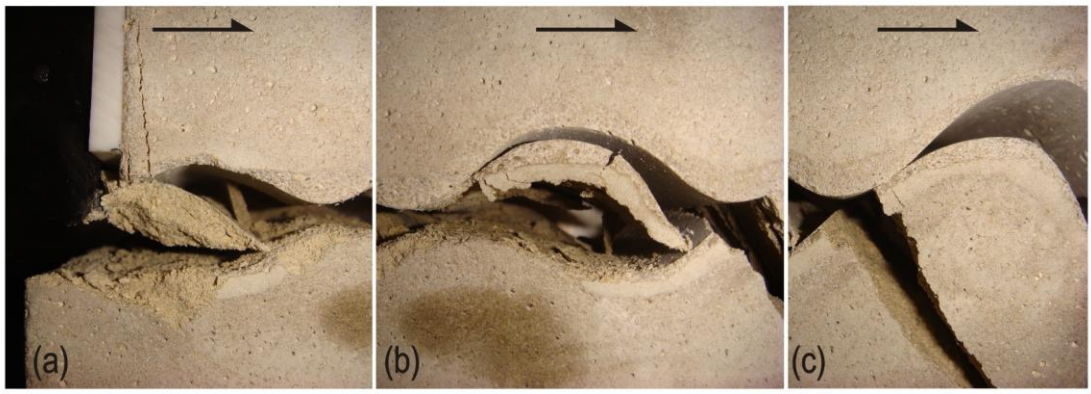


Figure 4.24 Profile B block view after shear tests at 2.5 MPa normal stress.

Similar to profile A, a large tensile crack was developed from this asperity's doglegs and propagated through the intact sample. The large asperity amplitude is responsible for this to happen (see Figure 4.24). This implies that, in a fracture with a number of asperities, the asperity with the largest amplitude will be the one which dominates the failure response of the fracture.

Here, the PFC2D shear simulation of sample B was performed under the same conditions as the lab shear tests. Figure 4.25 shows the PFC2D samples after being sheared under the 2.5 MPa normal stress in two different directions (i.e. RL and LR).

It can be seen that if the fracture is sheared in a RL direction, it immediately faces the largest asperity located to the most right. Considering the applied normal stress is large enough (here 2.5 MPa), most of the shear stress is consumed to develop a tensile crack in this asperity while the other two asperities experience minimum failure (see Figure 4.25, top). In LR shearing however, (see Figure 4.25, bottom), it can be seen that all asperities are sheared-off and a small dilation is observed in this case.

In comparing Figure 4.25 with Figures 4.23 and 4.24, a good agreement is seen in general between the results of the lab tests and the PFC2D simulations. However in PFC2D models where shearing takes place in a LR direction, the largest asperity experiences not only the tensile crack as observed in the lab but asperity cut-off was also observed which could be due to fracture particles size and distribution along the surface (compare Figures 4.24.c and 4.25, bottom).

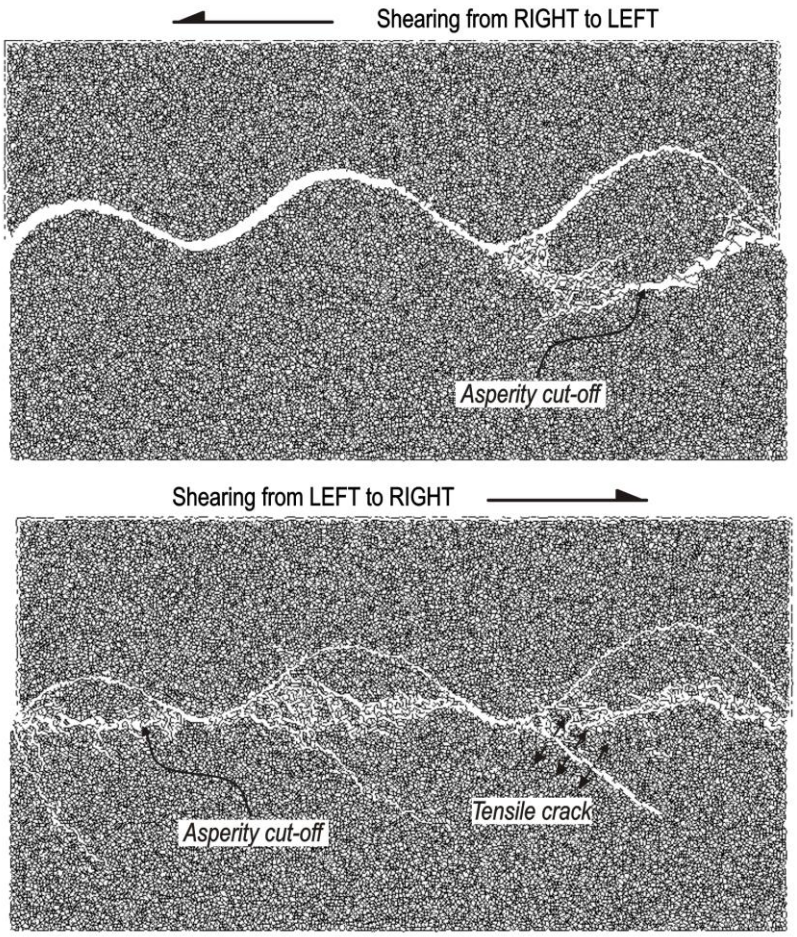


Figure 4.25 PFC2D simulation of profile B shearing in opposite directions, RL (top) and LR (bottom) at 2.5 MPa normal stress.

Figure 4.26 shows the plot of shear stress versus shear displacement obtained from both lab shear tests and PFC2D simulations. Results are shown for shearing in a LR direction corresponding to normal stresses of 1.5 and 2.5 MPa.

From the lab results (Figure 4.26.a), it can be seen that there is a large difference between the peak shear strength of the two fractures and that by increasing the normal stress the peak shear strength increases. Interestingly, the residual shear strength of both curves approach to an almost similar level (≈3.0 MPa) after the peak shear strength is reached.

A similar trend is seen from the PFC2D simulation results as shown in Figure 4.26.b. It should be noted that the values of peak shear strengths obtained from the simulations are slightly larger than that of lab tests at low normal stress, but at high normal stress, this variation reduces and close values are observed from both approaches. Comparing the peak shear strengths in Figure 4.26.a and 4.26.b for normal stress of 2.5 MPa, a shear strength of ≈ 8.0 MPa is obtained.

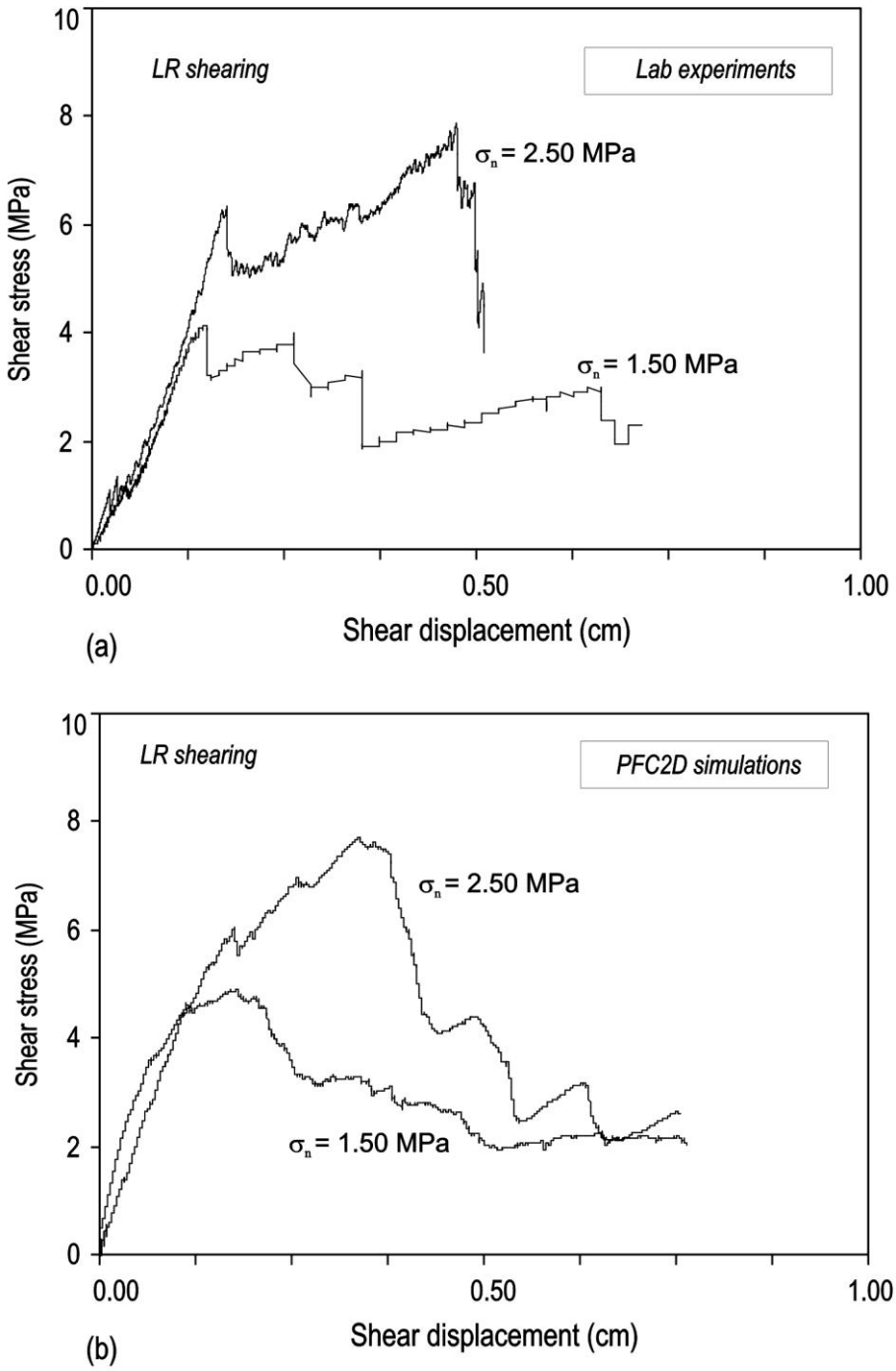


Figure 4.26 Shear stress versus shear displacement curves for sample B sheared at 1.5 and 2.5 MPa normal stresses: results of (a) lab shear tests and (b) PFC2D simulations.

The results presented so far demonstrate the capabilities of PFC in the shear simulation of fractures and the lab results obtained from FSC experiments confirm this to a large extent. In the next Section, the lab shear experiment performed on a rock-like fracture sample will be presented and some conclusions are made from the observed results. Confirmation of the results requires 3D simulations of the model, which is not within the scope of this work and therefore is left as a subject for a future study.

### 4.4.3 A rock-like fracture

To generate a replica of the geometry of a real rock fracture, we placed the real sample inside the mould (shown in Figure 4.7) and filled the part opposite to the fracture face with mortar material. This generates a sample geometry, which can be used to produce the opposite face of the discontinuity in a similar way. Indeed, the mechanical properties of the created sample is different from that of the real rock but in this study it is the geometry of the fracture which is important to us and the approach adopted here provides a reasonable replica of rock fracture geometry. The produced sample has the micro and macro properties explained in Section 4.4.1, and the sample is shown in Figure 4.27.

High resolution photos were taken from each surface of the fracture (i.e. lower and upper) and were subjected to photogrammtery techniques using Siro3D software to produce 3D and wireframe images of upper and lower surfaces of this rock fracture as shown in Figure 4.28. Siro3D generates a spatially fully referenced 3D image from overlapping digital images taken from a rock surface (CSIRO, 2009; Haneberg, 2006).

The rock fracture block was tested in the lab using FSC in a similar procedure explained in Section 4.4.1. The sample was sheared in opposite directions along *x*-*y* plane and under 2.5 MPa normal stress. Each sample was tested twice in order to examine the evolution of surface roughness after one cycle of shearing. After the first cycle it is expected that some of the asperities are broken and therefore lesser shear strength is to be observed for the second cycle, assuming that both experiments are conducted under an identical normal stress.

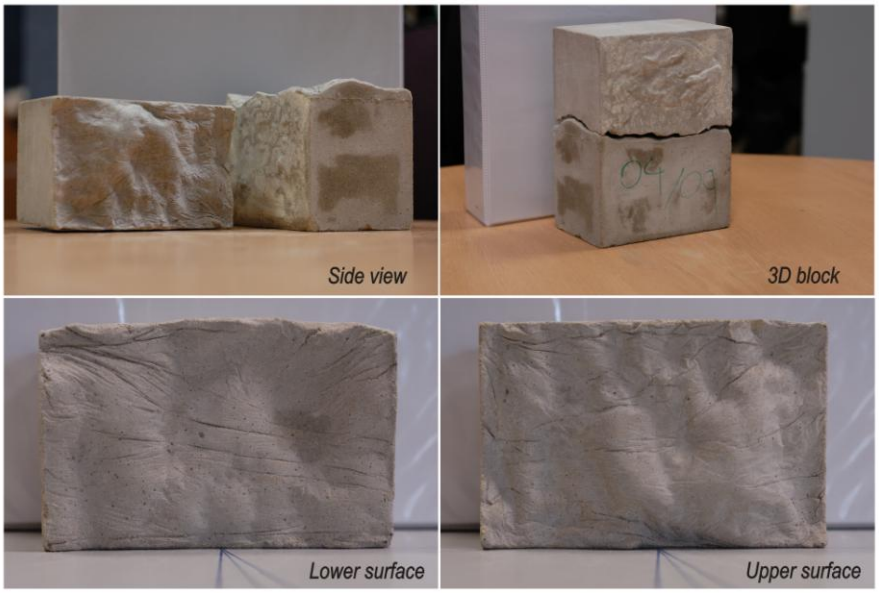


Figure 4.27 Artificial rock-like fracture made of mortar.

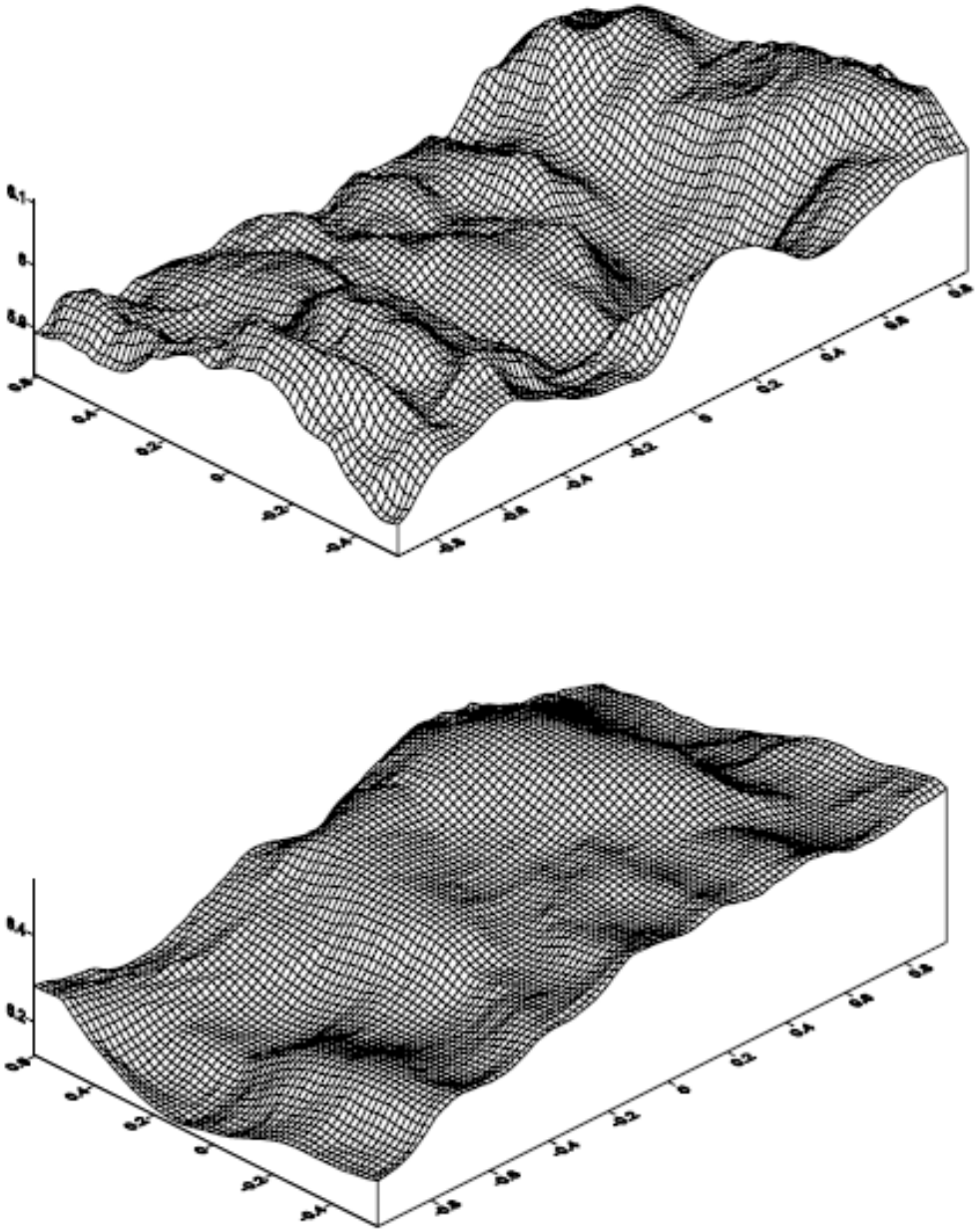

Figure 4.28 Rock-like fracture lower (top) and upper (bottom) surfaces.

The fracture sample after shearing in a LR direction is shown in Figure 4.29 which gives the results of shearing for two cycles of shearing. In the first cycle, the fracture was allowed to displace up to 1.0cm and is seen that a limited amount of asperity contact degradations occurred. Thereafter, fracture surfaces were brought to their initial position (i.e. matched surfaces) and the second cycle of shear tests were performed at the same level of normal stress (here 2.5 MPa). The view of the sample after the second cycle is also shown in Figure 4.29 where it is observed that the amount of degradations has been increased. Locations of the damaged area on the fracture surface are marked in this figure which clearly shows that all asperity contacts were damaged at this cycle of the test.

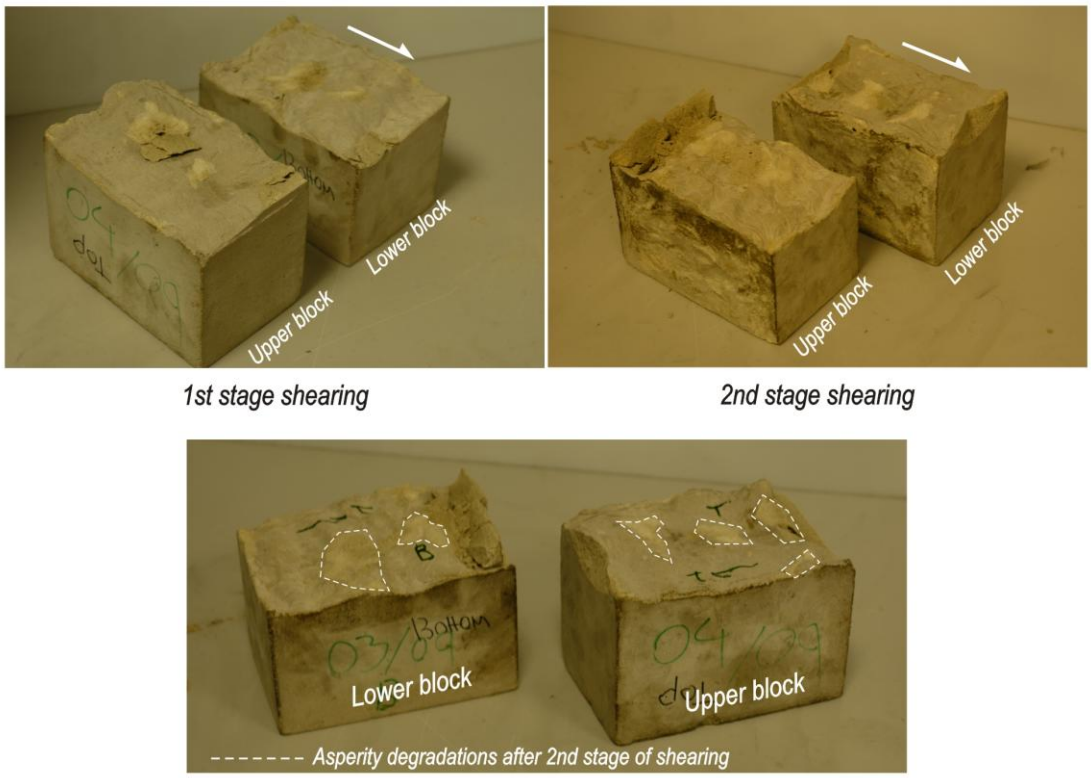


Figure 4.29 Rock fracture block sheared in the lab at 2.5 MPa normal stress and at two shearing cycles.

Considering the analysis, reproducing the 3D image of the fracture after each cycle of shearing will be useful in the prediction of mobilised roughness of the fracture surface which is not the purpose of this study. Figure 4.30 shows the plot of shear stress versus shear displacement obtained from lab shear tests for this rock fracture. Results are shown for shearing in both LR and RL directions at a normal stress of 2.5 MPa. Curves corresponding to each cycle of shearing are also given.

Figure 4.30.a gives the results of lab shear tests where the fracture is sheared in a LR direction. It can be seen that there is a large difference between the peak shear strength obtained in the first and second cycles of shearing. This is due to the predominant effects of fracture surface geometry (i.e. roughness) on shear strength.

From the first to second cycle, fracture roughness evolves and therefore a different shearing response is observed in the second cycle. The peak shear strength of ≈4.7 and ≈2.7 MPa were measured for the first and second cycles of the shear test, respectively. It is seen that peak shear strength reduces in the second cycle, as expected, comparing to the first cycle which demonstrates that large asperities were damaged during the first cycle of the shear test.

From Figure 4.30.a, a sharp drop of shear stress is recorded which is most probably because of a large asperity cut-off followed by the development of micro-cracks in the

fracture surface. A different response is seen in the second cycle as no major sharp asperities exist at this time but instead the broken asperities which fill in the fracture will make a contribution in fracture shear strength during the second cycle of the shearing test.

The average asperity angle can be calculated based on the mobilised friction angle of fractures in both cycles of shearing.

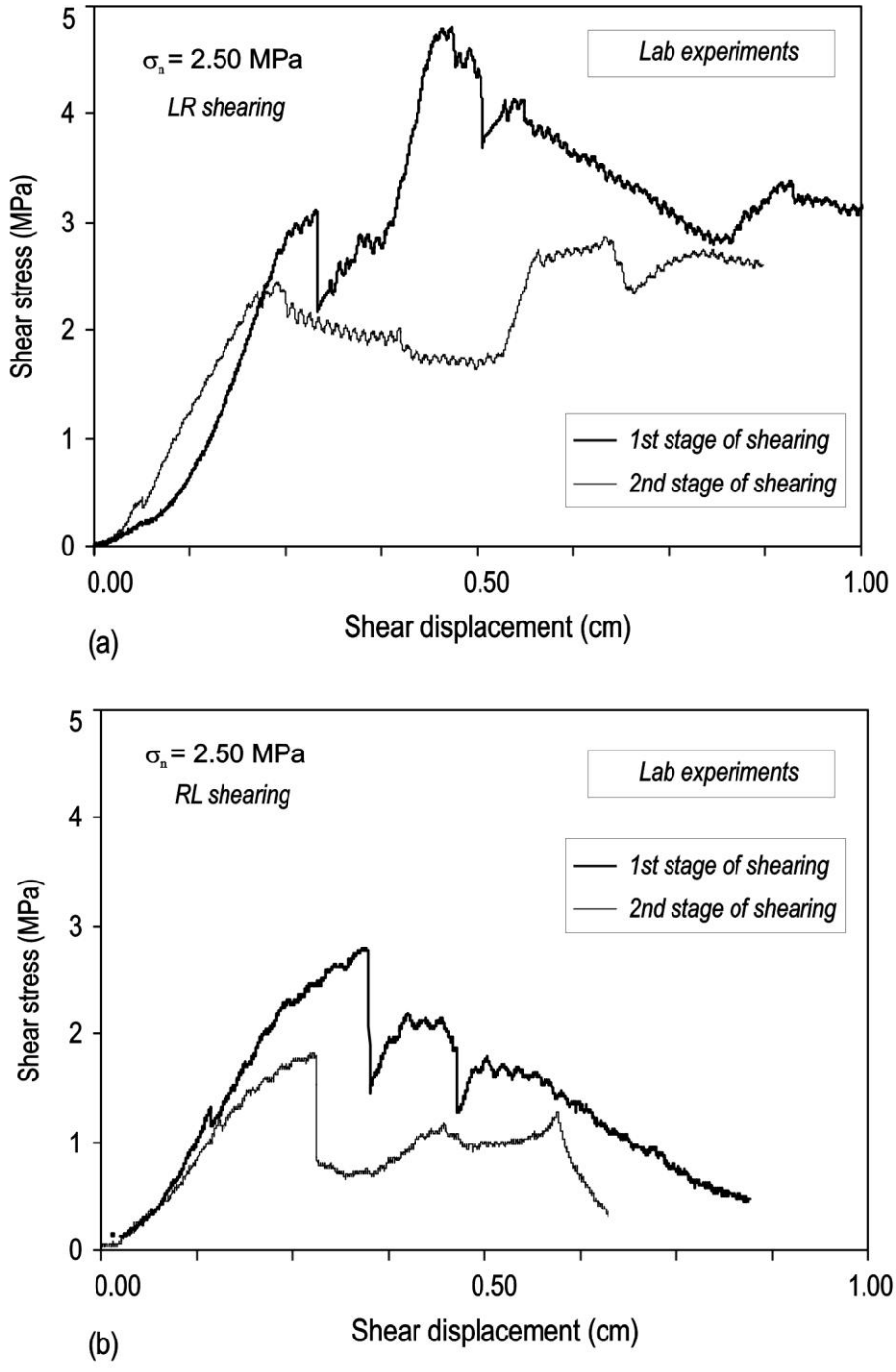


Figure 4.30 Plots of shear stress versus shear displacement at 2.5 MPa normal stress, (a) shearing in LR direction and (b) shearing in RL direction.

Assuming the basic friction angle of 31° for this fracture as discussed in Section 4.4.1, the average asperity angle (i.e. roughness) estimated using the Patton bilinear equation after the first and second cycles of shear tests are 30.9° and 16.2°, respectively. It is seen that the asperity angle is reduced in the second cycle as twice as in the first cycle: this indicates the effects of asperity degradation in shear strength.

Comparing the peak shear strengths in Figure 4.30.a and 4.30.b for normal stress of 2.5 MPa, shows that fracture shear strength is much larger if it is sheared in a LR direction than that of a RL direction. This is in agreement with the expectations from a visual observation of the sample.

For PFC simulation of this fracture, a 3D simulation is required which is not the purpose of this study. However, performing a 3D simulation of rock fracture shear strength is highly recommended for future studies.

## 4.5 Summary

In this Chapter, modifications applied to use an existing true triaxial stress cell (TTSC) for fracture shearing experiments were reported. Large shear and normal load capacities, adjustability of the specimen size, and highly controlled shearing velocity are the main features of this fracture shear cell.

In the next part of this Chapter, UCS tests were performed in the lab for mortar samples and the results compared with corresponding PFC2D models.

The shear experiments carried out on samples with symmetric triangular asperity fractures, pseudo real fracture and a rock-like fracture at a constant normal load indicated that the shearing mechanism changes from sliding to asperity shearing (i.e. degradation) as the fracture surface becomes rougher.

The results of the PFC2D simulations of both synthetic and pseudo fracture profiles presented here indicated a general agreement with the results obtained from corresponding lab experiments.

Fracture shear strength directionality was investigated by performing lab shear tests on synthetic samples along their horizontal plane in two opposite directions.

In the last part of this Chapter, a rock-like fracture was subjected to shear tests and its directional dependency was studied in two shearing cycles. The results indicated that shear strength is reduced in the second cycle due to a reduced roughness after the first shearing cycle.

# 5 Summary, conclusions and recommendations

In this thesis, the progressive shear behaviour of rock fractures with different surface roughness and normal stress acting perpendicular to a fracture direction was studied. It was shown how the shear behaviour of a fracture was different under low and high normal stresses. Also, fracture sliding (dilation), asperity shearing (cut-off), and asperity contact damage (degradation), were outlined as the three common modes of failure during fracture shearing and were simulated using PFC2D.

In the current study, the shearing process and failure modes of rough fractures were studied. The analysis was limited to single unfilled rough fractures and analytical, numerical and experimental approaches were used for modelling and data analysis. A detailed summary and conclusions made from this study are presented in Sections 5.1 to 5.3 with Section 5.4 outlining some of the future studies recommended as a continuation of this work.

## 5.1 Shear strength and roughness

- The 1D Riemannian dispersion parameter ($D_{R1}$) proposed by Rasouli (2002), corresponding to the standard deviation of unit normal vectors to a fracture profile, is perhaps the most recently developed roughness parameter. Correlation between $D_{R1}$ and fracture shear strength was examined in this study. A good correlation was found for synthetic fractures including symmetric and asymmetric triangular and sinusoidal profiles.
- A review of analytical solutions and empirical expressions of fracture shear strength showed that the current constitutive models such as the Barton empirical relation and Patton bilinear criterion are useful to estimate the shear strength of fractures where asperity degradation does not take place.
- For rough fractures sheared at high normal stresses, it was shown that a fracture failure mechanism includes both dilation and surface damage.
- A simple equation was derived based on the initial work of Huang et al (2002). Using this equation, the critical normal stress, above which the asperities are

completely degraded, can be estimated. This equation was also used to fit a parametric cubic spline to peak shear strength data obtained from simulations.

- Based on an analysis of the asperity cut-off expression, it was understood that the shearing process of fractures is expected to be a combination of contact sliding at low normal stresses, asperity cut-off at relatively high normal stresses, and rock failure at normal stresses larger than the values of critical normal stress.
- A review of rock fractures deformation and degradation models showed that due to evolutional effects of surface roughness on shear strength and asperity degradation, a single parameter used in constitutive models was unable to take into account the effects of roughness on asperity degradation.
- To obtain a more realistic model in studying the progressive shear behaviour and degradation process of rough fractures, an explicit numerical method could be used which could monitor the deformation process of fracture surface and intact rock through time. This results in the development of a complete stress-strain relation for the fracture. The simplistic assumptions in developing analytical solutions make their applications limited to very special scenarios.

## 5.2 Numerical analysis of fracture shearing

- The literature review indicated that most of the existing numerical studies on fracture shearing, which are mostly developed based on a continuum medium (e.g. FEM based models), predict the onset of failure. However, a number of simulators, which use the discrete element method (DEM) such as PFC, enable us to investigate the failure progression of a fracture surface during shearing by tracking the extent of the damage zone boundary. In this study, PFC2D was used for the simulation of fracture shearing.
- In PFC simulations, the detection of contacts between circular objects is much simpler than that of angular objects as used in other simulators. Also, unlimited displacements can be modelled in PFC and more importantly the blocks can break, unlike the majority of other DEM codes such as UDEC.
- The bonded particle model (BPM) implemented in PFC has proven to be a good representative of rock material environment. Asperity sliding, development of micro-cracks, asperity damage, and intact material failure are the deformation mechanisms which can be explicitly modelled in BPM as force-displacement

curve progresses in time that enables real-time tracing of the fracture shearing behaviour.

- Using PFC2D the shearing behaviour of a fracture can be simulated as an interface between the two opposite blocks along which the particles are at initially unbounded contacts.
- PFC2D uses simple laws to establish interactions at the particle and contact level to represent the behaviour of a material. Therefore, the PFC can simulate the effect of the fracture roughness, and more specifically, the asperity degradation during shearing in a direct and realistic manner.
- The total number of particles required to represent a real rock situation is limited because of the limited computing capacity.
- A sensitivity analysis of the model micro-properties using a PFC2D biaxial test simulation demonstrated the existence of a relationship between micro and macro properties.
- Micro properties are usually not known and must be calibrated for any specific rock type. In this study, this was done using available literature data and performing biaxial and Brazilian test simulations to determine the macro-mechanical properties of the model such as UCS, Young's modulus, and tensile strength.
- It was observed that UCS is linearly correlated with contact bond strength and average particle size. Contact elastic modulus is also correlated with Young's modulus, and the ratio of contact normal to shear stiffness correlated with Poisson's ratio and Young's modulus. Parametric correlations were developed in order to estimate macro mechanical parameters of the model based on micro properties.
- The micro-properties calibration process must be done for the PFC fracture shear test model to investigate shear behaviour of the model in addition to those performed for intact samples using biaxial test simulations. Also, Macro-response of the intact sample as well as its fracture shear behaviour must be calibrated against lab experiments to ensure the reliability of the results.
- Normal and shear contact bond strengths must be distributed uniformly in a shear box to ensure a consistent response under different loading conditions and fracture geometries. Failure to do so may result in some spurious damage occurring where bond strength is distributed non-uniformly.

- It was observed, as noted by others previously, that a fracture plane in a PFC2D model has an intrinsic roughness even if it is planar. This is because of the different size distribution of particles in the model. This micro-roughness increases with increasing particle size, so by reducing the particle size in the model, this effect becomes less important. Accordingly, the sensitivity analysis indicated that an average particle size of $R_{ave}$ = 0.257 mm is small enough for the purpose of our modelling.
- The simulations indicated that selection of an adequate number of particles was crucial as it affected the behaviour of the entire model. By changing the number of particles in the assembly, the mean particle radius would change, which in turn affected the ultimate response of the model: the larger the particle size, the greater the final porosity, which in turn reduced the UCS.
- Effects of particle size on peak shear strength of a symmetric triangular profile were investigated using a parametric study in which particle radius ranged from 0.1 to 1.0 mm. It was observed that the peak shear stress reached a maximum at a mean particle radius of 0.6 mm and then reduced.
- In current fracture models it was seen that the peak shear strength reduced with $R_{ave} \leq 0.4$ mm which was due to the reduction in strain localisation in particles along the fracture.
- Simulations were performed to investigate the effects of fracture particles friction coefficient on the shear behaviour of fractures. The results showed that roughness had larger effects on cohesion than those of friction angle of fracture in PFC2D models. Assigning large values for friction coefficients would result in the overestimation of the fracture apparent cohesion.
- Micro-cracks development in the PFC2D model showed that at low normal stresses, sliding was the dominant failure mechanism, whereas at high normal stresses, asperity degradation and intact rock failure were dominant. As a result, the model appeared to be capable of simulating both asperity sliding and degradation during fractures shearing.
- Simulation of symmetric triangular profiles with different asperity angles showed that asperity damage increased as the asperity base angle θ increased, but in some cases asperity failure did not occur equally on all the asperities. This is thought to be due to the inherent roughness of the contact asperities which is related to the particle size distribution along asperity contacts.

- For synthetic triangular profiles it was explicitly observed that the orientation of the cut-off plane was nearly horizontal under a higher normal stress regardless of the roughness as the asperities all failed and the effect of profile roughness became insignificant. This corresponds to asperity degradation. By increasing the shear displacement, the amount of local degradations increased, which affected the residual shear stress and dilation considerably.
- For symmetric triangular profiles, the simulations corroborated the general expectations for shear strength of these profiles: the larger the asperity base angle (roughness) or correspondingly $D_{R1}$, the greater the peak shear strength.
- An analysis of critical normal stress at the transition between sliding to cut-off obtained from both analytical solutions and simulations for fractures with asperity angles of 15°, 30° and 45° showed a close agreement between the results of the two approaches. However, the simulation results appeared to be lower than those of analytical solutions. This is due to a more complicated failure mechanism at high normal stresses, which may be asperity degradation. This complexity has not been adequately captured using a simple analytical formula and therefore the PFC2D simulation results are thought to be more applicable.
- Asperity degradations for synthetic and rock-like fractures modelled in this study were observed dominantly in the post-peak shear stress region (i.e. no damage was observed before the peak); therefore the difference between residual shear strengths of fractures with different profile roughness can be identified as the rate of degradation and used for calculation of the effective degraded area of asperity contacts.
- In the simulations carried out, it was found that fracture shear behaviour was more sensitive to material internal strength (here bond strength) at high normal stresses and high asperity angles (i.e. larger profile roughness) than surface frictional properties. This is believed to be due to the extent of micro-cracks developed within the process of bond breakage.
- PFC2D simulation of a sinusoidal profile with the aspect ratio corresponding to a triangular symmetric profile showed that micro-cracks in both profile geometries developed at almost similar locations. In contrast, sinusoidal profiles exhibited larger shear strength as well as more damage compared to triangular profiles. This, from a mechanical point of view, is perhaps due to the larger surface exposed to shear in a sinusoidal profile than that of a triangular profile. This

demonstrates why $D_{R1}$ is thought to be a good representative parameter for profile roughness, as $D_{R1}$ is larger for a sinusoidal profile than a symmetric triangular profile with a similar symmetry ratio.

- A PFC2D simulation of asymmetric triangular profiles with different symmetry ratios demonstrated the effects of shearing direction on fracture shear behaviour and asperity degradation.
- For an asymmetric triangular profile, it was observed that peak shear strength and asperity degradation effectively changed when it was sheared in two opposite directions of the fracture horizontal plane (i.e. from left to right and vice-versa). This suggests that for a fracture profile, using a single roughness parameter for the estimation of its shear strength may not be appropriate but different roughness values need to be used depending on the shearing direction.
- Effects of asperity amplitude, wavelength, and number on the shear behaviour of fractures were studied based on the analysis of randomly generated profiles. It was observed that shear strength increased as the number of asperities (roughness) along the fracture plane increased. A large directional dependency of shear strength was also observed through these analyses.
- The residual shear strength of profiles with more asperities is much larger than those with fewer asperities. This shows how the existence of large amplitude asperities increases the fracture shear strength and asperity degradation.
- The shear strengths of ten randomly generated profiles obtained in both directions from PFC2D simulations were ordered according to their $D_{R1}$ values. The results demonstrated how shear strength is a function of profile roughness (here $D_{R1}$). A linear correlation fitted the data, however small fluctuations were observed.
- PFC2D simulation of shear strength of randomly generated profiles showed the applicability of this model in shear strength estimation of rough fracture profiles. Good correlations between profile roughness, $D_{R1}$ and peak shear strength of profiles were also observed.
- Four rock fracture profiles were analysed using PFC2D shearing simulations under different normal stresses and shear stress data were plotted against normal stress. The shear strength of these profiles was found to be highly correlated with the roughness parameter, $D_{R1}$.

## 5.3 Experimental analysis of fracture shearing

- Modifications applied on an existing true triaxial stress cell were explained, which was used for rough fractures shear experiments under CNL.
- Large shear and normal loading capabilities as well as large shear box size are the main features of the fracture shear cell (FSC), which enable a study of the shear behaviour and asperity degradation of rough fractures at high normal stresses.
- A duplex high pressure cylinder (DHPC) was designed and used in conjunction with the FSC to keep the normal load constant within the shear tests.
- One type of mortar was used for sample preparations to ensure similar mechanical properties for all testing samples, which also allowed a consistent comparison between lab and simulation results. The consistent geometry of synthetic and rock-like fractures allowed the reasonable comparisons of the lab results with PFC2D models.
- Similar micro-properties for both mortar material and the generated PFC2D model were used to ensure similar mechanical responses for both lab samples and the PFC2D model.
- The average UCS obtained from testing the five samples in the lab was 29.2 MPa. Based on PFC2D biaxial simulations, an average UCS of 32.0 MPa was estimated for this sample which is very close to the one obtained in the lab.
- Based on UCS tests in the lab, cohesion and internal friction of the intact sample was measured as 7.5 MPa and 29°, respectively, which is in close agreement with those of PFC2D biaxial test simulations.
- The experimental results obtained from shearing symmetric triangular fractures with different asperity angles showed how, for samples with high angle asperities (e.g. 30º and 45º asperity base angles), the induced tension cracks developed from asperity contacts, propagated through the interior of the block to some extent and then stopped. Good agreements were observed between 2D numerical simulations and lab tests.
- Large peak shear stress followed by a sharp reduction to a residual stress was observed for the rougher sample (i.e. 45° asperity angle). However, the results for the sample with a lesser asperity angle under high normal stress showed a gradual increase in shear stress but leveled off with no sudden reduction in shear stress.

- The failure pattern of the samples after the shear test showed a good agreement between the lab tests and the PFC2D results.
- A plot of $\tau$-$\sigma_n$ for the fracture with an asperity angle of 30°, corresponding to both lab experiments and PFC2D simulations, showed a similar trend for both approaches, but PFC2D appeared to overestimate the peak shear strength. This is believed to be due to the cohesive effects of the fracture particles friction coefficient laying on opposite sides of the fracture.
- From fracture failure envelopes, friction angles of 29° and 27.3° were measured from lab tests and PFC2D simulations, respectively, which showed a good correlation between the two approaches.
- Pseudo-real fracture blocks where a variation of fracture surface elevation is only in the *x-z* plane (i.e. along the sample thickness) were used for lab tests as this was thought to be the closest approach for comparison of the lab results with PFC2D simulations.
- Results of testing two fracture blocks indicated a distinguished shear behaviour depending on the shearing direction. Fracture shearing in one direction caused sliding of the upper block against the lower block and minor asperity contact damage, whereas when shearing in the opposite direction, the development of a large crack through the intact sample was observed.
- The lab experiments on both synthetic and rock-like surfaces showed that the asperity degradation affected the post peak behaviour of sheared fractures to a significantly greater extent than that of peak shear strength.
- In comparing the lab and PFC2D results, a good agreement was observed in terms of location and extent of tensile cracks after shearing of the pseudo-real fractures.
- Both PFC2D simulations and lab tests performed on pseudo-real fractures showed that the asperity with the highest amplitude would be the one which dominated the failure response of the fracture.
- A shear test of pseudo-real fracture with three sinusoidal asperities, having different amplitudes and wavelengths, showed that at high normal stresses asperities were completely detached from the lower block and could fill in the fracture aperture space as gouge material. This could, depending on the mechanical properties of the material, affect the post peak shear strength of the fracture.

- It was observed that in some cases, the values of peak shear strengths obtained from simulations were slightly larger than those obtained from lab tests at low normal stress. But at high normal stress, this difference decreased and similar values were observed from both approaches.
- Analyses of pseudo-real fractures showed why the shearing direction, as well as the state of shear stress, i.e. pre- or post peak, must be taken into account when characterising the ultimate shear strength of fractures. This is caused by surface roughness and therefore proposing an appropriate method to quantify roughness and integrate it with shear strength of the surface is important.
- The effects of shearing cycle and direction were investigated through the lab shear tests of a rock-like fracture sample. After the first cycle, a limited amount of asperity contact degradations occurred, while after the second cycle of shear test at the same level of normal stress, it was observed that the amount of degradations increased. Locations of the damaged area on fracture surface showed clearly that most of the asperity contacts were damaged after the second cycle of shear test.
- For the rock-like fracture, a large difference was observed between the peak shear strengths obtained in the first and second cycles of shearing. This is because of the predominant effects of fracture surface geometry (i.e. roughness) on shear strength. From the first to second cycle, fracture roughness evolved and therefore different shearing responses were observed in the second cycle. Expectedly, the peak shear strength of the fracture reduced as the number of cycles increased.
- Similar to symmetric triangular and pseudo-real fracture profiles, a large directional dependency was observed for the shear strength of a rock-like fracture sample.
- Assuming the basic friction angle of 31° for a rock-like fracture, the average asperity angle (i.e. roughness) estimated using Patton bilinear equation after first and second cycles of shear tests were 30.9° and 16.2°, respectively. This shows a reduction in the average asperity angle corresponding to the second cycle, which is due to the effects of asperity degradation during shearing.
- The results presented in this thesis demonstrate the capabilities of PFC2D in the estimation of fracture shear strength. The model is capable of predicting different fracturing scenarios as tested in the lab.
- For a symmetric triangular profile with a base angle, θ, a correlation was developed between profile's $D_{R1}$ and peak shear strength estimated based on

PFC2D simulations. The results indicated that the larger the $D_{R1,}$ the greater the peak shear strength of the fracture profile. Parametric cubic spline curves were used to express the shear strength in terms of profile's $D_{R1}$.

- Critical normal stress at which fracture shear strength curves intersects the intact rock material was used as the end point of cubic splines.
- The mechanical properties of the rock (cohesion and friction angle, $c$ and $\phi$) and the roughness parameter ($\theta$, which is $D_{R1}$ for a symmetric triangular profile) were other factors integrated in the correlation developed for the peak shear strength.
- Spline curves were fitted well to the shear strength data obtained from PFC2D simulations for both synthetic and rock fracture profiles. For any particular value of $D_{R1}$, it is straightforward to identify the spline control point value that gives the best fit spline to the numerical analysis output.
- Although the applicability of this correlation may be limited at this stage, it clearly indicates that $D_{R1}$ is a representative parameter to characterise profile roughness and could be employed in shear strength estimation and asperity degradation of synthetic and rock fractures.

## 5.4 Recommendations for Future work

- Using a bonded clump model to generate a rock-like assembly in PFC models is seen as a significant benefit since it may represent a more realistic mechanical behaviour of rock fractures.
- Using a smooth-joint contact model in PFC fracture shearing simulations, and assigning this contact model to all particles laying on opposite sides of the fracture track, is useful in terms of reducing the effects of the fracture particles friction coefficient on shear strength.
- Employing an expansion of the PFC models to 3D for simulations of both synthetic and real rock fracture surfaces would clearly be an important future development of this work.
- The correlation of the equivalent Riemannian roughness parameter in 3D (i.e. $D_{R2}$) with shear strength could be an interesting future investigation.
- Development of a mobilised roughness parameter which accounts for fracture shearing mechanisms, shearing direction, and evolution of surface roughness (e.g. asperity degradation) could be another future research direction.

- The lab shear experiments presented here are limited to simplified geometry for comparison with PFC2D results. Further lab experiments on more complicated fracture geometries are suggested to verify the results of PFC3D simulations.
- An investigation of scale effect and anisotropy of fracture shear strength using the presented fracture shear cell and PFC3D model is also recommended for future studies.
- One of the unfavourable incidents in hydrocarbon production is fault reactivation due to reservoir depletion or injection. Therefore, performing large scale simulations using PFC to study deformation behaviour of large scale fractures (i.e. faults) in the presence of insitu stresses and pore pressure is strongly recommended.

# References


Asadi, M.S. and Rasouli, V., 2011, PFC2D simulation of directionality in rough fractures shear strength, *in* Itasca Consulting Group, I., ed., 2nd International FLAC/DEM Symposium: Melbourne, Australia.

Asadi, M.S., and Rasouli, V., 2010, Direct shear test simulation of real rough rock fractures, Eurock2010: Luasanne, Zwitzerland.

Asadi, M.S., Rasouli, V., and Tokhmechi, B., 2009, Wavelet analysis of JRC exemplar profiles, *in* Vrkljan, I., ed., Regional Symposium of ISRM, Proced EUROCK2009: Dubrovnik, Croatia, Taylor & Francis Group, p. 215-220.

Asadollahi, P., Invernizzi, M., Addotto, S., and Tonon, F., 2010, Experimental Validation of Modified Barton's Model for Rock Fractures: Rock Mechanics and Rock Engineering, v. 43, p. 597-613.

Asadollahi, P., and Tonon, F., 2010a, Constitutive model for rock fractures: Revisiting Barton's empirical model: Engineering Geology, v. 113, p. 11-32.

Asadollahi, P., and Tonon, F., 2010b, Degradation of rock fracture asperities in unloading, reloading, and reversal: International Journal for Numerical and Analytical Methods in Geomechanics, p. n/a-n/a.

Bandis, S.C., Lumsden, A.C., and Barton, N.R., 1983, Fundamentals of rock joint deformation: International Journal of Rock Mechanics and Mining Sciences & Geomechanics Abstracts, v. 20, p. 249-268.

Barla, G., Barla, M., and Martinotti, M., 2009, Development of a New Direct Shear Testing Apparatus: Rock Mechanics and Rock Engineering, v. 43, p. 117-122.

Barton, N., and Choubey, V., 1977, The shear strength of rock joints in theory and practice: Rock Mechanics and Rock Engineering, v. 10, p. 1-54.

Barton, N., 1973, Review of a new shear-strength criterion for rock joints: Engineering Geology, v. 7, p. 287-332.

Barton, N., Bandis, S., and Bakhtar, K., 1985, Strength, deformation and conductivity coupling of rock joints: International journal of rock mechanics and mining sciences & geomechanics abstracts, v. 22, p. 121-140.

Belem, T., Souley, M., and Homand, F., 2007, Modeling surface roughness degradation of rock joint wall during monotonic and cyclic shearing: Acta Geotechnica, v. 2, p. 227-248.

Belem, T., Souley, M., and Homand, F., 2009, Method for Quantification of Wear of Sheared Joint Walls Based on Surface Morphology: Rock Mechanics and Rock Engineering, v. 42, p. 883-910.

Brady, B.H.G., and Brown, E.T., 2004, Rock strength and deformability, Rock Mechanics for underground mining, Springer Netherlands, p. 85-141.

Brady, B.H.G., and Brown, E.T., 1993, Rock mechanics for underground mining, Chapman & Hall, 571 p.

Bruno, M.S., and Nelson, R.B., 1991, Microstructural analysis of the inelastic behavior of sedimentary rock: Mechanics of Materials, v. 12, p. 95-118.

Carr, J.R., and Warriner, J.B., 1987, Rock mass classification using fractal dimension, *in* Farmer, D., Desai, Glass and Neuman, ed., Proc. 28th US Symp. on Rock Mech.: Tucson, p. 73–80.

Cho, N., Martin, C.D., and Sego, D.C., 2008, Development of a shear zone in brittle rock subjected to direct shear: International Journal of Rock Mechanics and Mining Sciences, v. 45, p. 1335-1346.

Cho, N., Martin, C.D., and Sego, D.C., 2007, A clumped particle model for rock: International Journal of Rock Mechanics and Mining Sciences, v. 44, p. 997-1010.

CSIRO, 2009, SiroVision manual: Brisbane, CSIRO earth science and engineering devision.

Cundall, P.A., 2000, Numerical experiments on rough joints in shear using a bonded particle model, *in* F.K. Lehner and J.L. Urai, E., ed., Aspects of tectonic faulting: Berlin, Springer, p. 1-9.

Cundall, P.A., and Lemos, J.V., 1990, Numerical Simulation of Fault Instabilities with the Continuously Yielding Joint Model, *in* Fairhurst, C., ed., Rockbursts and Seismicity in Mines: Rotterdam, Balkema, p. 147-152.

Cundall, P.A., and Strack, O.D.L., 1979, Discrete numerical model for granular assemblies: Geotechnique, v. 29, p. 47-65.

Dight, P.M., and Chiu, H.K., 1981, Prediction of shear behaviour of joints using profiles: International journal of rock mechanics and mining sciences & geomechanics abstracts, v. 18, p. 369-386.

Fakhimi, A., Carvalho, F., Ishida, T., and Labuz, J.F., 2002, Simulation of failure around a circular opening in rock: International Journal of Rock Mechanics and Mining Sciences, v. 39, p. 507-515.

Fardin, N., 2003, The effect of scale on the morphology, mechanics and transmissivity of single rock fractures, KTH, Sweden.

Fardin, N., Stephansson, O., and Jing, L., 2001, The scale dependence of rock joint surface roughness: International Journal of Rock Mechanics and Mining Sciences, v. 38, p. 659-669.

FJÆR, E., Holt, R.M., Horsrud, P., Raaen, A.M., and Risnes, R., 2008, Petroleum Related Rock Mechanics: Hungary, Elsevier B.V.

Giacomini, A., Buzzi, O., and Krabbenhoft, K., 2008, Modeling the asperity degradation of a sheared rock joint using FEM, 8th World Congress on Computational Mechanics (WCCM8): Venice, Italy.

Goodman, R.E., 1976, Methods of geological engineering in discontinuous rocks.

Grasselli, G., Wirth, J., and Egger, P., 2002, Quantitative three-dimensional description of a rough surface and parameter evolution with shearing: International Journal of Rock Mechanics and Mining Sciences, v. 39, p. 789-800.

Grasselli, G., 2001, Shear strength of rock joints based on quantified surface description: Lausanne.

Haneberg, W.C., 2006, Book and Software ReviewsSirovision: Environmental and Engineering Geoscience, v. 12, p. 283-285.

Hans, J., and Boulon, M., 2003, A new device for investigating the hydro-mechanical properties of rock joints: International Journal for Numerical and Analytical Methods in Geomechanics, v. 27, p. 513-548.

Herdocia, A., 1985, Direct shear tests on artificial joints, Proc. Int. Sym. on Fundamentals of Rock Joints: Bjoerkliden, p. 123-132.

Huang, T.H., Chang, C.S., and Chao, C.Y., 2002, Experimental and mathematical modeling for fracture of rock joint with regular asperities: Engineering Fracture Mechanics, v. 69, p. 1977-1996.

Huang, S.L., Oelfke, S.M., and Speck, R.C., 1992, Applicability of fractal characterization and modelling to rock joint profiles: International journal of rock mechanics and mining sciences & geomechanics abstracts, v. 29, p. 89-98.

Huang, T.H., and Doong, Y.S., 1990, Anisotropic shear strength rockjoints, Proc. Ink. Symp. on Rock Joints: Loen, Rotterdam: Balkema, p. 211-218.

Hudson, J.A., and Harrison, J.P., 1997, Engineering Rock Mechanics: an Introduction to the Principles: Oxford, Elsevier Science.

Hutson, R.W., and Dowding, C.H., 1990, Joint asperity degradation during cyclic shear: International Journal of Rock Mechanics and Mining Science & Geomechanics Abstracts, v. 27, p. 109-119.

Indraratna, B., and Haque, A., 2000, Shear Behaviour of Rock Joints: Rotterdam, Balkema.

ISRM, 1978, International society for rock mechanics commission on standardization of laboratory and field tests: Suggested methods for the quantitative description of discontinuities in rock masses: International Journal of Rock Mechanics and Mining Sciences & Geomechanics Abstracts, v. 15, p. 319-368.

Itasca Consulting Group, I., 2008, PFC2D-Particle Flow Code in two dimentions: Minnesota, USA.

Ivars, D.M., Potyondy, D.O., Pierce, M., and Cundall, P.A., 2008, The Smooth-Joint Contact Model, 8th. World Congress on Computational Mechanics (WCCM8): Venice, Italy.

Jafari, M.K., Amini Hosseini, K., Pellet, F., Boulon, M., and Buzzi, O., 2003, Evaluation of shear strength of rock joints subjected to cyclic loading: Soil Dynamics and Earthquake Engineering, v. 23, p. 619-630.

Jaeger, J.C., Cook, N.G.W., and Zimmerman, R.W., 2007, Fundamentals of Rock Mechanics (4th Edition), John Wiley & Sons.

Jiang, Y., Xiao, J., Tanabashi, Y., and Mizokami, T., 2004, Development of an automated servo-controlled direct shear apparatus applying a constant normal stiffness condition: International Journal of Rock Mechanics and Mining Sciences, v. 41, p. 275-286.

Jing, L., and Stephansson, O., 2007, Fundamentals of Discrete Element methods for Rock Enginnering: Theory and Applications, Elsevior Science

Karami, A., and Stead, D., 2008, Asperity Degradation and Damage in the Direct Shear Test: A Hybrid FEM/DEM Approach: Rock Mechanics and Rock Engineering, v. 41, p. 229-266.

Kim, D.-Y., Chun, B.-S., and Yang, J.-S., 2006, Development of a direct shear apparatus with rock joints and Its verification Tests: Geotechnical Testing Journal, v. 29.

Koyama, T., and Jing, L., 2007, Effects of model scale and particle size on micro-mechanical properties and failure processes of rocks--A particle mechanics approach: Engineering Analysis with Boundary Elements, v. 31, p. 458-472.

Kulatilake, P., Balasingam, P., Park, J., and Morgan, R., 2006, Natural rock joint roughness quantification through fractal techniques: Geotechnical and Geological Engineering, v. 24, p. 1181-1202.

Kulatilake, P.H.S.W., 1998, General Report for the session entitled Numerical Modelling – Part B, Proceedings of the 3rd North American Rock Mechanics Conference: Cancun, Mexico, p. 151-158.

Kulatilake, P.H.S.W., Shou, G., Huang, T.H., and Morgan, R.M., 1995, New peak shear strength criteria for anisotropic rock joints: International Journal of Rock Mechanics and Mining Science & Geomechanics Abstracts, v. 32, p. 673-697.

Ladanyi, B., and Archambault, G., 1980, Direct and Indirect Determination of Shear Strength of Rock Mass: Las Vegas, Preprint 80-25.

Ladanyi, B., and Archambault, G., 1970, Simulation of shear behavior of a jointed rock mass, Proc. 11th US Symp on Rock Mech: Berkeley, p. 105-25.

Lambert, C., Buzzi, O., and Giacomini, A., 2010, Influence of calcium leaching on the mechanical behavior of a rock-mortar interface: A DEM analysis: Computers and Geotechnics, v. 37, p. 258-266.

Lee, H.S., Park, Y.J., Cho, T.F., and You, K.H., 2001, Influence of asperity degradation on the mechanical behavior of rough rock joints under cyclic shear loading: International journal of rock mechanics and mining sciences, v. 38, p. 967-980.

Lessard, J.S., and Hadjigeorgiou, J., 1996, Quantifying Joint Roughness Using Artificial Neural Networks: International Journal of Rock Mechanics and Mining Sciences and Geomechanics, v. 35, p. 499-499.

Li, B., Jiang, Y., Koyama, T., Jing, L., and Tanabashi, Y., 2008, Experimental study of the hydro-mechanical behavior of rock joints using a parallel-plate model containing contact areas and artificial fractures: International Journal of Rock Mechanics and Mining Sciences, v. 45, p. 362-375.

Maerz, N.H., Franklin, J.A., and Bennett, C.P., 1990, Joint roughness measurement using shadow profilometry: International journal of rock mechanics and mining sciences & geomechanics abstracts, v. 27, p. 329-343.

Odling, N.E., 1994, Natural fracture profiles, fractal dimension and joint roughness coefficients: Rock Mechanics and Rock Engineering, v. 27, p. 135.

Olsson, R., and Barton, N., 2001, An improved model for hydromechanical coupling during shearing of rock joints: International Journal of Rock Mechanics and Mining Sciences, v. 38, p. 317-329.

Park, J.-W., and Song, J.-J., 2009, Numerical simulation of a direct shear test on a rock joint using a bonded-particle model: International Journal of Rock Mechanics and Mining Sciences, v. In Press, Corrected Proof.

Patton, F., 1966, Multiple modes of shear failure in rock, Proceedings of the1st international congress on rock mechanics, Volume 1: Lisbon, p. 509-13.

Piegl, L., and Tiller, W., 1997, The NURBS Book: Berlin, Heidelberg., Springer-Verlag.

Plesha, M.E., 1987, Eigenvalue Estimation for Dynamic Contact Problems: Journal of Engineering Mechanics, v. 113, p. 457-462.

Potyondy, D.O., and Cundall, P.A., 2004, A bonded-particle model for rock: International journal of rock mechanics and mining sciences & geomechanics abstracts, v. 41, p. 1329.

Power, W.L., and Tullis, T.E., 1991, Euclidean and Fractal Models for the Description of Rock Surface Roughness: J. Geophys. Res., v. 96, p. 415-424.

Priest, S.D., 1993, Discontinuity analysis for rock engineering.

Rasouli, V., 2002, Application of Riemannian Multivariate Statistics to the Analysis of Rock Fracture Surface Roughness: London, UK., Imperial College of Science, Technology and Medicine.

Rasouli, V., and Evans, B.J., 2010, A True Triaxial Stress Cell (TTSC) to simulate deep downhole drilling conditions: APPEA Journal, 50th Anniversary issue.

Rasouli, V., and Harrison, J.P., 2010, Assessment of rock fracture surface roughness using Riemannian statistics of linear profiles: International Journal of Rock Mechanics and Mining Sciences, v. 47, p. 940-948.

Rosso, R.S., 1976, A comparison of joint stiffness measurements in direct shear, triaxial compression, and In Situ: International journal of rock mechanics and mining sciences & geomechanics abstracts, v. 13, p. 167-172.

Sagy, A., Brodsky, E.E., and Axen, G.J., 2007, Evolution of fault-surface roughness with slip: Geology, v. 35, p. 283.

Saiang, D., 2008, Determination of specific rockmass failure envelope via PFC and its subsequent application using FLACD, Continuum and distinct element numerical modeling in geo-engineering 2008 : Proceedings of the 1st International FLAC/DEM Symposium: Minneapolis, USA, Itasca.

Son, B., Lee, C.I., and Lee, Y.K., 2001, A numerical modeling on the shear behavior of the rock joint with consideration of a discrete joint finite element, Frontiers of Rock Mechanics and Sustainable Development in the 21st Century

Swan, G., 1983, Determination of stiffness and other joint properties from roughness measurements: Rock Mechanics and Rock Engineering, v. 16, p. 19-38.

Tse, R., and Cruden, D.M., 1979, Estimating joint roughness coefficients: International journal of rock mechanics and mining sciences & geomechanics abstracts, v. 16, p. 303-307.

Vallier, F., Mitani, Y., Boulon, M., Esaki, T., and Pellet, F., 2010, A Shear Model Accounting Scale Effect in Rock Joints Behavior: Rock Mechanics and Rock Engineering, p. In press.

Verma, A., and Singh, T., 2010, Modeling of a jointed rock mass under triaxial conditions: Arabian Journal of Geosciences, v. 3, p. 91-103.

Wakabayashi, N., and Fukushige, I., 1992, Experimental study on the relation between fractal dimension and shear strength, *in* Tahoe, L., ed., ISRM Int. Conference Fractured and Jointed Rock Masses: California.

Wang, X.-b., 2006, Entire deformational characteristics and strain localization of jointed rock specimen in plane strain compression: Journal of Central South University of Technology, v. 13, p. 300-306.

Wang, C., Tannant, D.D., and Lilly, P.A., 2003, Numerical analysis of the stability of heavily jointed rock slopes using PFC2D: International Journal of Rock Mechanics and Mining Sciences, v. 40, p. 415-424.

Wu, T.H., and Ali, E.M., 1978, Statistical representation of joint roughness: International journal of rock mechanics and mining sciences & geomechanics abstracts, v. 15, p. 259-262.

Yang, Z.Y., and Chiang, D.Y., 2000, An experimental study on the progressive shear behavior of rock joints with tooth-shaped asperities: International journal of rock mechanics and mining sciences, v. 37, p. 1247-1259.

Yin, Y., Sun, P., Zhang, M., and Li, B., 2011, Mechanism on apparent dip sliding of oblique inclined bedding rockslide at Jiweishan, Chongqing, China: Landslides, v. 8, p. 49-65.

Yoon, J., 2007, Application of experimental design and optimization to PFC model calibration in uniaxial compression simulation: International Journal of Rock Mechanics and Mining Sciences, v. 44, p. 871-889.

Zhu, Z.-q., Liu, Q.-y., Zeng, F.-h., and Qing, D.-g., 2009, Effective grouting area of jointed slope and stress deformation responses by numerical analysis with FLAC<sup>3D</sup&gt: Journal of Coal Science and Engineering (China), v. 15, p. 404-408.

# Appendix

## Appendix A: Exemplar JRC profiles

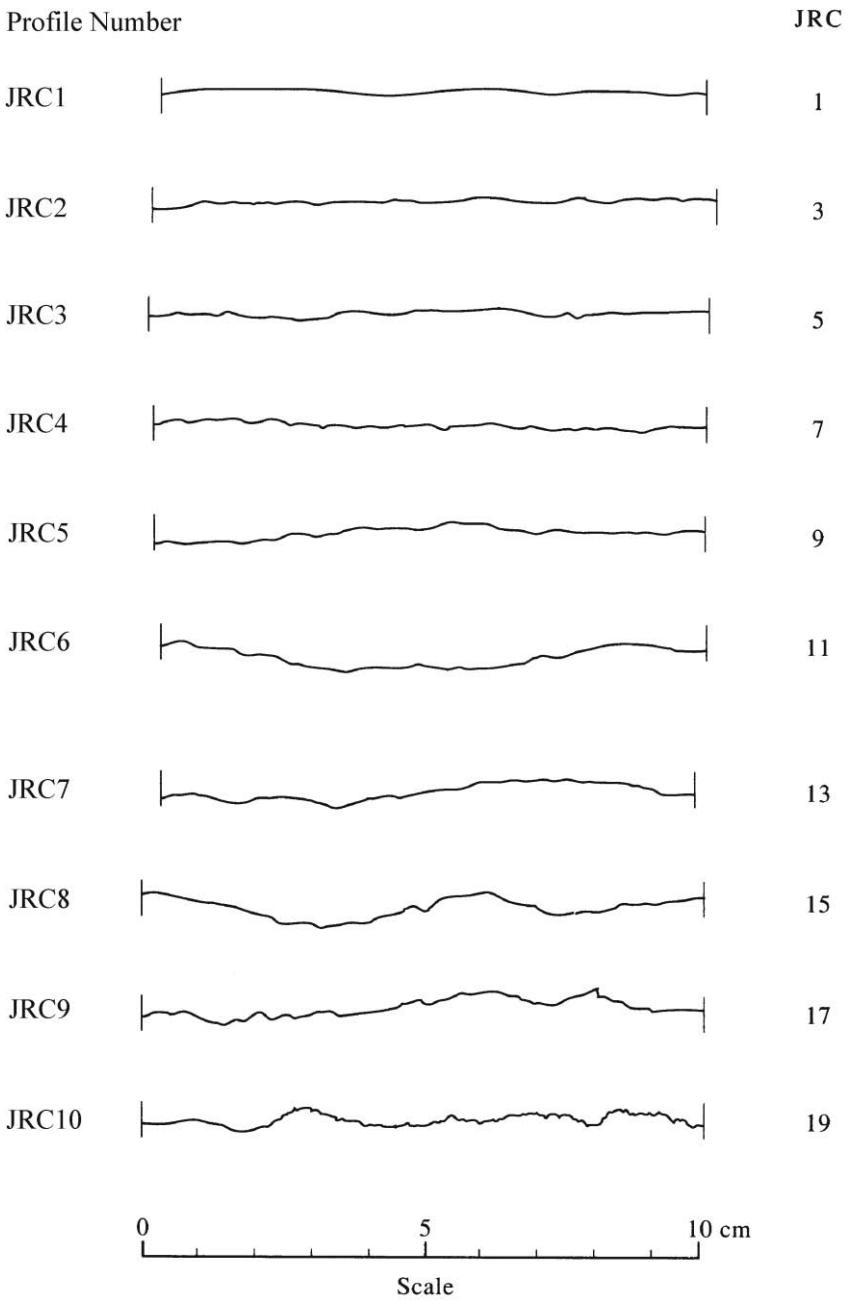


Figure A.1 Exemplar JRC profiles (Hudson & Harrison 1998).

## Appendix B: Derivation of asperity cut-off (shear) strength

As stated in Section 2.2.7, Huang et al (2002) proposed a simplified analytical model to estimate shear strength of synthetic symmetric triangular profiles with symmetric triangle asperities, as shown in Figure B.1. This mathematical expression gives the shear strength of the profile acting on the cut-off plane along which the asperity is sheared-off (broken). This model was developed based on the Mohr-Coulomb failure criterion and employs the limit equilibrium analysis of normal and shear forces acting on asperity contacts. A derivation of this equation is given here.

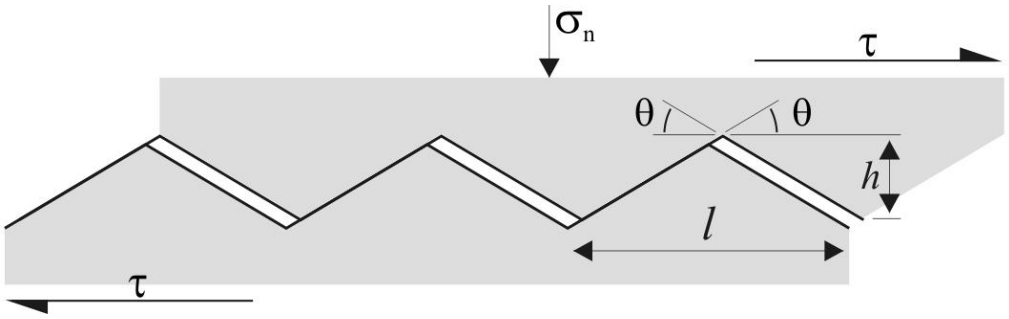


Figure B.1 View of a shear box with symmetric triangular asperity profile.

Figure B.2 shows a shear box with a symmetric triangular asperity profile with angle θ, chord length *s*, and asperity base length *l* in a material that obeys a linear Coulomb strength criterion. This profile is subjected to both a horizontal shear stress τ acting from a left to right direction and a normal stress $\sigma_n$ applied vertically, as shown in Figure B.1. The stiffness of the system is assumed sufficiently high to ensure that failures occur at the asperities' upslope (i.e. chord *s*).

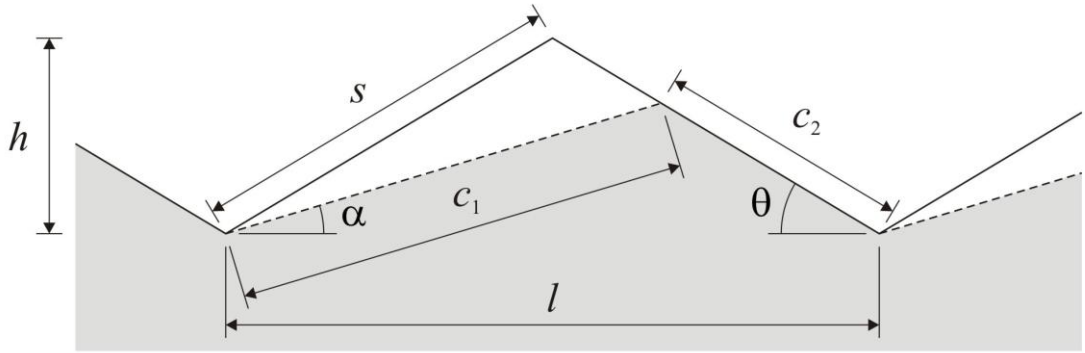


Figure B.2 Geometrical features of asperity Cut-off in a symmetric triangular profile.

The limit equilibrium analyses of the free body diagram of the broken asperity gives the resultant normal and shear forces acting on the asperity upslope (chord *s*) as $f_n$ and $f_s$, respectively (see Figure B.3). Assuming that the asperity profile is sheared-off at large normal stresses, a cut-off plane (chord $c_1$ in Figure B.3) appears through the asperity with an inclination angle of $\alpha$ (smaller than $\theta$) with respect to the horizontal plane. Accordingly, *N* and *S* are the transformed normal and shear forces acting on the cut-off plane, as shown in Figure B.3.

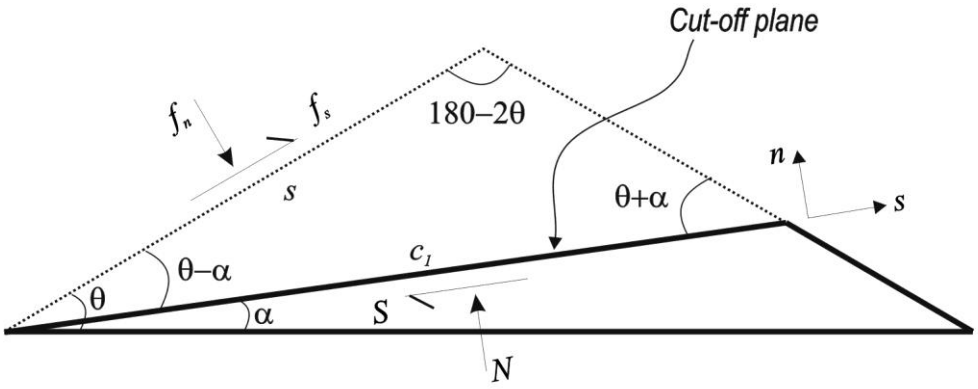


Figure B.3 Free body diagram of the sheared asperity with cut-off plane.

From this figure, *N* and *S* are determined based on a limit equilibrium analysis as follows:

$$\begin{aligned} &\sum F_s = 0 \\ &l\,\tau\cos\theta - l\,\sigma_n \sin\theta - f_s = 0\,, \\ &f_s = (\tau\cos\theta - \sigma_n \sin\theta)\,l \end{aligned} \tag{B.1}$$

$$\begin{aligned} &\sum F_s = 0 \\ &f_s\cos(\theta-\alpha) + f_n \sin(\theta-\alpha) - S = 0\,. \\ &S = f_s\cos(\theta-\alpha) + f_n \sin(\theta-\alpha) \end{aligned} \tag{B.2}$$

and

$$\begin{aligned} &\sum F_n = 0 \\ &-l\,\tau\sin\theta - l\,\sigma_n \cos\theta + f_n = 0\,, \\ &f_n = (\tau\sin\theta + \sigma_n \cos\theta)\,l \end{aligned} \tag{B.3}$$

$$\begin{aligned} &\sum F_n = 0 \\ &f_s\sin(\theta-\alpha) - f_n \cos(\theta-\alpha) + N = 0\,. \\ &N = f_n\cos(\theta-\alpha) - f_s \sin(\theta-\alpha) \end{aligned} \tag{B.4}$$

Substituting Equations B.1 and B.3 into Equations B.2 and B.4, resultant normal and shear forces (*N*, *S*) acting on broken asperity's (cut-off) plane are expressed as

$$\begin{aligned} S &= (\tau\cos\theta - \sigma_n \sin\theta) l\cos(\theta-\alpha) + (\tau\sin\theta + \sigma_n \cos\theta) l\sin(\theta-\alpha) \\ &= l\tau\cos\alpha - l\,\sigma_n \sin\alpha \end{aligned} \tag{B.5}$$

and

$$\begin{aligned} N &= (\tau\sin\theta + \sigma_n \cos\theta) l\cos(\theta-\alpha) - (\tau\cos\theta - \sigma_n \sin\theta) l\sin(\theta-\alpha) \\ &= l\,\tau\sin\alpha + l\,\sigma_n \cos\alpha \end{aligned} . \tag{B.6}$$

Considering Figure B.2, the following equation is derived for the length of asperity's chord $c_1$:

$$\begin{aligned} &\frac{l/2}{s} = \cos\theta \\ &\frac{s}{\sin(\theta+\alpha)} = \frac{c_1}{\sin(180-2\theta)} \\ &c_1 = \frac{l\sin\theta}{\sin(\theta+\alpha)} \end{aligned} . \tag{B.7}$$

Applying the Mohr-Coulomb failure criterion, the shear strength of the critical plane along which the shear failure occurs is defined in terms of stresses as

$$\tau = c + \sigma_n \tan\phi\,, \tag{B.8}$$

or in terms of forces as

$$S = c(c_1) + N\tan\phi\,. \tag{B.9}$$

By substituting amounts of $N$, $S$, and $c_1$ from Equations B.5, B.6, and B.7 into Equation B.9, this equation is expressed as

$$\tau = \frac{c\sin\theta / \sin(\theta+\alpha)}{\cos\alpha - \sin\alpha\tan\phi} + \sigma_n \frac{(\sin\alpha + \cos\alpha\tan\phi)}{(\cos\alpha - \sin\alpha\tan\phi)}\,, \tag{B.10}$$

which is reduced to

$$\tau = \frac{c\sin\theta / \sin(\theta+\alpha)}{\cos\alpha - \sin\alpha\tan\phi} + \sigma_n \tan(\alpha+\phi)\,. \tag{B.11}$$

where $\alpha$ is the inclination angle of the cut-off plane (found by evaluating $d\tau/d\alpha = 0$ which determines the minimum shear stress of the asperity along cut-off plane), $\theta$ is the asperity base angle, and $c$ and $\phi$ are the cohesion and internal friction angle of the intact rock, respectively.

Equation B.11 was initially developed based on the assumption that horizontal displacement of the specimen has caused the right chord of the lower block to have

previously separated from the upper matched block, and hence forces acting on the right side chord are zero.

From Figure B.2 it is seen that after asperity failure has taken place, the profile geometry changes to an asymmetric triangular profile with angles $\alpha$ and $\theta$ corresponding to chords $c_1$ and $c_2$, respectively, where

$$c_1 = l \sin\theta \Big/ \sin(\theta + \alpha) \tag{B.12}$$

and

$$c_2 = l \sin\alpha \Big/ \sin(\theta + \alpha). \tag{B.13}$$

As stated in Chapter 2, the normal stress above which the profile roughness will be sheared completely smooth is obtained by evaluating $(d\tau/d\alpha)_{\alpha=0} = 0$, which is expressed as

$$\frac{d\tau}{d\alpha} = \frac{c \sin\theta[\tan(\alpha+\phi) - \cot(\alpha+\theta)]}{\sin(\theta+\alpha)(\cos\alpha - \sin\alpha\tan\phi)} + \sigma_n \Big/ \cos^2(\alpha+\phi). \tag{B.14}$$

if $\alpha = 0$, then expressed as

$$\left.\frac{d\tau}{d\alpha}\right|_{\alpha=0} = \frac{c \sin\theta[\tan\phi - \cot\theta]}{\sin\theta} + \sigma_n \Big/ \cos^2\phi = 0. \tag{B.15}$$

rewriting Equation B.15, $\sigma_n|_{\alpha=0}$ corresponding to critical normal stress is defined as

$$\sigma_n|_{\alpha=0} = c(\cot\theta - \tan\phi)\cos^2\phi. \tag{B.16}$$

This estimates the normal stress at which the fracture shear strength curve intersects the intact rock failure envelope. It is noted that at normal stresses larger than the critical level, failure occurs through the intact rock. This equation was used in Chapters 2, 3 and 4 where fracture failure envelopes were plotted together with intact material failure envelopes to estimate the transition points.